The University of Sheffield

TEMPERATURE MEASUREMENT IN RAIL GRINDING

Gloria Adenike Taiwo-Adegbola

Supervisors: Professor Roger Lewis, Professor Matthew Marshall

Thesis submitted to the Department of Mechanical Engineering, University of Sheffield in partial fulfilment of the requirements for the degree of Doctor of Engineering

September 2024

Abstract

Rail grinding is now widely adopted in the rail industry as a means to maintain and renew track through damage removal and profile restoration. Conventional applications of rail grinding employ vitreous aluminium oxide grinding stone at reduced wheel speeds, feed rates and inherently, material removal rates. In an answer to the industrial driving force to increase the material removal rate without detriment to the rail surface, the use of superabrasive tooling has been proposed. To exploit its benefits of improved productivity and rail workpiece quality, superabrasive grinding must be performed using the high speed grinding (HSG) approach. However, further information is required about the thermal influence of this novel tooling application on the rail.

In this EngD research, grinding trials were performed using grinding tools suited for various grinding orientations including superabrasive and conventional grinding wheels. In addition, different temperature measurement approaches were applied during the grinding trials to ascertain and map out the temperatures induced at various depths from the surface of the rail during a grinding pass. Results show that the forces induced during the grinding action generate grinding temperatures which can be measured by the selected methods of temperature measurement.

To understand the magnitude of grinding temperatures which can be measured in the field and provide possible information regarding the range of temperatures induced on the rail during the process, temperature observations were also conducted in field settings on multiple in-service tracks during their respective grinding campaigns. Methods have been recommended for the implementation of temperature measurement in field situations.

Finally, a dedicated grinding trolley has been introduced as a vehicle for use to trial the superabrasive tooling against conventional wheels for use on actual rail. In addition to its capability for grinding facets on the rail, this machine presents the potential for use in areas where a grinding train cannot be used.

Acknowledgements

Technical Acknowledgements

I would like to thank my supervisors, Professor Roger Lewis and Professor Matthew Marshall for their indelible guidance and insight throughout the research. I am grateful for the opportunities that I have experienced, the encouragement, indelible discussions and for getting me to the finish line despite the obstacles. I am also grateful to the Industrial Doctorate Centre (IDC) for the funding opportunity and access that I had during my research. I am also grateful to my IDC colleagues for their friendship and will never forget the kindness of those who joined me to shovel ballast for the track panel barriers.

I would also like to acknowledge the contributions of various people for their close collaboration and for sharing their expertise towards this research in a variety of ways.

Name	Contribution
Mr Jamie Booth, Department of Mechanical Engineering, University of Sheffield	Machining trial instrumentation (force plate design & prototyping; fixturing) and machine operation, Grinding trolley prototype development (hydraulics)
Mr Chris Todd, Department of Mechanical Engineering, University of Sheffield	Grinding trial software instrumentation, Grinding trolley prototype development (electronics)
Mr David Butcher, Department of Mechanical Engineering, University of Sheffield	Rail sectioning and specimen extraction
Mr. Gary McKee, Advanced Manufacturing Research Centre (AMRC), University of Sheffield	Mini-project machining operation Power monitoring consult
Dr Michael Mesaritis, Department of Mechanical Engineering, University of Sheffield	Force plate design Optical microscopy Grinding trolley conceptualisation
Lucas Biazon Cavalcanti, Department of Mechanical Engineering, University of Sheffield	Force plate design iteration

Finally, I must thank the following industrial entities: Network Rail, Colas Rail, Drax and Metro dé Medellin for granting access to view grinding operations and grinding equipment during the trolley conceptualisation phase and grinding trials for temperature measurements.

Personal Acknowledgements

To God who has brought me this far, I will forever be amazed at Your grace and mercy. You have carried me through heartbreak and loss and given me the strength to finish. Thank you, Jesus.

To my very dearest husband, Oludare, thank you. For the nights you slept on the floor in the study to motivate and encourage me while I wrote, for every cup of tea, for every apple slice, for every word of prayer, for the making dinner after long shifts, for bearing with me since the day we met, thank you. Mo nífé re tọkàn tọkàn.

To my Ma, Abigail and my dad Felix, thank you for the prayers and all of your support. Mum, thank you for being the blueprint, thank you for always being a sounding board for all my random ideas during this research.

To my siblings, Hannah and Daniel. I cherish you both more than I could ever explain. Your unwavering belief in me astounds and motivates me. I could never repay you, but I will always try with cake.

To my friends, Temi, Blessing, Doja (and the beanie babies on the way), and Dara thanks for all the times you have asked me if I've graduated yet. Thank you for helping me with wedding planning while I conducted my research. You made the load easier to bear, may God bless you.

To Engr. Anthony Taiwo, my Uncle who passed away on the 8th of August 2023, thank you for paving the way and showing me that I could also become an engineer. You never got to read this thesis, but I know you are proud of my journey.

To Uncle David, who passed away in June 2019. Your loss is a huge gap, and you are sorely missed.

Table of Contents

List of Figures

List of Tables

Nomenclature

The following tables of nomenclature present the symbols and notations utilised in the thesis as well as their descriptions.

Symbol	Description	Units
α	Thermal diffusivity	$m^2 s^{-1}$
β_w	Thermal effusivity	$J \cdot (m^2 \cdot s^{1/2} K)^{-1}$
ρ_w	Workpiece density	$kg \cdot m^{-3}$
a_e	Minimum depth of cut	mm
b_w	Width of contact	mm
c_w	Workpiece specific heat capacity	$J \cdot kg^{-1} \cdot K^{-1}$
C	C-Factor	$no\ units$
d_e	Wheel diameter	mm
F_t	Tangential Force	N
h_{ch}	Chips convection coefficient	$W \cdot m^{-2} K^{-1}$
h_f	Coolant convection coefficient	$W \cdot m^{-2} \cdot K^{-1}$
h_s	Grinding wheel convection coefficient	$W \cdot m^{-2} \cdot K^{-1}$
h_w	Workpiece convection coefficient	$W \cdot m^{-2} \cdot K^{-1}$
k_g	Grinding wheel thermal conductivity	$W \cdot m^{-1} \cdot K^{-1}$
k_w	Workpiece thermal conductivity	$W \cdot m^{-1} \cdot K^{-1}$
l_c	Contact length	mm
P_t	Total grinding power	W
q_{ch}	Heat flux through chips	$W \cdot m^{-2}$
q_f	Heat flux through coolant	$W \cdot m^{-2}$
q_s	Heat flux through grinding wheel	$W \cdot m^{-2}$
q_t	Total heat flux	$W \cdot m^{-2}$
q_w	Heat flux through workpiece	$W \cdot m^{-2}$
Q_w	Material Removal Rate	$mm^3 \cdot s^{-1}$
Q'_w	Specific material removal rate	$mm^3 \cdot mm^{-1} \cdot s^{-1}$
R_w	Energy partition ratio of workpiece	$no\ units$
R_{ws}	Energy partition ratio of workpiece to the grinding wheel	$no\ units$
t	Instantaneous time	s
t_c	Duration of heating across the contact area	s
T_{max}	Maximum temperature	K
T_{mp}	Melting point	$°C$
v_s	Wheel speed	$m \cdot s^{-1}$
$v_{spindle}$	Spindle Speed	$m \cdot s^{-1}$

v_w	Feed rate	$mm \cdot min^{-1}$
z	Depth below the surface	mm
r_0	Average abrasive edge radius	μm

Abbreviation	**Definition**
CBN	Cubic Boron Nitride
HEDG	High Efficiency Deep Grinding
HPC	High Performance Cutting
HPG	High Performance Grinding
HSG	High Speed Grinding
HSS	High Spindle Speed
LFR	Low Feed Rate
LSS	Low Spindle Speed
MRR	Material Removal Rate
RCF	Rolling Contact Fatigue
WEL	White Etching Layer

1 Introduction

1.1 Motivation for the Research

Rail grinding is a contemporary maintenance process which is applied to renew the rail profile and to remove defects and damage. While in service, the rail is subject to phenomena such as prolonged cycles of rolling contact fatigue and wear which generate surface asperities such as fatigue cracks, corrugation and squats on the railhead. As such, grinding is essential for profile maintenance to ensure adequate rail-wheel contact and to forestall fatigue crack propagation.

The grinding operation is achieved through the use of rotating grinding wheels (stones) which are traversed across the length of the rail to remove material. In grinding, material removal is achieved through mechanisms such as cutting, sliding and/or ploughing, of which cutting is most optimal. The efficiency of the grinding process is largely dependent on the interaction of the grinding parameters. These include the forward feed rate, the wheel speed of rotation and the grinding pressure.

Inordinate application of these parameters may result in adverse effects on the rail surface quality. For example, increasing the feed rate may lead to increased surface roughness but decrease the subsurface hardness as a result of plastic deformation; whereas, increasing the wheel speed may result in increased material removal rate, but may also increase the surface hardness and reduce the surface roughness. The conventional method of rail grinding is performed at relatively reduced feed rates when compared to conventional surface grinding machines and increased material removal rates using a vitreous bonded grinding stone.

Conventional rail grinding methods which have been established within the rail grinding industry utilise aluminium oxide (AlO_x) grinding wheels predominantly in the face grinding and peripheral grinding orientations. Though susceptible to high rates of wear, the sustained use of AlO_x wheels in rail grinding over the years may be attributed to conservatism and adherence to the status quo. However, a significant priority of the rail grinding industry is the need to enhance productivity, efficiency whilst reducing machining costs. Therefore, the major driving force of the rail grinding process is the requirement for increased rate of material removal while improving the surface quality. This calls for innovative improvements to be made to the current conventional practice of rail grinding.

To achieve this, new technologies must be introduced or adopted into the grinding process. A novel High Performance Grinding (HPG) technology has been developed at the University of Sheffield to incorporate the superabrasive grinding approach for the grinding of rail. Effective use of this approach requires the High Speed Grinding (HSG) practice along with the implementation of a declogging mechanism. Likewise, in the implementation of this new technology, the surface quality, which is a key performance indicator of the grinding process, must be examined.

The surface quality of the grinding process is largely affected by the high temperatures which are generated as a result of the friction contact between the wheel and the rail during the grinding action. These high temperatures may result in what is known as bluing (or grinding burn), these high temperatures may also give rise in further microstructural changes in the surface layer in the form of White Etching Layer (WEL), a martensitic layer which is formed by the rapid cooling of the surface material from the high temperatures.

Little is known about the influence of the quantified thermal input on the surface quality of rail. The thesis research explores the introduction of superabrasive grinding technology this new high performance grinding practice for full size rail grinding with respect to the thermal influence on the surface quality of the rail. Along with the surface roughness, it is paramount that the subsurface microstructural effect of the new approach be understood.

To practically assess the viabilities of superabrasive grinding and temperature measurement within the rail grinding process, laboratory research is required. In addition, this research must be scaled up to industrial application in the form of field assessments on track with the implementation of these technologies. The research will therefore also provide insight to the application of the novel superabrasive technology.

1.2 Aims and Objectives of the Research

In considering the background of this research, it is clear that there is an industrial requirement to understand and predict the thermal effects of rail grinding on the track quality. As such, the aim of this research project is determined as follows:

To advance the knowledge of the thermal input on the rail surface in the use of superabrasives for the rail grinding process.

In order to achieve the aim of research, the following objectives were identified.

- To assess different temperature measurement technologies and identify new approaches to improve temperature measurement in rail grinding operations.
- To measure process temperatures during laboratory based conventional and superabrasive grinding.
- To measure rail temperature during conventional grinding in field operations.
- To assess the temperature effect on the track quality through assessment criteria which include workpiece surface roughness and microstructure.
- To develop apparatus suitable for the trial of superabrasive grinding on actual track.

These objectives have been addressed through experimental rail grinding trials, field grinding observations as well as the development of a grinding trolley with capabilities for superabrasive grinding of actual rail.

1.3 Novelty and Impact of the Research

The novelty of the research is established via multiple aspects. These are detailed as thus:

- Through the lens of in-process temperature measurement and post grind microstructural analysis, the research will provide a benchmark of the conventional approaches to grinding against the new technology via laboratory experimentation and field grinding experiments.
- In addition, the thesis will introduce a new grinding apparatus (The Grinding Trolley), through which superabrasive grinding may be performed on actual track on a smaller scale to grinding trains.

1.4 Scope of Study

The planned research methods are broken down into two overarching streams, which include field observations and laboratory experiments (Figure 1). The first aspect concerns the laboratory experiments, while the second aspect was focused on the field observation approach. The field observation approach concerned the measurement of grinding temperature during routine rail maintenance campaigns and understanding the issues associated with temperature measurement within current rail grinding conventions. The laboratory approach was adopted to allow for the implementation of multiple temperature measurement approaches within a more controlled environment.

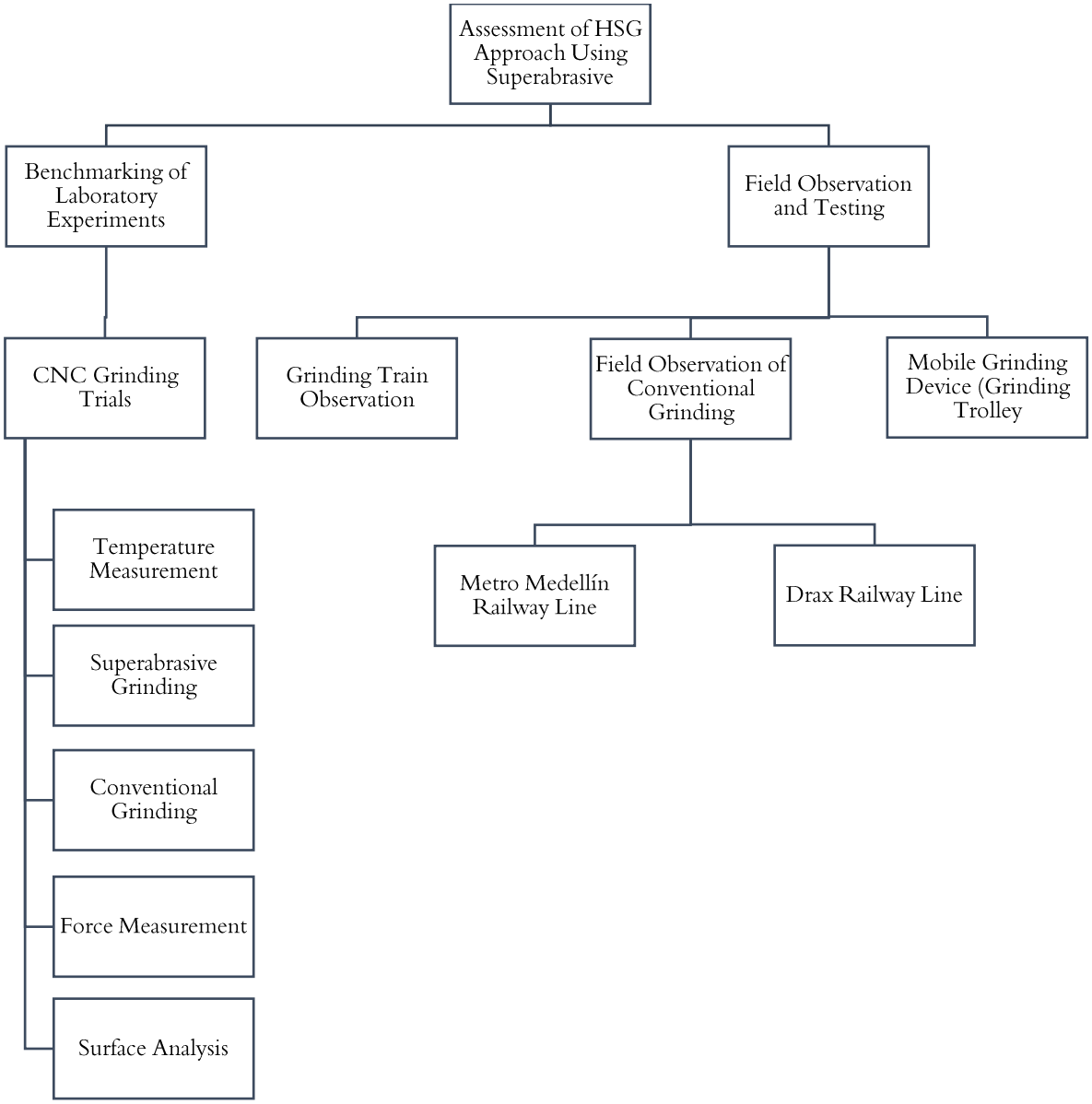

Figure 1: A breakdown of the approaches undertaken in the doctoral research

1.5 Structure of the Thesis

The work presented in this thesis focuses on the understanding of temperature measurement for rail grinding applications. The thesis is organised into 7 chapters. The current chapter provides a background to the project, details the aims and objectives of the project and presents an overview of the research methods employed in the course of study.

To establish the scene of the thesis, the subject of rail grinding will be discussed in the context of the current state of the art, the influence of temperature as well as the introduction and application of superabrasive technology within the practice. A detailed literature review is presented in Chapter 2, which considers background of rail grinding, the effects of temperature on ground rail surfaces as well as the current techniques of temperature measurement implemented in rail grinding as well as temperature modelling in the area.

Chapter 3 presents details of the field assessments of grinding which were carried out as well as the data gathered from them. Chapter 4 focuses on the methodology of the multiple phases of experiments which were performed through rail grinding trials within a laboratory setting using modified CNC machines as well as the force and temperature data gathered from them. The results of the thermal model are presented in Chapter 5.

Chapter 6 focuses on the design and development of the trolley as well as the proposed methodology to apply it for grinding operations on actual track in the field. Chapter 7 provides a discussion of the results presented in Chapters 3 and 4. Finally, Chapter 8 draws the conclusions of the research and presents causes and recommendations for further study.

1.6 Industrial Collaborators

This thesis presents a significant contribution to the development of a viable approach to improve the rail grinding process as part of the Shift2Rail, In2Track2 Rail Project at the University of Sheffield. The aim of this grinding project was to implement superabrasive grinding on a grinding trial. The objectives detailed to achieve this aim include:

- To design and develop a grinding trolley suited for superabrasive grinding.
- To develop a superabrasive grinding wheel for the grinding trolley
- To trial superabrasive wheel on a grinding train
- To compare the thermal and metallurgical effects of the conventional and superabrasive approaches on the rail surface integrity

The EngD research has been supported by a number of collaborators who have made contributions through various means. The research related to the grinding trolley was carried out in partnership with Network Rail. Likewise, British Steel provided rail sections as well as a dedicated CNC machine for possible use during the laboratory grinding trials.

2 Review of The Literature

Grinding is a machining process which is widely utilised in various industries ranging from aerospace to automotives, rail and general manufacturing. Increasingly across all industries, there is a persistent drive to improve the efficiency and productivity by finetuning different aspects of the process. This has led to the development of High Performance Grinding (HPG) techniques which are utilised in grinding practices such as Creep Feed Grinding, Speed Stroke Grinding, High Speed Grinding and others.

This research focuses on the adoption and utilisation of superabrasive HSG techniques for rail grinding. Therefore, the chapter introduces an overview of the fundamentals of the grinding process and the state of the art of rail grinding. The recent HPG technologies are described along with the processes used to improve their efficiency. Finally, temperature measurement techniques which are utilised in grinding will be presented within the context for adoption for superabrasive HSG of rail.

2.1 Fundamentals of Grinding

Grinding is an abrasive machining process which is achieved by the engagement of a grinding wheel with multiple geometrical undefined cutting edges with a workpiece to generate a defined surface through the removal of chips. Previously used as a finishing step within production, grinding has been developed into a singular machining process, as a result of the improved high accuracy at lower tolerances, high material removal rates and part quality which can be achieved. Surface grinding is performed in two modes which include up grinding and down grinding. These modes relate to the directional relationship of the wheel and the workpiece speeds. Therefore, up grinding is counter-directional while down-grinding is co-directional. The interactions of the basic elements of surface grinding strongly influence the efficiency and productivity of the process. Figure 2 depicts the peripheral down grinding mode including the basic grinding elements include the machine tool, workpiece, grinding wheel, coolant, chips formed as well as a dressing tool [1].

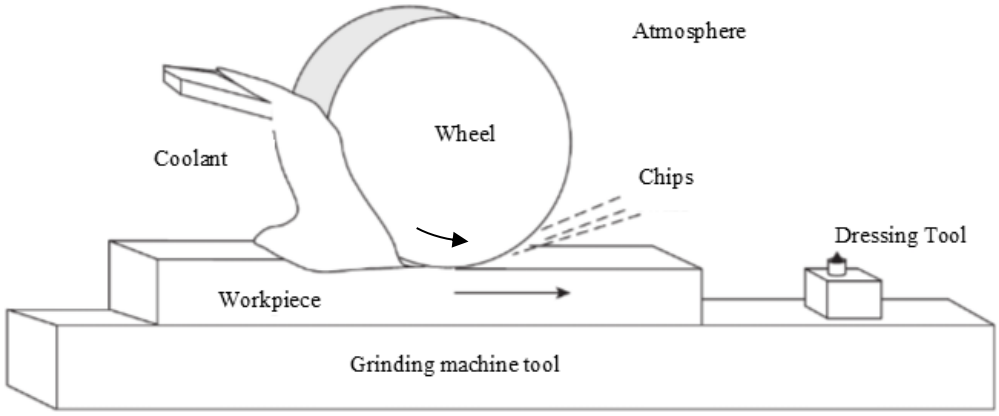

Figure 2: The basic elements of the grinding process [1]

The grinding wheel is comprised of a bond matrix and abrasive grits whose exposed cutting edges perform the cutting action on the workpiece. In the cutting action of a single grit, which is controlled by the force and path of grind, chip formation is initiated by elastic deformation and is succeeded by the plastic flow of material on the workpiece surface [2]. As depicted in Figure 3, the chip formation mechanism corresponds to the three aspects of material deformation known as rubbing (sliding), ploughing and cutting (chip formation) [3].

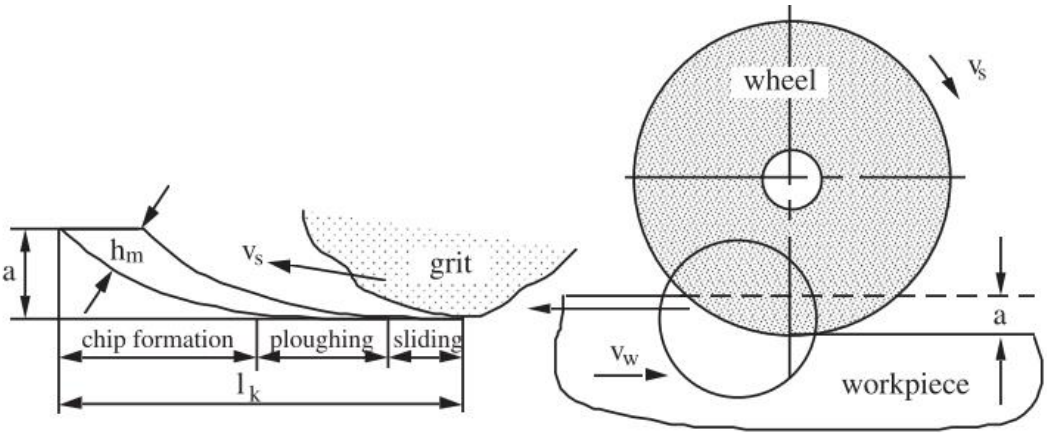

Figure 3: The stages of material deformation for chip formation [3]

In the rubbing phase, energy consumption is increased as a result of friction, while negligible material removal is realised. During the ploughing mechanism, energy consumption is increased due to the increasing force on the abrasive grit and plastic deformation is increased, but with continued negligible material removal. As such, scratch marks and ridges may be observed as the workpiece material flows onto the side of the cutting edge or beneath the grit away from the cutting edge. As a result of the unproductive friction and high energy input, measures must be taken to minimise the inefficient stages of sliding and ploughing. Chip formation occurs in the cutting phase, thus making this stage the most energy efficient phase. These numerous repetitive actions of the grits per second create a permanent superposition of engagement and result in continuous material removal.

2.2 State of the Art of Rail Grinding

Rail grinding is an industry standard maintenance process which is carried out using grinding stones (wheel) with aluminium oxide as the abrasive grains. The process is employed as a preventive or corrective measure to alleviate damage to the rail *in situ*, thus prolonging the service life of the rail. Primarily, rail grinding is carried out using the face grinding orientation, where the grinding wheel is rotated on the railhead with the end face in contact with the rail. A typical array of face grinding wheels on a grinding train is shown in Figure 4. These grinding wheels are subject to high rates of wear and are changed frequently during each grinding campaign.

Figure 4: An assembly of abrasive AlO_x grinding wheels at various stages of use beneath a grinding train.

As a defined maintenance measure, preventive rail grinding is routinely performed to remove a defined top surface layer of rail to re-impose the optimum profile for rail-wheel contact. Such operations are carried out on both straight and curved railway tracks at small and larger depths of cut respectively. As a result of the increased profile complexity and increased MRR, the preventive grinding of curved railway tracks is performed at reduced speeds. Corrective rail grinding is employed to regenerate the profile of defective or worn rail tracks and for the removal of surface cracks. Compared to preventive operations, corrective rail grinding is performed on smaller lengths of rail; however, there is an increase in the specific MRR requirement due to the increased depths of cut. The typical parameters related to preventive and corrective rail grinding processes are presented in Table 1.

Table 1: Typical parameters of current rail grinding practices. Adapted from [4]

Rail Grinding Practice		**Spindle speed (rpm)**	**Wheel diameter, d_e (mm)**	**Wheel speed, v_s (m/s)**	**Feed rate, v_w (m/s) (km/h)**	**Minimum depth of cut, a_e (mm)**
Preventive Grinding	Straight track	3500	279	51	3.4–4.5 *(12.2-16.2)*	0.1
	Curved track	3500	279	51	2.2 *(7.92)*	0.2
Corrective Grinding		1500	152–279	12–22	0.4–2.2 *(1.44-7.92)*	1mm per pass $a_{total} \geq 10$

In recent years, the surface properties resulting from rail grinding have become important due to the noise emissions on the rail network. These noise emissions are attributed to the rough surfaces generated from rail grinding as shown in Figure 5, as smoother rail surfaces have been found to reduce noise levels. The rail defects which cause these surface roughness issues may be classified into periodic and non-periodic defects [5]. Periodic defects include grooves as well as long and short waves. Non-periodic defects include cracking, chipping, burrs, overlaps, flatten joints and roll splitters. Likewise, other defects such as squats may be periodic or non-periodic.

Figure 5: Post-grind conditions of two sections of rail

The maintenance of railway infrastructure plays a significant role in ensuring its safety and quality [6]. Factors such as the high frequency loads as well as high line speeds may lead to rail degradation through rail fatigue, prolonged stress periods as well as temperature fluctuations. These factors all directly affect the surface and subsurface metallurgical properties and generation of fatigue cracks. The types of damage which occurs as a result of the continuous contact between the train wheels and the steel rails are observed on the rails as rolling contact fatigue (RCF) as well as other irregularities [7].

Rolling Contact Fatigue (RCF) constitutes a deformed layer of rail which is generated as a result of ratchetting of stress concentration and cyclic loading which leads on to crack initiation and propagation (Figure 6). Previous studies have attributed the development of RCF to several contributory factors. Rong et al. [8] determined that environmental conditions such as humidity and atmospheric temperature present a detrimental effect on the rolling contact behaviour of wheel and rail.

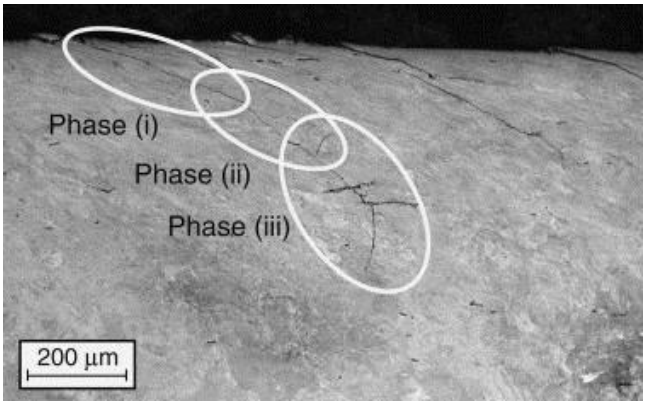

Figure 6: The three stages of a RCF crack from initiation at surface to propagation within bulk material [9]

A frequent type of rail defect which may arise as a result of RCF is gauge corner cracking in the form of shallow cracks which may appear in uniform distributions on extended section of rail or in short arrays (Figure 7) [10]. Other rail defects include squats, transverse defects (resulting in splitting of the railhead) and shelling [11].

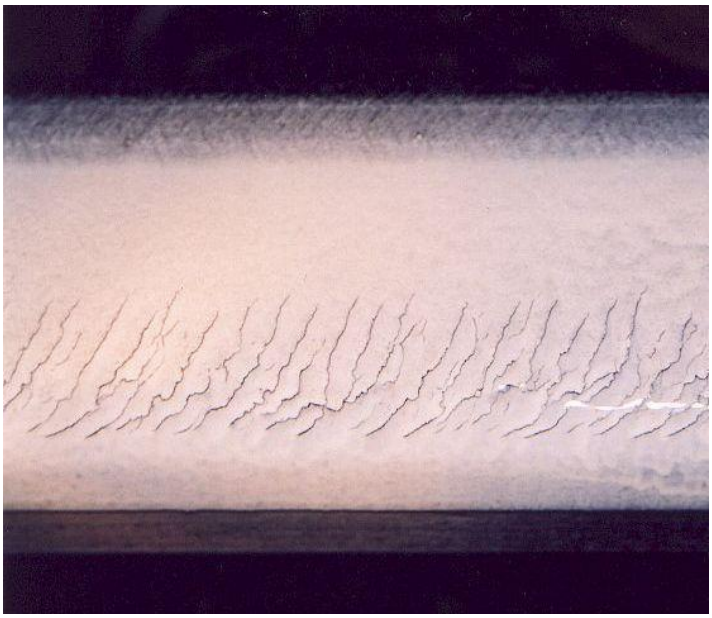

Figure 7: Gauge corner cracking obeserved on a high-speed rail [11]

Grassie [12] presents rail grinding as the industry-standard treatment solution for the alleviation of rail corrugation and periodic irregularities. Therefore, rail grinding allows for the maintenance of dimensional accuracy during rail reprofiling as well as the improvement of surface roughness.

As with other grinding processes, the productivity of the rail grinding process is dependent on the interaction of the major parameters such as the depth of cut a_e, the wheel speed v_s and the feed rate v_w (which is equivalent to the speed of the grinding train) as well as the frequency of the grinding operation. In his report, Taubert [13] previously found that the combination of increased wheel speed (High Speed Grinding) with shallow depths of cut increased the productivity of the operation.

As such, the benefits in relation to this increased efficiency can be applied to the rail grinding process.

As observed by Satoh and Iwafuchi [14], the process of the surface layer removal is achieved through the action of cumulative rolling contact fatigue, thus allowing for regions of rail with increased strain or plastic deformation to be removed. Different forms of defects may be present on in-service rails at various depths, sufficient depths of cut must be selected for effective rail grinding. However, as observed in the literature, increased depth of cut can lead to an increase in surface roughness and surface layer transformation [15, 16]. This can be attributed to the corresponding increase in the chip thickness and contact length as well as the number of engaged cutting edges which increase the grinding force.

Unlike other surface grinding processes such as creep feed and speed stroke grinding, modern rail grinding is considered a high performance dry grinding operation due to the high feed rates and cutting speeds. Additionally, the wheels employed in conventional rail grinding generally comprise of larger grain sizes with other grinding technologies [15]. Also known as grinding stones, conventional rail grinding tools are of the form of cylindrical grinding wheels which are often composed of fused AlO_x or/and ZrO_x abrasive grits in a resinoid bond [17]. Examples of typical rail grinding stones utilised in the UK rail network are shown in Figure 7. In order to maintain a self-sharpened cutting surface, the grits undergo fracturing sue to their friability or are dislodged from the bond during the grinding action. This aggressive operation results in increased wear and incessant consumption of the grinding stones during the rail grinding process.

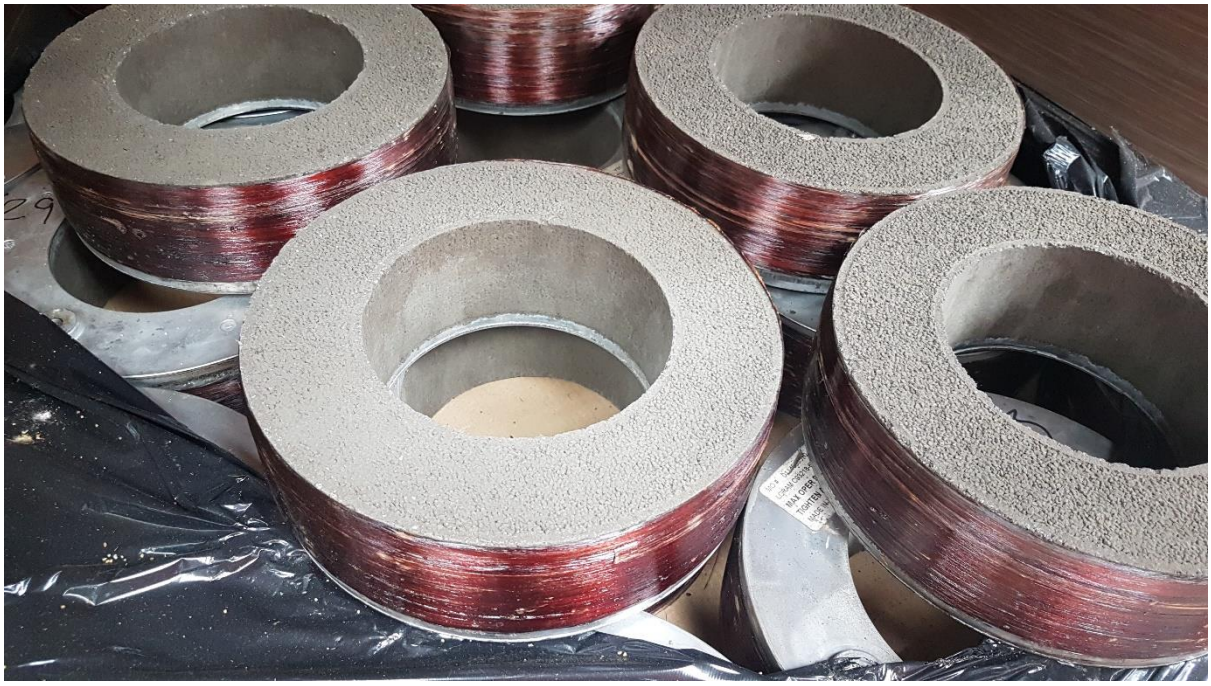

Figure 8: Typical AlO_x rail grinding stones with the exposed active surfaces

Typically, rail grinding is carried out by grinding trains which are equipped with multiple electrical motor-driven grinding wheels situated just above the rail. It is primarily a face grinding operation, where grinding is performed using the face of the grinding wheel on a non-rotational workpiece (i.e., rail); however, peripheral rail grinding is also performed for the removal of features such as lipping which could occur during face grinding on the sides of the railhead. The high cutting speed as well as the size and shape of the abrasive grits of the rail grinding wheel largely influence the material removal behaviour of the grinding operation [18, 19]. Additionally, these factors can also influence the thickness of the white etching layer (WEL) observed on the rail [20]. The brittle nature of this martensitic WEL causes the further susceptibility to crack initiation on the railhead. Steenbergen [21] discussed the behaviour of WEL following a grinding operation and presented further micrographs in the days following the return of the rail into service (Figure 9). This study asserts that the thickness of the WEL and the growth of any such cracks may be dependent on the hardness of the rail and the tonnage frequency on the rail.

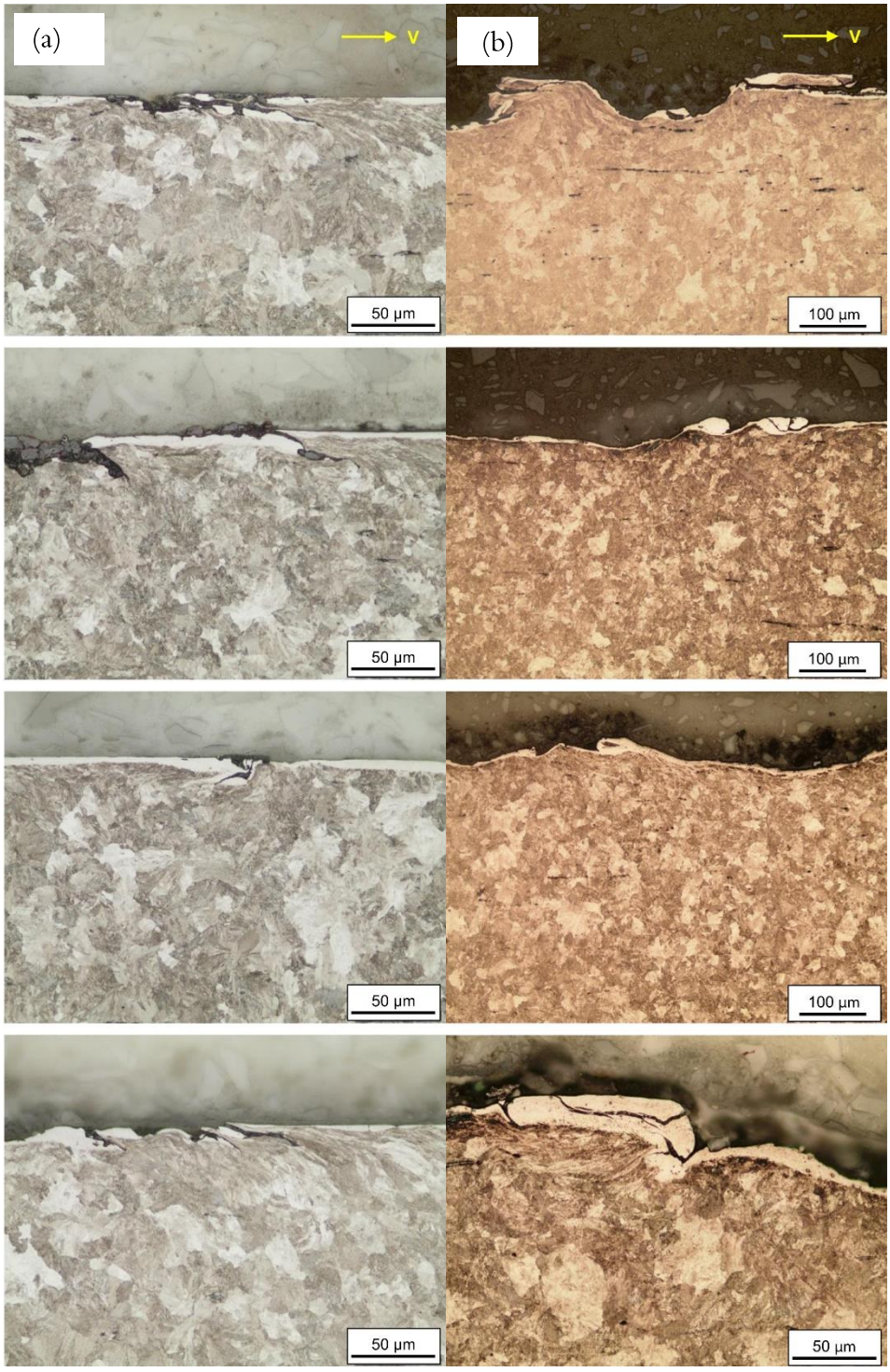

Figure 9: Micrographs depicting the presence of WEL on the longitudinal cross-section of heat-treated R370crHT rail (a) immediately after the grinding operation and (b) days after rail was returned to service [21].

As shown in Figure 10, the face grinding method of rail grinding results in a larger contact area, thus causing higher heat generation than the peripheral grinding method. Due to the dry nature of the operation (wherein no coolant is present during grinding), the heat generated by the face grinding method may not be sufficiently eliminated from the grinding zone and the grinding wheel is therefore prone to clogging. Improper grinding techniques may result in significantly detrimental

metallurgical effects on the rail surface subsequent to the rail grinding operation. This is observed as a WEL, a hardened layer on the rail surface which is brought about by two mechanisms [22]. One mechanism is the incessant increase in strain energy which causes the dissolution of cementite in the pearlitic matrix, thus forming a hardened non-crystalline nano-structure of higher hardness than the bulk material [23]. The second mechanism is attributed to the increase in the thermal input at the contact zone which results in the surface material achieving austenisation temperature, thus causing a martensitic phase transformation [24].

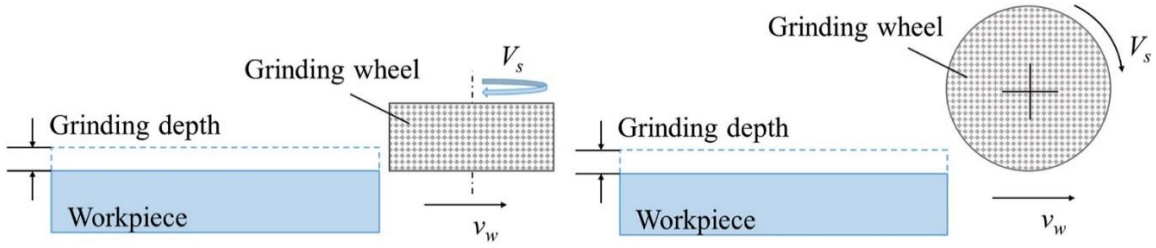

Figure 10: Fundamental principle of face and peripheral grinding of a workpiece [25]

Through metallographic assessments, studies have observed the effect of rail grinding on the rail contact [7, 26]. Steenbergen [27] discusses the severity of the effects of rail grinding on the initiation of RCF in typical and heat-treated pearlitic rails. Following grinding operations, this study found the presence of friction-induced martensite (FIM) on both the standard and non-standard rails; however, differing behaviours were observed in the rails when subject to rail-wheel contact under train operation. The grinding of the heat-treated rail caused the accumulation of FIM in groove edges which were lodged deeper into the bulk pearlite matrix upon the return of rail to service under train operation.

The presence of FIM in groove edges were observed immediately after the grind and in the days after the rail was returned to service. These FIM features are detrimental to the heat-treated rail, as they heighten the susceptibility of the rail to severe crack initiation. On the other hand, the FIM which resulted from the grinding of the standard pearlitic rail was eliminated by delamination subsequent to its return to service under train operation.

The study by Zhou et al. [25] showed that the dominant wear mechanism of the rail grinding wheel is abrasive grain fracture. This is attributed to the adhesion of rail material to the grains as well as wear flats which result in the increase in grinding forces, thus subsequently causing abrasive grain fracture. This dominant wear mechanism is deemed beneficial as it allows for the regeneration of the surface of the grinding wheel; however, this benefit is diminished as a result of material adhesion which reduces grinding efficiency while the grinding forces and temperature increase.

In their experimental simulation of rail grinding, Zhou et al. [28] determined that the surface quality of the rail was inversely affected by the applied normal grinding forces; however, due to the reduce chip thickness, a reduction in the grinding efficiency can be observed at lower forces. The influence on the grinding efficiency is consistent with the material removal behaviour, wherein

spherical debris with higher oxygen content was observed at lower grinding forces and curled chips with reduced oxygen content observed at higher forces (Figure 11). This indicative of the occurrence of oxidation of chips during the grinding operation.

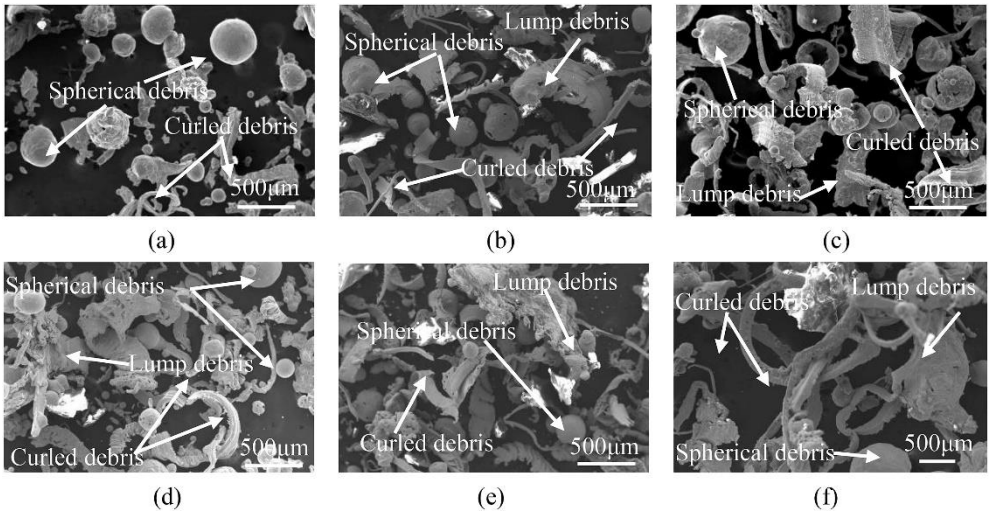

Figure 11: A compilation of SEM images depicting the presence of spherical grinding debris at lower forces grinding compared to curled chips at higher forces for various rail grades ((a) R80, 1600 N, (b) R80, 1800 N, (c) R80, 2000 N, (d) R80, 2200 N, (e) R300, 2200 N, (f) R13, 2200 N) [28]

In addition to material removal mechanisms, the workpiece surface integrity is largely affected by the temperatures generated which can cause grinding burn on the rail head. Other important process variables which govern the rail grinding process include the angle of contact between the rail and the grinding wheel as well as the applied grinding pressure. In their research, Kuffa et al. [29] found that separating the rail grinding operation into the roughing and finishing stages by grinding at different depths of cut can lead to improved surface roughness as well as reduced acoustic emissions. This is corroborated by the findings of the finite-element based study by Zhang et al. [16], which found that despite a reduction in MRR, increasing the number of grinding passes results in reduced forces which lead to improved transverse and longitudinal surface roughness (Figure 12).

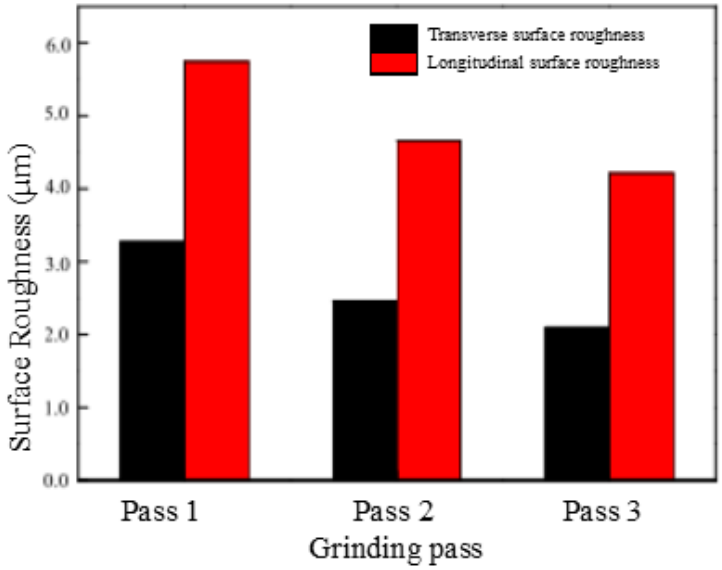

Figure 12: Experimental results depicting the change in surface roughness with multiple passes in rail grinding [16]

Besides the effect of roughness on acoustic emissions, the surface roughness of the ground rail can greatly influence the topography and inherent interaction of the train wheel/rail contact. Subsequent to a grinding campaign, the rail roughness is likely to rapidly decline within the first few days of traffic. An example of this is observed in the work by Lundmark et al. [30], which reported a decrease in the surface roughness S_a from 10 μm for a newly ground rail to 1 μm over 32 hours of 260, 800 tonnes of traffic. This rapid decline of the surface roughness gives some basis for more frequent rail grinding; however, a balance is required between the productivity of the process (including cost) and managing the rail roughness post-grinding.

2.3 High Performance Grinding Practices and Apparatus

Subsequent to other machining processes such as milling and broaching of components, conventional grinding was initially considered a finishing process which was employed to achieve desired surface finish and dimensional accuracy. Conventional surface grinding methods include pendulum (reciprocal) grinding. Pendulum grinding is characterised by a shallow depth of cut and high feed rate. Material removal is achieved by reciprocally passing the workpiece in a backwards and/or forward motion while also simultaneously incrementing its downward movement.

High performance grinding (HPG) is a broad term which refers to grinding practices driven by requirement to improve productivity, reduce the cost of production while maintaining and improving the product quality. These practices also contribute to higher efficiency and precision in conventional grinding process. HPG techniques provide various opportunities for improvement to conventional grinding processes. HPG includes practices such as increased wheel speeds (high speed grinding), higher feed rates (high performance cutting) and higher feed rates at larger depths of cut

(high efficiency deep grinding). In this section, multiple HPG grinding techniques are discussed and presented.

2.3.1 Creep Feed Grinding

Creep feed grinding (CFG) is a surface grinding technique which has been implemented by the machining industry as a result of its combination of high shape accuracy with high material removal rates [31]. It is often defined in comparison to the conventional pendulum grinding and is characterised by slow feed rates and larger depths of cut. Theoretically, these features of CFG generate high productivity and good surface finish for components with simple to more complex profiles and precise shapes. As such, with most finishing processes, CFG can be employed for grinding of components in a minimal number of passes.

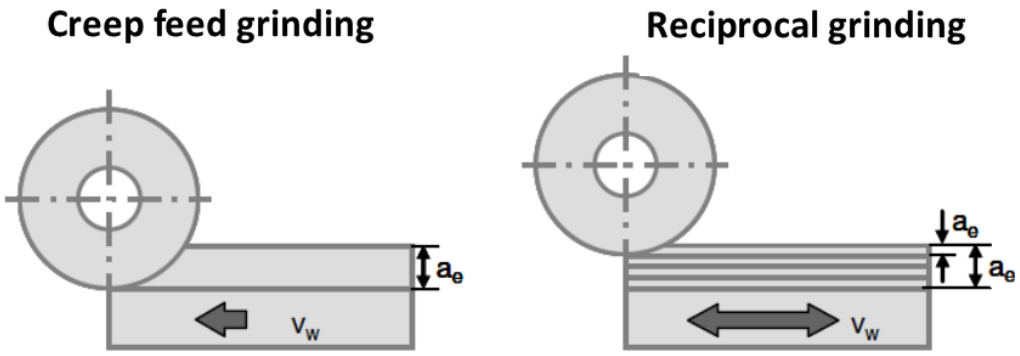

Figure 13: Fundamentals of creep feed grinding and reciprocal grinding [2]

As shown in Figure 13, the change in parameters leads to longer contact arcs lengths (l_c) as well as an increased contact distance for each abrasive grit. This increases the grit's susceptibility to a rubbing wear mechanism and exacerbates the rate of dulling of the grinding wheel and increased wheel loading. In turn, these factors lead to increased sliding forces, specific energy and subsequently grinding temperature. Likewise, the reduced feed rates also allow for longer periods of heat conduction into the workpiece, thereby contributing to grinding burn.

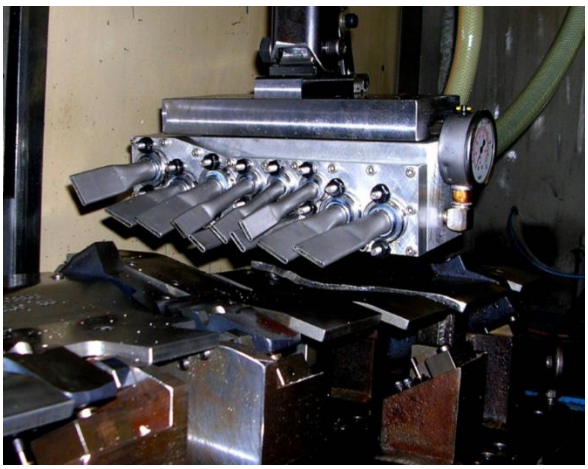

Figure 14: A manifold array of flat nozzles for creep feed grinding [32]

Though heat is conducted through the chips generated from the workpiece, the high temperatures generated in the process of CFG has led to a requirement of effective coolant delivery methods. In order to allow for adequate delivery across the full arc contact length, complex coolant jet delivery is critical to CFG processes. As shown in Figure 14, flat nozzles are employed in CFG processes to flood the grinding zone. This is adapted in processes such as VIPER grinding, which employ adjustable nozzles that become important in the light of wheel consumption as the operation progresses. On the other hand, the primary purposes of copious coolant application in CFG processes are to primarily reduce the onset of thermal damage in the form of grinding burn onto the workpiece, and secondarily to flush chips away from the grind zone. However, Malkin and Guo [33] have shown that effective cooling may be achieved below the critical burnout temperature, above which film boiling is likely to occur.

The advantage of the larger depth of cut and reduced feed rates of the CFG process is the reduced force per grit at a constant specific material removal rate (Q_w'). The grinding wheels employed in the CFG process are often comprised of grits with softer grades than in conventional grinding. This allows for attrition of the grits which leads to self-sharpening action and wheel regeneration [34]. With the CFG process, wheel regeneration is commonly achieved through continuous or intermittent dressing.

2.3.2 Speed Stroke Grinding

As the demand for more efficient grinding processes have increased, so have the requirements for improved the surface properties of workpiece. The high residual stresses observed in the surface layer are largely influenced by the thermochemical influences on the workpiece during the grinding operation. For rail workpieces made of steel, the thermochemical loading often leads to alteration of the surface microstructure, microcracks, tempering as well as rehardening as a result of martensite formation [35]. Likewise, the high residual stresses in the workpiece are tensile in nature and increase the propensity for crack formation; whereas compressive residual stresses are more desirable in their prevention of crack formation and improved fatigue properties.

Speed stroke grinding (SSG) is an alternative to conventional surface grinding processes which allows for the input of high compressive stresses and low temperatures into the workpiece though the application of extremely high feed rates as well and reduced depth of cut [36]. According to Duscha et al. [37], reciprocal grinding operations are classified as SSG grinding processes when the workpiece feedrate exceeds 50,000 mm/min. The process is characterised by the high workpiece feed rates as well as shallow depths of cut (Figure 1) and thus features smaller values of l_c in comparison with CFG. The reduced arc length of contact results in a lower for rubbing therefore allows for reduced engagement of each grit with the workpiece.

In contrast to the conventional reciprocal grinding methods which employ feed rates of up to 30,000 mm/min [1], feed rates of up to 200,000 mm/min may be achieved with SSG [36]. In order

to perform SSG, the machine's workpiece table is subject to high accelerations of up to 50m/s^2, which is achieved through direct linear drives comprising of an impulse decoupling system which consists of eddy current brakes and spring dampening elements [38].

The increased specific material removal rate of the SSG process is achieved as a result of the large amount of active cutting edges which are engaged in quick succession over a short period of time [39]. Likewise, the chip formation mechanics (Equation 1) show that the simultaneous reduction of depth of cut and increase in feed rate results in the increase of the chip thickness, $h_{cu,max}$.

$$h_{cu,max} = c_{gw} \cdot \left(\frac{v_w}{v_s}\right)^{e_1} \cdot \left(\frac{a_e}{d_{eq}}\right)^{\frac{e_1}{2}} \quad (1)$$

where c_{gw} is the constant of grinding wheel topography, e_1 is an exponent to define the influence of the inputs in the brackets and d_{eq} is the equivalent grinding wheel diameter. Based on the chip formation mechanics, the reduction in the speed ratio v_s/v_w increases the chip aspect ratio (the ratio of chip thickness to chip length). The reduced length of the run-in and run-out phases of speed stroke grinding may generate high force gradients; however, the specific grinding forces are reduced at higher feed rates. This reduces the friction, thus decreasing the thermal effects on the workpiece surface as well as the effect of the workpiece material hardness [40]. The interaction of these parameters results in the generation of high material removal as well as reduced forces [41].

Previous studies by Zeppenfield [38] and Duscha et al. [39] alluded to the effects of speed-stroke grinding on the chip formation mechanisms. The high feed rates of the speed-stroke grinding process favours earlier chip formation which improves the propensity for an increased maximum undeformed chip thickness [38, 42, 39]. Likewise, the simultaneous increase in feed rate and decrease in depth of cut favours a higher aggression factor for a constant specific material removal rate.

The aggression factor, F_a, is a grinding measure which was introduced by Badger (Equation 2) [43]. This factor relates to the chip thickness value previously mentioned and is an indicator used by machine operators to determine optimal values of Q'_w without affecting performance indicators such as the chip thickness, grinding force and surface quality [44, 45].

$$F_a = 16.7 \frac{v_w}{v_s} \sqrt{\frac{a_e}{D}} \quad (2)$$

where F_a is the aggression factor (dimensionless), v_w is the feed rate (mm/min), v_s is the wheel speed (m/s), a_e is the effective radial depth of cut (mm) and D is the wheel diameter (mm).

Wheel wear is expected to increase with increasing aggression. Therefore, a significantly low value of aggression increases the propensity for dulling of the grains in the grinding wheel, while a relatively high value of aggression is indicative of grain pullout and bond fracture within the wheel [45]. As Equation 2 shows, a reduction in the speed ratio v_s/v_w results in an increase in F_a. An

increasing feed rate results in the increase in the number of active cutting edges over time [42, 39]. Therefore, with the high feed rates which can be achieved by the speed-stroke grinding process, the overall interaction of these parameters must be considered.

2.3.3 VIPER Grinding

Very Impressive Performance Extreme Removal (VIPER) grinding is a high efficiency grinding process which was developed as an iteration and alternative the machining of components such as turbine blade roots, which require indexing within a single clamping operation to generate complex profiles and features of which CFG may be unsuitable [1, 46]. It is a patented process which was developed by Hill et al. [47] to increase productivity of conventional grinding through advances to the machine tool, coolant delivery as well as the composition of the conventional grinding wheel (e.g., AlO_x).

In the VIPER process, coolant is directed both through the spindle and into the grinding wheel at high pressure (50–70 bar) ahead of the grind zone. Through the centrifugal force of the wheel during the grinding action, the coolant is expelled onto the grinding zone, thus enabling simultaneous cooling and cleaning of the wheel (Figure 15). The major characteristic of the VIPER process is the programmable nozzles which allows for the optimisation of nozzle orientation for the operation which is carried out [46].

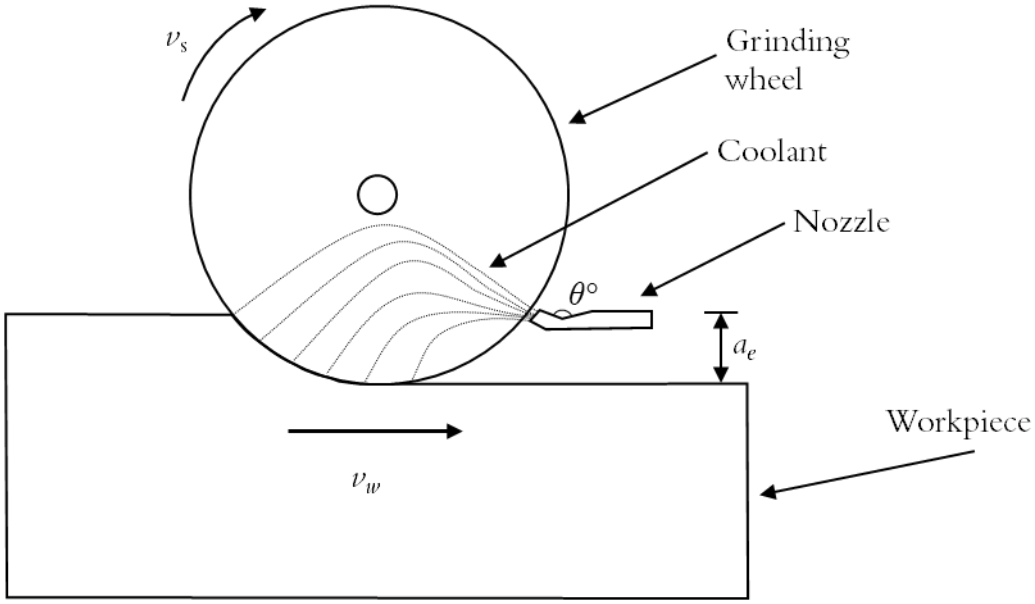

Figure 15: Principle of VIPER grinding

In order to support the higher porosity, the grinding wheels which were designed for the VIPER process by Tyrolit (Viper Ultra, Figure 16) are specialised with higher bond strength than the typical wheels of CFG [48]. The open structure of the VIPER wheel increases coolant ingress within the wheel and chip retention whilst maintaining the wheel form or profile.

Figure 16: The Tyrolit Viper Ultra Wheel which is specialised for the VIPER Grinding Process [49]

In comparison to conventional creep feed grinding, the VIPER process provides reduced grinding temperatures as well as mechanical and thermal loads thus reducing the propensity for thermal damage to the workpiece and improving the surface integrity. As a result, the increased specific material removal rate Q'_w can be achieved with 100 $mm^3/mm{\cdot}s$ in intermittent dressing and up to 300 $mm^3/mm{\cdot}s$ under continuous dressing [50]. Other advantages provided include reduced cycle time as well as production costs, prolonged wheel life and the achievement of higher aggression based on the increased scope of parameters (depth of cut and feed rate).

2.3.4 High Speed Grinding (HSG)

High speed grinding (HSG) comprises of the use of increased peripheral cutting speeds v_s to achieve increased specific material removal rates increased as with. According to Tawakoli [51], HSG includes any grinding processes where the peripheral wheel speed is greater than 60–80 m/s. The benefits recognised with the increased v_s is the reduction of the maximum chip thickness which allows for reduced surface roughness and grinding forces.

However, a major disadvantage is the initial increased thermal input to the workpiece surface [52]. According to Hitchiner [53], this may be avoided by increasing the wheel speed above 100 m/s (Figure 17). At these higher wheel speeds, the thermal input is dissipated across the workpiece surface prior to penetration into the depth of the workpiece. However, due to the higher wheel speeds, the heat is expelled by subsequent chips which are generated from that surface. At speeds less than 100 m/s, the influence of temperature on the surface can be mitigated through the combination of HSG with increased workpiece feed rates. Although the single abrasive loads are minimally increased, very high specific material removal rates can be achieved without adverse effect on the workpiece material.

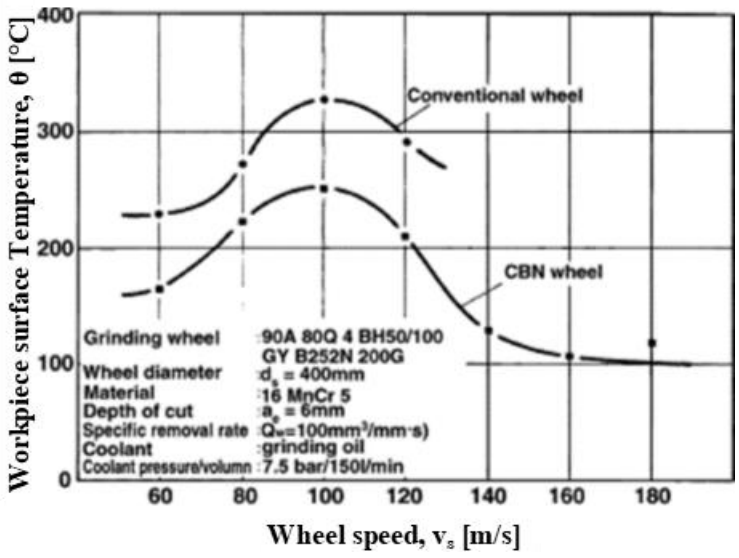

Figure 17: Relationship between workpiece surface temperature and wheel speed for conventional and CBN grinding wheels [53, 54]

In order to withstand the operational speeds in HSG, advanced grinding tools for these practices require properties such as high hardness, wear and fracture resistance as well as improved damping, stiffness and higher thermal stability. Typical grinding wheels employed in HSG include superabrasives such as cubic boron nitride (CBN) and diamond, as well as efficient aluminium-based conventional abrasives such as sintered aluminium oxide (Al_2O_3) and sintered aluminium oxide-nitride (AlON) [54].

Through CAD/CAM simulations, a viability study carried out between the Department of Mechanical Engineering and the Advanced Manufacturing Research Centre (AMRC) at University of Sheffield [4] explored the opportunities for HPG practices to improve the efficiency of rail grinding applications. The options presented include HSG and HEDG, a grinding process which involves the use of high feed rates and wheel speeds. The study considered the use of superabrasive tooling for rail grinding application as an alternative to the conventional AlO_x grinding wheels which are in current use in the industry. This method is potentially beneficial in the reduction of specific grinding energies within the current rail grinding operations and can therefore achieve higher rates of productivity. This was attributed to the longer wheel life and reduced wear rates of superabrasive grinding wheels when compared to conventional corundum grinding wheels.

There is potential for knowledge about the surface quality of the rail under these HSG and HEDG practices; however, the influence of temperature is yet to be largely explored. In their investigation, Liu et al. [55] employed a passive (peripheral) grinding machine in their study of the influence of the grinding time and number of passes on the HSG of rail. Unlike the active face grinding method, the motion of the grinding wheel is propelled solely by the grinding train; likewise, the contact of the grinding wheel to the rail surface is achieved solely by the grinding pressure and the deflection angle θ (Figure 18). Therefore, the HSG is achieved by the speed of the grinding train. Their research reported improved surface quality and reduced grinding temperature

influence for multiple passes conducted at shorter intervals than with passes conducted at longer interval.

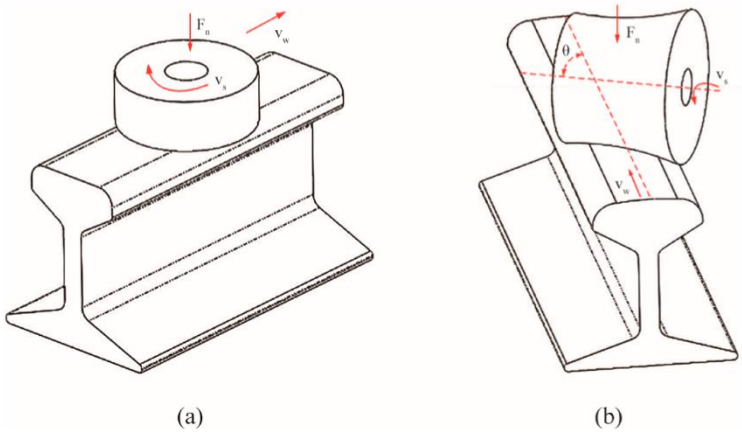

Figure 18: A schematic of the interaction of the grinding wheel in (a) the face (active) and the peripheral (passive) rail grinding approaches [56].

The measurement of temperature in the HSG processes can provide a basis for the understanding of the workpiece quality and surface integrity for these applications. As such, several temperature measurement technologies are presented in the following section with a further exploration into the current measurement practices in the context of rail grinding.

2.4 Temperature Assessment Technologies in Grinding

As an energy intensive machining process, the interaction of the governing parameters of the grinding process requires careful selection to avoid the introduction of high temperatures into the workpiece. In metallic materials, the presence of high grind zone temperatures results in grinding burn, which may be physically observed as discolouration of the workpiece surface. Surface burn may be attributed to both thermal and mechanical influences. This is known as grinding burn, which occurs as a result of oxidation.

A review by Komanduri and Hou [57] elucidated the experimental temperature measurement techniques which are used in manufacturing processes. Figure 19 shows the historical timeline of measurement techniques developed for thermal measurement in material removal processes, some of which include thermocouples, thermography, and radiance thermometry [58]. These techniques are influenced by factors such as surface emissivity, reflection, surface characteristics and resolution of sensor. As observed by Davies et al. [58], thermocouples and infrared technology are the common apparatus which have been iterated over the years as the promising methods of temperature measurement.

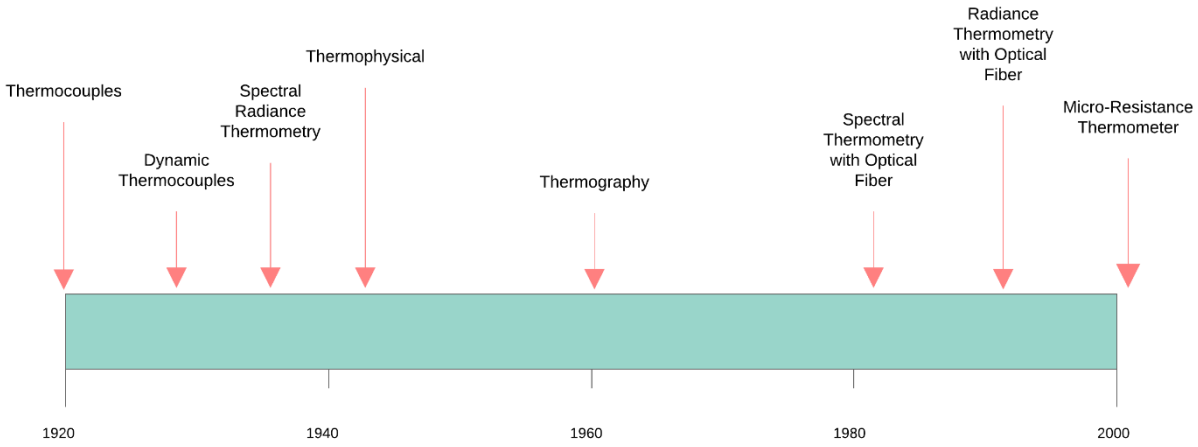

Figure 19: Historical timeline of thermal measurement techniques for material removal processes (adapted from [58])

The potential quicker response times of optical fibres in comparison to thermocouples led to the research of their application within the grinding process. Ueda et al. [59] developed the infrared radiation pyrometer technique in an attempt to improve the sensor response time. In this technique, optical fibres are used in conjunction with an InAs and Ge cell to guide infrared radiation onto single active grains in order to sense the temperature in the immediate aftermath of a cutting operation.

The delayed measurement of the temperature response of the grains subsequent to cutting introduced an inaccuracy into the system. As such, Ueda et al. [60] further iterated the technology by employing a fused fibre coupler, thus developing a two-colour pyrometer (Figure 20) which improved the measurement of rapid temperature changes on the single grains. Results from this study showed that over the course of the cutting action of the grains on the workpiece, the rate of increase in temperature could extend up to 10^7 °C/s.

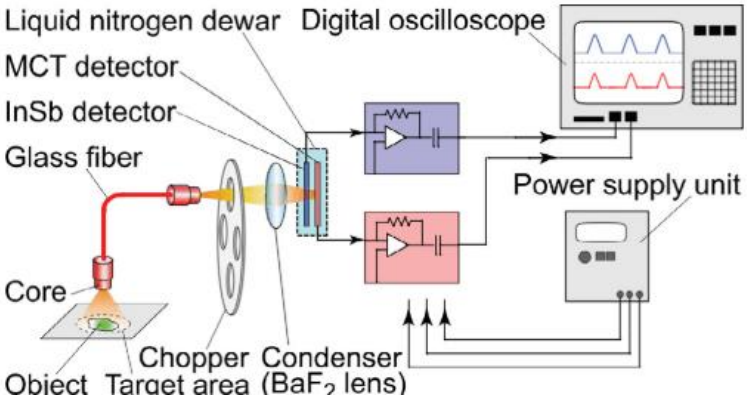

Figure 20: Two-Colour pyrometer developed by Ueda et al. for the measurement of single grain temperatures subsequent to cutting action [61]

It has been observed that most of the existing experimental temperature measurement techniques typically present the maximum temperature of the workpiece. However, when related to the material thermal properties, knowledge of the temporal gradient may also prove beneficial to the prediction and detection of the onset of phase transformation and effectually grinding burn. This is

addressed in the work by Baumgart et al. [62], who employed a two-colour pyrometer comprising of coupled rotary and stationary fibres for cylindrical grinding. In their assessment of different depths along the workpiece, they found that the heating rates of the workpiece was up to 50 times higher than the cooling rates relative to the surface. Although this method was employed in cylindrical grinding, it is promising for the development of a temperature profile across the workpiece depth, thus allowing for an understanding of the depth profile evolution of the subsurface microstructural in response to heating and cooling rates.

The use of optical fibres presents several practical issues such as the possible loss of accuracy as a result of signal decay along the fibre due to its fragile nature. Likewise, the high cost required to maintain the low temperature photon detectors further prevents the application from being implemented in the industry [63]. The solutions discussed therefore provide an understanding of thermal behaviour in the grinding process; however, the challenge to implement useful monitoring techniques in industrial applications still remained.

More recently, the research of process of monitoring techniques has seen the integration of sensor systems within the grinding tool. Wheel based monitoring was investigated by several researchers [64, 65] to measure temperature, force and vibration. This allowed for the exploitation of the modular design of some superabrasive grinding wheels as well as the wearing ability of thin-film thermocouples. The method was achieved by embedding a thin-film thermocouple within a segment of CBN grinding wheels (Figure 21). The technique was limited by the detrimental influence of the oil coolant on the connection of the thermo-pair as well as the high costs associated with segmented superabrasive grinding wheels. Likewise, this technique is not applicable for conventional grinding wheels.

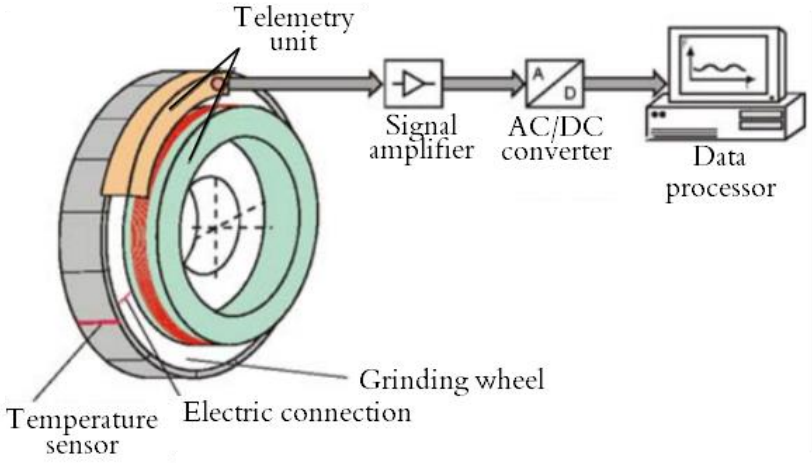

Figure 21: Design of the measurement chain for in-process monitoring of temperature through an integrated thin-film thermocouple [66, 67]

Tool-integrated temperature measurement was implemented in conventional grinding wheels by Brinksmeier et al. [67]. Through the detection of infrared (IR) radiation, this method employs an embedded optical fibre as well as a quick-response infrared photodiode to obtain temperature

information within the grinding zone (Figure 22). The data obtained by the IR sensor is processed by a data converter which is also located within the wheel and is transferred wirelessly to a display unit for continual monitoring.

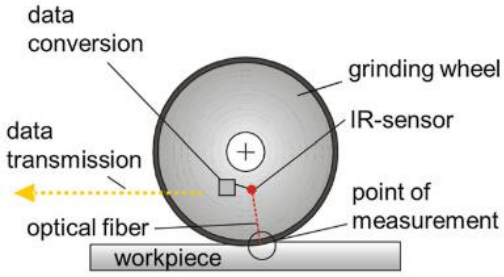

Figure 22: Grinding wheel with embedded sensor for temperature measurement [67]

The current practical operational issues with temperature measurement in most grinding processes including surface grinding is the presence of coolant which impedes access to the grinding zone. However, the use of cryogenic cooling methods also promises a means for the investigation of thermal behaviour within the grind zone. This was observed in investigation by Paul and Chattopadhyay [68] who studied the grindability of steels under liquid nitrogen with thermocouples which were embedment into the workpiece.

2.5 Temperature Measurement in Rail Grinding

A major consequence of the use of face grinding in conventional rail grinding is the increased material removal rate and surface deformation. The inordinate interaction of grinding parameters can lead to the rise of contact zone temperatures which influence the surface integrity as a result of grinding burn and microstructural alterations in the rail surface [22, 35].

Due to their direct influence on the surface integrity of the rail, understanding of the thermal and energy input is particularly essential in rail grinding processes due to the absence of coolant. Rail grinding is performed using a grinding train equipped with several abrasive grinding wheels to increase Q_w through increased number of passes, thereby reducing the grinding forces per wheel [69]. The contact between the successive grinding wheels and the rail head generates a high amount of friction which causes increased temperature distribution across the rail surface and subsurface.

The influence of temperature is typically assessed by observing the rail subsequent to the grinding operation. As discussed in Section 7.4, several practical temperature measurement approaches have been explored in the literature for grinding operations. However, there is minimal research of in-process temperature measurement technologies specific to rail grinding. This may be largely because most of the viable practical measurement techniques (e.g., thermocouples and optical fibres) require ingress into the rail, which poses a challenge to the rail structure. As such, recent research has

focused on the prediction of grind zone temperature through the use of analytical and numerical models and practical means such as thermography.

The use of thermography and thermal imaging within the rail industry has remained scarcely explored. While little has been found to have included rail grinding, some research has been caried out to explore the adoption of thermography to visualise and understand the train wheel/rail contact. Burstow et al. [70] proposed a method to implement thermography on a train bogie to observe the local temperature increase while Yamamoto et al. [71] Expounded on the work by Burstow et al. to map out the local temperature rice within the wheel/rail contact through the use of thermography. In addition, through the thermal imaging of the wheel/rail interface, Firlik et al. [72] ascertained rail wear causalities such as longitudinal creepage and rolling noise generation for a tram vehicle.

The study by Zhang et al. [73] employed infra-red thermal imaging to record the temperature variation in conventional rail grinding operation (Figure 23), with results confirming that the highest temperature is located at the contact surface between the rail surface and the wheel face. The observed temperature progression is confirmed by the prediction carried out by Finite Element Analysis (FEA). In a similar study, Lin et al. [35] utilised infra-red thermal imaging to validate the use of a grindable thermocouple inserted within a rail specimen.

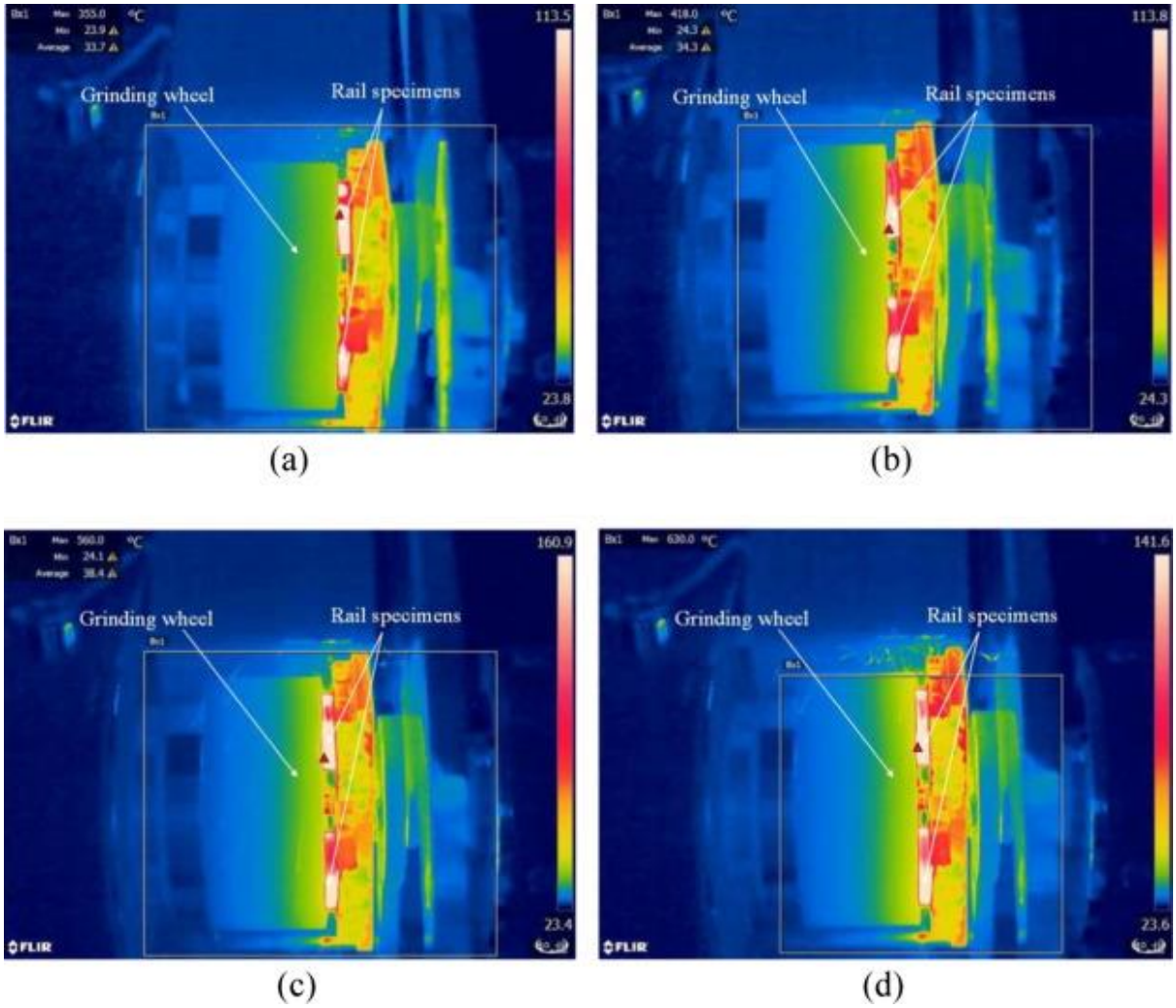

Figure 23: Thermographic images of peak temperatures distributions of four rail grinding passes [73]

Furthering this study, Lin et al. [35] correlated the grinding burn occurrence to the thickness of the white etching layer and the grinding temperature. Using an inserted thermocouple, the results showed an increase in the maximum grinding rail temperature with increased wheel speed v_s as well as an initial increase in force from 1000 N to 1500 N, but a reduction of temperatures above 1500 N. The burn behaviour of the samples observed may be directly attributed to the surface temperatures which are induced during the grinding passes. The grinding burn colours were also classified in this study to establish the relationship between the surface burn colours as normal ($\leq$ 471 °C), yellow (471 – 600 °C), yellow-blue (600 – 735 °C) and dark blue/ purple ($\geq$ 735 °C). The study by Lin et al. also found that aside from the white etching layers formed above 600 °C, they increase above the austenizing temperatures. Likewise, high grinding temperatures (>802 °C) results in the quenching of the surface thus leading to visible grinding cracks. The initiation of such cracks may also be due to the tensile stresses generated by these higher temperatures.

2.6 Temperature Assessment Through Thermal Modelling

Inordinate grinding parameters can lead to the generation of elevated temperatures which affect the surface quality of the workpiece through the transformation of the metallurgical properties of the workpiece surface and subsurface regions. Through thermal modelling, the influence of grinding parameters on the resulting grinding temperatures can be explored. This research adopts a simplified model which incorporates the theoretical backgrounds presented in the literature.

The temperatures which are produced during a grinding operation relate to the energy input to the grinding zone. The specific grinding energy of the system can be derived from the grinding power which can be measured alongside the grinding forces, as these cannot be accurately estimated from empirical data. As a result of friction, grinding power is converted into heat within the contact zone which is then dissipated into the workpiece. The total grinding power supplied is calculated using the measured tangential force F_t and the wheel speed v_s as shown in Equation 3.

$$P_t = F_t \cdot v_s \tag{3}$$

The heat energy which is dissipated into the workpiece as heat can be transferred by convection, conduction and radiation. According to Rowe et al. [74], the net flux of energy into the grinding area (q_t), may be quantified through the sum of the conducted heat flux into the workpiece (q_w), by the chips (q_{ch}) and the grinding wheel (q_s) as well as the assumed heat energy which is transferred by the coolant through convection (q_f). The net heat flux workpiece (q_t) is also resolved using the grinding power and the contact area, which is the product of the contact length and the width of contact (Equation 4).

$$q_t = q_w + q_{ch} + q_s + q_f = \frac{P_t}{l_c \cdot b} \tag{4}$$

The heat flux into the workpiece, grinding wheel and coolant are related to the maximum temperature T_{max} in terms of their conduction or convection coefficients through the expressions shown in Equation 5.

$$q_w = h_w \cdot T_{max}, q_s = h_s \cdot T_{max}, q_f = h_f \cdot T_{max}, q_{ch} = h_{ch} \cdot T_{mp} \tag{5}$$

The heat flux into the chips is dependent on the melting temperature T_{mp} of the workpiece material. The heat flux into the coolant q_f is dependent on the type of coolant used. However, due to the absence of grinding coolant under the dry grinding conditions employed in rail grinding, this parameter was not considered in this research.

As shown in Equation 6, the heat conducted by the chips can then be estimated using the chip specific energy e_{ch}, which is the energy required to raise the workpiece material temperature to a melting point as well as the depth of cut a_e, feed rate v_w and contact length l_c.

$$q_{ch} = e_{ch} \frac{a_e \cdot v_w}{l_c} \tag{6}$$

The heat flux into the workpiece can be considered based on the moving triangular heat source model, which is based on the sliding heat source model of Carslaw and Jaeger [75, 76]. The two-dimensional triangular heat source model and the rectangular heat source model have been noted to provide better accuracy compared to the original uniform heat flux model [77]. The triangular model assumes that the heat distribution takes place within a flat grinding zone; however, the heat input increases towards the leading edge of the grinding zone as depicted in Figure 24.

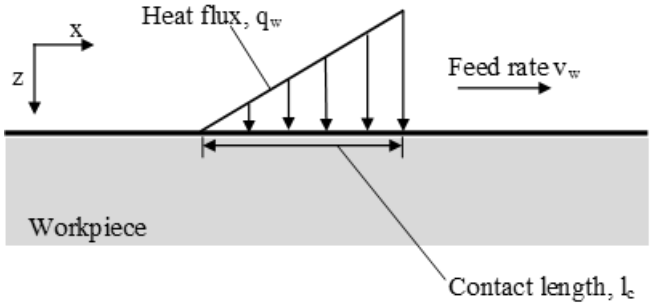

Figure 24: A schematic of the moving triangular heat source model

The triangular heat flux source model may be applied to the peripheral grinding process, whereas more complex analysis is required for the face grinding process. Therefore, in order to obtain a simplified estimation of the grinding temperature, the triangular heat source approach will be adopted going forward in this research.

The predicted maximum temperature increase at the workpiece surface T_{max} $(°C)$ is dependent on the conducted heat flux q_w. This relationship is shown through the simplified expression in Equation 7:

$$T_{max} = q_w \cdot \frac{C}{\beta_w} \cdot \sqrt{\frac{l_c}{v_w}} = \frac{q_w}{h_w} \qquad 7$$

where h_w is the workpiece conduction coefficient and C is a factor which is dependent on the Peclet number and the contact angle. For most grinding operations, the C-factor can be estimated based on the Peclet number, such that if $Pe < 0.2, C = 0.76; 0.2 < Pe < 10, C = \frac{0.95}{\pi}\sqrt{2\pi + \frac{Pe}{2}}$; or if $Pe > 10, C = 1.06$ [78, 79]. However, the C-factor may be approximated to 1 for shallow grinding operations and higher feedrates [74]. The property β_w $(J \cdot (m^2 \cdot s^{1/2}K)^{-1})$ is the thermal effusivity, which is related to the thermal conductivity (k_w), density (ρ_w) and specific heat capacity (c_w) of the workpiece and is determined by the Equation8.

$$\beta_w = \sqrt{k_w \cdot \rho_w \cdot c_w} \qquad 8$$

Combining the relationships in Equations 4 and 5 and assuming the absence of coolant as is in dry grinding, the maximum change in temperature ΔT_{max} (K) at the grinding contact zone can be estimated through the Rowe model which is shown in Equation 9. It must be noted that during

calculations, the value of the ambient temperature must be included in order to estimate the overall maximum temperature.

$$\Delta T_{max} = \frac{q_t - q_{ch}}{\frac{h_w}{R_{ws}}} \quad 9$$

R_{ws} is the partition ratio of workpiece to the grinding wheel which was introduced by Rowe et al. [77]. As the heat flux conducted through the workpiece q_w is a fraction of q_t, it is related to q_t by the energy partition ratio to the workpiece R_w. Ignoring the convection of coolant and chips, R_w can be approximated to R_{ws}, and calculated through the grinding wheel parameters such as the thermal conductivity of the abrasive, k_g, the thermal effusivity of the workpiece β_w, radius of a single grain r_0, and the wheel speed v_s as shown in Equation 10.

$$R_{ws} = \left(1 + \frac{k_g}{\beta_w \cdot \sqrt{r_0 \cdot v_s}}\right)^{-1} \quad 10$$

Rowe et al. [1] determined a solution for the one-dimensional conduction of temperature within a semi-infinite solid which can be used to create a depth profile of the subsurface temperatures. This accounts for the heat flux at an origin over an infinitesimal period of contact. This time period was broadly approximated based on the length of contact l_c and feed rate v_w. Using the one-dimensional solution for moving triangular heat source, the subsurface temperature profile of the rail workpiece can be evaluated through Equation 11.

$$T_{max} = \frac{q_w}{\sqrt{\pi \cdot k \cdot \rho \cdot c}} \cdot t^{1/2} \cdot \left(1 - \frac{2}{3} \cdot \frac{t}{t_c} - \frac{z^2}{6\alpha t_c}\right) \cdot e^{z^2/4\alpha t} - \frac{2q_w \cdot z}{k}\left(1 - \frac{t}{t_c} - \frac{z^2}{6\alpha t_c}\right) \cdot \left[1 - erf\left(\frac{z}{\sqrt{4\alpha t}}\right)\right] \quad 11$$

where t is the instantaneous time, t_c is the duration of heating across the contact area, z is the depth below the surface and α is the thermal diffusivity obtained by the Equation 12.

$$\alpha = \frac{k_w}{\rho_w \cdot c_w} \quad 12$$

The temperature estimations in this section are performed based on the typical thermal properties of rail presented by Zhou et al. [80] which are listed in Table 2. The material properties of the CBN grinding wheel which were utilised in these calculations are presented in Table 3 and Table 4. The average abrasive edge radius was approximated based on Rowe et al. [1] as well as Duscha et al. [37] who indicated an average radius of a reasonable sharp abrasive edge of a grinding wheel to be between 10-50 μm, therefore, for uniformity, 25 μm was assumed for both wheels.

Table 2: Rail thermal properties utilised for temperature calculations [80]

k_w (W/mK)	c_w $(J \cdot kg^{-} \cdot K^{-1})$	ρ_w $(kg \cdot m^{-3})$	T_{mp} $(°C)$
51	500	7800	1400

Table 3: Material Properties of CBN Grinding Wheel utilised in analytical model calculations

r_0 (μm)	k_g (W/mK)
25	240

Table 4: Material Properties of AlO_x Grinding Wheel utilised in analytical model calculations

r_0 (μm)	k_g (W/mK)
25	8.4

2.7 Background Research for Experimental Work

Within the rail grinding industry, it is in the best interest of rail use and maintenance to achieve a long rail life. It is therefore desirable that the rail wears from long life use as opposed to protracted issues which may come with exacerbated wheel/rail contact fatigue. In maintaining the rail profile, the wheel/rail contact stresses can be reduced, and the maintenance process of grinding can be optimised to alleviate damage to the rail while in service.

Preventive grinding is characterised by the removal of minimal material from the rail to maintain the rail profile and to prevent the incidence of rolling contact fatigue. As such, it is paramount that the preventive grinding practice does not contribute to a further detrimental influence on the rail surface for which the approach was designed to maintain. On the other hand, corrective grinding is carried out with larger depths of cut to renew damaged rail and remove cracks without leaving potential for further damage.

As the viability study by Singleton et al. [4] showed that the utilisation of superabrasive tooling for rail grinding could provide improved surface properties in comparison to conventional practices, it is essential that the viability of these metallurgical benefits be assessed through experimental exploration.

This current research is therefore built on the aforementioned viability study carried out to advance the implementation of the superabrasive grinding approach in real life applications. The implementation of superabrasive grinding requires the development of novel technology which is adapted for the rail grinding process. Therefore, the background research for the approaches employed in this research and the associated challenges encountered is presented.

2.7.1 Field Observation and Testing

2.7.1.1 Grinding Trolley

Following the preliminary study to implement superabrasive tooling into the grinding process [4], it was established that the next step for this tooling approach would be testing on a larger scale such as with a grinding train and in similar operating conditions on an actual rail line. In order to develop this field test approach, the 4 major steps depicted in the flow chart presented in Figure 25 were considered.

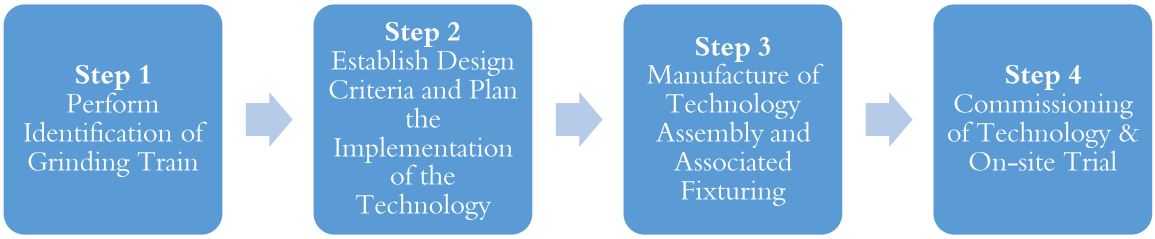

Figure 25: An outline of the steps required to develop a field test approach for the implementation of superabrasive grinding

In order to carry out the identification survey of the grinding train, multiple visits were carried out to view a grinding train. During these visits, a mainline Loram C21 series in-traffic grinding train (Figure 26) was surveyed. This grinding machine is a 4-car maintenance grinder equipped with 64 grinding wheels and 80 electric grind motors (Figure 27). On the C21 train surveyed, only 48 grinding wheels are utilised within a grinding operation. For each grinding stone, a depth of cut of up to 0.1 mm can be achieved and corrective grinding is performed at 4 m/h (6.43 km/h).

Figure 26: The C21 series rail grinder investigated for the possible implementation of superabrasive grinding

With the focus on the possibility of implementing superabrasive grinding on the train, the proposed method was developed:

- To remove a single drive unit within a buggy and replace a conventional tool and drive with a superabrasive tool and its accompanying spindle drive. This must conform to the current space envelope on the train and should utilise the same fittings other gauging issues on the train body.
- The superabrasive grinding tool and drive will be independently operated and controlled away from the remaining existing conventional stones in the buggy. This would prevent further changes to the overall control system which operates the conventional stones and drives.
- The declogging system for the superabrasive tool must also be controlled independent of the conventional stone system. It can preferably be located on the train but may also be situated in the track side for application near the grinding area.

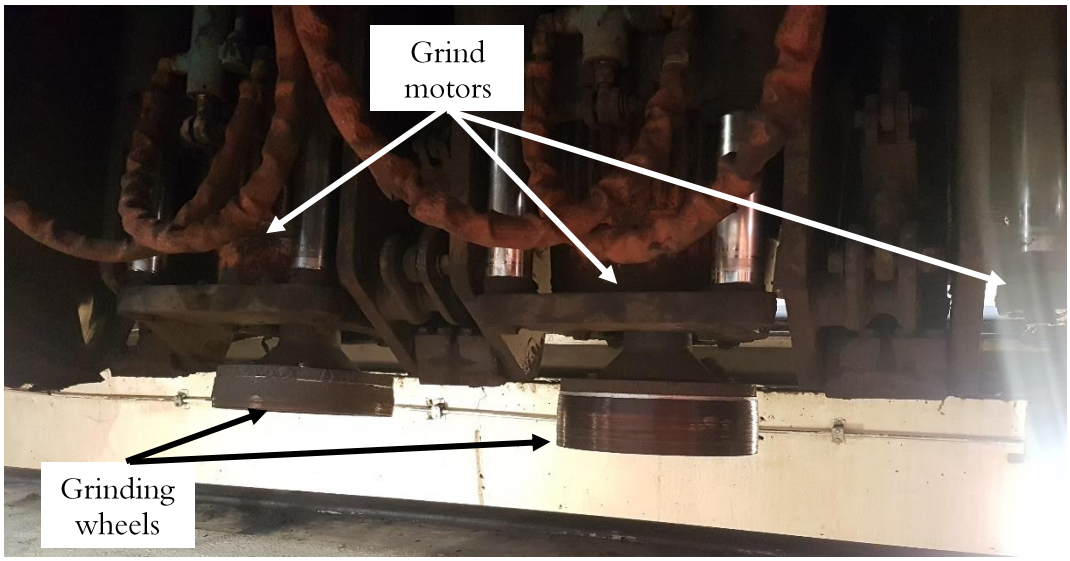

Figure 27: Image of the underside of a C21 grinding train depicting the individual spindle motors for each grinding wheel as well as conventional grinding wheels at different stages of wear.

The visits to observe the grinding train provided a background for the identification of the hazards associated with a typical rail grinder. An assessment of the hazards related to the grinding train also gave basis for the identification of the potential hazards which might be associated with the implementation of the new grinding technology. The manufacturer specifications of the C21 series rail grinder are provided in Table 5.

Table 5: Manufacturer specifications of the Loram C21 series grinding train

Parameter	Specification
Maximum Travelling Speed (km/h)	80
Grinding Speed (km/h)	16
Number of Stones	64
No of Grind Motors	80 (electric)
Range of Grinding Head Angle (°)	75 Gauge, 25 Field
Grinding Motor Rating (kW)	22
Coolant application	No

Following the identification and survey of the grinding train in **Step 1**, a design criterion as well as a plan for implementation were formulated (**Step 2**). However, due to the scale of operation required to implement the technology, the bureaucratic complexities and the associated costs of reserving the grinding train for the tooling experimentation, it was determined that the initial implementation of the superabrasive technology on track would need to be trialled on a smaller scale. Therefore, the use of a manually operated grinding trolley was explored.

The commercially available manually operated grinding trolleys which were evaluated for possible use were the Vertical Track Grinder (MV3) as well as the Frog and Switch Grinder (MC3). The MV3 grinder (Figure 28) is a grinding machine which utilises a conventional alumina face grinding wheel to grind the railhead, as well as welded joints and on the rail running surface.

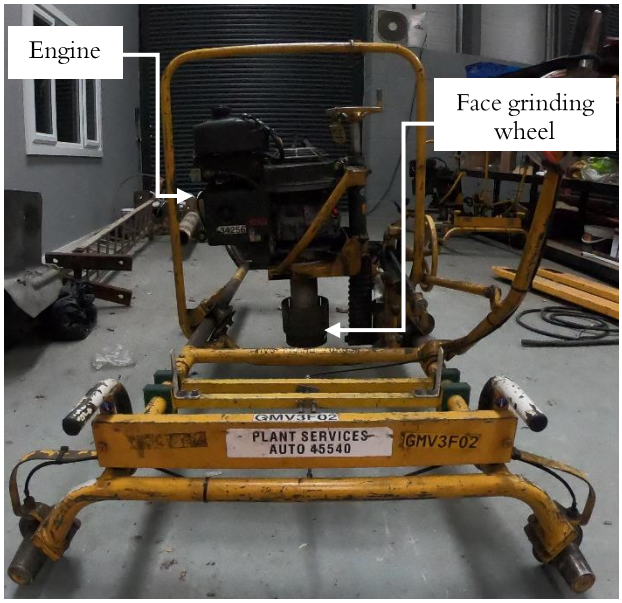

Figure 28: Image of the Vertical Track Grinder (MV3) used for face rail grinding

On the other hand, the MC3 grinder (Figure 29) is also a conventional peripheral grinding machine which is used for the grinding switches and frog points, crossings, and stock rails.

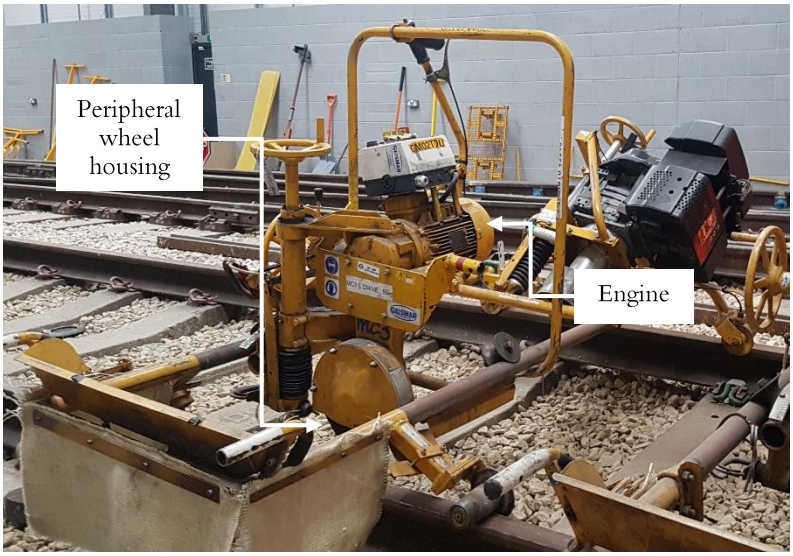

Figure 29: Image of the Frog and Switch Rail Grinder (MC3) used for peripheral rail grinding

In parallel to the observation of the grinding train, a suitable superabrasive grinding wheel was developed in collaboration with Tyrolit. The major design criterion of this wheel was its suitability for use in the face as well as peripheral grinding orientations. Likewise, it was further determined that neither the motors of the manual grinders (MV3 or MC3) were equipped to produce the high speeds required for superabrasive grinding. Therefore, a spindle drive was developed with the additional capability for modular substitution of a single current spindle drive within the grinding train buggy.

It was essential that the high speed spindle drive also had the capability for the increased wheel speeds required for the optimum performance of the superabrasive grinding wheel. Additionally, a further design criterion was the ability to include the declogging mechanism developed for the superabrasive grinding method. Finally, though the initial plan was to incorporate the superabrasive grinding system onto the frame of the commercially available grinding trolley, it was later determined that the spindle drive would require a more robust frame.

Following the design criteria discussed above, a decision was made to develop a mobile grinding trolley which could accommodate the design requirements and be used on the test track available at the University of Sheffield. The development of this Mobile Grinder is presented in Chapter 5.

2.7.1.2 Field Observations of Grinding

In order to develop a field test approach, several factors were considered. A major challenge which is typically encountered when planning a field test approach is the on-track access for the researcher. This is due to the safety risks and the complexities of the rail network infrastructure owners and managers. However, access to perform temperature measurements was secured on two grinding sites. An added benefit of performing field measurements was chance to discuss with the rail grinding operators and to obtain information on the typical parameters used as well as how these parameters are achieved with the existing equipment. The temperature measured during both field grinding observations are elucidated further in Chapter 3.

The first field grinding temperature assessment was carried out during the routine maintenance of an in-service mainline track which was located in Medellín, Colombia. In this campaign, the grinding operation was performed on a passenger railway line by a grinding train both owned by Metro dé Medellín.

Temperature measurements were further performed in a second field grinding assessment which took place on tracks located at the Drax Power Plant. The grinding was performed by a road-to-rail vehicle which utilises grinding wheels that are of a similar size to those utilised in the laboratory grinding experiments.

2.7.2 Laboratory Testing Approach

It has been established that the inordinate application of the process parameters of the grinding operations may result in adverse temperature influences on the rail surface which could lead to the formation of martensitic WEL on the surface of the rail. To assess the influence of the temperature induced on the rail surface, it is beneficial to perform temperature measurement on the grinding zone.

The laboratory testing aspect of the research was focused on benchmarking the conventional grinding of rail and providing a comparison against the superabrasive grinding technique. Performing the rail grinding operation within a laboratory setting allows for the control of the

grinding environment (as is possible within a Computerised Numerical Controlled Machine) and enables the variance or fixing of multiple parameters which may be difficult to achieve in real life grinding train operations. Likewise, carrying out trials in this manner negates the requirement for sample extraction for further surface integrity assessments.

Under the laboratory testing approach, grinding trials were performed using a CBN superabrasive grinding as well as two conventional AlO_x grinding wheels which are designed for face and peripheral grinding orientations. The aim of this grinding trial was to perform grinding passes on samples of full-sized rail in order to record the force and temperature generated during each pass. Each grinding trial was an iteration of the previous test, thus, not all measurement techniques were applied across all trials. The temperature measurement approaches employed in each trial are presented in the Table 6.

Table 6: A list of the grinding trials and their corresponding techniques used for temperature measurement

Grinding Trial	Measured Output (Measurement Technique)
Superabrasive (Peripheral) Grinding	Temperature (Thermal camera); Temperature (Thermocouples)
Conventional Face Grinding	Force (Load cells / force plate); Temperature (Thermal camera)
Conventional Peripheral Grinding	Force (Load cells / force plate); Temperature (Thermal camera); Temperature (Thermocouples)

The effects of induced temperature on the rail following the grinding operation may be visible on the rail in the form of grinding burn. Likewise, to investigate the surface integrity of the ground rail sections, the surface roughness of the rail was measured following each grinding trial. Additionally, to observe the possible presence of thermally-induced martensitic WEL, samples were extracted from three regions across the rail to be prepared for further microstructural analysis on the cross-section of the rail.

2.8 Summary

In this chapter, the literature review has been conducted to provide a brief overview of the general grinding process. Given the broad utilisation of grinding in several industries, the literature review is whittled down to the context of the application of grinding in rail maintenance. Due to the complexities associated with implementation, temperature measurement is a condition monitoring practice that is often not explored in the grinding process.

However, the typical workpiece materials present in rail grinding operations are steels which are ground in dry conditions. Therefore, as the grinding temperatures approach the austenitizing

temperatures, rail grinding materials are more susceptible to white etching layer (WEL) formations due to the thermo-mechanical impacts of inordinate grinding parameter interactions. In relation to the rail industry's drive for improved grinding performance through increased material removal rate (MMR), the review of the literature addressed the state of the art of High Performance Grinding (HPG) approaches.

A major driving force of HPG technologies such as High Speed Grinding (HSG), Creep Feed Grinding, High Efficiency Deep Grinding (HEDG), and VIPER Grinding is increasing economic profitability through the incorporation of innovative manufacturing technologies into the grinding.

The introduction of superabrasive grinding tools for the purpose of rail grinding is explored within this research project. Likewise, the induced temperatures in the grinding tool/material interface remains of particular interest, particularly in relation to the integrity of the material post-grinding, so methods for assessing this were analysed. With this, the thermomechanical effects of the use of superabrasive tooling in the rail grinding process must be understood. Thus, the review of the literature has also explored the utilisation of the temperature measurement technologies. Technologies such as thermocouples, optical fibres and thermography are considered for use in actual rail grinding. The challenges which have been identified for investigation in this thesis are presented as questions as below:

- What is the benchmarking performance of the use of superabrasive in rail grinding against conventional tooling with respect to surface integrity and temperature?
- How can superabrasive grinding be implemented into current rail grinding practices such as on a grinding train?
- How can the in-situ measurement of temperature be applied to augment the implementation of superabrasive tooling in rail grinding?

3 Rail Grinding and Temperature Measurement in A Field Setting (Grinding Train)

This chapter concerns an investigation into grinding temperatures measured during actual rail grinding operations in the field. Multiple routine grinding operations were observed during grinding campaigns initiated by Metro dé Medellín in Medellín, Colombia as well as the Drax Power Station in Selby, North Yorkshire, UK.

3.1 Temperature Observations at Metro dé Medellín

As part of a 2-week research visit made to the National University of Colombia in Medellín (UNAL), a routine grinding operation was observed. The field observations were done in additional collaboration with Metro dé Medellín who granted access to the track during their night-time routine maintenance operation.

The lines A and B make up the railway portion of the Metro dé Medellín Integrated Mass Transport System, which also comprises of other lines which also include cable car lines (Metrocable Lines K, J, L, H, M and P), trams and electric bus services. The railway lines A and B span over 23 km and 5 km respectively, with the former running from North to South Medellín and the latter running from the centre to the Western part of the city. The railway Line A currently has an estimated annual tonnage passing of 20 – 25 MGT (Mega Gross Tonnes), while Line B has an estimated traffic of 10 – 12 MGT per year.

Due to the high tonnage frequency on the tracks at Metro dé Medellín, issues related to fatigue cracks, shallow shelling and rail corrugation are often observed in the rail [81]. As such, in their grinding campaigns, more aggressive grinding practices may be required to excoriate the damage and to maintain the rail profile, with a combination of preventative and corrective grinding occurring every few months. As such, one of such grinding campaigns was observed.

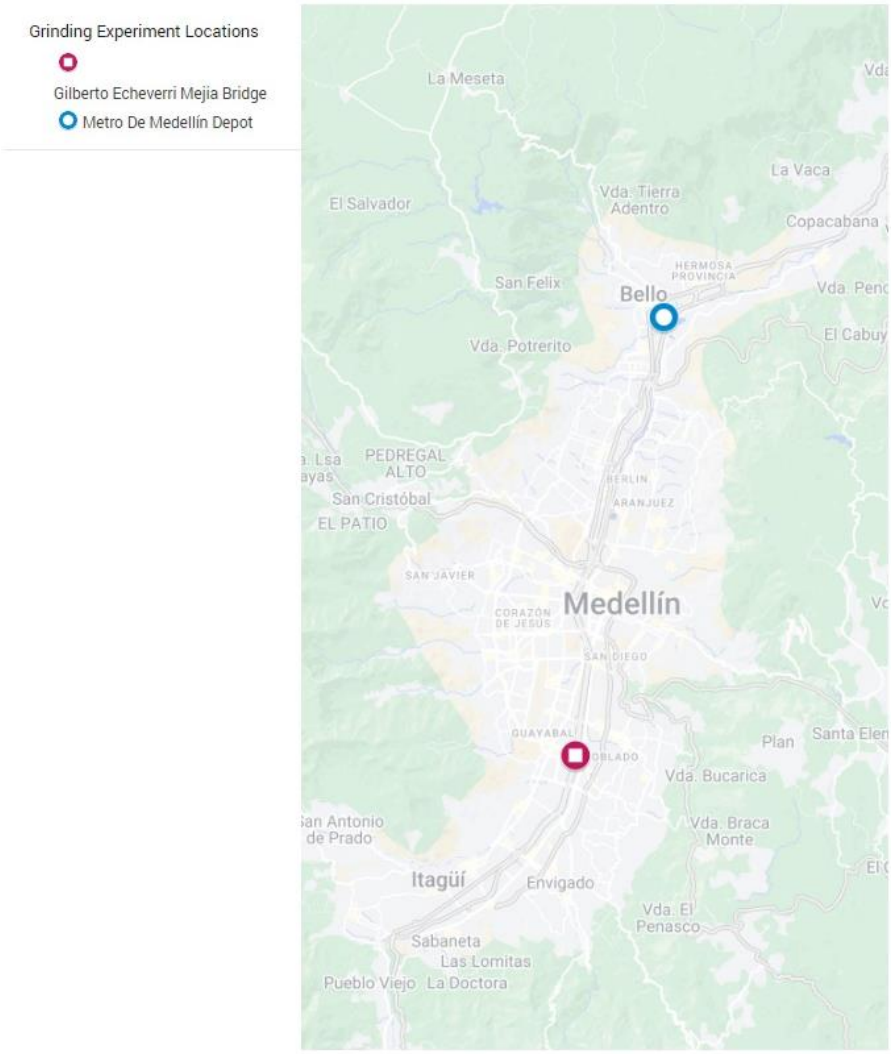

Figure 30: Location of Metro dé Medellín depot and subsequent grinding trial on the Line A (North-South)

An overnight grinding campaign was carried out by Metro dé Medellín on the southbound section of the A railway line. The grinding train commenced its journey from the Metro dé Medellín depot, located in Bello, a suburb of the city of Medellín. However, the maintenance operation was carried out on a section of active passenger railway situated in the beneath the Gilberto Echeverri Mejía Bridge and bordering the Medellín River.

3.1.1 Grinding Equipment – Harsco RGH10C

This section presents the equipment employed in the research conducted on the Metro dé Medellín. This includes the machine tools as well as the auxiliary tools used during the trials.

Figure 31: The Harsco RGH10C rail grinder employed for the grinding operation in Medellín Colombia

For this grinding operation, a single-car Harsco Track Technologies RGH10C transit rail grinder was employed. The rail grinding train is depicted in Figure 31. A typical rail grinder is equipped with grinding modules which can adapt to targeted grinding patterns and rail profiles for grinding rail switches and crosses. The manufacturer specification of the RGH10C transit rail grinder is presented in Table 7.

Table 7: Details of the machine specifications of the Harsco RGH10C

Parameter	Specification
Maximum Travelling Speed (km/h)	80
Maximum Towing Speed (km/h)	100
Number of Stones	10
Range of Grinding Head Angle (°)	75 (Gauge) to 45 (Field)
Wheel size (mm)	150
Travel Velocity Range (km/h)	1.6 – 13

Water hoses are located on the front and back of the grinding train for spark suppress to reduce the risk of fires. This conventional rail grinder was composed of one working car equipped with 10 aluminium oxide (AlO_x) grinding wheels – 5 wheels are placed in an array on either side of the train for both the inner and outer rails. Each array of wheels is covered by side curtains in order to prevent the grinding sparks from impacting the track. It was anticipated that the side curtains would impact the temperatures recorded. This is further discussed later in the chapter.

For proprietary reasons, it was impossible to obtain images of the wheel arrangements on the RGH10C grinding train. However, the grinding was performed using 150 mm coarse AlO_x wheels with the average grain density of about 16 grain/cm^2. In order to grind different facets of the rail profile, the active contact surfaces of the grinding wheels were set up in varied attack angles in an end-face contact with the rail as it moved longitudinally along its surface.

In following the recommendations through studies presented by Grassie [5, 12] as well as Satoh and Iwafuchi [14], the grinding operation was carried out as a preventive practice. This practice was done to restore the rail to its optimal profile and to arrest initiated surface microcrack growth before devolution into accelerated growth. However, studies have shown that the formation of hardened martensite on the rail surface may occur as a result of the generated localised temperatures and subsequent rapid cooling. As such, the interaction of the associated grinding parameters plays a significant role in achieving a desired outcome of the grinding operation. The governing parameters which were utilised in this Metro dé Medellín grinding campaign include the applied grinding pressure, the grinding train velocity, the prior condition of the grinding wheels as well as their angle and rotational velocity. The basic operating parameters and the environmental conditions of the rail grinding process are detailed in Table 8 and Table 9.

Table 8: An overview of the basic operating parameters of the observed rail grinding operation on the Metro dé Medellín A-line

Parameter	Value
Material removal per 3 passes (mm)	≈ 1 (with conventional stones)
Train travel velocity (km/h)	5
No of passes	15 passes per rail (inner and outer rails)
Operating Conditions	Rain

Table 9: Environmental Conditions recorded during the grinding campaign witnessed in Medellín

Environmental Conditions	Value
Average Air Temperature (°C)	20.7
Average Relative Humidity (%)	86.7

A pre-operation appraisal of the process with the operators determined that the shallow depths of cut might cause a difficulty in controlling the depths. Therefore, the typical practice employed by the grinding operator was to estimate the equivalent material removal for every 3 passes as shown in Table 8. In the rail grinding industry, the achieved depth of cut is determined by the applied grinding pressure [82]. Each grinder is equipped with a maximum grinding loading pressure, which is symbolic of a percentage of the available power in the grinding motors. As such, in order to achieve a grinding pass, a percentage of the maximum loading pressure is applied.

In the Metro dé Medellín grinding campaign, 19 grinding passes were recorded. Based on the discussions with the grinding operators, it was understood that 15 of the passes assessed were conducted on the inner rail while the remaining 4 passes were performed on the outer rail.

3.1.2 Analysis Equipment

a) Temperature Measurement

To conduct in-process temperature measurements during grinding, a FLIR-E95 24° thermal camera was employed. In this trial, the camera was held by hand due to the nature of the test environment. The camera's object temperature range was set to '0-650 °C', to account for the possibility of recording the higher temperatures which may fall within the austenisation temperature range where phase transformation occurs to cause the formation of the martensitic WEL on the surface material. The stored thermal information was initially analysed using the FLIR Tool+ software on a computer. The camera also possessed a spectral range of 7.5 to 14 μm, a thermal sensitivity of 40 mK at 30 °C and an infrared resolution of 464 × 348 pixels. A thermal progression was recorded through a video imaging mode at an image frequency of 30Hz. This allowed for continuous measurement of the grinding region from the start to end of each pass done. Two approaches were applied in order to direct the camera at the rail surface. They included the following:

- Direct the camera at a certain region on the rail to be ground to observe the temperature progression as the grinding train traverses that point. To achieve this, applying this approach required prior knowledge of which rail was to be ground. However, due to the language barrier (Spanish and English), this approach was initially limited.
- The second approach was to direct the camera to the region where the grinding stones are located and follow their action across the rail during the grinding operation.

In general, both approaches were limited as a result of the thermal camera having to be held by hand. This was due to the complexities associated with getting the camera mounting equipment (tripod) onto the grinding site. This affected the stability of directing the camera to the desired region with ease.

b) Data Analysis

The files obtained by the thermal camera were saved as mp4 files. To analyse the obtained data in robust manner, each file was initially analysed in both Python and MATLAB software respectively. A python code was written to process the video files using publicly available python modules such as *OpenCV*, *Numpy* and *Pytessaract* to allow for image processing, application of functions, artificial intelligence for image recognition, as well as assessment and storage of numbers in the video files. The numerical data files obtained using Pytessaract were individually analysed to filter out erroneous predictions which were flagged up in the plotting phase.

Following the numerical data extraction, the corresponding MATLAB code was used to plot the recorded temperature progression per pass along with the associated thermal video. A total of 19 thermal video files were recorded and those not presented in the result section can be found in in Appendix E. Each video taken corresponded to a performed grinding pass made.

It should be of note that the results presented from this Medellín study would vastly be affected by the following factors:

- continuous relocation of the thermal camera / variation of the distance of the thermal camera from the grinding stone-rail contact area
- The environmental conditions of temperature and humidity (Table 9).

3.1.3 Results and Analysis

A series of thermographic video recordings were made for each grinding pass observed. Each video was observed frame-by-frame and further analysed through the use of the aforementioned image recognition applications in MATLAB.

An example of the measured temperature progression of the first observed pass through the software analysis is shown in the plot presented in Figure 32. To describe the thermographic images presented in this section, it should be noted that the value shown in Label 1 is indicative of the maximum instantaneous measurement of the region upon which the cursor shown in Label 4 is directed. An on-the-ground grinding personnel situated in the central track spacing is indicated by Label 2. Label 3 depicts the opposite tracks of the Line A railway, where the grinding campaign took place, while Label 5 shows the grinding train used in this campaign. Likewise, Label 6 illustrates the rail upon which the grinding operation was performed. Finally, the temperature scale which is shown Label 7 indicates the maximum and minimum recorded temperature of the surrounding environment. The value taken as the maximum temperature during each pass is the value which was displayed by the indicator in Label 1.

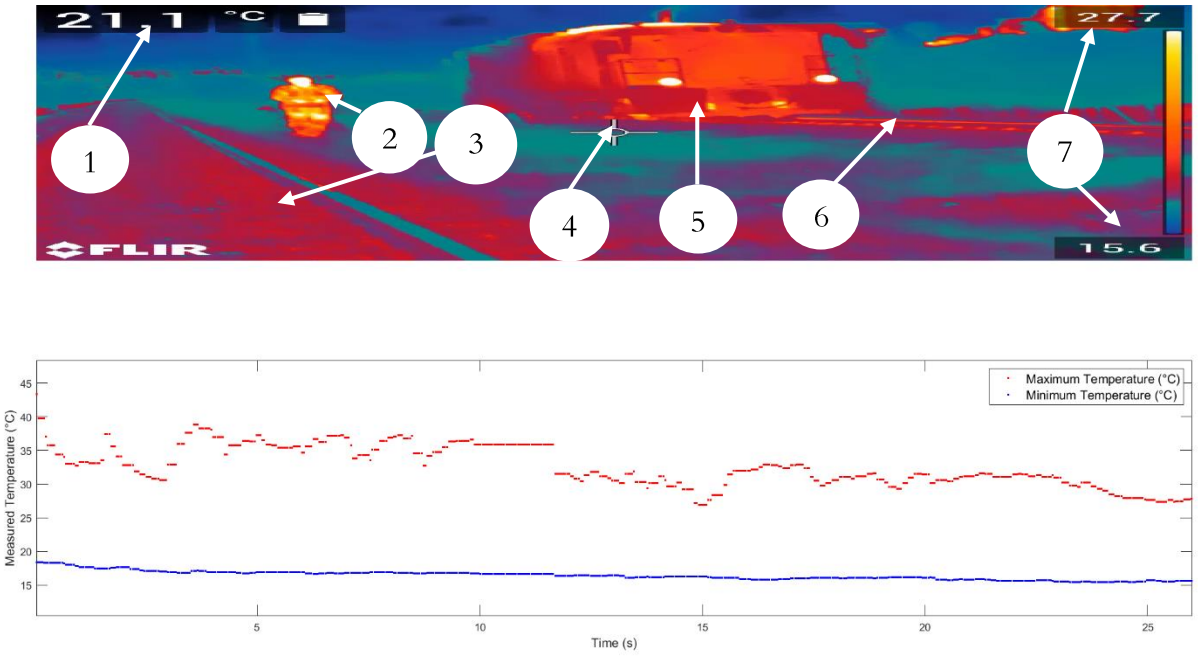

Figure 32: A still image of the RGH10C grinding train and rail as well as temperature progression of grinding (Pass 1)

During the first pass, which is also shown in Figure 32, the location of recording using the thermal camera on the opposite set of tracks across from the tracks which underwent grinding. This was due to the initial health and safety advice. Therefore, it is likely that the distance from the track

being ground may have negatively influenced the maximum recorded temperature values which may have been recorded in this manner. In addition to this Pass 1, the recorded temperature progression of the other measured grinding passes in this campaign are presented in the next section (3.1.3.1).

3.1.3.1 Analysis of Footage of Temperature Readings

The corresponding plot of the temperature progression of the first pass (Pass 1) which is presented in Figure 32 shows peaks at the start of the recording correspond to the moments where the grinding train was in front of the camera. As the train traverses away from the direct line of vision of the camera, the recorded temperature decreases till the end of grind.

By running the video file through the MATLAB code, the maximum temperature identified was 43.4 °C and the recorded values varied around an average of 32.6 °C. The temperature range which was observed here (15.4 – 43.4 °C) contradicts the range of temperatures expected based on the study carried out by Zhang et al. [73], who from their numerical heat transfer simulations predicted grinding temperature ranges of 395.4 – 510 °C for a range of 11 – 15 kW grinding motor power.

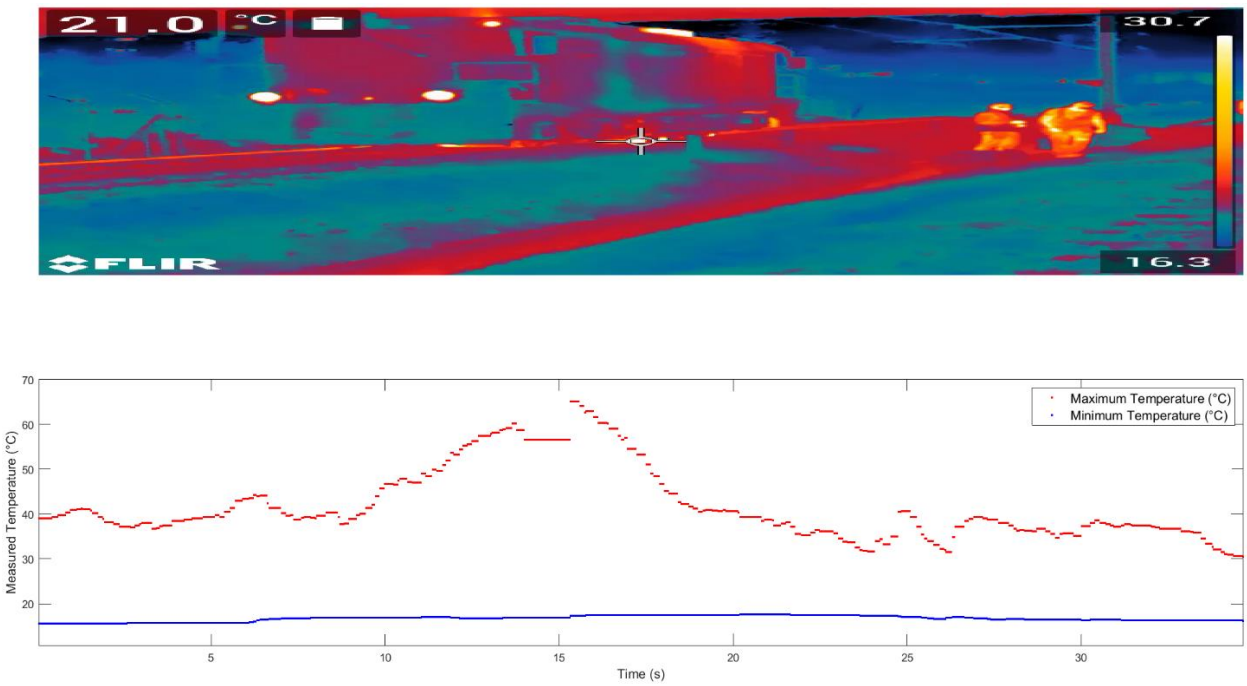

Figure 33: The final thermal image of the grinding Pass 2 and a plot of the corresponding temperature progression recorded at the Metro dé Medellín line (after adjustment of camera position)

The final frame of the footage as well as the corresponding temperature progression plot of the second pass (Pass 2) is presented in Figure 33. In this image, the grinding train is shown at its final stop following the completion of a grinding pass. Assessment of the thermal video of Grinding Pass 2 using the MATLAB code shows that a maximum temperature of 65.1 °C was recorded.

However, further frame-by-frame analysis of the raw thermal footage of Pass 2 indicated that temperatures of above 130 °C were measured by the thermal camera at various instances. One of such instances where this maximum was identified by the thermal camera is shown in the still in Figure 34. The exact temperature recorded could not be displayed due to the calibration of the thermal camera. As such, the exact values of any temperatures measured that exceeded 130 °C could not be displayed by the camera. In the image presented in Figure 34, a dispersing cluster of hot spots can be observed leading away from the indicated grinding contact zone. This dispersing cluster is understood to be the grinding sparks, steel dust and debris which were expelled as a result of the contact between the rail and the grinding wheel in operation. Despite the sparks curtain which was utilised on the grinding train, the grinding sparks generated during the grinding passes were observed at a distance beyond the boundary of the sleepers.

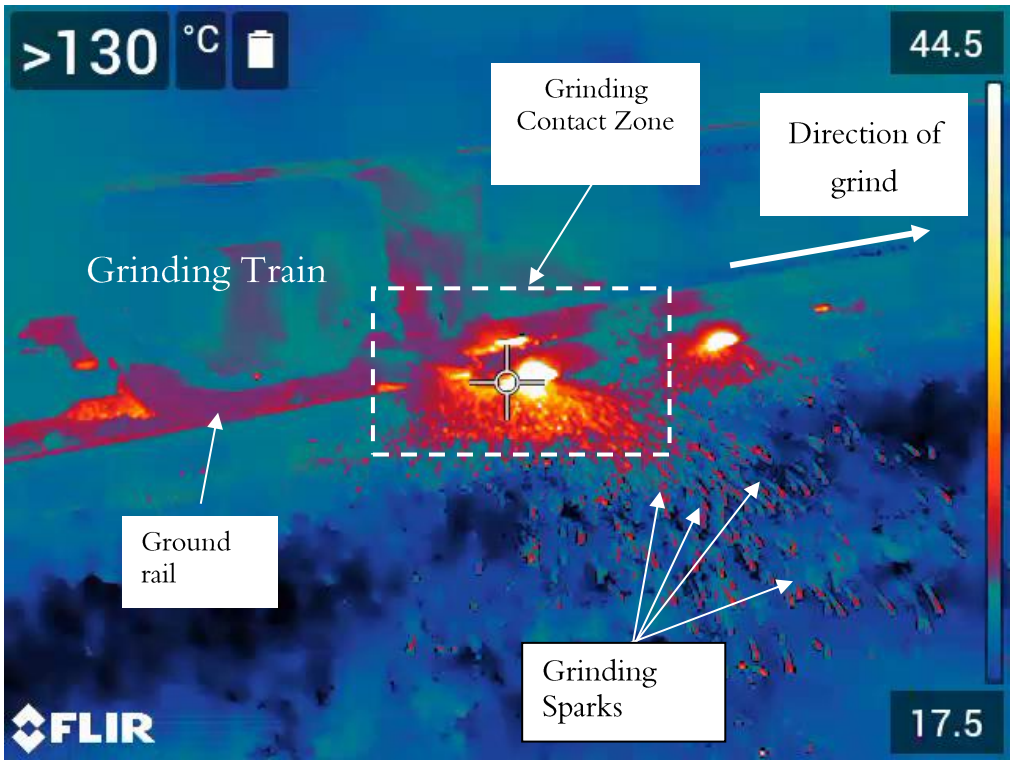

Figure 34: A close-up of the contact zone during the grinding operation of Pass 2.

Following these initial recordings of Passes 1 and 2, it was decided that a more optimal measurement might be attained at a closer distance to the rail being ground and inherently towards the grind contact zone. As such, based on this assessment, for Passes 3 the camera was set up closer to the rail tracks to be ground.

The third grinding pass (Pass 3) was carried out in the forward direction. However, in a similar fashion to the recording done in the previous grind, the camera was directed at the location of the grinding wheels and the grinding action was followed from start to end from across the tracks. The temperature progression of this third pass is shown in Figure 35. Similar to what was observed in the previous pass, analysis of the thermal video indicates that temperatures higher than 130 °C were

recorded during the pass. When the thermal video was put through the MATLAB analysis, the maximum observed value was 80.5 °C. However, frame-by-frame inspection also showed that the threshold of >130 °C was also achieved in this pass.

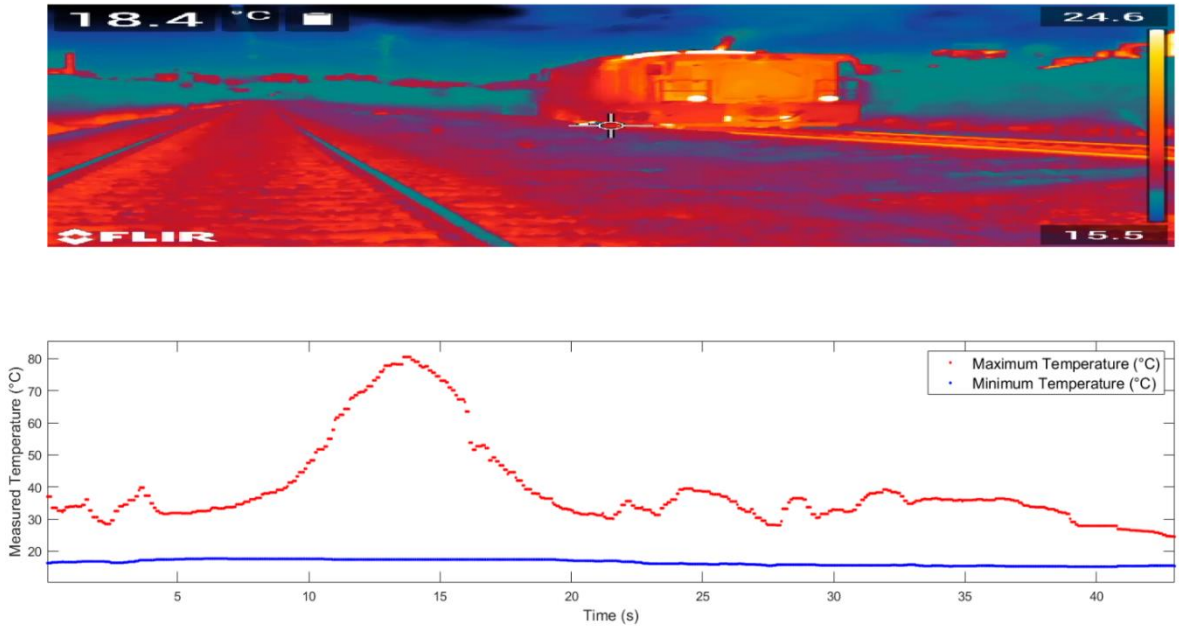

Figure 35: The final thermal image of the grinding Pass 3 and a plot of the corresponding temperature progression recorded at the Metro dé Medellín line

For the Passes 4 to 11, the camera cursor was focused on the railhead of the inner rail at the start of the recording and traversed along on the railhead, following the visibly hottest region to the end of the grinding action. As a sample, the temperature progression of Pass 4 is presented in Figure 36. The highest peak observed indicates when the camera is at the shortest distance to the camera. This temperature behaviour is common in the thermal images of the grinding passes (Pass 4–11) which were recorded in this manner. In Pass 4, the maximum temperature observed by through the MATLAB code was 130 °C; however, the frame-by-frame inspection shows that the maximum recorded temperature is the threshold of >130 °C. This is also common for the subsequent Passes 5–11 which were recorded in this orientation.

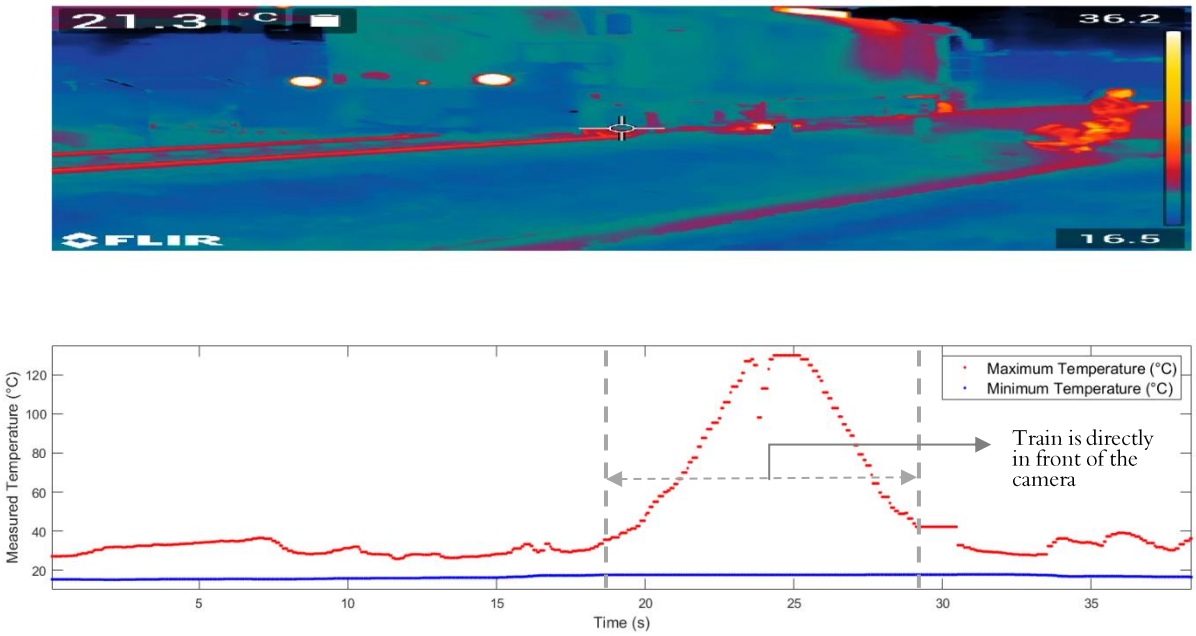

Figure 36: The final thermal image of the grinding Pass 4 and a plot of the corresponding temperature progression recorded at the Metro dé Medellín line.

The subsequent Passes 5-11 can be found in Appendix C. In Passes 16 to 19, the camera was held steady and focused on the outer rail. The temperature progression plots show a level reading on the rail as the recording starts. However, the temperature values recorded are higher than the air temperatures. This is attributed to the temperature buildup as the number of passes increased. Further on as the time increases, these progression plots indicate a sudden reduction (trough) in the temperature values. The troughs observed in the passes in which measurements were attempted on the outer rail show a reduction in the temperature. This is due to the train body obscuring the rail from the view of the thermal camera. Therefore, the reduced readings may be regarded as the temperature of the train body. Following the passage of the train, the rail temperatures appear to reduce but do not immediately return to their original readings (> 40 °C). An example of the temperature progression of one of the passes (Pass 16) with the thermal camera focused on the outer rail is shown in Figure 37, while subsequent Passes 17 to 19 may also be found in the Appendix C.

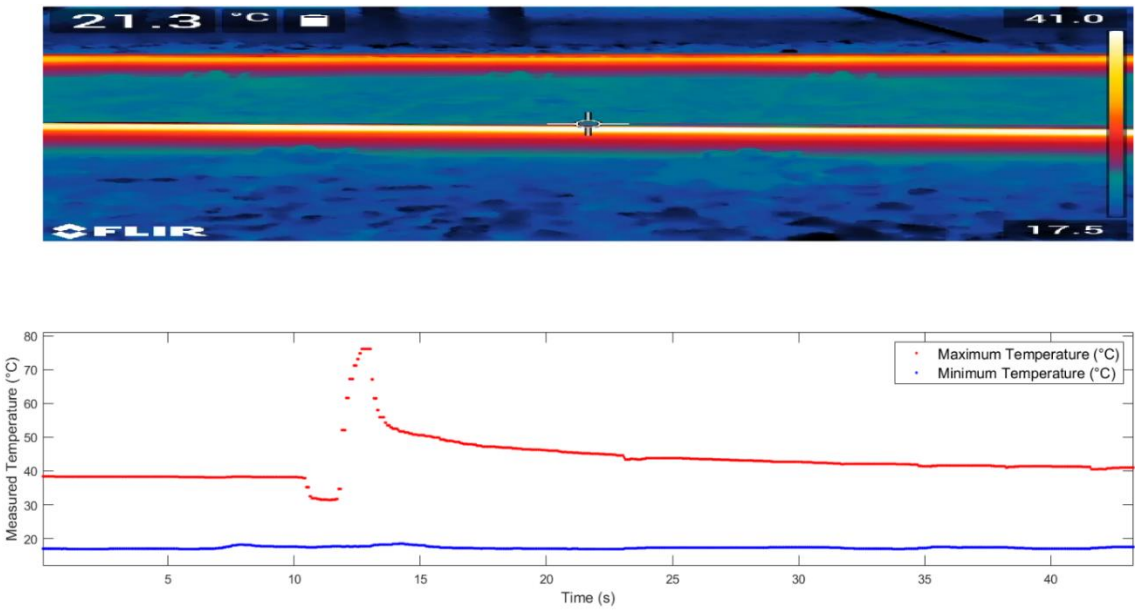

Figure 37: The final thermal image of the grinding Pass 16 and a plot of the corresponding temperature progression recorded at the Metro dé Medellín line

3.1.3.2 Post-Grind Condition of Rail

The initial conditions of the rails prior to the grinding operation are shown in Figure 38. Prior to grind, the surface was characterised by periodic asperities which are believed to be early stages of rail corrugation wear. If left unchecked, these features will exacerbate and may lead to detachment of material from the rail head.

Figure 38: Initial rail surface conditions of rail prior to grinding operation on the Metro dé Medellín tracks.

Due to the rails being in-service, it was impossible to perform the typical post-grind analyses of the rail surfaces. However, the condition of the rail during the grinding passes is presented in Figure 39. The mid-grind rail condition shown in Figure 39 shows some ground facets as well as the facets which require further passes to complete the grinding of the facet.

Figure 39: The mid-grind condition of the railhead during the grinding operation at Metro dé Medellín.

The post-grind conditions of the rail can be observed in the figures presented in Figure 40 (a) and (b).

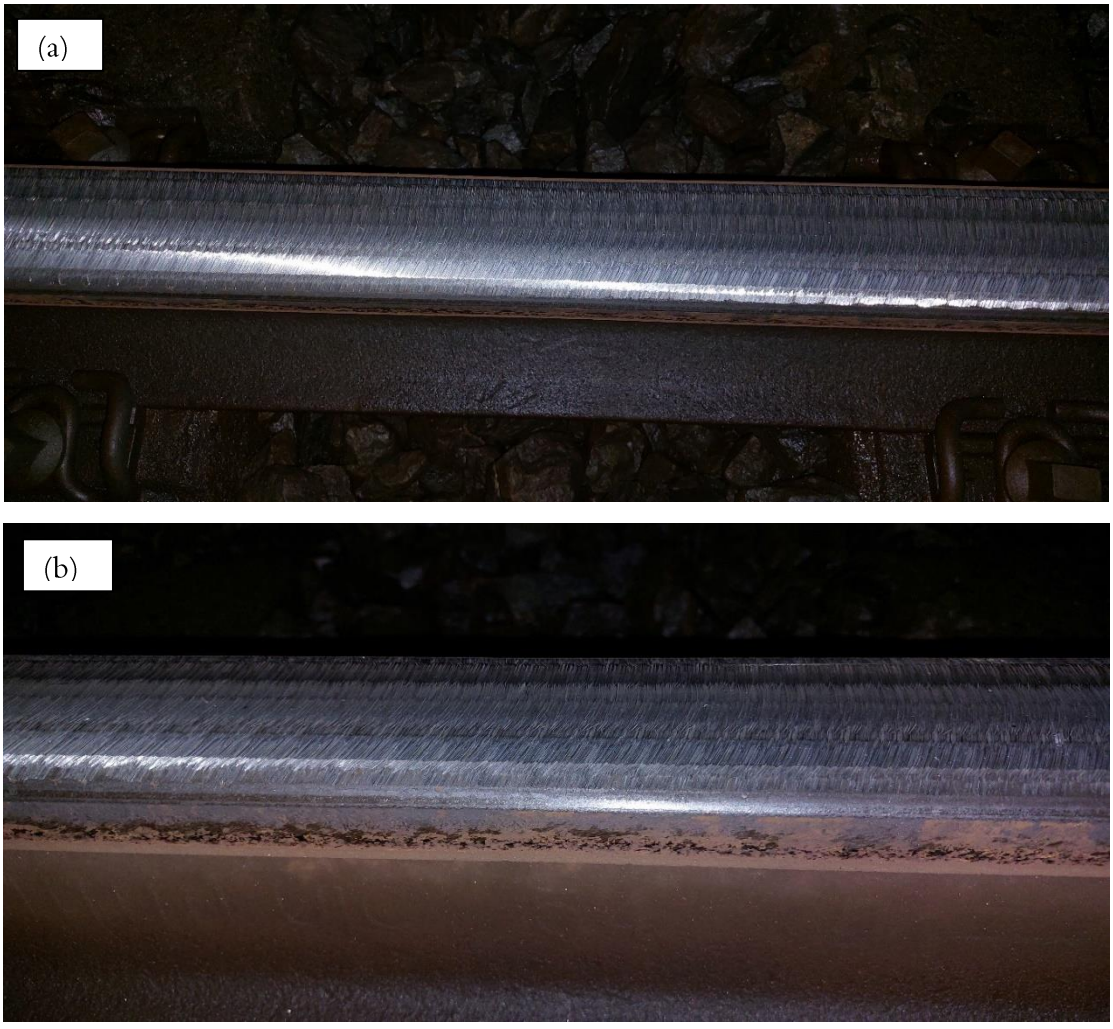

Figure 40: The post-grind conditions of the rail after the grinding operation conducted on the Metro dé Medellín tracks.

3.2 Temperature Observations at Drax Power Station

Multiple train lines serve the Drax Power Station which is located in Selby, North Yorkshire UK. The Drax plant (Figure 41) is the largest renewable power station in the UK which converts biomass into electricity and receives a daily freight tonnage of up to 30,000 tonnes. Routine grinding campaigns are undertaken on the tracks in order to maintain and reprofile these tracks.

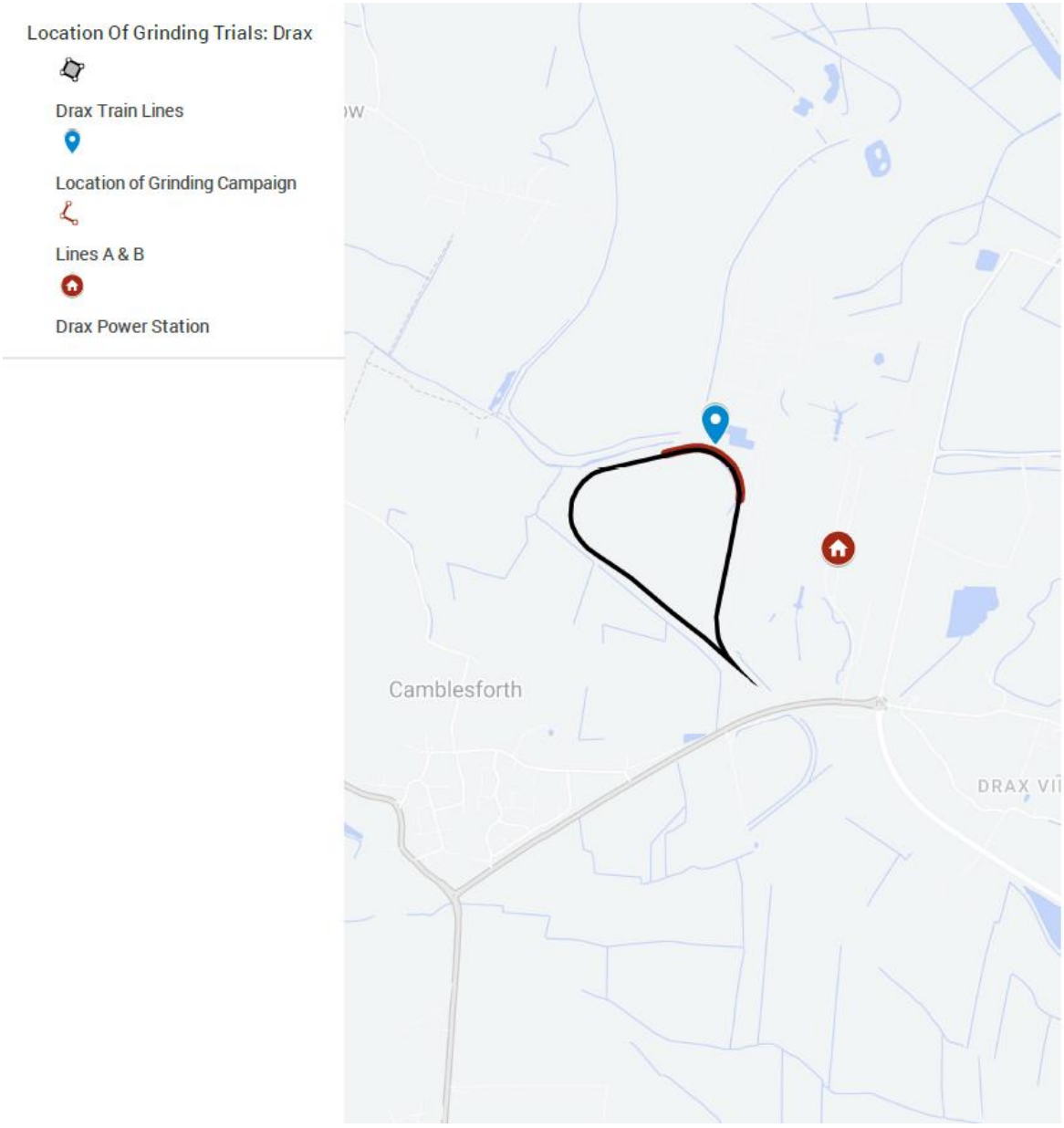

Figure 41: Location of the Drax Power Station and the Grinding Campaign Location on Tracks L201A & L201B.

The switches on the curved L201A and L201B tracks (Figure 42) leading up to the Drax Power Station were recently changed from the standard R260 to a premium rail HP335 grade. This grade is characterised by a higher hardness which results in lower plastic deformation in comparison to

the standard R260 grade. As a result of its higher hardness, the HP335 rail is subject to less wear and therefore requires a grinding at a less frequent rate.

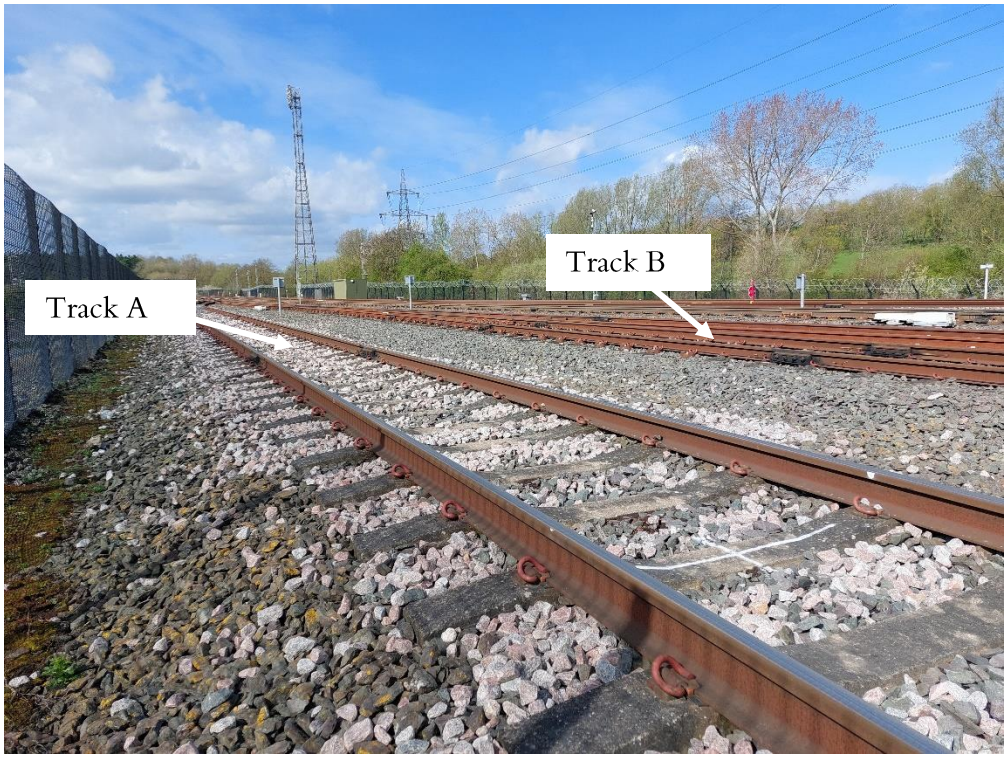

Figure 42: HP335 Rails on the Tracks L201A and L201B on the Drax Power Station Railway Line

As part of a research collaboration with British Steel, access was granted to observe the grinding campaign of the L201A track in the area close to the power station. The condition of the rail prior to grinding is shown in Figure 43. The rail's running surface was characterised by a snakeskin-like pattern on the railhead. If left unchecked and unground, these surface asperities may transform into spalling defects which may develop along the rail length and transverse defects on the railhead.

The rail grinding campaign was performed to remove any mill scale as well as the snakeskin-like defects on the rail head using the face grinding approach, while any lipping defects were deburred using the peripheral grinding wheels. At Drax, the ideal frequency of grinding would be every three months; however, this is dependent on the availability of the grinding equipment.

Figure 43: Condition of HP335 rail surface prior to grinding action at Drax Power Station, showing snakeskin-like asperities on the rail head.

The grinding operators describe the grinding campaign as a basic Network Rail corrective grinding operation which was done to remove the millscale and the snakeskin defects present on the railhead. Other severe defects such as spalling would require reprofiling of the rail at higher depths of cut.

3.2.1 Grinding Equipment – Harsco Möser Road/Rail Grinder

In the Drax grinding campaign, a Harsco Möser Road/Rail Grinder (RO-V149) was utilised (Figure 44). The grinding machine is typically favoured for use in urban and industrial areas, due to its reduced noise levels (up to 75 dB) and its ease of adaptation from the road onto rail tracks.

Similar to the large RGH10C grinder observed in Metro dé Medellín, this Road/Rail grinder is also used to grind crossings, switches as well as rail curves. As highlighted by the grinding operators, the difference between this Road-to-Rail grinder and a typical grinding train is the ability to change parameters such as the wheel speed, pressure and feed rate during the grinding process. This differs from grinding trains, where the wheel speeds are fixed for grinding operations.

A portable Digital Cross-section Measurement System (DQM) is used to scan the rail profile prior to and after the grinding operation. The RO-V149 was equipped with a laser scan which informs the operator of the achieved rail profile. As such, the grinding parameters may be adjusted to achieve the target profile in-situ.

Figure 44: The Harsco Möser Road/Rail Grinder (RO-V149) used in grinding operations at the Drax Power Station

The manufacturer's technical specifications for this Harsco Möser grinder are detailed in the Table 10 below.

Table 10: Manufacturer-supplied specifications of the Harsco Möser Road/Rail grinder

Parameter	Specification
Maximum Travelling Speed (km/h)	20
Maximum Working Speed (km/h)	0-5
Number of Stones	6 (4 cup; 2 peripheral)
Maximum Grinding Power (kW)	7.5/11
Dimensions (m)	5.152 × 2.020 × 2.577

Due to proprietary restrictions of the industry partner, it was impossible to obtain the full operating conditions of the grinding process. However, the obtained conditions are presented in Table 11. The grinding operation was performed in dry weather conditions, therefore, visibility for the thermal camera was desirable.

Table 11: Process parameters and grinding conditions of the grinding operation

Parameter	Value
Train travel velocity (km/h)	4
Wheel Speed (rpm)	5000

No of Passes	8 (Gauge to Field)
Power Requirement (%)	60-70
Operating Conditions	Dry

The cutting tools which were used during the Drax Grinding campaign were standard AlO_x grinding wheels. The grinder is equipped with 4 cup wheels with two on each side to perform grinding on the railhead and 2 peripheral grinding wheels on either side for the removal of lipping defects on the side of the rail or for the adjustment of the gauge. An image of the wheel arrangements is shown in Figure 45. To grind a complete railhead profile, up to 8 grinding passes are conducted from the gauge to field. However, the number of passes done on a facet is typically determined by the grinding operator based on the overall target profile.

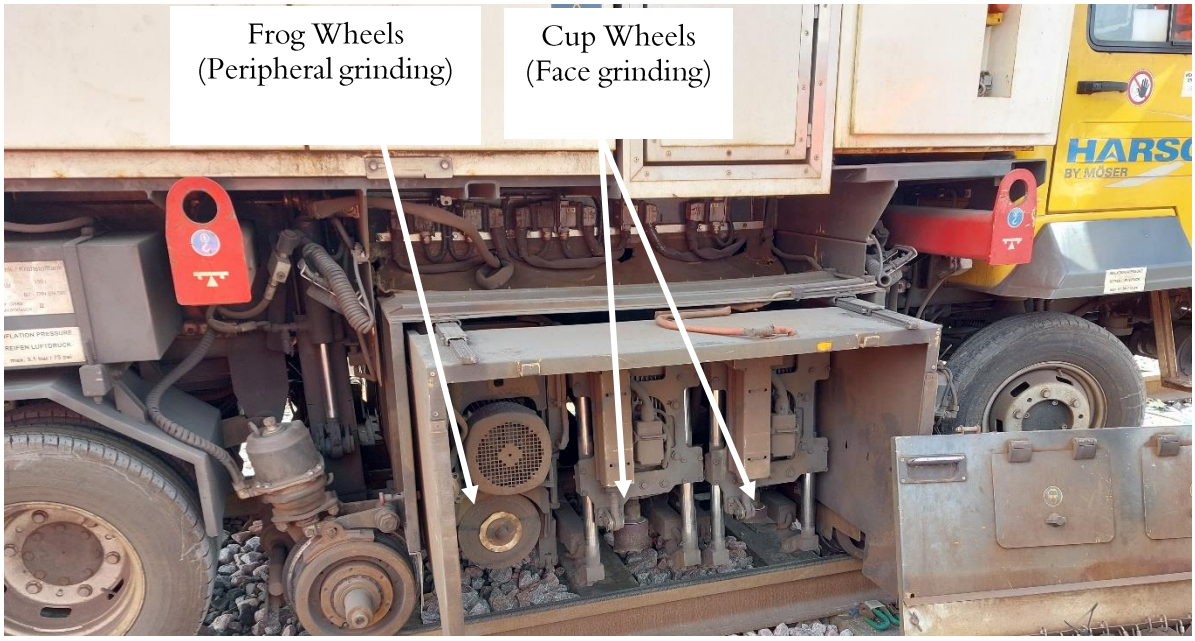

Figure 45: The arrangement of the grinding wheels employed during the rail grinding operations at the Drax Power Station

Due to the aggressiveness of the grinding action, high wheel wear is expected during the grinding of these premium rail. As such, no measures were taken during the grinding operation to alleviate wheel wear and the wheels are changed often during the grinding operation. The condition of the face grinding wheel which was taken out of use is shown in Figure 46. The active surface shows the coarse grits which had performed the grinding action.

Figure 46: Condition of a used face grinding wheel at end-of-use for the rail grinding operation at Drax Power Station.

The mid-grind condition of the rail can be observed in Figure 47. The image shows a section of the rail which had been partially ground. On this rail, the snakeskin-like pattern is visible beneath the ground facet. Also observed on the mid-grind condition is a spalling (flaking) defect, which is generated as a result of high contact stresses.

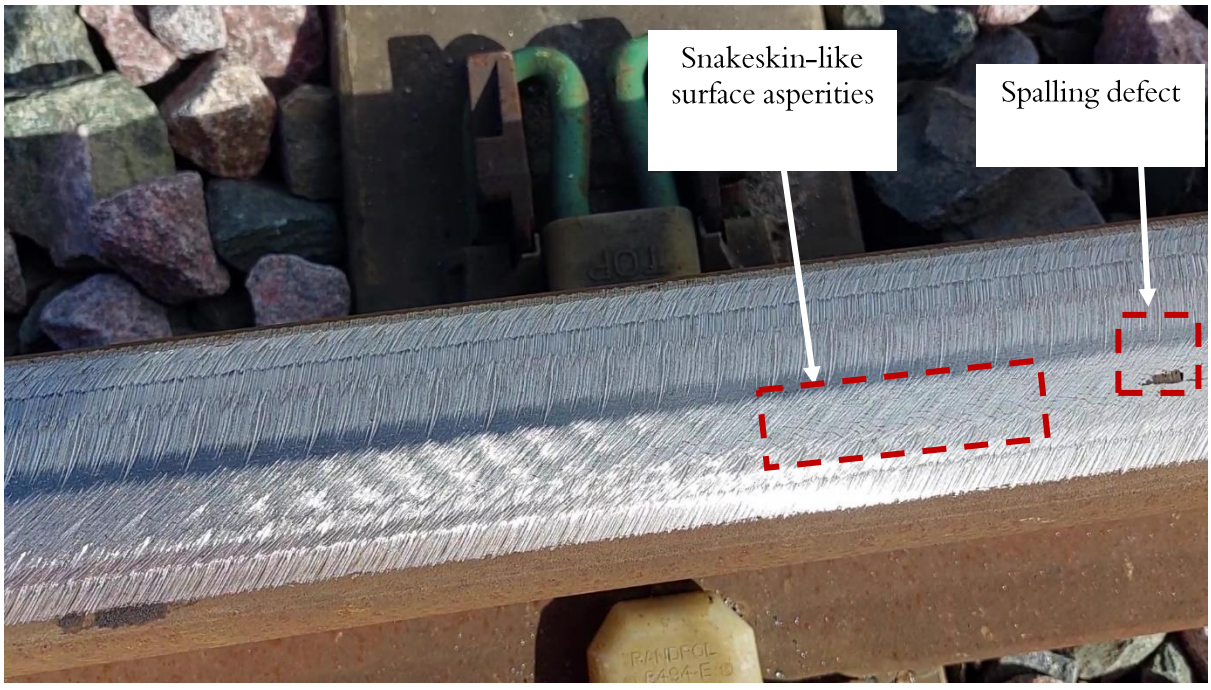

Figure 47: Mid-grind condition of the rail during the grinding operation at the Drax Power Station, showing rail surface asperities such as spalling.

The post-grind condition of a section of fully ground rail is also presented in Figure 48, which shows that grinding has been performed on all facets across the crown of the railhead. Upon visual inspection of the length of rail, it was observed that the snakeskin-like defects had been removed and there was minimal presence of spalling defects. Regions where the spalling defects could not be eliminated following the grinding of the rail profile were identified and recommended for full reprofiling.

Figure 48: The post-grind condition of a section of the rail which was ground during the Grinding Campaign at Drax Power station.

3.2.2 Analysis Equipment

To assess the grinding operation at the Drax facility, the thermal camera utilised and discussed in Section 3.1.2. Likewise, the analysis of the thermographic video readings was performed using the same software as also discussed in the Section 3.1.2.

3.2.3 Results and Analysis

During the Drax Grinding Campaign, the temperature progression of 11 grinding passes was measured. The first recorded pass is shown in Figure 49. The image shows a steady rise in the temperature from the start to end of grind. This was common for the first 4 passes observed. Therefore, it was determined that the camera be moved closer to the tracks at a closer viewing distance but remain within the safe zone along the track sidings.

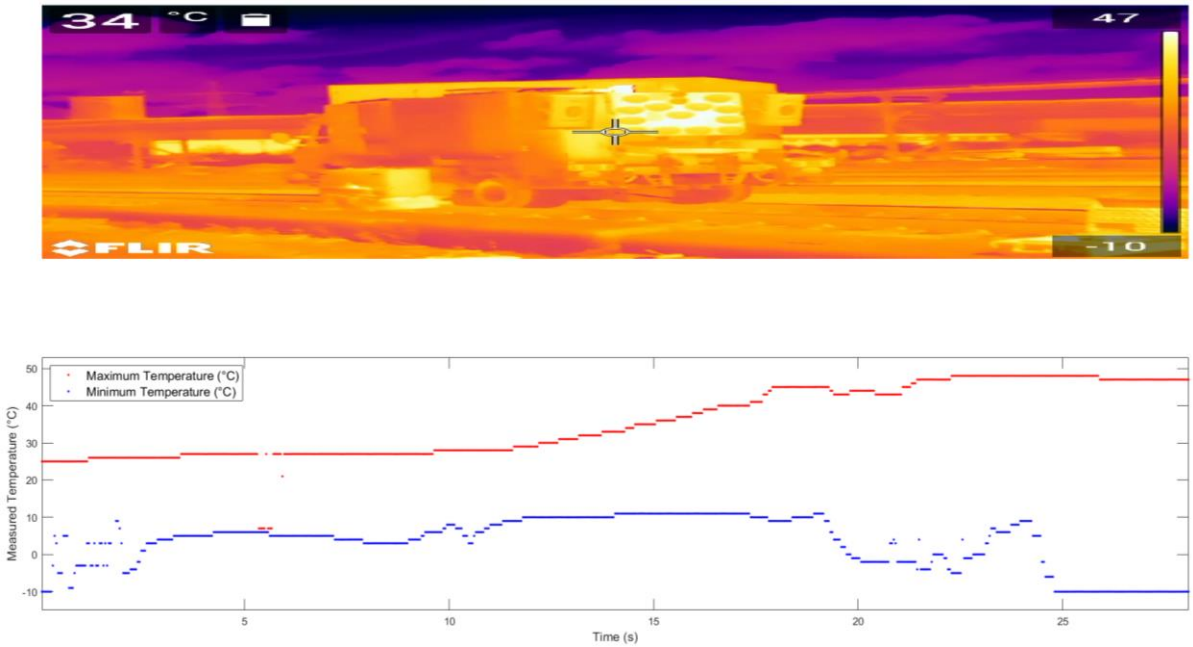

Figure 49: The final thermal image of the first grinding pass (Pass 1) and a plot of the corresponding temperature progression recorded at the Drax Facility

During the Passes 5 to 8, the thermal camera was repositioned and focused such that the thermal camera was directed at the grinding area and then trailed behind the grinding vehicle as it traversed along the railhead. At these grinding passes, the highest maximum temperature values were recorded at 127 °C, 62 °C, 181 °C and 100 °C respectively. Examples of the temperature progression of these passes (Pass 5, Pass 7) are also presented in Figure 50 and Figure 51.

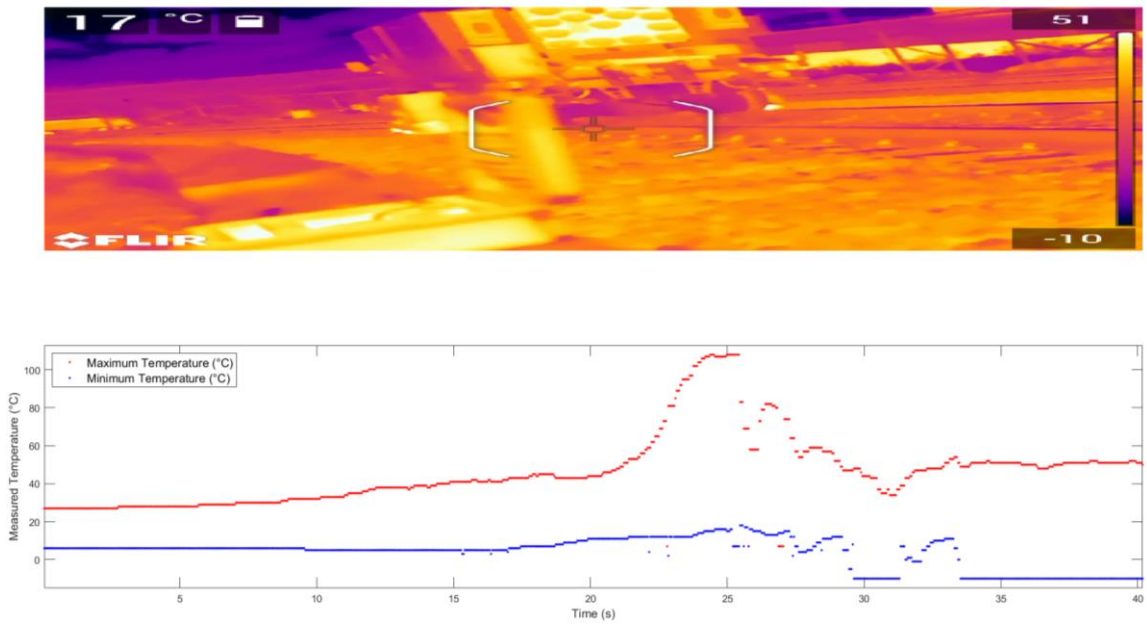

Figure 50: The final thermal image of the grinding pass 5 and a plot of the corresponding temperature progression recorded at the Drax Facility

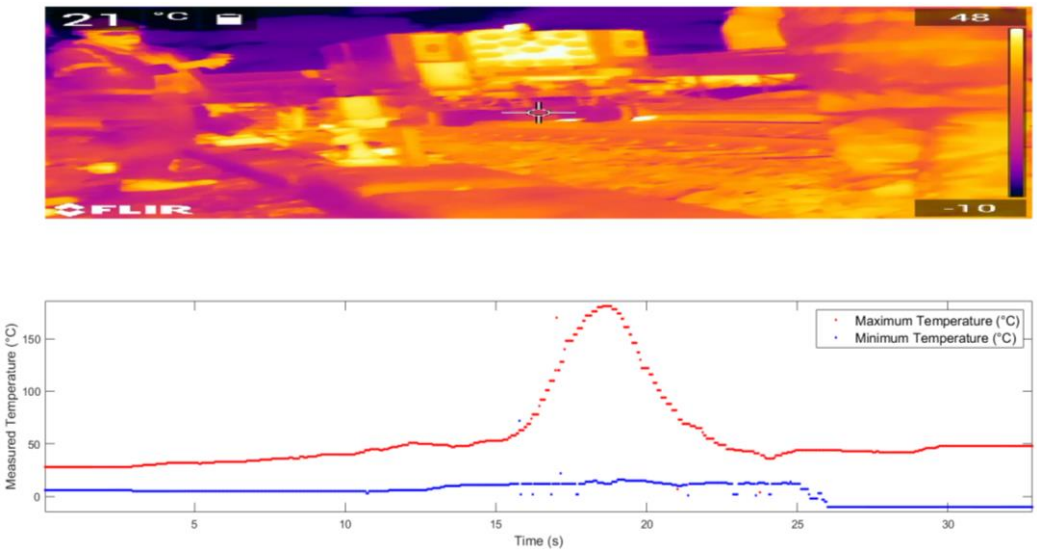

Figure 51: The final thermal image of the seventh grinding pass (Pass 7) and a plot of the corresponding temperature progression recorded at the Drax Facility

Further frame-by-frame analysis of the thermal video recording showing the grinding sparks generated during the seventh grinding pass (Pass 7) is also presented in Figure 52. The grinding sparks observed in the grinding passes conducted at Drax appear to have remained close to the grinding zone, with the furthest sparks being observed within the boundary of the sleepers.

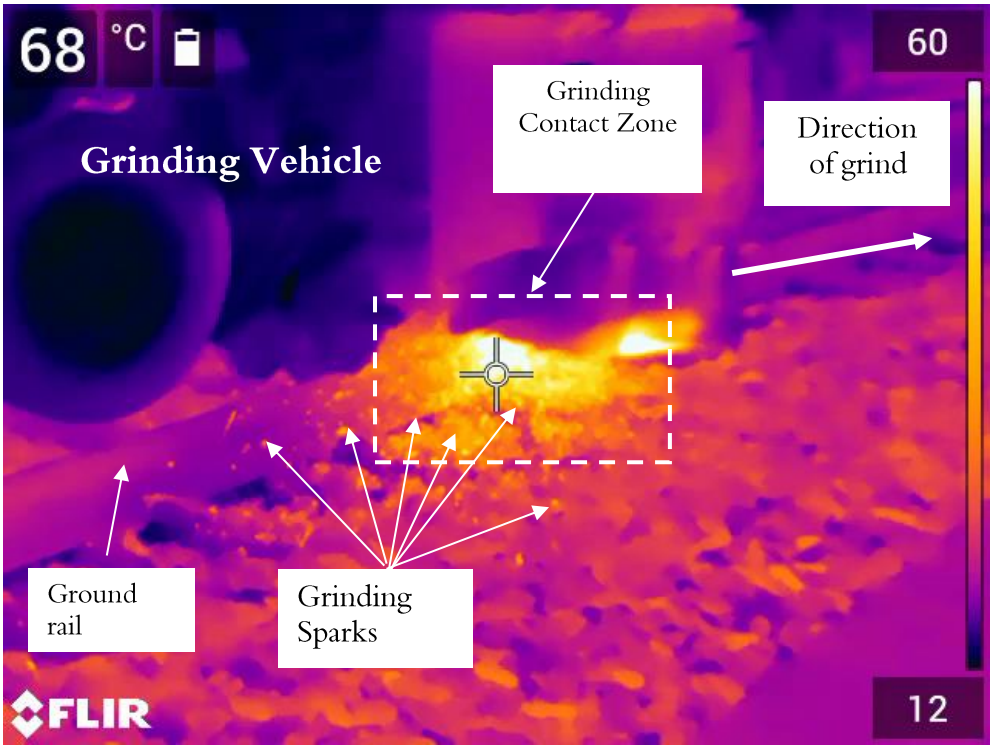

Figure 52: The grinding sparks generated during the seventh grinding observed at the Drax Facility

3.3 Summary

The results from the grinding temperatures recorded during field observations of grinding at two locations have been presented. Through the thermal readings conducted, it has been established that the thermal camera may be used to ascertain a thermal event during the grinding operations.

Additionally, in comparing the recorded temperatures captured at Metro dé Medellín and the Drax, it was difficult to determine a trend in the maximum temperatures. It is possible that the temperatures recorded are representative of the bulk temperatures of the rail during the grinding operation. However, due to the short contact time between the grinding wheel and the rail, this is difficult to establish.

The maximum values recorded per pass are presented in Figure 53. The recorded highest values of the maximum temperature per pass (≥130 °C – Metro dé Medellín; 181 °C – Drax) differ greatly from the maximum temperatures recorded by simulation in the literature where a thermal camera was employed to measure simulated train grinding passes on a passive machine [73]. Likewise, the significantly low correlation coefficients of the linear regression analysis performed for the maximum temperature values (Grinding Train: $R^2 = 0.114$ & Adjusted $R^2 = 0.0623$; Road-to-Rail Grinder: $R^2 = 0.0734$ & Adjusted $R^2 = -0.0296$) indicate that there is likely no correlation between the recorded maximum temperature and the number of passes with respect to the grinding operation.

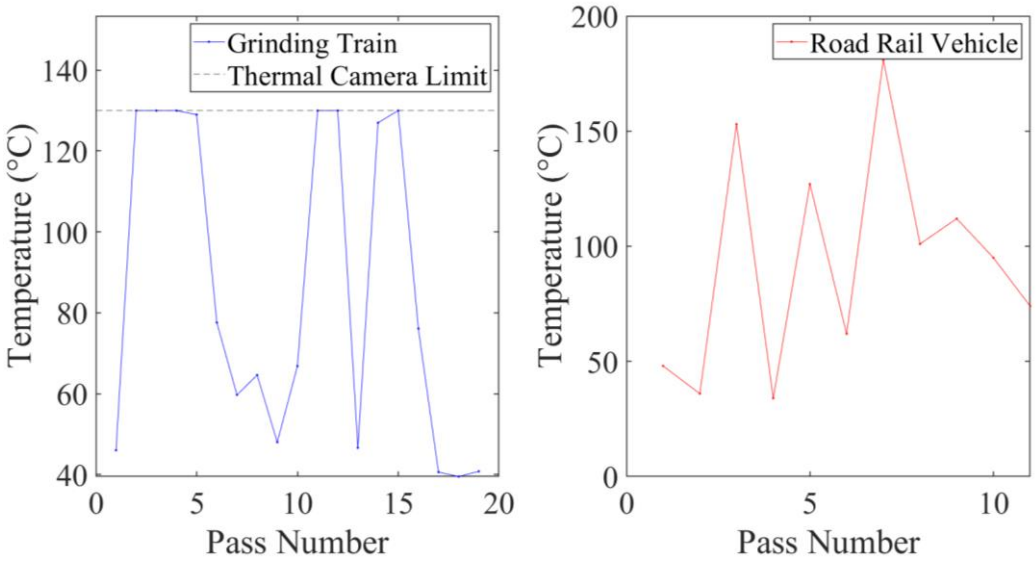

Figure 53: Maximum temperature values recorded during the grinding operations by grinding train (Medellin) and Road-to-Rail Grinder (Drax).

Alternatively, the difficulties associated with measuring higher temperatures than the ranges observed may also be attributed to the bulk temperature of the rail rapidly minimising the thermal energy generated on the surface before the action of the thermal camera. Therefore, the sampling frequency of the thermal camera may be insufficient in counteracting the cooling rate of the ground rail.

The thermal camera may provide useful information regarding the dispersal of sparks during grinding passes. This may prove useful for spark suppression endeavours in the industry. The thermal images of the grinding sparks which were generated by the grinding train at Metro dé Medellín appeared to be of greater dispersal volume in comparison to the sparks generated by the Road-to-Rail grinder utilised in Drax.

4 Laboratory Grinding Experiments

This chapter concerns the equipment and experimental procedure and techniques related to the grinding trials which were carried out to resolve the proposed research questions in Chapter 1. Rail surface grinding trials were performed on two modified Computer Numerical Control (CNC) machines. A pilot trial as well as subsequent trials based on the initial lessons learned are presented along with the results obtained. Further to this, the analysis and evaluation of the test data from the various rail surface grinding experiments are presented and followed by a detailed discussion of obtained results.

4.1 Experimental Apparatus

This section pertains to the machine tools used to achieve the grinding operations, the grinding wheels, temperature measuring equipment, possible calibrations of equipment and the identification of any sources of error. All grinding trials conducted in this section were performed on sections of standard grade non-heat treated flat bottom R260 rail and profile 60E1 (UIC60). The chemical composition and properties as specified by EN 13674-1:2011+A1:2017 [83] and produced by British Steel [84] are presented in Table 12.

Table 12: The basic typical composition and properties of the R260 rail as utilised in the research [83, 84]

Element	C	Si	Mn	S	Cr	R_m (MPa)	Hardness (HB)
Weight percentage (%)	0.62-0.80	0.15-0.58	0.7-1.2	0.008 – 0.025	≤ 0.15	≥ 880	260-300

4.1.1 Machine Tools

The CNC machine used at the University of Sheffield was a standard vertical machining centre which was manufactured by XYZ Machine Tools in the UK. The machine is designed for high precision and high speed machining of aerospace and mould-making components equipped with the capability for high speed spindle operations.

4.1.1.1 XYZ 1060 HS Vertical Machine Centre

The XYZ 1060 HS Vertical Machine Centre is a high-speed 3 axis vertical machine which is typically used in milling operations. The machining centre is presented in Figure 54. Though there was capability for its use, all grinding trials conducted in this CNC machine were performed in the absence of coolant. In addition, a single point diamond (SD) dressing tool was attached to the machine table at select intervals during the conventional grinding trials to renew the stone's cutting surface. A dressing tool was utilised to true the grinding wheels to ensure their concentricity. Later

on, between two grinding conditions, the dresser was also used to remove dull grits and to expose sharper grits. This type of dresser was also used due to its ease of set up within the grinding machine. Both conventional grinding tools used in the grinding trials were straight faced wheels, with active surfaces on the periphery of the wheels, therefore, the point dresser could be aligned and fixed relative to the active face of the wheel of the different grinding orientations utilised.

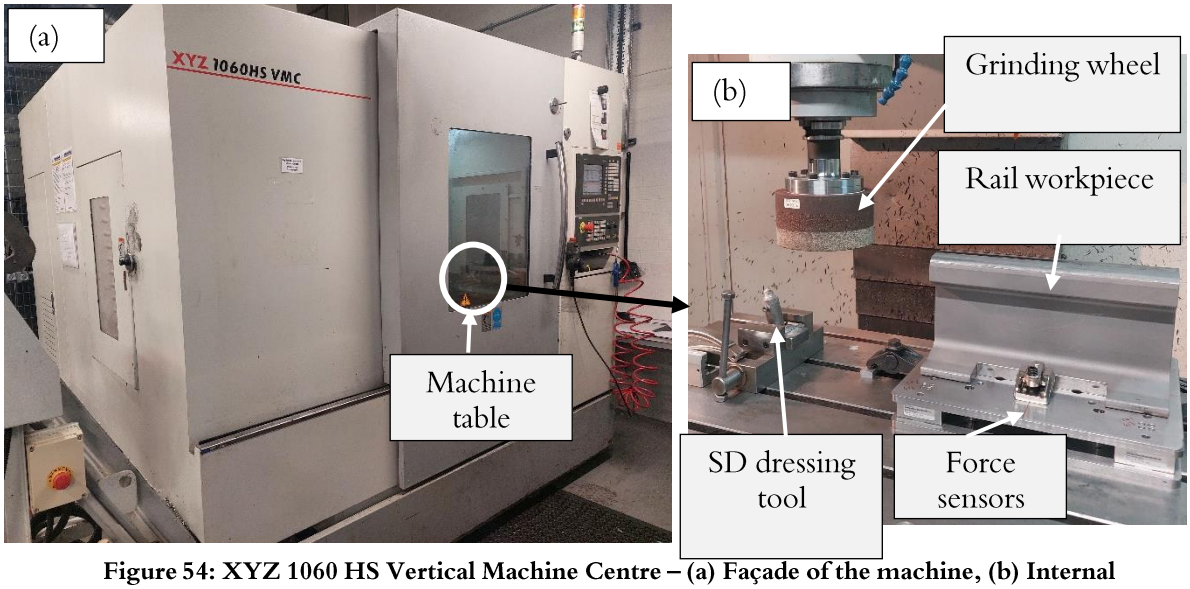

Figure 54: XYZ 1060 HS Vertical Machine Centre – (a) Façade of the machine, (b) Internal view of the machine bed and basic set up of the dresser, grinding wheel, rail workpiece and force sensors.

The manufacturer specifications of the XYZ 1060 HS machine are detailed in Table 13.

Table 13: Details of the manufacturer's specification of the XYZ 1060HS Vertical Machine Centre

Parameter	Specification
X-axis Travel (mm)	1,020
Y-axis Travel (mm)	610
Z-axis Travel (mm)	620
Spindle Speed Range (rpm)	5 – 12,000
Spindle Motor Power (kW)	21
Power Requirements (A)	71
Cutting Feed Rates (mm/min)	1 – 43,000
Maximum Table Load (N)	7,845
Spindle Taper	BT40

4.1.2 Grinding Tools

4.1.2.1 Conventional Grinding Tools (MV3 Cup Stone & MC3 Frog Stone)

The conventional grinding wheels utilised in this research include the MV3 Cup Stone and MC3 Frog Stone which are shown in Figure 55 (a) and (b). These wheels are commercially available stones

which are supplied by Aerotech Group and are utilised in Network Rail track maintenance routines on manually operated grinders. The wheels which are typically utilised on a grinding train are plate mounted AlO_x wheels which are glass fibre wrapped to prevent bursting of the wheel at high speeds. However, the stones utilised in this research are used within hand operated grinders for both corrective and preventive track maintenance within the UK rail network.

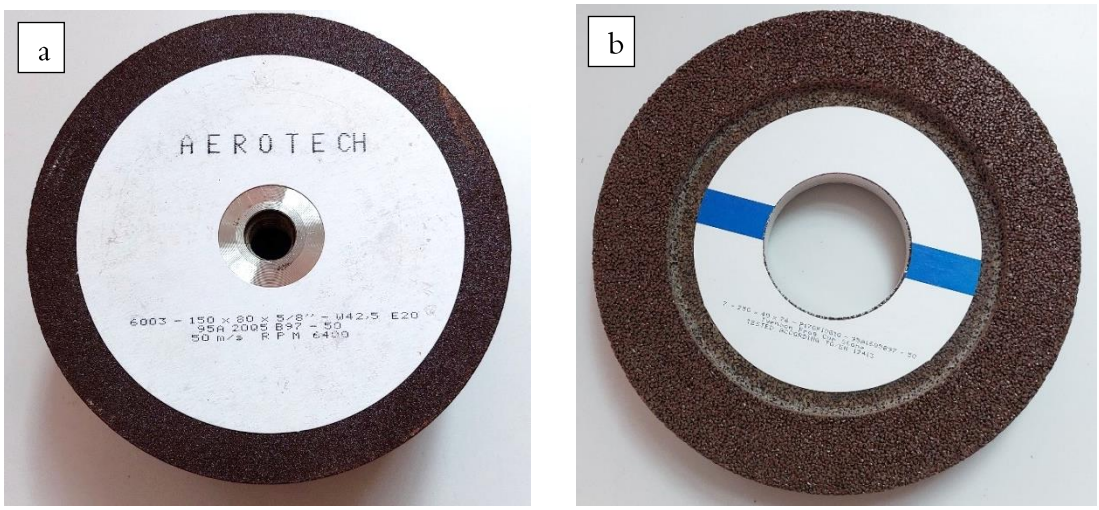

Figure 55: Conventional rail grinding wheels (stones) utilised in grinding trials – (a) MV3 Cup Stone and (b) MC3 Frog Stone

The Typhoon MV3 is a cup stone which is used for face grinding operations on the rail head, welded joints, as well as the rail running surface. The wheel possesses a large active surface area; therefore, it is designed for use on the vertical track grinders which can tilt up to ± 30°. Likewise, the Typhoon MC3 grinding stone is used for peripheral and/or face grinding operations as well as the removal of lipping on the railhead. Typically, the MC3 stone is used on the manually operated Frog and Switch Grinders.

In general, these grinding stones are particularly useful for the manually operated grinding of switches and crosses across the UK rail network. Both wheels are composed of brown Aluminium Oxide (AlO_x) abrasives. AlO_x abrasives are suited for these operations as a result of desirable properties such as high friability, which improve the durability of the grinding wheel through the resharpening of the grains. This in turn reduces the generated grinding forces and may reduce the overall wheel wear.

The specification for the MV3 Cup Stone is *1220R5B*, while that of the MC3 Frog Stone is *A14Q4BF*. These specifications indicate that both grinding wheels are resin bonded; however, the MC3 Frog Stone is a reinforced resinoid wheel in order to allow for increased cutting speeds. Likewise, both wheels are of comparably similar grades of high hardness (R and Q), which is desirable as a result of diminished susceptibility to wheel wear. At first use, the MV3 Cup stone was Ø 150 mm in diameter and 64.45 mm in thickness, while the MC3 Frog Stone was Ø 250 mm in diameter and 40 mm in thickness.

The methodologies of the grinding experiments for which the MV3 and MC3 stones were adapted and primarily utilised are detailed in Section 4.2.

4.1.2.2 Superabrasive Grinding Tools

Although typically employed for precision machining, a commercially available superabrasive (CBN) grinding wheel was selected for use due to its high resistance to wheel wear. A CBN grinding wheel (Figure 56) was utilised during the preliminary grinding tests in order to explore the declogging methods as well as the high speed grinding techniques which are later explored in the subsequent grinding trials discussed in 4.3.1. The retailer-supplied (Abtec Abrasives) specification of the wheel used was B252, which represents the grit size of the directly plated single abrasive layer that is electroplated onto a steel hub.

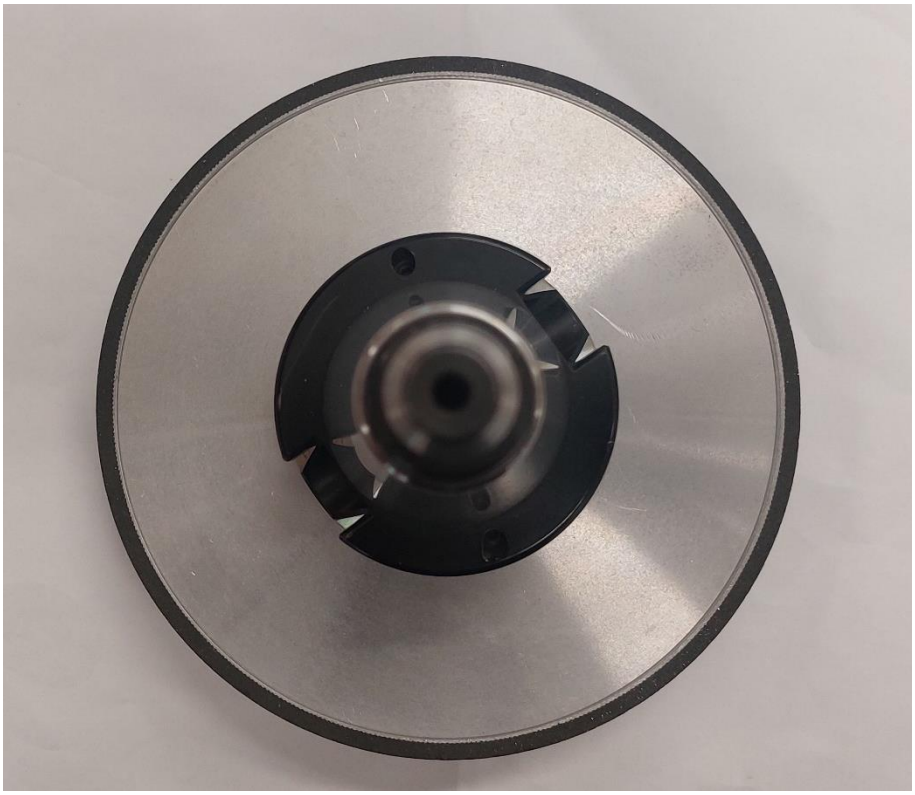

Figure 56: Electroplated CBN grinding wheel utilised in grinding trials.

Due to the short grinding lengths and times, it was anticipated that the superabrasive would undergo minimal wheel wear. As such, a single wheel was employed for both the pilot trial as well as the subsequent trial which involved the superabrasive grinding. At first use, the superabrasive wheel was Ø 156 *mm* in diameter.

4.1.3 Auxiliary Tools

4.1.3.1 Thermocouples

In this study, commercially available K-type thermocouples (diameter 0.5mm) of chromel-alumel base metal were selected for the measurement of the temperature distribution. This thermocouple type was chosen based on their wide operating temperature range (-200 - 1100 °C) while exposed-end thermocouples were chosen for the increased junction sensitivity (≈41 μV/°C) and quicker response in comparison to other thermocouple end configurations. Though the thermocouples were calibrated by the manufacturer, further checks were performed to assess the current state of calibration of the thermocouples to be used in the grinding trials. For this, thermocouple was placed at a set temperature within an oven calibrated oven and its measured output compared with the oven temperatures.

4.1.3.2 Thermal Camera

To augment the use of thermocouples in this grinding trial, thermography was carried out during the passes of each grinding parameter condition. Measurements were performed through the use of the FLIR E-95 advanced thermal camera (Figure 57 (a)). For the Pilot Trial which is discussed further on in Section 4.2.1, the thermal images using the E-95 camera were analysed using the FLIR Tools software. When carrying out measurements using the thermal camera, it was established that the camera lens must be in direct line of sight with the area being assessed. This was due to the glass window of the machine which was observed to have obscured the view of the lens and distorted the viewing image.

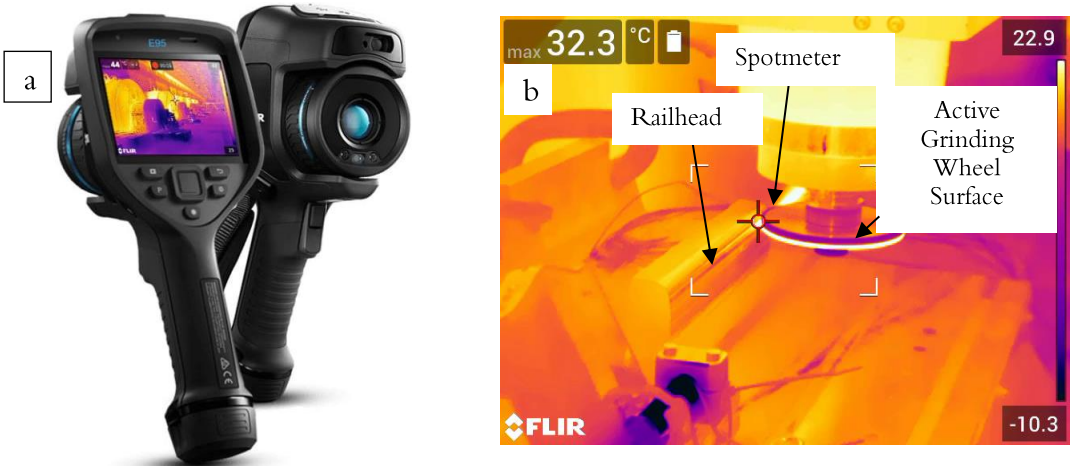

Figure 57: (a) FLIR E-95 thermal camera and (b) corresponding thermal image obtained in its use during a grinding pass

Therefore, during its use, the FLIR E-95 thermal camera was held by hand through the side window of the CNC Machine. An example of the thermal images obtained using the camera is also shown in Figure 57 (b). It should also be noted that for each recording taken, an attempt was made to direct the measurement tool (spotmeter) towards the visible grinding contact zone.

In subsequent grinding trials (conventional grinding), for health and safety reasons, it was determined that a different thermal camera be employed for thermographic readings. Therefore, subsequent thermographic readings were carried out using the MicroEpsilon Thermoimager TIM

160 (Figure 58 (a)). An advantage of this camera is its portability and ease of mounting within the enclosure of the CNC machine. The readings obtained during the corresponding grinding passes were analysed using the camera's accompanying computer software, which was TIM Connect. An example of the image obtained using the Thermoimager is presented in Figure 58 (b). With this camera, three regions were measured, with Area 1 corresponding to the moving hottest spot (the grinding contact area) while Areas 2 and 3 correspond to fixed areas on the rail surface.

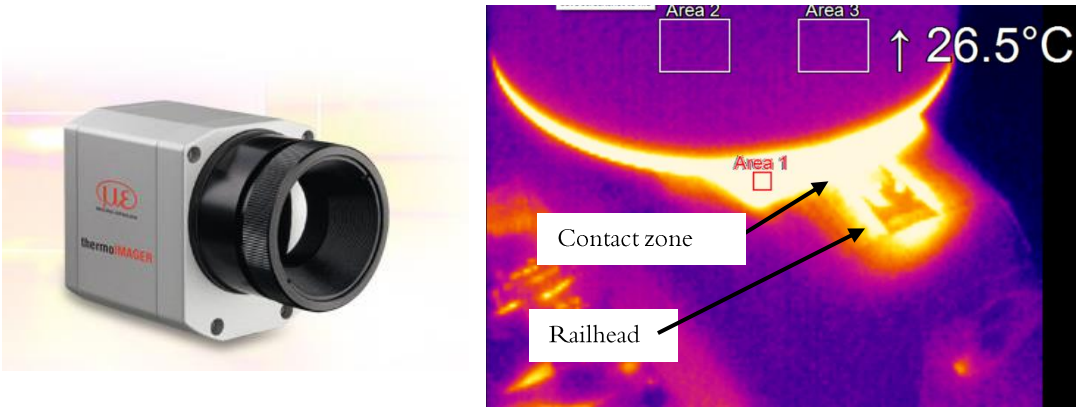

Figure 58: (a) MicroEpsilon Thermoimager TIM 160 and (b) corresponding thermal image obtained during a grinding pass

4.1.3.3 Force Measurement

To calculate the grinding forces generated, a force plate system was developed. The force plate system consisted of a steel top plate, steel base plate, four three-axis force sensors and a signal amplifier. The force sensors used were load cells produced by Interface Force Ltd. which were each rated up to a capacity of 200 N and fixed between the steel plates. The locations of the force sensors are depicted in Figure 59.

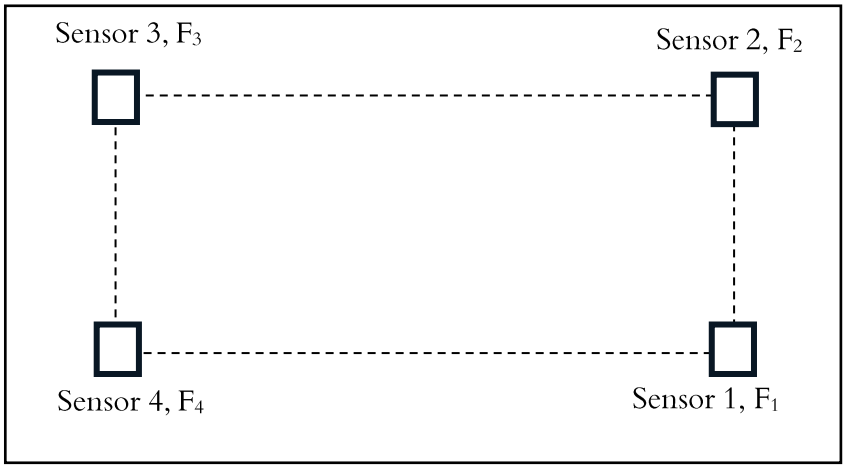

Figure 59: Position of force sensors used to measure the total component forces on rail sample

The implementation of the force plate system required the design of multiple fixtures to accommodate the two grinding orientations adopted in the experiments. The plates were designed for placement on two orientations of the grinding wheel:

- Orientation 1 – Horizontal Grinding: This rail placement orientation concerned the trials where face grinding was performed. As such, the rail was oriented in the vertical (upright) position. The base of the rail workpiece was fixed onto the force plates, which were then attached directly to the machine table through the use of T-slot fixtures. This configuration is further discussed in Section 4.2.2.1 which details the grinding trial where the conventional cup wheel was employed.
- Orientation 2 – Vertical Grinding/Horizontal placement of the rail: For grinding trials where the rail was to be placed horizontally, the bottom force plate would be connected to an angle plate support which was fixed to the CNC machine table. This configuration was primarily adopted for the superabrasive grinding trials which is discussed in Section 4.2.1 and the conventional peripheral grinding trials presented in Section 4.2.2.2. As later shown, the sensors were situated such that the rail workpiece was fixed centrally relative to them.

Fixtures were designed to measure the grinding forces and to inherently quantify the grinding pressure which was exerted during the grinding process. The force data acquisition was carried out using the National Instruments Flexlogger software. The three-component forces for each load cell (F_1, F_2, F_3 and F_4) were recorded as an output. As such, the combined force for each axis is calculated using the Equations 13, 14, 15:

$$\sum F_x = F_{1x} + F_{2x} + F_{3x} + F_{4x} \quad 13$$

$$\sum F_y = F_{1y} + F_{2y} + F_{3y} + F_{4y} \quad 14$$

$$\sum F_z = F_{1z} + F_{2z} + F_{3z} + F_{4z} \quad 15$$

4.1.3.4 Post-grind Analysis

The post-grind assessment of the rail surface was carried out through the investigation of the surface integrity of the ground rail. Surface roughness measurements were carried out using two measurement apparatus. Following each set of grinding passes, a roughness measurement was taken using the Mitutoyo Surftest SJ-400 profilometer which is shown in Figure 60 (a). The first set of readings were obtained following each pass (or parameter combination). In this case, a quick average roughness (R_a) and ten-point roughness (R_z) measurements were taken along the longitudinal direction (in the direction of grind) and axially (perpendicular to the direction of grind). Roughness measurements were taken at 3 regions on the ground surface. These locations are also detailed in Figure 60 (b).

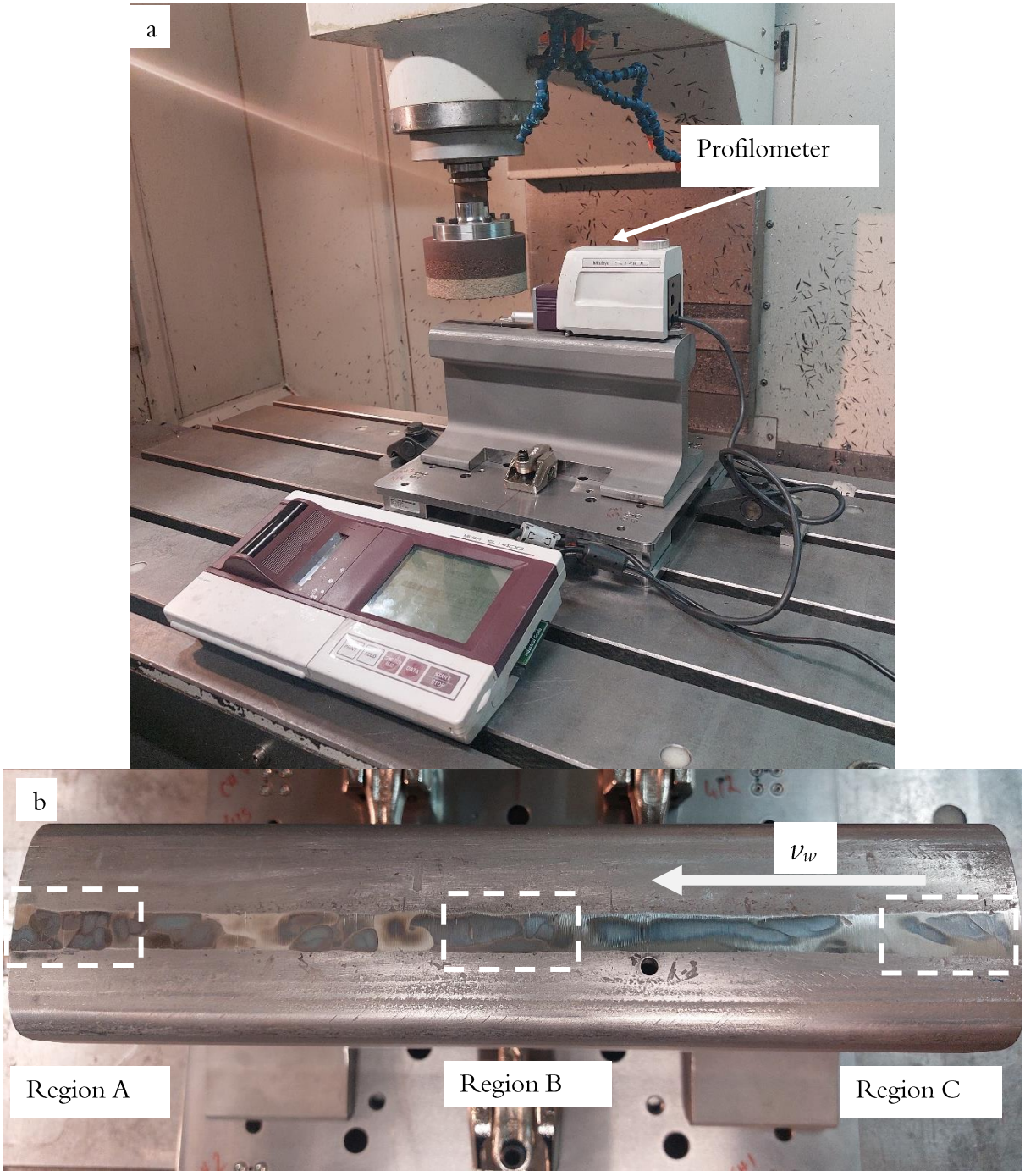

Figure 60: (a) Photograph of the surface profilometer being used on the rail surface following a grinding pass; (b) the ground rail surface with locations of roughness measurement

Additionally, secondary roughness measurements to assess the final state of the rail surface following the grinding trials using each stone. The secondary roughness measurements were performed using the Alicona RL focus variation microscope (Figure 61). The portable nature of this microscope allows for this measurement tool to be employed for use on full size rail on tracks. However, due to its size, the placement of the Alicona measurement tool was not feasible for use within the CNC machine enclosure. Therefore, the microscope was used on full-size rail samples subsequent to the grinding trials.

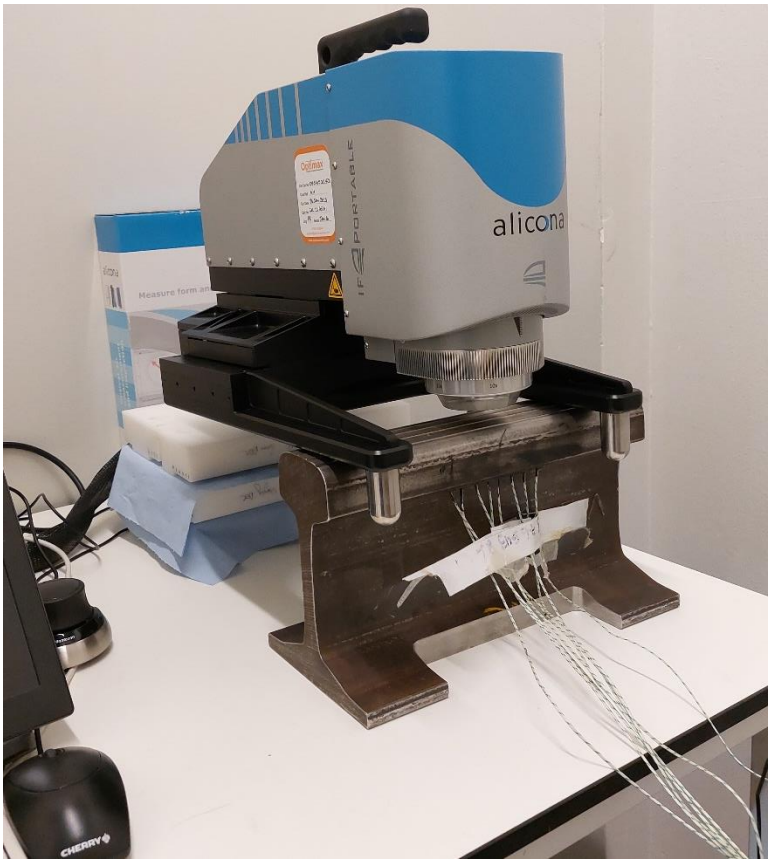

Figure 61: Set up of the Alicona RL focus variation microscope used for secondary roughness measurements

Sectioning was performed on the ground rail to extract samples for microstructural analysis. For the rail which had been subjected to superabrasive grinding, a sample was extracted from each grinding facet which corresponded to each grinding condition and sectioned along the longitudinal cross-section to allow for etched optical microscopy. To expose the cross-sectional microstructure, the samples were etched using 2 % Nital. Optical microscopy was performed using the Nikon Eclipse LV150 light microscope. The obtained micrographs are presented in the corresponding sections for each related grinding approach.

Following the observation of the microstructure through optical microscopy, microhardness tests were carried out to characterise the subsurface of the polished sample and to ascertain the presence of WEL which was first observed through optical microscopy. The microhardness tests were performed through the use of a Struers Duramin-40 microhardness indenter which performed indents using a 0.3 kg load to measure the hardness from the near surface into the bulk material, thus providing a depth profile of the metallurgical sample.

The cutting face of the MV3 Cup Stone was observed using the AM7915MZTL DinoLite Edge Digital Microscope. The images taken were done using the Extended Dynamic Range feature (EDR), which compiles images from various exposure levels.

4.2 Test Methods

4.2.1 Peripheral Grinding with Superabrasive Wheel

In order to establish a means to incorporate temperature measurement apparatus within a rail section, a preliminary machining trial was planned within a laboratory setting. To assess the viability of the thermocouple insertion method, a grinding trial was carried out on the XYZ 1060 CNC machine which is described in Section 4.1.1 using the commercially available superabrasive grinding wheel which is also discussed in Section 4.1.2.

4.2.1.1 Sample Preparation and Configuration

To perform this preliminary grinding trial, the selected workpiece used was a standard 300 *mm* long full-sized, flat-bottomed rail workpiece of R260 grade. To evaluate the grinding temperature as close to the surface of the rail as possible, k-type thermocouples were embedded near to the surface. 8 blind holes were drilled 12 *mm* apart in a linear array along the underside of the rail head to various depths from the top surface and such that the bottom ends of the holes were situated directly beneath the facet towards the centre of the rail. Additionally, a through-hole was also drilled in as a reference for dimensioning and was not employed for thermocouple input. A single thermocouple was placed within each blind hole and secured into position using a highly conductive epoxy resin adhesive. To enable adequate space of movement for the thermocouples, a cutout was made on the foot of the rail, so that the thermocouple wires could be easily passed onto the data acquisition module. The depth of each allocated thermocouple from the workpiece top surface is also presented in Table 14.

Table 14: Thermocouple locations relative to the surface of the rail workpiece.

Thermocouple ID	**T1**	**T2**	**T3**	**T4**	**T5**	**T6**	**T7**	**T8**
Depth from rail surface (mm)	0.55	0.6	0.65	0.7	0.8	0.9	1	1.5

The grinding facets as well as the location of thermocouple placement for the rail are presented in Figure 62). Prior to drilling and to prepare the rail sample workpiece, a skimming pass was made on the rail to ensure uniformity of the rail surface before thermocouple embedment.

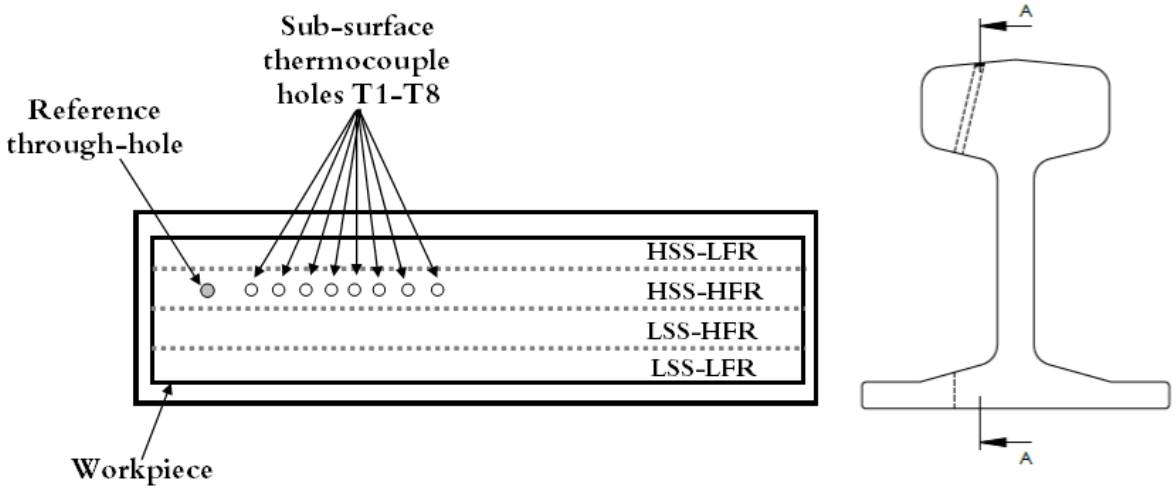

Figure 62: Schematics of (a) the thermocouple placement and test pass configuration on the ground rail workpiece (b) cross-section of location of thermocouple hole in rail Invalid source specified..

The trial was carried out within the XYZ 1060 High Speed CNC machine discussed in Section 4.1.1.1 in the horizontal peripheral grinding orientation. Employing the superabrasive wheel which is detailed in Section 4.1.2.2, a BT40 tool holder grinding tool used to adapt the grinding wheel to the spindle of the machine tool. Using the superabrasive grinding tool, single peripheral grinding passes were performed at four parameter combinations. The parameters used in this pilot study are detailed in Table 15. Temperature data was captured using the National Instruments data module and was transferred via USB onto a PC using the Labview software. A hybrid schematic of the experimental set-up and the rail section employed in this preliminary grinding trial are detailed in Figure 63.

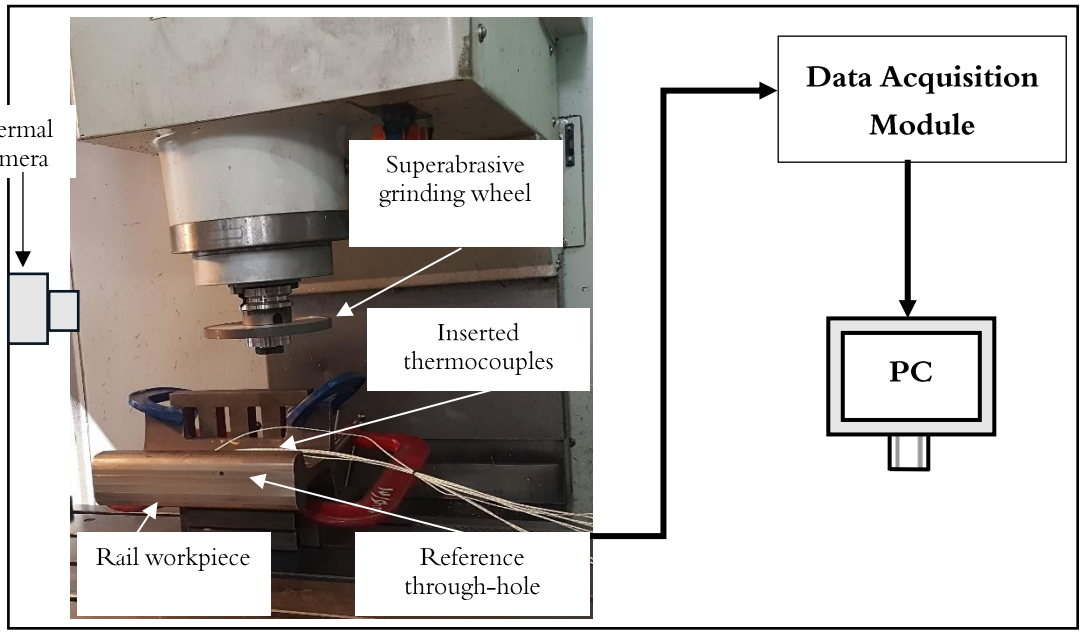

Figure 63: Experimental configuration in XYZ machine tool depicting the rail workpiece, superabrasive grinding wheel and thermocouples for temperature measurement.

An example of the temperature output obtained from a single grinding pass is shown in Figure 64. For all temperature plots, the temperature progressions as recorded by the eight embedded thermocouples during the grinding operations for each parameter are plotted against time. The plots show the temperature in °C as measured by the thermocouples prior to the onset of the grinding pass (time prior, t_p), during the pass (time during, t_d) and in the aftermath of the grinding pass (time after, t_a). The indicators T1 – T8 signify the 8 thermocouples which were embedded beneath the rail head at various depths from the top surface.

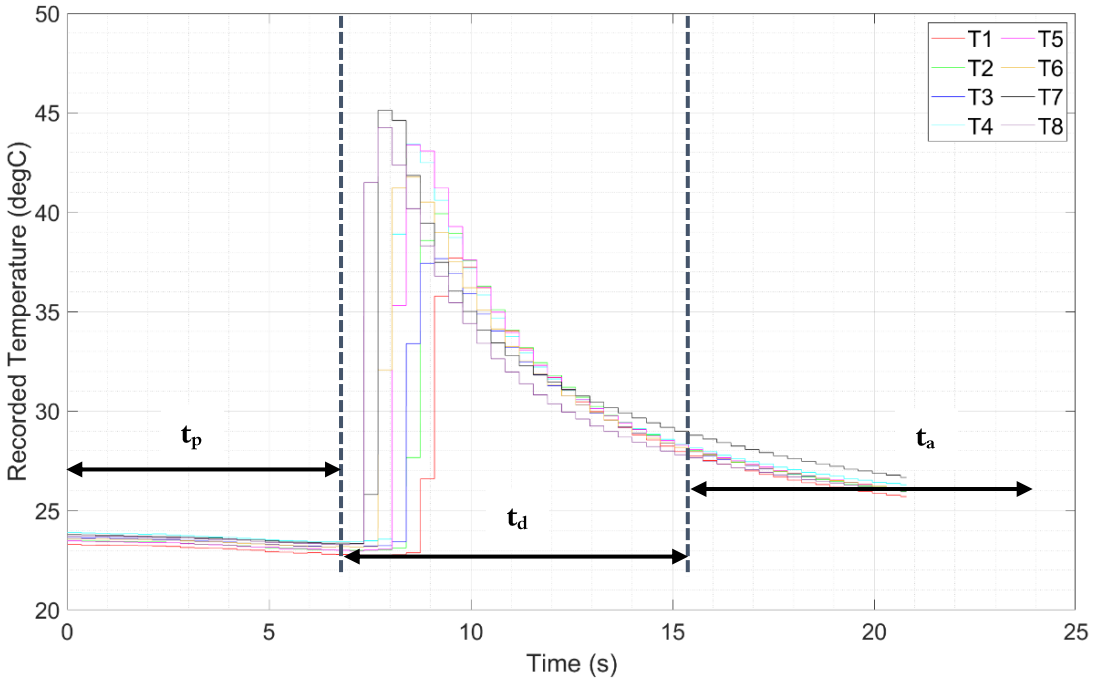

Figure 64: An example plot of the thermocouple output of temperature against the time elapsed

A series of grinding passes were performed at various interactions of parameters. Although the values of spindle speeds in km/hr represent the industry standard parameters for rail grinding, the values have been converted to surface speeds to be consistent with possible calculations. This conversion was performed using Equation 16 below.

$$v_s = \frac{v_{spindle} \cdot \pi \cdot d_s}{6000} \qquad 16$$

where $v_{spindle}$ is the spindle speed in *m/s* and d_s is the wheel diameter in *mm*. The conducted passes were classified into Low Spindle Speed-Low Feed Rate (LSS-LFR), Low Spindle Speed-High Feed Rate (LSS-HFR), High Spindle Speed-Low Feed Rate (HSS-LFR) and High Spindle Speed High Feed Rate (HSS-HFR). The LSS parameter corresponds to a surface speed $v_s = 6000\,rpm$, while HSS corresponds to $v_s = 12000\,rpm$; likewise, the LFR and HFR values selected for this study were $v_w = 10{,}000\,mm/min$ and $v_w = 43{,}000\,mm/min$ respectively. The

parameter combinations of the tests performed correspond to two values of specific material removal rate which are calculated using Equation 17. The specific material removal rate Q'_w provides an indication of the efficiency of the grinding process in relation to the energy consumption and allows for a comparison between different grinding conditions. Through the combination of the depth of cut a_e and the feed rate v_w, the specific material removal rates achieved in this superabrasive grinding trial were $Q'_w = 16.7\ mm^3/mm \cdot s$ and $Q'_w = 71.7\ mm^3/mm \cdot s$.

$$Q'_w = a_e \cdot v_w \qquad 17$$

The tests performed at LSS-LFR conform to the current industrial rail grinding practices which generate low material removal rates; however, the tests carried out at HSS-HFR conform to HSG practices, thus enabling the comparison of temperatures with both opposing parameters and the variations in-between.

Table 15: Grinding parameters employed in the grinding trial with thermocouple embedment.

	LSS-LFR	LSS-HFR	HSS-LFR	HSS-HFR
v_s (rpm)	6000	6000	12000	12000
v_w (mm/min)	10,000	43,000	10,000	43,000
No of Passes	5	5	5	5
a_e (mm)	0.1	0.1	0.1	0.1
Q'_w ($mm^3/mm \cdot s$)	16.7	71.7	16.7	71.7

Grinding was performed on the rail head and the grinding passes were made at a constant depth of cut $a_e = 0.1\ mm$. Five consecutive passes were carried out for the four parameter interactions in the grinding trial leading to a total depth of cut of $0.5\ mm$. All grinding passes were performed with the same direction of grind; however, only the passes related to the HSS-HFR test configuration were made directly above where the thermocouples were situated as previously shown in Figure 62. The test parameters combinations which were used during this grinding trial are outlined in Table 15.

4.2.1.2 Declogging Implementation for the Prevention of Wheel Loading

As a result of the dry grinding approach, which is typically employed in rail grinding applications, the introduction of superabrasive tooling necessitates a means to prevent wheel loading (the adhesion of workpiece material to the wheel surface). As such, a novel method of declogging has been developed at The University of Sheffield. Trialled applications of this method have presented the potential for the reduction of wheel loading which in turn reduces the propensity for the formation of WEL in the rail surface following a grinding operation.

As such, for the successful utilisation of the superabrasive grinding wheel, the declogging material was directed towards the contact zone of the wheel and the rail workpiece surface. Due to the nature of the intellectual property, further description may not be made of the novel declogging methods;

however, the range of relatively low temperatures which were observed can be attributed to this declogging mechanism.

4.2.2 Conventional Rail Grinding Trial to Benchmark Temperature Measurement Approaches within CNC Machine

To assess the implementation of temperature measurement techniques for conventional rail grinding, laboratory grinding trials were developed. The aim of this grinding trial was to compare the recorded temperatures with the expected temperatures based on the grinding forces. Therefore, the generated grinding forces were measured during each grinding pass, while the grinding temperatures were measured using thermocouples as well as a thermal camera. The following grinding approaches were achieved in this grinding trial:

- Face grinding with conventional cup wheel (MV3)
- Peripheral grinding with conventional frog wheel (MC3)

The grinding parameters which were adopted in this study were chosen based on the range of parameters and the Specific Material Removal Rates which are employed in actual rail grinding operations. Likewise, for all passes, the values of the feed rate and the depth of cut were fixed in order to allow for the direct comparison of the recorded forces of the different trialled orientations which are discussed in the chapter.

For each grinding condition, multiple passes were carried out to achieve a total depth of cut of 0.1 mm from the rail surface. This is similar to what is adopted in actual rail grinding, where, in order to achieve a desired depth of cut, the grinding operation is performed with an array of grinding wheels running concurrently across the track length. To vary the wheel speed, the two values were selected to ensure that the operating speeds remained within the manufacturer recommendations.

With both grinding approaches investigated in this study, the feed rate v_w was fixed at 2000 mm/min. This value falls within the range of the forward speeds that might be expected during the operation of the manually operated grinders which are propelled forward by human intervention. Though the selected feed rate may be considered low for the operations on grinding trains, resultant grinding force and their effect on the surface microstructure of the ground rail still provides a basis for comparison.

4.2.2.1 Face Grinding with Conventional Cup Wheel

To perform this grinding trial, a 300 mm rail sample was prepared in a similar configuration as in Section 4.2.1.1. The grinding wheel used to achieve this face grinding trial was the MV3 cup stone which was previously discussed in Section 4.1.2.1. Unlike in the face grinding approach which is employed on the grinding train, where the normal grinding force is controlled and the depth of cut, and material removal are the desired outputs of the grinding process. In this grinding trial, the

thermal camera was employed as the temperature measurement approach. Force measurement was achieved using Orientation 1, where face grinding was performed on a flatbottomed rail workpiece which was oriented in the upright position. The set-up of this grinding trial is shown in Figure 65. The image shows the following details:

1) The cup grinding wheel as per the details demonstrated in Figure 55 (a)
2) Thermal camera directed at the grinding contact zone
3) Force sensors
4) Top and bottom force plates fixtures
5) The rail workpiece clamped onto the plate fixtures

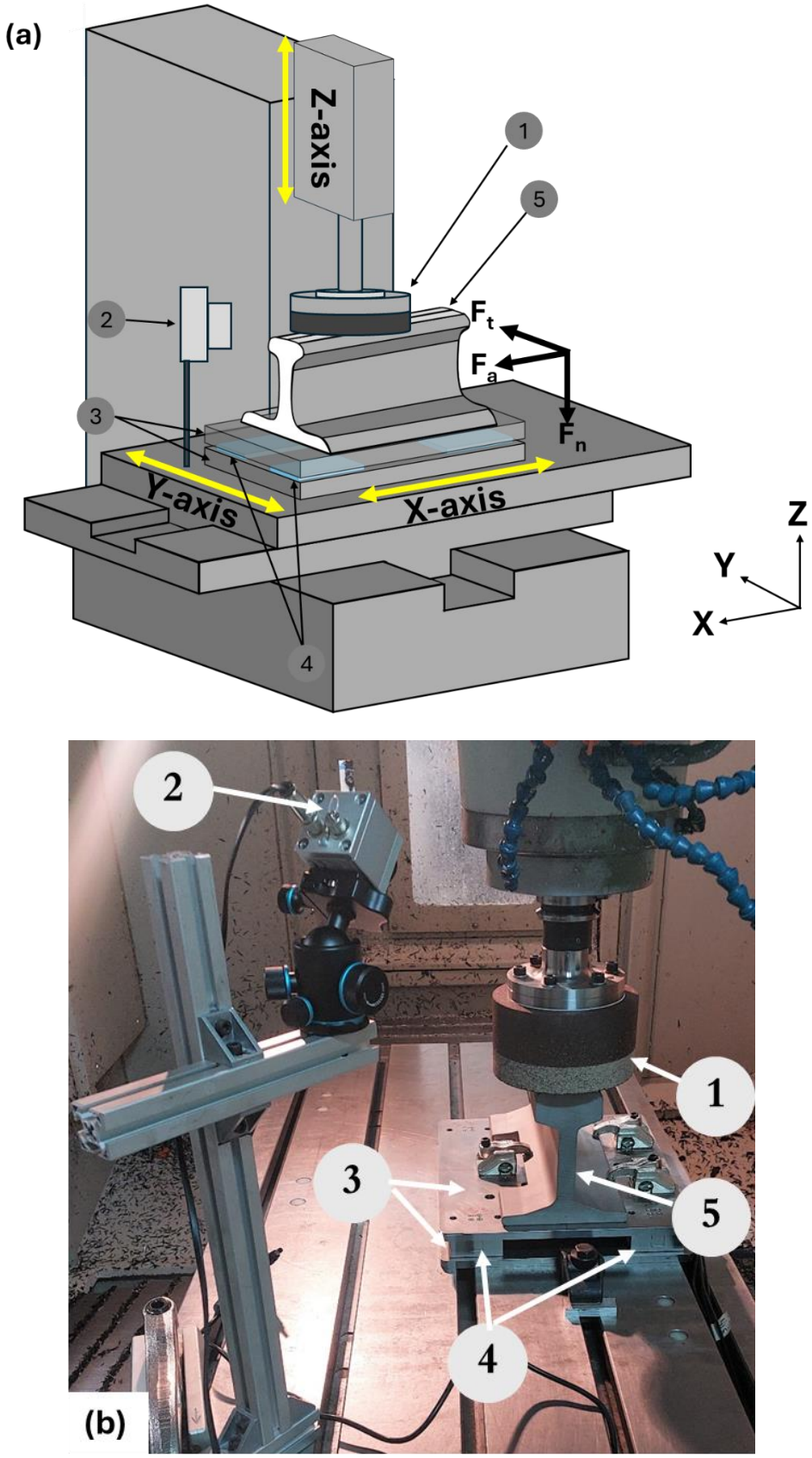

Figure 65: (a) Schematic and (b) photograph of the rail workpiece set-up using conventional cup wheel for face rail grinding within a CNC machine

The surface grinding parameters which were adopted in the face grinding trials are also detailed in Table 16. For each parameter combination, the passes were performed consecutively to enable the understanding of the accumulation of temperature with increasing passes. These parameters were selected as the benchmark for the conventional grinding of rail within the CNC machine. Using the conventional face grinding method with a cup wheel, a total of 4 grinding passes were conducted at a wheel speed of 2000 rpm, while another 4 grinding passes were made at a wheel speed of 3000 rpm.

Table 16: Surface grinding parameters for the rail grinding trials with a conventional face grinding wheel

Wheel Type	Wheel Speed v_s (rpm)	Feed rate, v_w (mm/min)	a_e (mm)	Total a_e (mm)	Specific MRR, Q_w ($mm^3/mm{\cdot}s$)
Cup Stone (MV3)	2000	2000	0.025	0.1	0.83
	3000	2000	0.025	0.1	1.25

4.2.2.2 Peripheral Grinding with Conventional Frog Wheel

This grinding trial was designed to investigate the effect of the measured temperature generated in the use of conventional frog wheels for the grinding of rail within a CNC machine and to record the grinding forces. Again, the modified XYZ 1060HS Vertical Machine Centre was used as the machine tool in this grinding trial. However, due to the configuration required which was in order to achieve peripheral grinding, a more complex approach (Orientation 2) was required.

The design of the rail sample in this grinding trial did not deviate from that which was described in the Pilot Trial in Section 4.2.1. However, the mounting fixtures were adapted in this trial. The rail section to be ground was mounted onto an angle plate support which was fixed to the machine bed. An independently fixed support was designed to support the top of the rail as it was fixed in the horizontal position. Figure 66 shows the set-up of the test components as utilised in this grinding trial. The image shows the following details:

1) The frog grinding wheel as per the details demonstrated in Figure 55 (b)
2) Diamond dresser mount
3) Top and bottom force plates fixtures
4) Rail workpiece
5) Thermal camera directed at contact zone
6) Rail head support

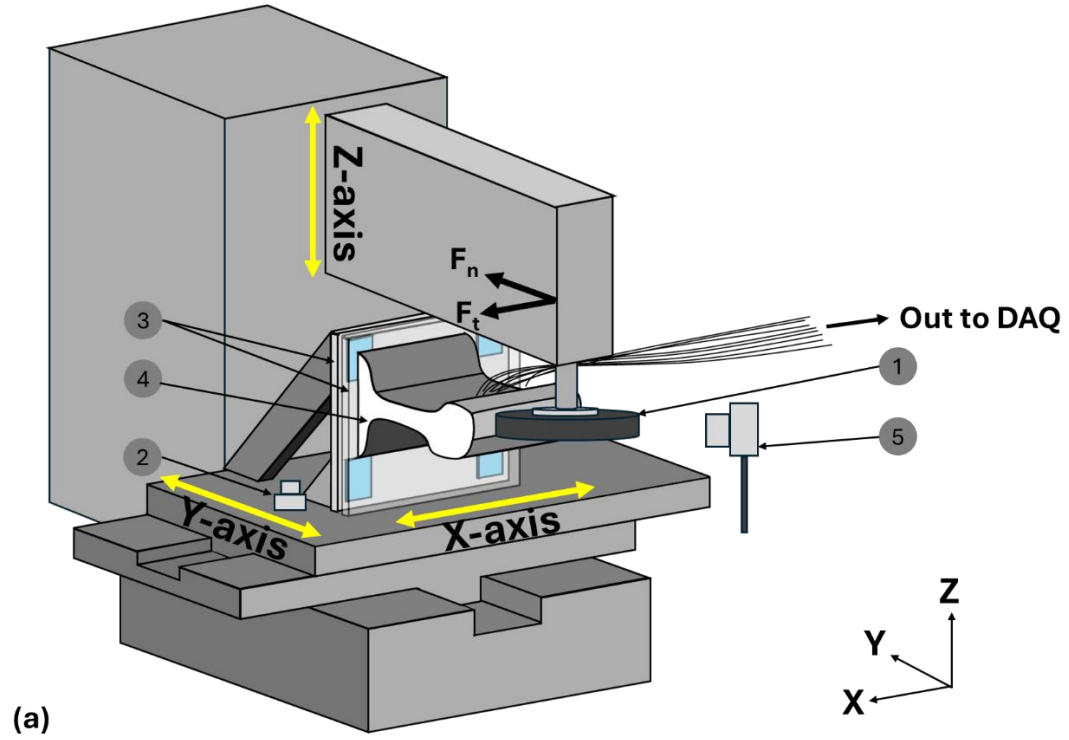

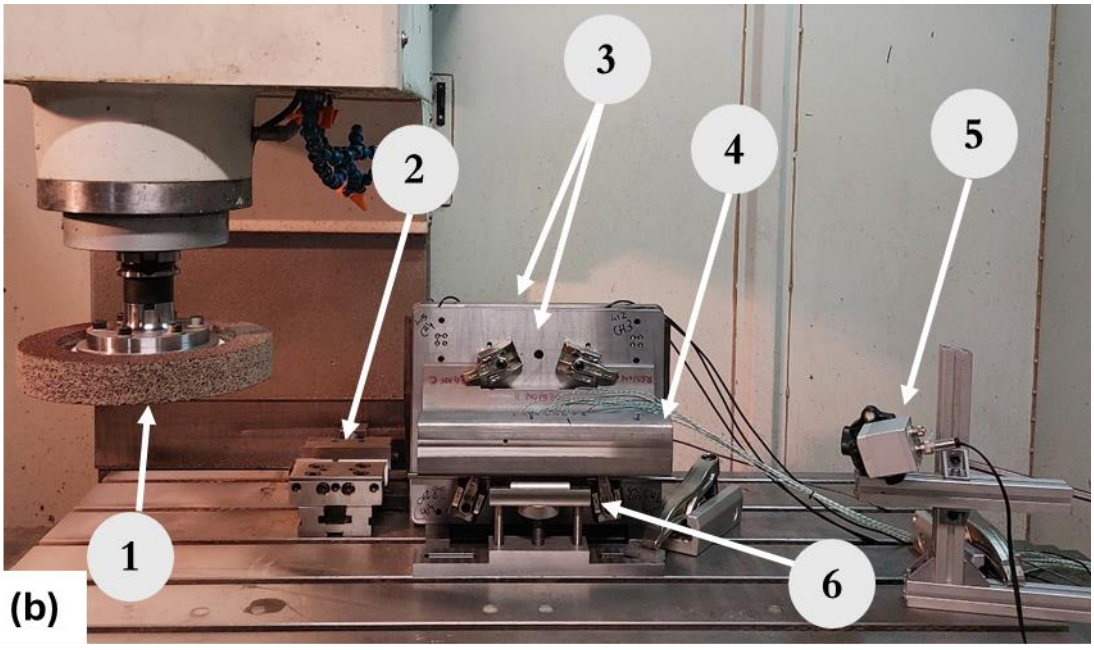

Figure 66: (a) Schematic and (b) photograph of the rail workpiece setup using a conventional frog wheel for peripheral rail grinding within a CNC machine

Table 17 details the surface grinding parameters which were selected for the peripheral grinding trials. Again, the passes were carried out consecutively for each parameter combination.

Table 17: Surface grinding parameters for the rail grinding trials with a conventional peripheral grinding wheel

Wheel Type	Wheel Speed v_s (rpm)	Feed rate, v_w (mm/min)	a_e (mm)	Total a_e (mm)	Specific MRR, Q_w ($mm^3/mm \cdot s$)
Cylindrical Peripheral Stone (MC3)	2000	2000	0.025	0.1	0.83
	3000	2000	0.025	0.1	1.25

4.3 Experimental Results and Analysis

4.3.1 Pilot Trial – Peripheral Grinding with Superabrasive Wheel

Section 4.3.1 considers the viability of the temperature measurement approaches employed in the superabrasive grinding process. The section considers the recorded temperatures using the embedded thermocouple approach against the temperatures recorded with thermal camera.

4.3.1.1 Temperature Data in Superabrasive Grinding

This section concerns the results of the temperature readings of during the grinding trials conducted using the superabrasive grinding wheel. The recorded temperatures for the eight embedded thermocouples are shown in each plot. These are represented by the indicators T1-T8, where T1 is represents the thermocouple depth which is closest to the rail surface at 0.55 mm, while T8 represents the thermocouple which is furthest from the surface at 1.5 mm. The temperature plots are indicative of a response in the thermocouples to the grinding operation. The maximum recorded temperatures for each pass conducted at the different grinding conditions LSS-LFR, LSS-HFR, HSS-LFR and HSS-HFR are presented in Figure 67.

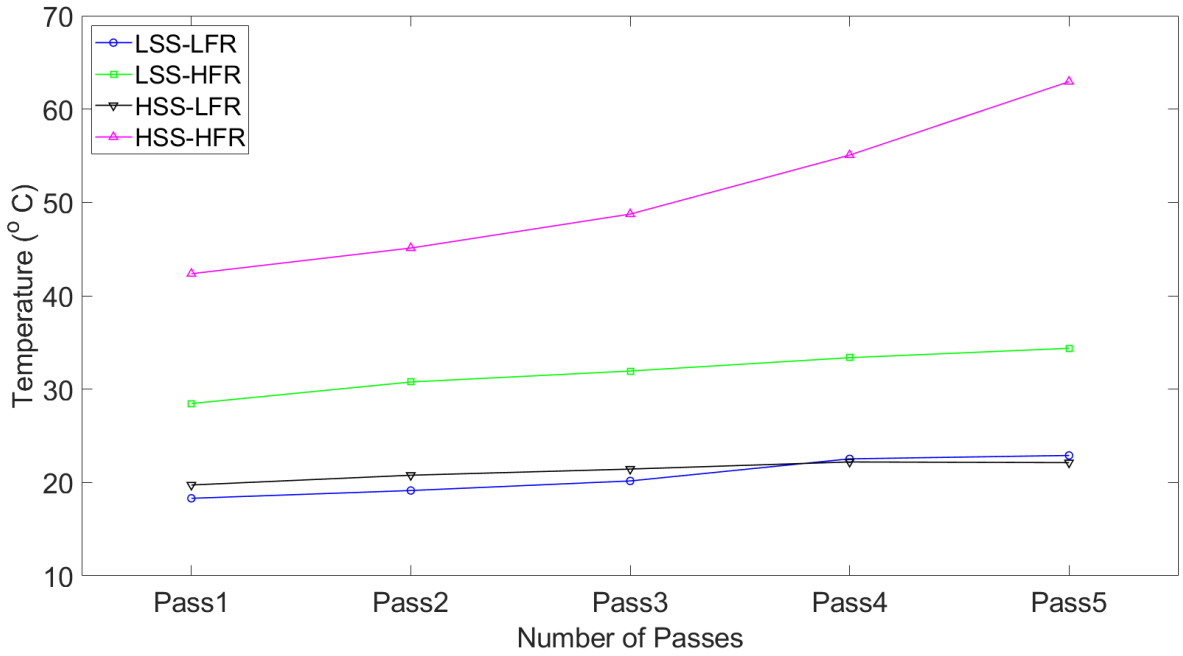

Figure 67: Maximum temperatures recorded by embedded thermocouples during the grinding passes conducted at grinding conditions LSS-LFR, LSS-HFR, HSS-LFR and HSS-HFR.

Figure 68 and Figure 69 show the respective plots of the temperature against time for the initial and final grinding passes which were carried out with the Low Spindle Speed - Low Feed Rate (LSS-LFR) grinding conditions. The spindle speed of the passes conducted was 49 m/s, while the feed rate was 1000 mm/min. It should be noted as previously depicted in Figure 62 and discussed in Section 4.2.1.1, that the grinding passes conducted with the LSS-LFR parameters were performed on the facet which was furthest away from the grinding facet beneath which the thermocouples were located. This distance away from the thermocouples is likely to have had a diminishing effect on the measured temperatures in the LSS-LFR facet.

Though the grinding facet was furthest from the location of the thermocouples, a distinct response is recorded for the LSS-LFR plots. This is depicted by the distinct rise in the recorded temperature as the grinding action commences just after 20 seconds into the recording. Likewise, an increase in the measured temperature from start to finish of grinding pass is consistent for all eight thermocouples.

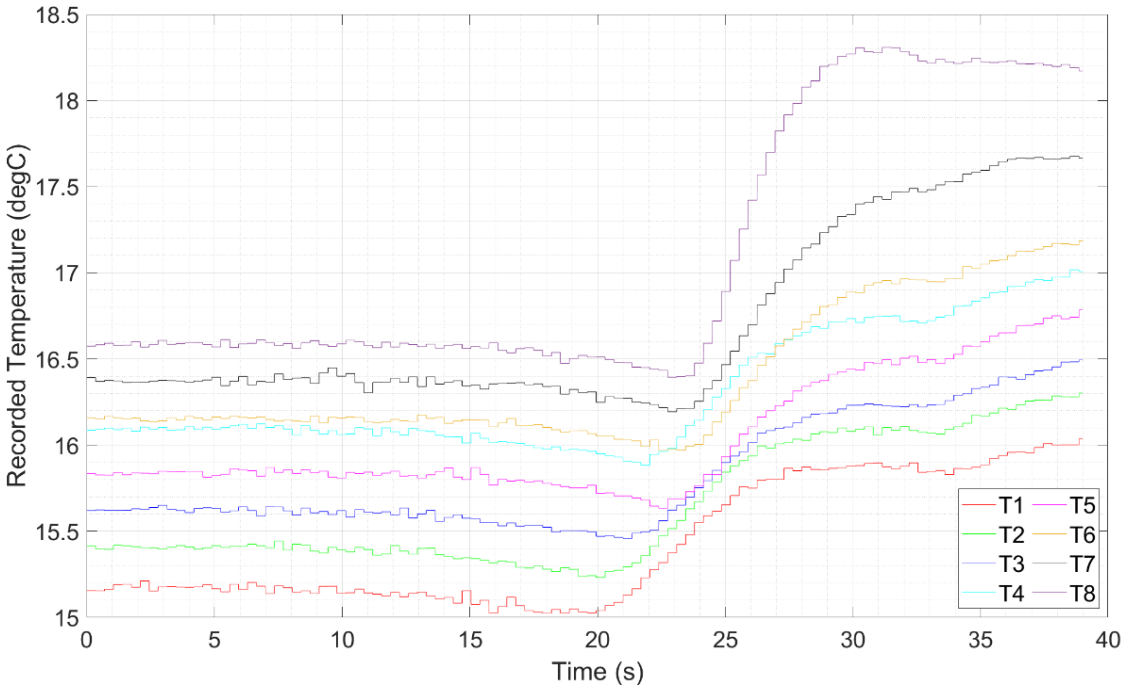

Figure 68: Temperature progression of workpiece subsurface during the initial grinding pass as recorded by eight thermocouples under the grinding conditions of Low Spindle Speed and Low Feed Rate (LSS-LFR)

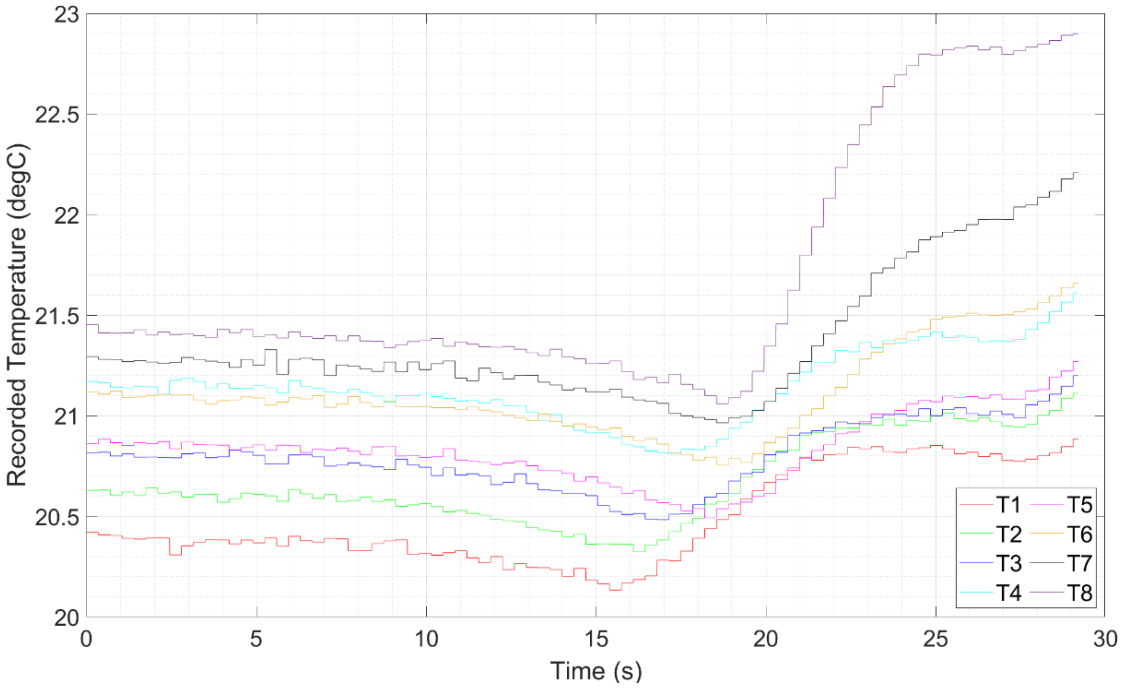

Figure 69: Temperature progression of workpiece subsurface during final grinding pass as recorded by eight thermocouples under the grinding conditions of Low Spindle Speed and Low Feed Rate (LSS-LFR)

Temperature measurement by the thermocouples was initiated shortly after the application of the declogging mechanism began. As such, the coldest temperature was recorded in thermocouple T1 which was closest to the surface (0.55 mm). The plots also show that the measured temperature

per thermocouple generally increases with the increased depth of the thermocouple from the surface. Likewise, the temperature measured furthest from the surface at 1.5 mm (T8) may be regarded as closest to the bulk temperature of the rail section. The initial and final passes also show that the largest temperature gradient was recorded in thermocouple T8, which is the thermocouple depth which was located furthest from the grinding surface.

For the thermocouple T8, there is approximately a 2 °C increase between the pre- and post-grind temperatures recorded by the thermocouples in both the first and final passes. For all thermocouple measurements, the starting temperature values recorded during the final pass is approximately 5 °C higher than the starting temperatures recorded during the initial pass. This increase is attributed to the accumulation and build-up of induced temperature by the grinding action of each subsequent pass.

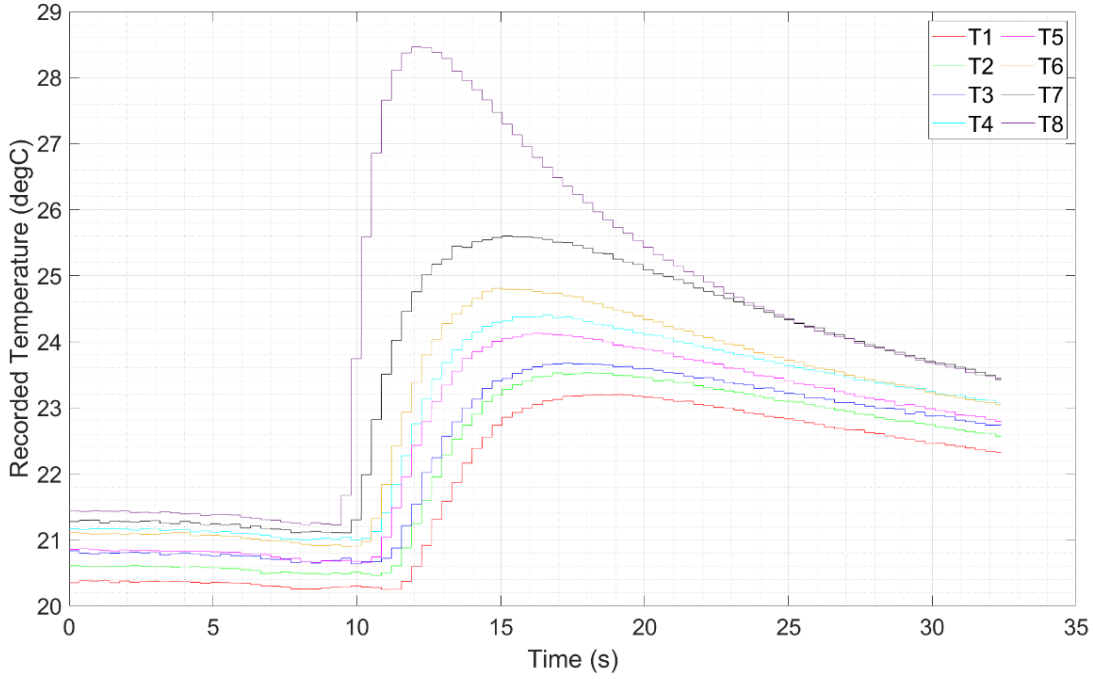

Figure 70: Temperature progression of workpiece subsurface during the initial grinding pass as recorded by eight thermocouples under the grinding conditions of Low Spindle Speed and High Feed Rate (LSS-HFR)

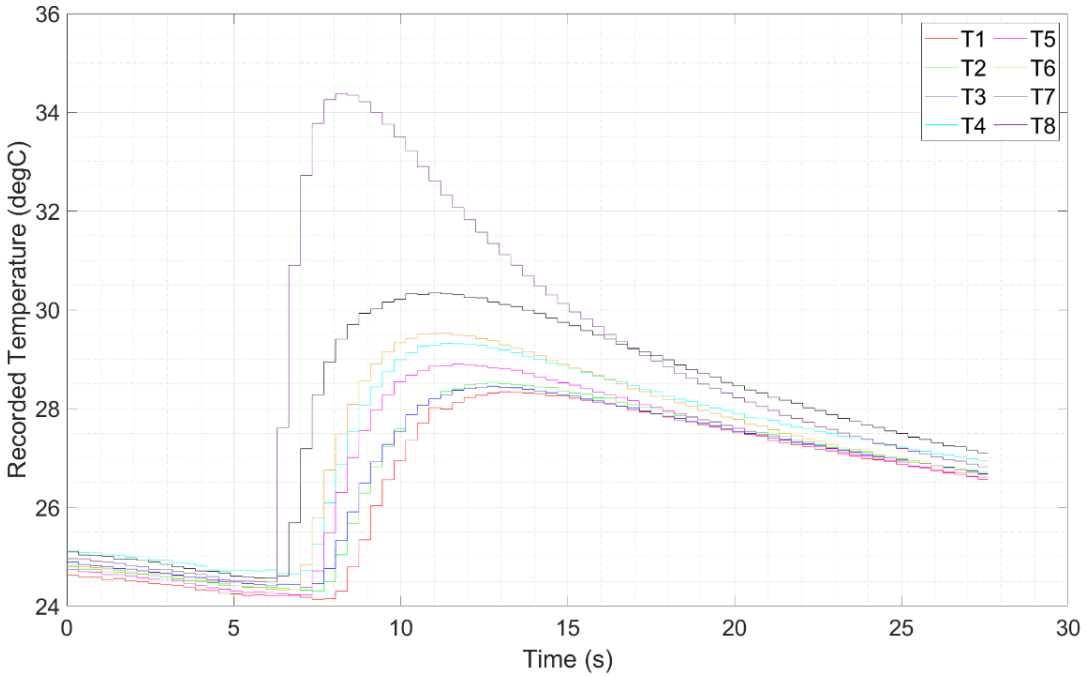

Figure 71: Temperature progression of workpiece subsurface during the final grinding pass as recorded by eight thermocouples under the grinding conditions of Low Spindle Speed and High Feed Rate (LSS-HFR)

The thermocouple-recorded temperatures for the first and final pass of the grinding tests under the Low-Spindle Speed-High Feed Rate (LSS-HFR) grinding conditions are shown in Figure 70 and Figure 71. As with the tests conducted with the prior grinding conditions, temperature responses area also observed in the thermocouples during the LSS-HFR grinding passes. As depicted in Figure 62, the grinding passes of this grinding condition were performed in the facet adjacent to the facet where the thermocouples were located. As such, the increase in temperature is from the start of grinding operation is distinct.

With the thermocouple which is closest to the surface (T1), the maximum temperature recorded in the first pass is 23.2 °C, while the maximum temperature it recorded in the final pass was 28.3 °C. On the other hand, the maximum temperature measured by T8 in the first pass was 28.4 °C, while the maximum temperature it recorded in the final pass was 34.4 °C. Additionally with the T8 thermocouple, both the initial and final LSS-HFR plots indicate a rapid increase in temperature at the highest gradient from the start of the grinding action to its end.

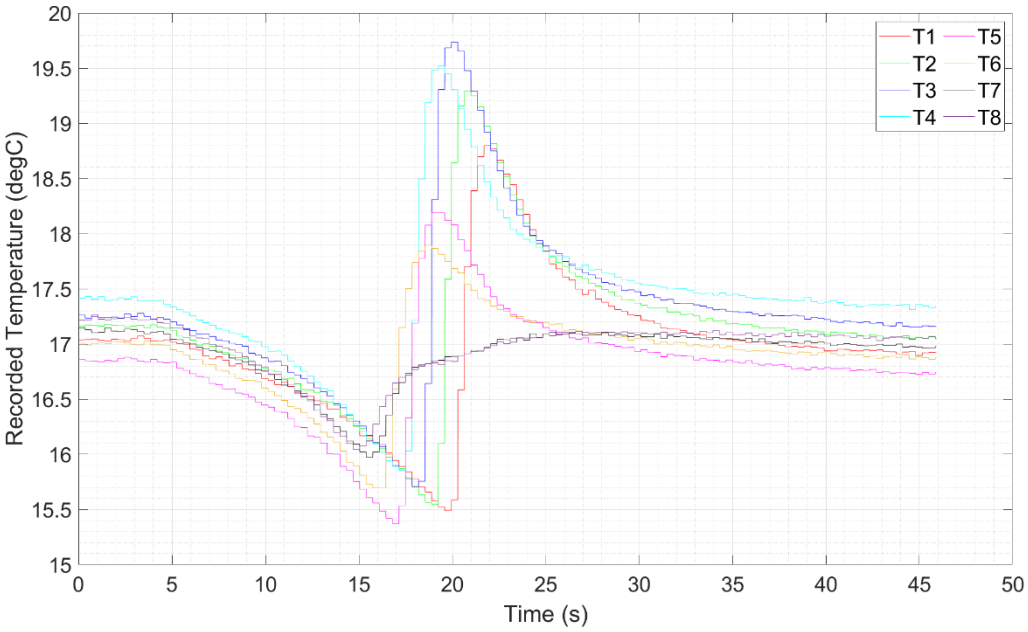

Figure 72: Temperature progression of workpiece subsurface during the final grinding pass as recorded by eight thermocouples under the grinding conditions of High Spindle Speed and Low Feed Rate (HSS-LFR)

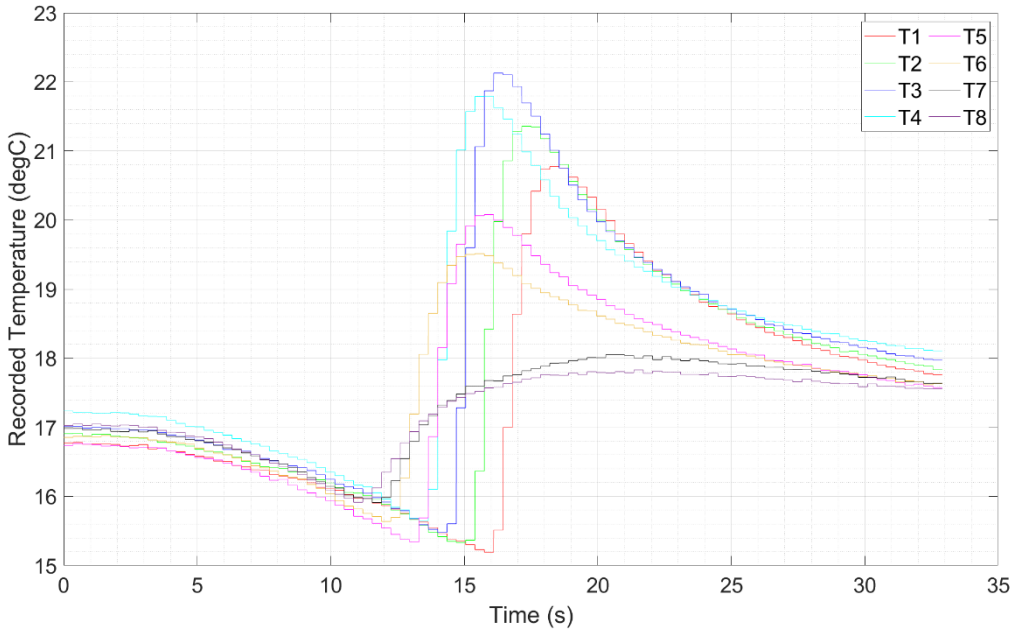

Figure 73: Temperature progression of workpiece subsurface during the final grinding pass as recorded by eight thermocouples under the grinding conditions of High Spindle Speed and Low Feed Rate (HSS-LFR)

The temperatures recorded by the thermocouples during the initial and final passes conducted in the grinding parameter conditions of High Spindle Speed – Low Feed Rate (HSS-LFR) are presented in Figure 72 and Figure 73. Similar to the set of passes conducted with the LSS-HFR, the grinding facet of the passes conducted in the HSS-LFR grinding combination was directly adjacent to the location of the thermocouples as depicted in Figure 62. The common characteristics of the temperature progressions shown in the HSS-LFR plots presented in Figure 72 and Figure 73 also

show an initial decrease in the recorded temperature when the grinding action commences, followed by an increase in the recorded temperatures to a maximum (during the grinding pass), and then a gradual reduction as the measurement is ended.

The decrease in temperature at the start of the grind is attributed to two influences of the declogging method. The first is the cooling of the surface and subsurface as the declogging material is applied on the grinding surface in the moments prior to the commencement of the grinding action. Secondly, the declogging material affects the contact of the abrasive grits and allows for sharper grits to perform the grinding action. This in turn reduces the induced grinding forces on the rail sample and inherently reduces the thermal input into the ground surface. This decrease in temperature is shortlived, lasting up to 10 s. Furthermore, during the grinding action, the temperature gradients observed in the deepest thermocouples (T7 and T8) are significantly lower than the other thermocouples (T1–T6) which are closer to the surface. The deepest thermocouples (T7 and T8) indicted a minimal response to the grinding action, as the difference in temperature from the start of grind to its end is approximate to 2 °C. It is therefore surmised that the thermocouples. It is therefore likely that the temperature effect of grinding action is less significant at the deepest depths where the thermocouples were placed.

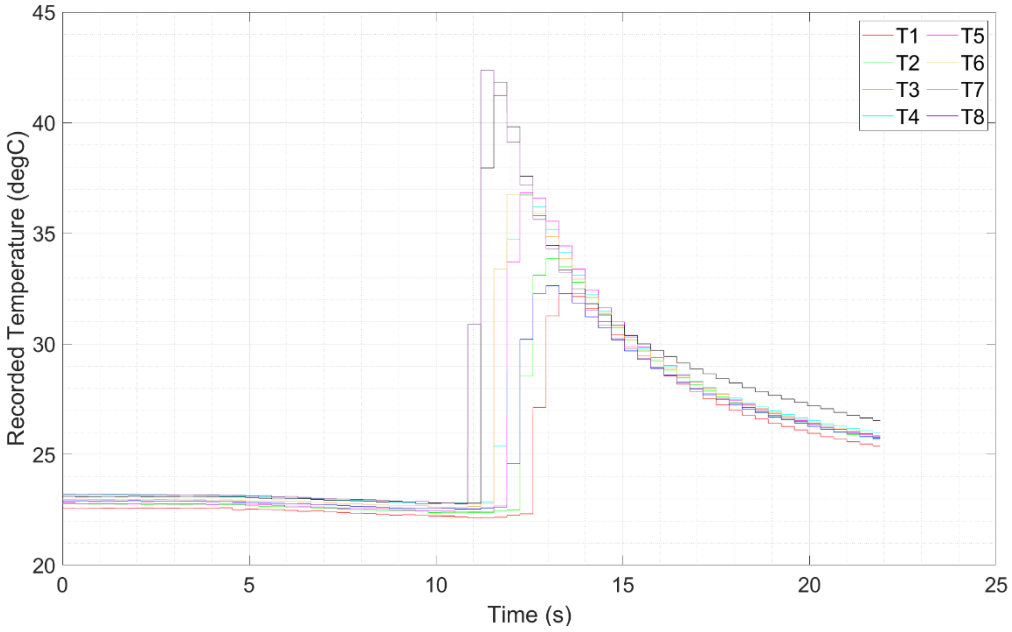

Figure 74: Temperature progression of workpiece subsurface during the initial grinding pass as recorded by eight thermocouples under the grinding conditions of High Spindle Speed and High Feed Rate (HSS-HFR)

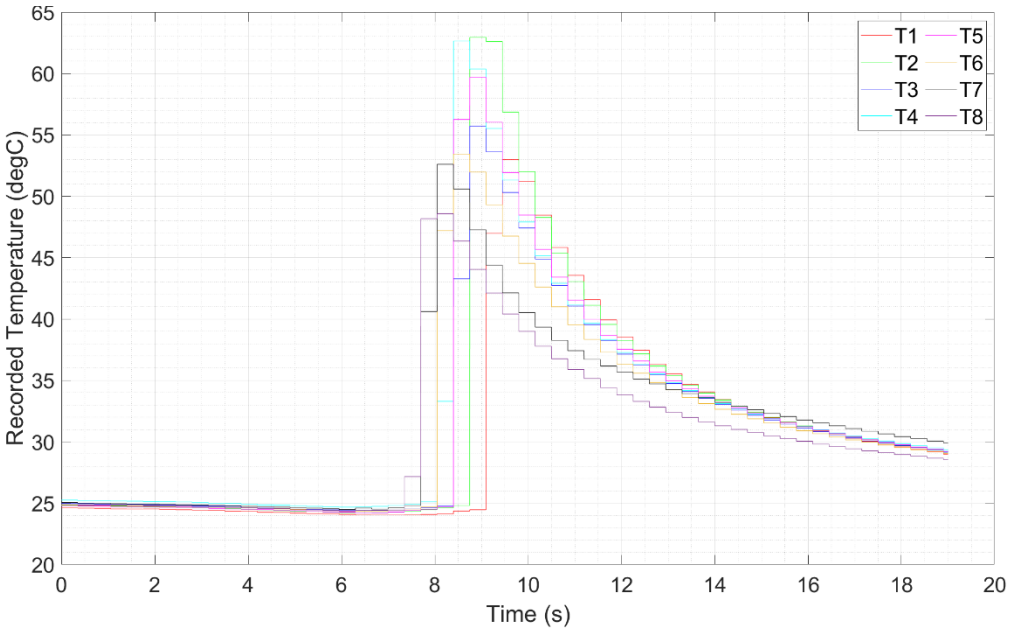

Figure 75: Temperature progression of workpiece subsurface during the final grinding pass as recorded by eight thermocouples under the grinding conditions of High Spindle Speed and High Feed Rate (HSS-HFR)

The plots of the temperatures recorded during the first and final passes of the grinding tests conducted under the grinding conditions of High Spindle Speed – High Feed Rate (HSS-HFR) are presented in Figure 74 and Figure 75. It should be noted that the grinding facet for this set of tests directly above the location of the thermocouple which are depicted in Figure 62. As such, in comparison to the previously presented tests, higher temperature responses were expected and observed as shown in the plots. In addition, for all observed grinding passes which were performed at the HSS-HFR grinding conditions, a direct rise in the temperature is observed in all thermocouples up to a maximum.

Prior to the start of the grinding pass, an overall decrease of 1-2 °C is observed in all thermocouples upon commencement of temperature recording and the concurrent application of the declogging material while all thermocouples measured temperature values which were similar to one another until the start of the grinding pass; however, the recorded values deviate from one another as the grinding pass commences.

The resulting thermal images of the thermographic readings which were obtained during the pilot trials detailed in Section 4.2.1 are presented in the form of still images which were extracted from video recordings. In the images obtained, a highlighted band of the active surface of the wheel in grinding action against the rail workpiece is shown. Likewise, the highest temperature values are observed at the contact area between the grinding wheel and the grind zone.

The thermal images of the initial and final grinding passes which were conducted with the grinding condition of Low Spindle Speed – Low Feed Rate are presented in Figure 76 (a) and (b). As indicated by the temperature scale, the range of maximum temperatures measured did not exceed

50 °C. This is in contrast with the range of grinding temperature values which are expected to generate in the grinding sparks which are also visible around the contact zone.

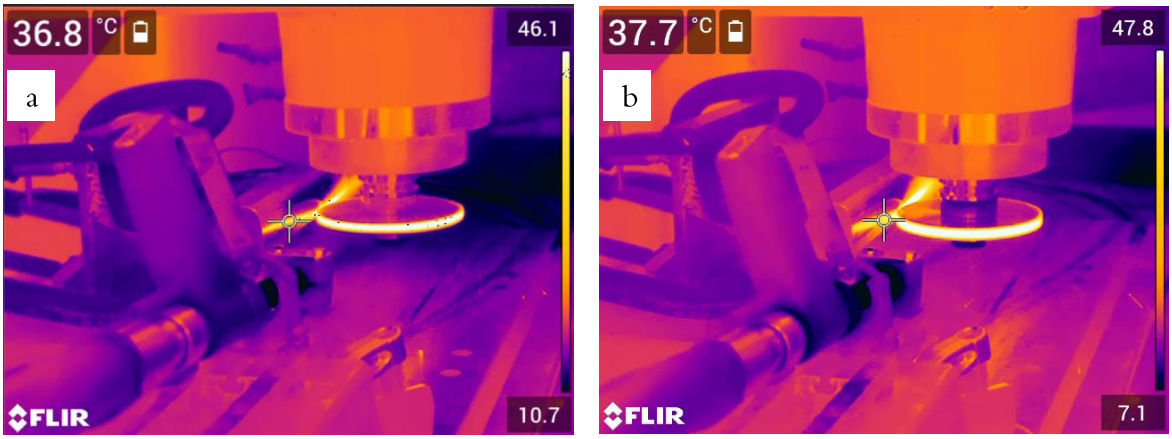

Figure 76: Thermal images of the initial (a) and final (b) grinding passes under grinding conditions at Low Spindle Speed and Low Feed Rate

The thermal images of the initial and final passes which were conducted at the grinding condition of Low Spindle Speed High Feed Rate (LSS-HFR) are presented in Figure 77 (a) and (b). For passes at these grinding conditions, higher contact temperatures were observed, as shown with the maximum temperatures of 99.3 °C and >130 °C detected in at the first and final passes respectively.

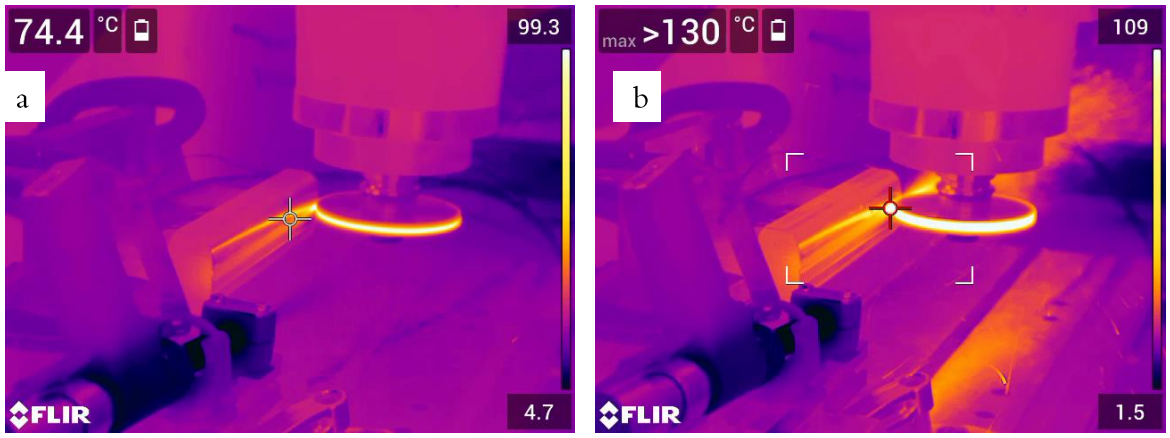

Figure 77: Thermal images of the initial (a) and final (b) grinding passes under grinding conditions at Low Spindle Speed and High Feed Rate

The thermal images which were generated for the initial and final grinding passes at the High Spindle Speed Low Feed Rate (HSS-LFR) grinding conditions are presented in Figure 78 (a) and (b). The maximum temperatures recorded at this parameter combination appear to be the lowest recorded using the thermal camera.

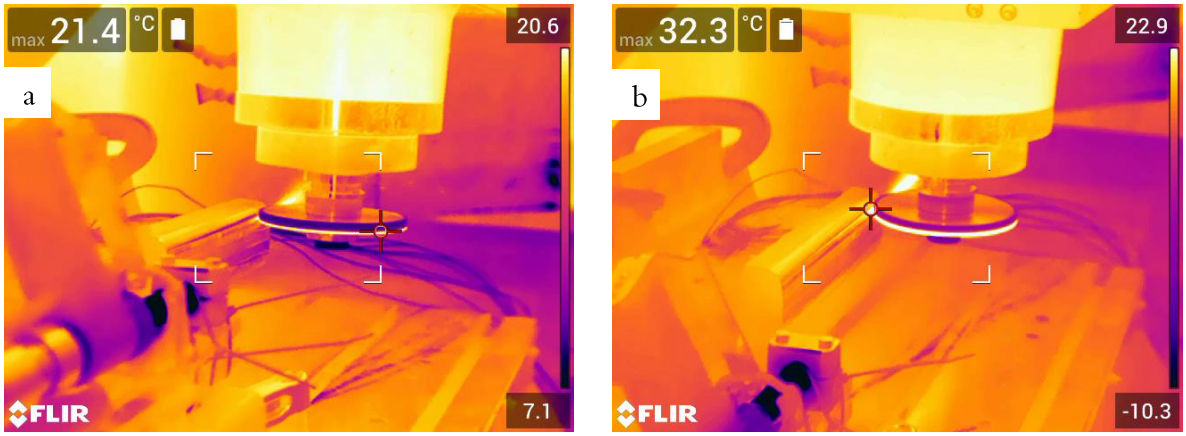

Figure 78: Thermal images of the initial (a) and final (b) grinding passes under grinding conditions at High Spindle Speed and Low Feed Rate

The thermographic images of the first and final passes conducted at the grinding conditions of High Spindle Speed High Feed Rate (HSS-HFR) are presented in Figure 79. As previously mentioned in this chapter, the passes which were conducted at these grinding conditions conform with the High Speed Grinding (HSG) practices; therefore, the temperatures recorded by the thermal camera can therefore be compared against the temperatures recorded by the thermocouples as they were located directly beneath the facet upon which the HSS-HFR passes were conducted.

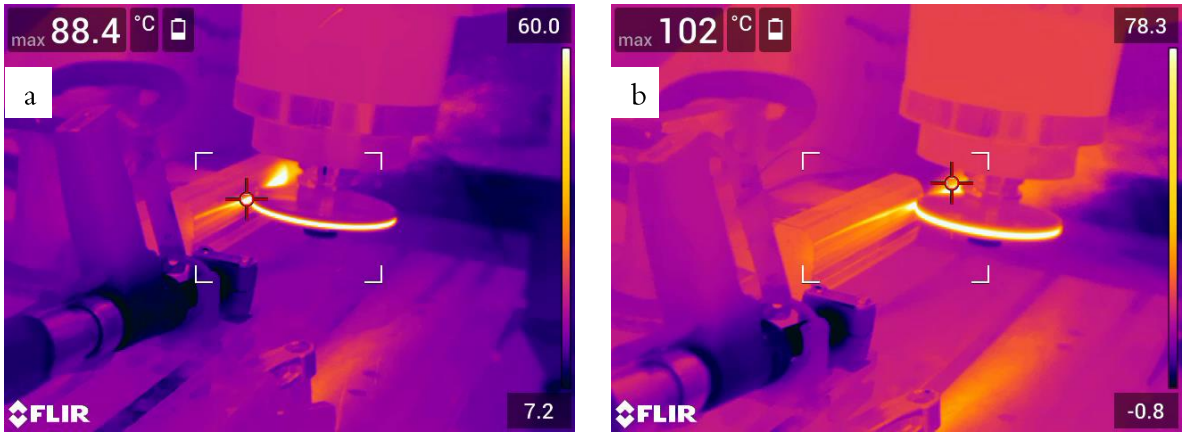

Figure 79: Thermal images of the initial (a) and final (b) grinding passes under grinding conditions at High Spindle Speed and High Feed Rate

4.3.1.2 Surface Roughness Data

The experimental surface roughness (R_a and R_z) of the various facets which correspond to the grinding conditions were obtained. As indicated in Figure 80, the roughness measurements were obtained in the longitudinal and transverse directions with respect to the grinding motion. An average of at least three measurements were obtained per grinding condition.

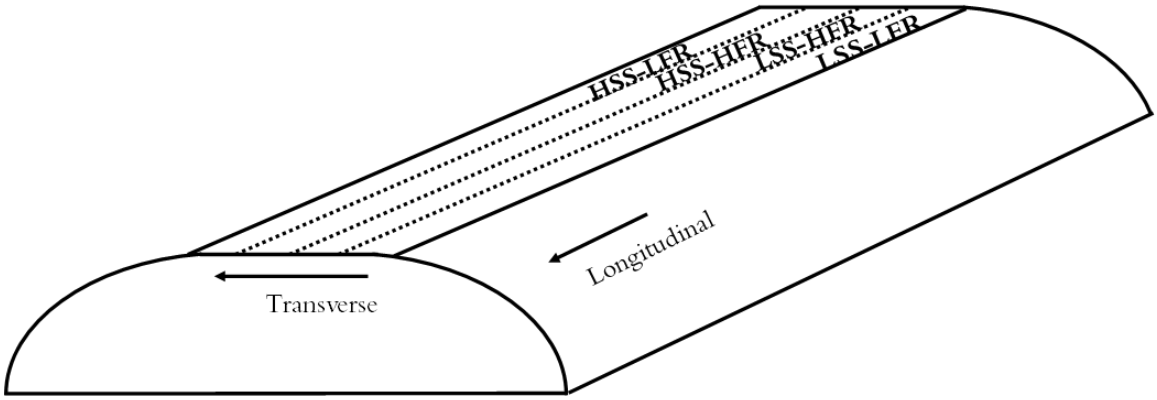

Figure 80: Schematic of the rail head to depict the transverse and longitudinal directions for surface roughness measurements

The surface roughness values which were measured following the final pass of each grinding condition are presented in the Figure 81 below. The roughness values measured for the performed grinding conditions were found to be 2.43 µm (LSS-LFR), 3.21 µm (LSS-HFR), 2.68 µm (HSS-LFR) and 3.10 µm (HSS-HFR). The highest average transverse roughness value is observed in the passes conducted at the grinding condition of Low Spindle Speed-High Feed Rate (LSS-HFR); however, these values are slightly higher than those recorded for the passes conducted at High Spindle Speed- High Feed Rate (HSS-HFR).

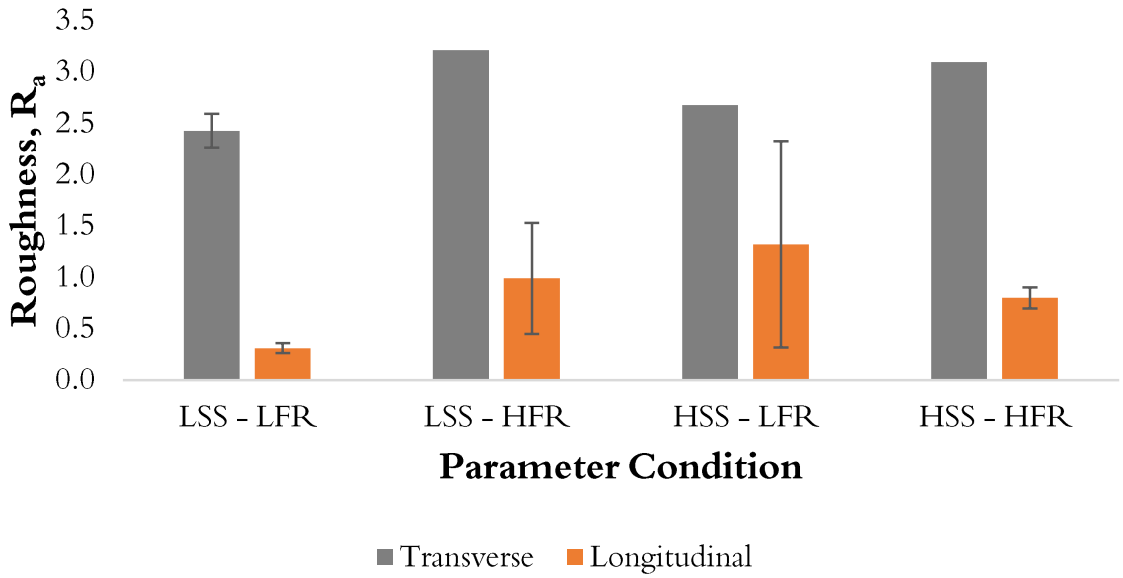

Figure 81: The post-grind surface roughness (R_a) which were measured following various grinding conditions

4.3.1.3 Microstructural Analysis

Micrographs of the longitudinal cross-section of the rail samples which were ground using the superabrasive grinding approach are presented in this section. The figures presented indicate the presence of the martensitic WEL layer to varying degrees above the pearlitic microstructure in the

bulk material. The measured thicknesses of the WEL are summarised in Table 18. The individual observations on the obtained micrographs are presented.

Table 18: Summary of the maximum thicknesses of WEL for samples ground at various grinding conditions

Grinding Condition	Maximum Measured WEL (μm)
LSS-LFR	2.36
LSS-HFR	9.67
HSS-LFR	2.21
HSS-HFR	4.44

The optical micrograph of the rail section which was ground under the grinding conditions of LSS-LFR is presented in Figure 82. The micrograph is characterised by the pearlitic microstructure in the bulk material as well as a martensitic layer at the top of the microstructure. The observed martensitic layer was continuous across the cross-section, with a measured maximum thickness at 2.36 μm.

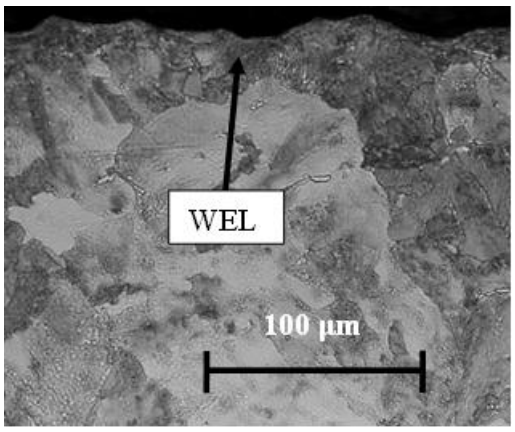

Figure 82: Optical micrograph of the longitudinal cross-section of the R260 rail surface layer after grinding with superabrasive grinding wheel under the LSS-LFR grinding conditions.

Figure 83 presents the optical micrograph of the longitudinal cross-section of the sample ground with the grinding condition of LSS-HFR. The micrograph indicates the presence of the martensitic WEL in a continuous layer on the top surface. This martensitic layer was measured at a maximum thickness of 9.67 μm. Jagged grinding grooves are also observed on the top surface along the cross-section. For this LSS-HFR sample, the grinding grooves observed are the most prominent of the grinding conditions. This corresponds with the highest surface roughness measured at 9.67 μm.

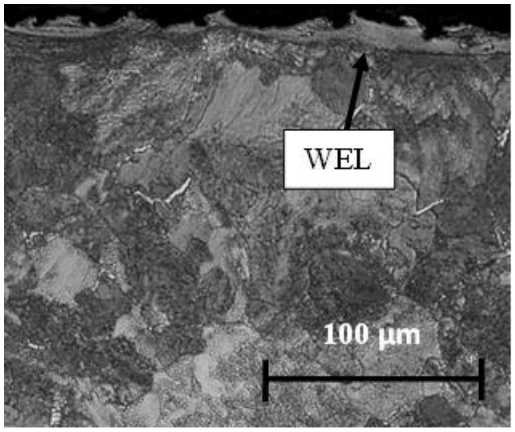

Figure 83: Optical micrograph of the longitudinal cross-section of the R260 rail surface layer after grinding with superabrasive grinding wheel under the LSS-HFR grinding conditions.

The optical micrograph of the longitudinal cross-section of the sample which was ground under the condition of HSS-LFR is presented in Figure 84. Across the top surface, deposits of martensitic WEL can be observed and was measured at a maximum thickness of 2.21 µm. The HSS-LFR micrograph also shows the presence of grinding grooves on the top surface.

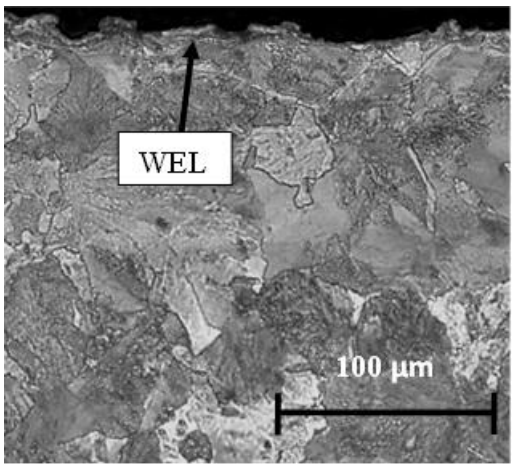

Figure 84: Optical micrograph of the longitudinal cross-section of the R260 rail surface layer after grinding with superabrasive grinding wheel under the HSS-LFR grinding conditions.

The optical micrograph of the grinding facet on which the HSS-HFR grinding condition was conducted is shown in Figure 85. The figure shows the presence of pockets of discontinuous martensitic WEL, of which a maximum thickness of 4.4 µm was measured. The presence of grinding grooves was also observed on the top surface layer of the HSS-HFR sample.

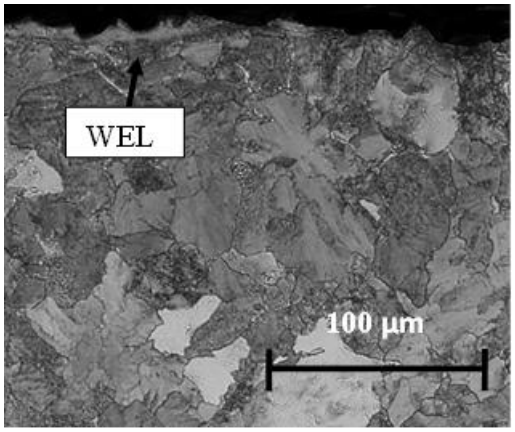

Figure 85: Optical micrograph of the longitudinal cross-section of the R260 rail surface layer after grinding with superabrasive grinding wheel under the HSS-HFR grinding conditions.

4.3.2 Face Grinding with Conventional Cup Wheel

4.3.2.1 Temperature Data in Conventional Face Grinding

The data obtained by the thermal imaging of the grinding passes are presented in this section. In contrast to the thermography equipment used in the superabrasive grinding process, the thermal measurements of the grinding area were obtained using the Thermoimager camera. With this camera, it was possible to record values of temperature at three different regions on the rail. An overview of the maximum temperatures recorded for each pass is shown in Figure 86.

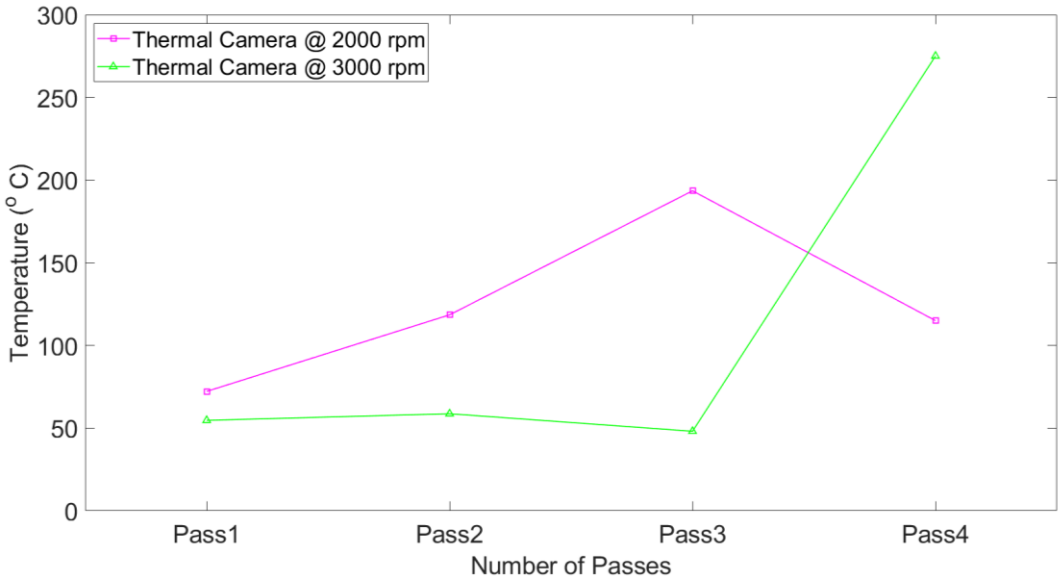

Figure 86: The maximum temperature per pass as recorded by thermal camera for conventional face grinding passes carried out at 2000 rpm and 3000 rpm.

It is observed that the grinding temperatures recorded for passes conducted at 3000 rpm are generally lower than those recorded in the passes conducted at 2000 rpm. With the exception of the final pass, the maximum temperatures recorded during the trial conducted at 2000 rpm tend to a general increase with the increasing number of passes. This is congruent with the thermal model

observed in the literature which indicates that the maximum temperature per pass will ratchet up with increasing number of face grinding passes at a constant wheel speed [73]. Similarly, the grinding temperatures recorded for the passes conducted at the wheel speed of 3000 rpm also indicate an overall increase in the grinding temperature per pass.

The recorded temperature progression for the Areas 1, 2 and 3 are presented in each individual plot per pass. The progressions as recorded by the thermal camera for the grinding trial performed in the face grinding orientation are presented individually for each pass. The progression of the temperatures recorded by the thermal camera during the first pass is presented in Figure 87.

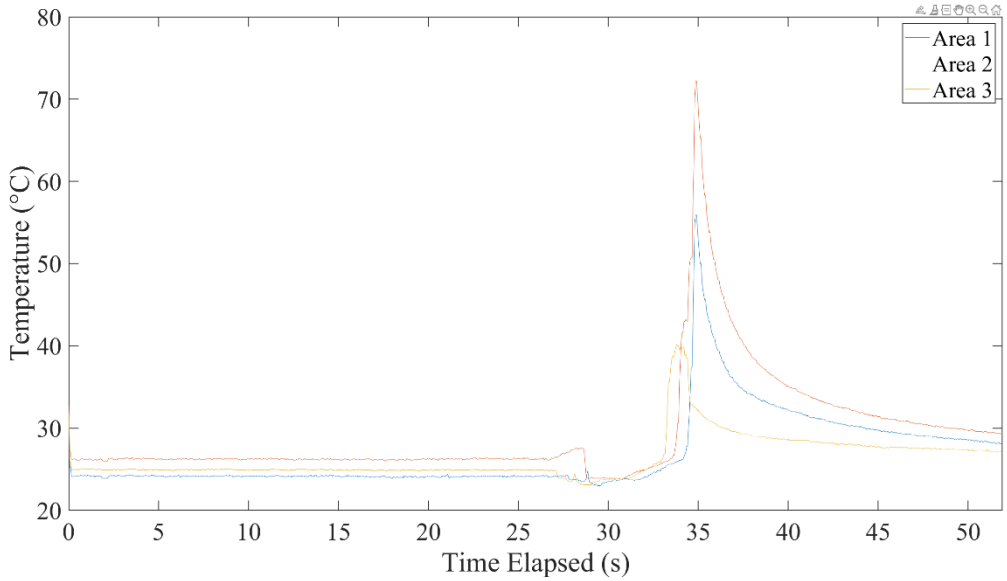

Figure 87: Recorded temperature of the grinding contact zone as recorded by a thermal camera during the first face grinding pass conducted at 2000 rpm.

The temperature progression of the second grinding pass which was performed at 2000 rpm and recorded by the thermal camera is presented in Figure 88.

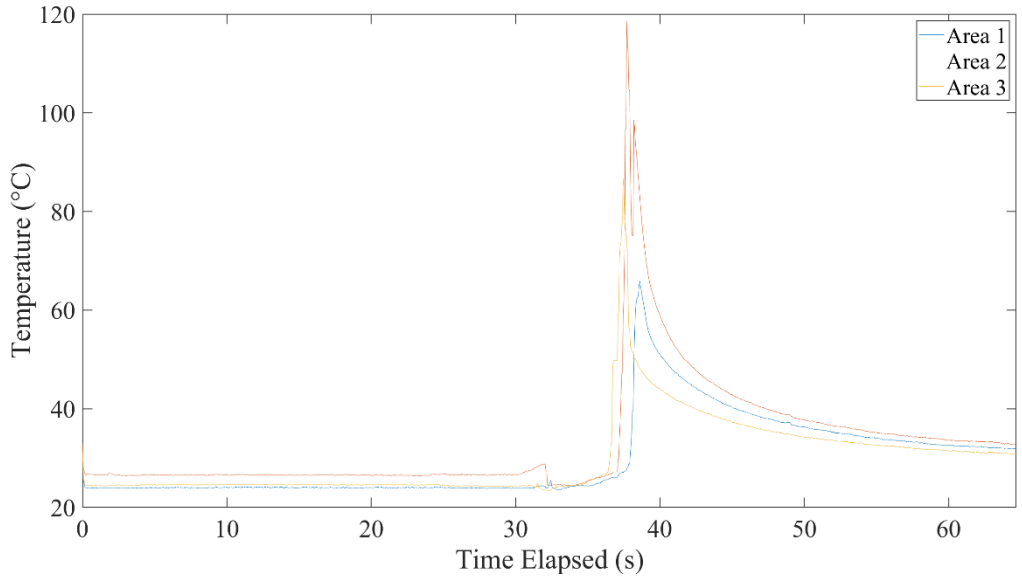

Figure 88: Recorded temperature of the grinding contact zone as recorded by a thermal camera during the second face grinding pass conducted at 2000 rpm.

The temperature progression of the third grinding pass which was performed at 2000 rpm and recorded by the thermal camera is presented in Figure 89.

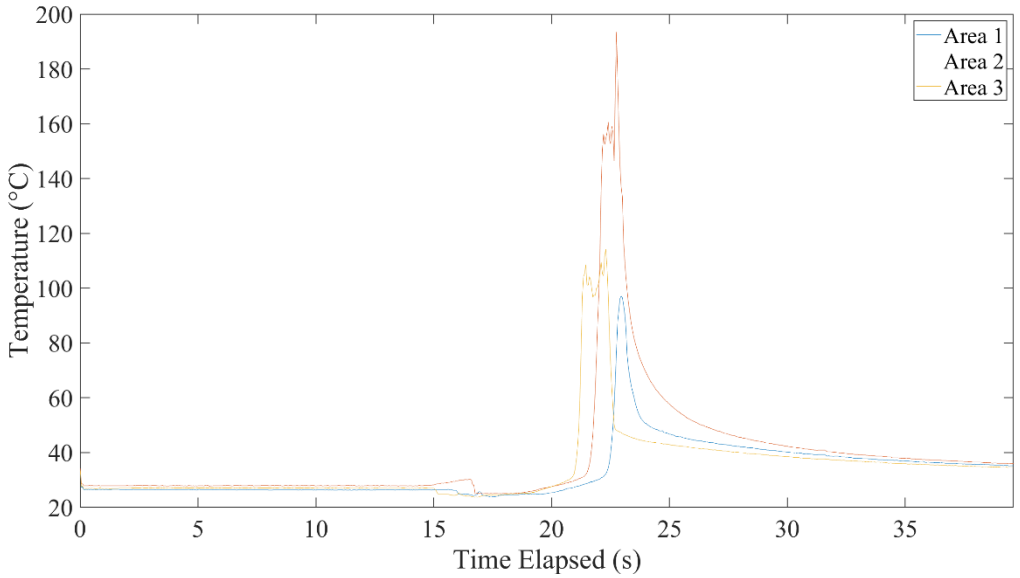

Figure 89: Recorded temperature of the grinding contact zone as recorded by a thermal camera during the third face grinding pass conducted at 2000 rpm.

The temperature progression of the fourth grinding pass which was performed at 2000 rpm and recorded by the thermal camera is presented in Figure 90.

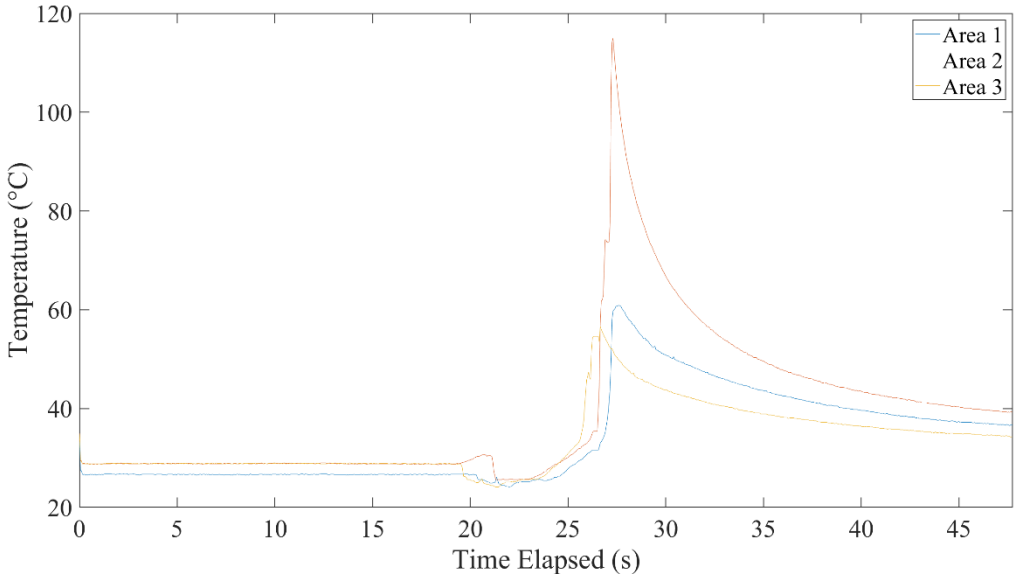

Figure 90: Recorded temperature of the grinding contact as recorded by a thermal camera during the fourth face grinding pass conducted at 2000 rpm.

The temperature progression of the first grinding pass which was performed at 3000 rpm and recorded by the thermal camera is presented in Figure 91.

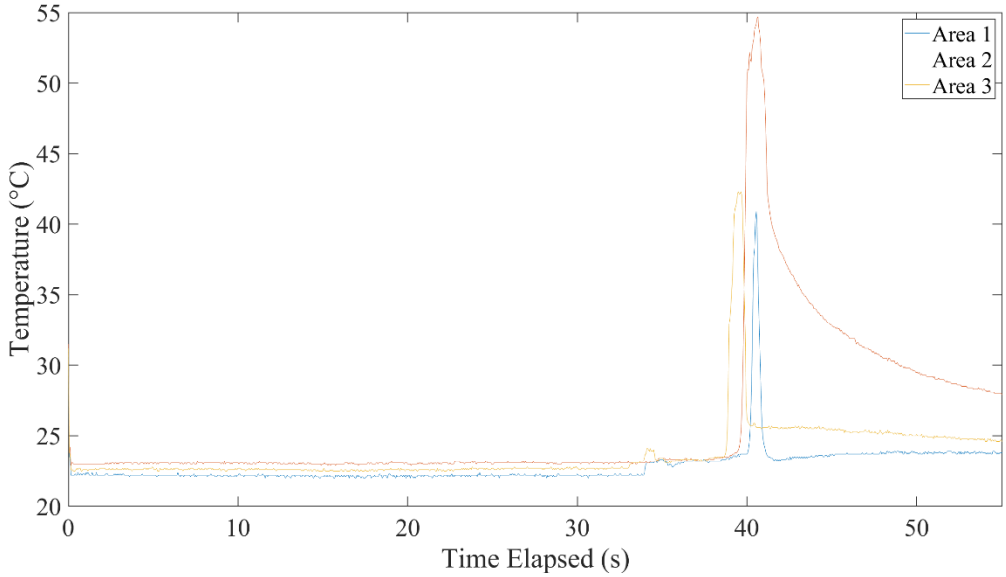

Figure 91: Recorded temperature of the grinding contact zone as recorded by a thermal camera during the first face grinding pass conducted at 3000 rpm.

The temperature progression of the second grinding pass which was performed at 3000 rpm and recorded by the thermal camera is presented in Figure 92.

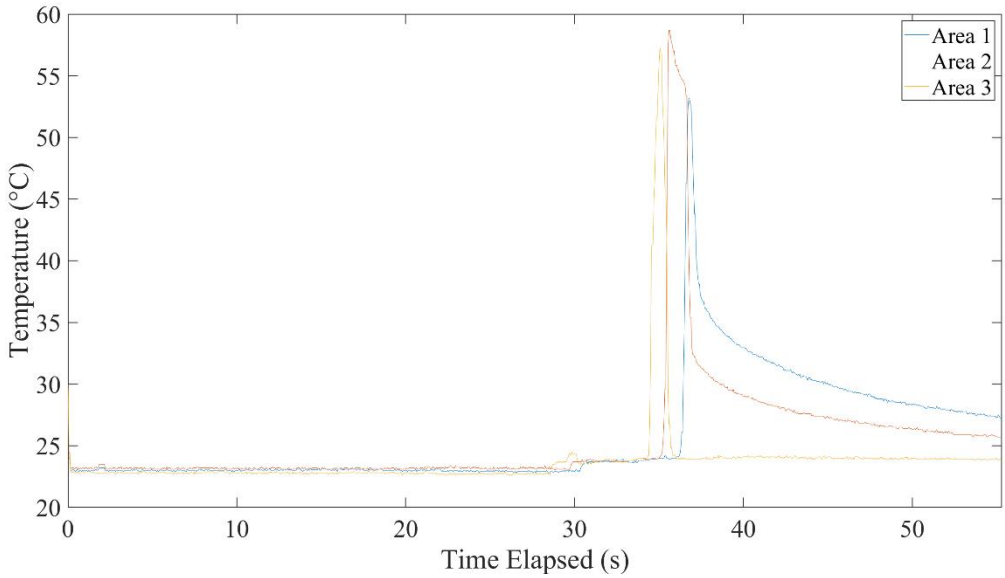

Figure 92: Recorded temperature of the grinding contact zone as recorded by a thermal camera during the second face grinding pass conducted at 3000 rpm.

The temperature progression of the third grinding pass which was performed at 3000 rpm and recorded by the thermal camera is presented in Figure 93.

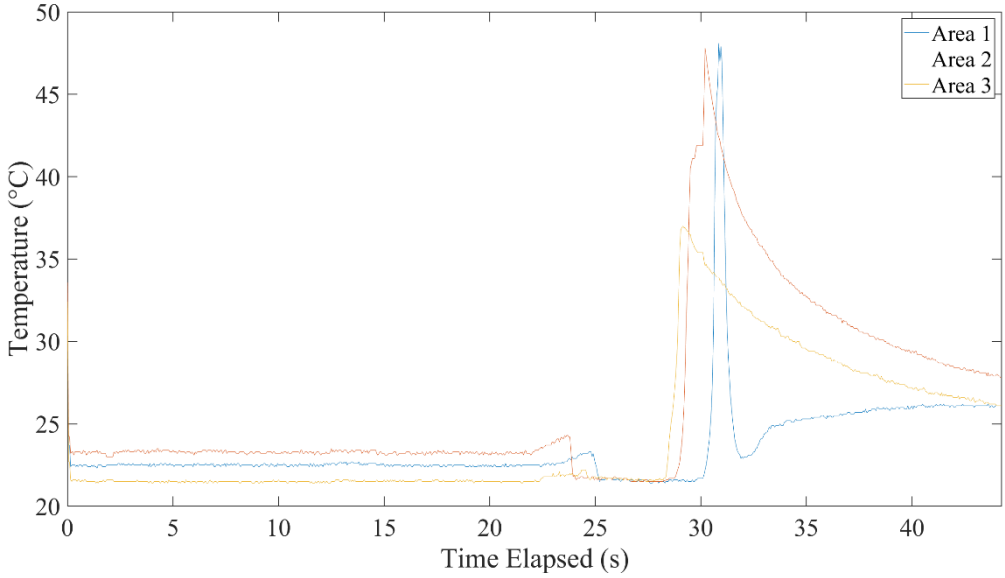

Figure 93: Recorded temperature of the grinding contact zone as recorded by a thermal camera during the third face grinding pass conducted at 3000 rpm.

The temperature progression of the third grinding pass which was performed at 3000 rpm and recorded by the thermal camera is presented in Figure 94.

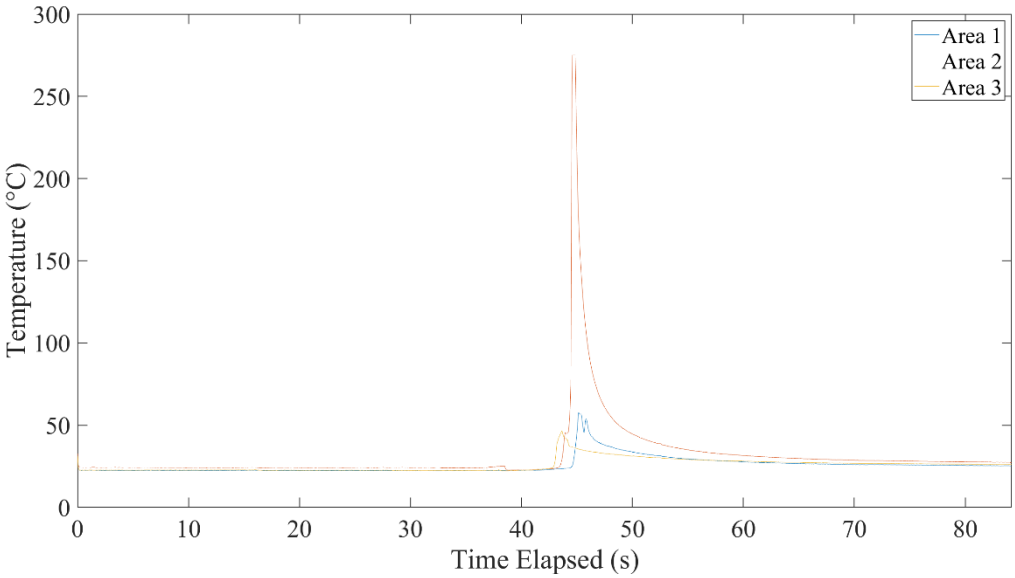

Figure 94: Recorded temperature of the grinding contact zone as recorded by a thermal camera during the fourth face grinding pass conducted at 3000 rpm.

4.3.2.2 Force Data in Face Grinding

In this section, the resultant total forces of the individual grinding passes conducted are presented. The component grinding forces acting on the rail are depicted in Figure 95, where F_a is the axial forward force along the direction of grind, F_t is the tangential force and F_n is the normal force applied on the grinding interface.

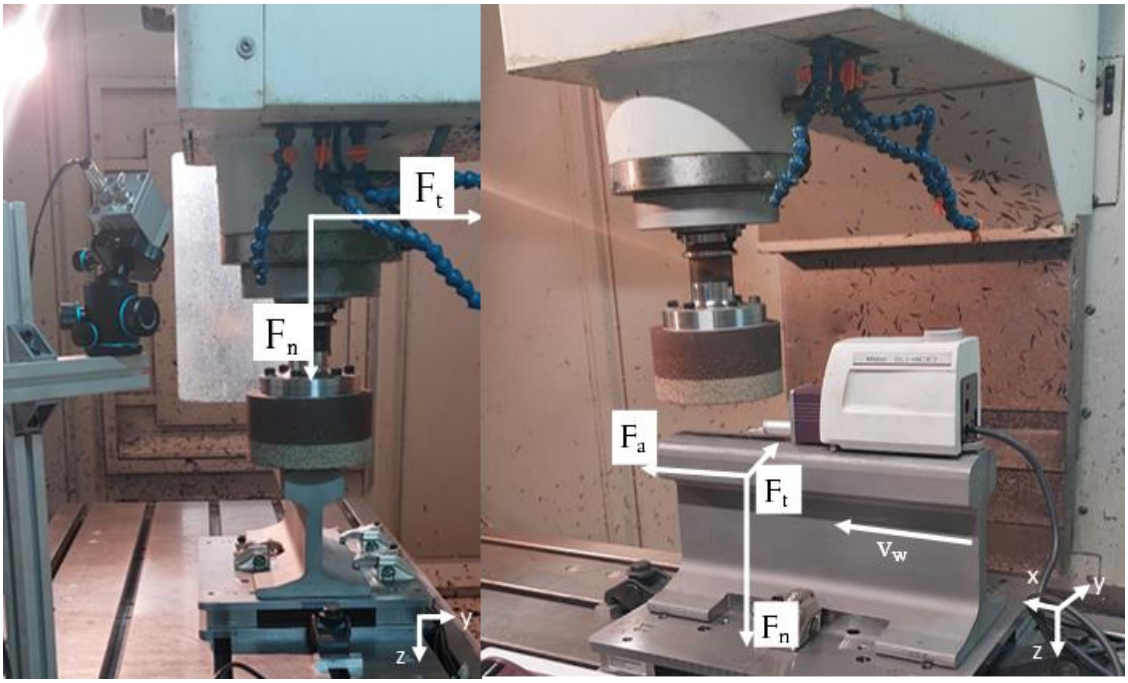

Figure 95: Depiction of the component grinding forces (F_a, F_n, F_t) exerted during the grinding of rail using conventional face grinding.

A summary compilation of the component grinding forces recorded during the passes conducted at 2000 rpm and 3000 rpm are shown in Figure 96 and Figure 97.

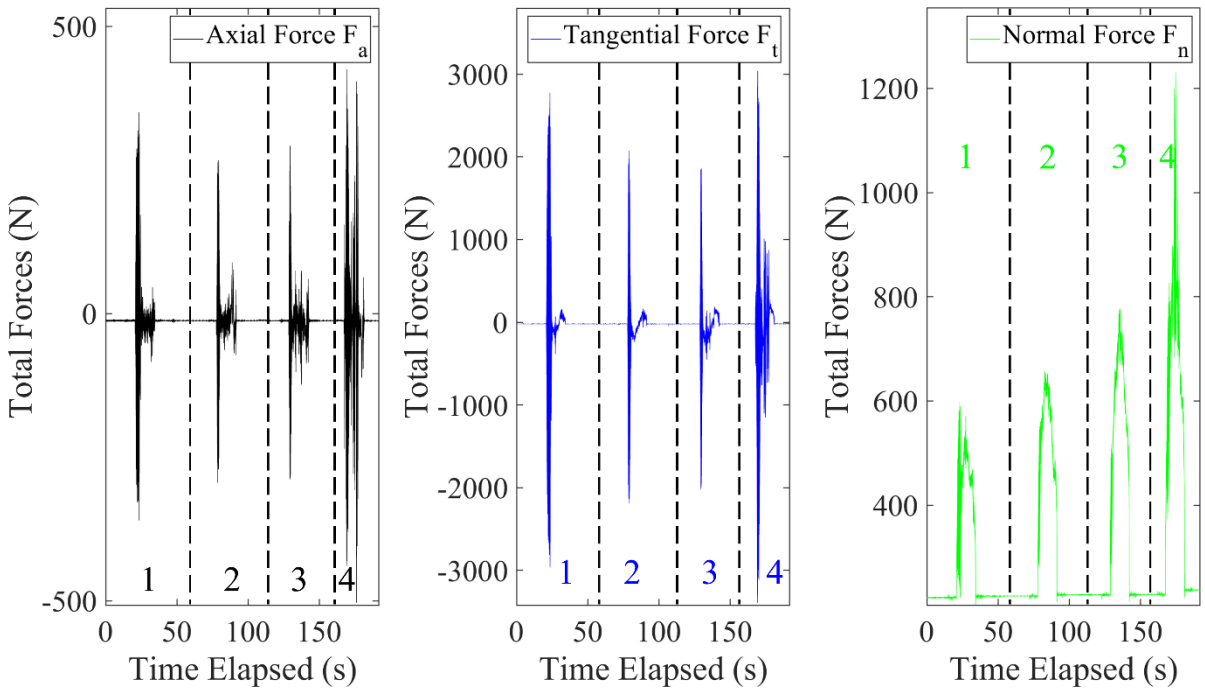

Figure 96: Progression of the grinding forces measured during the face grinding passes conducted at 2000 rpm

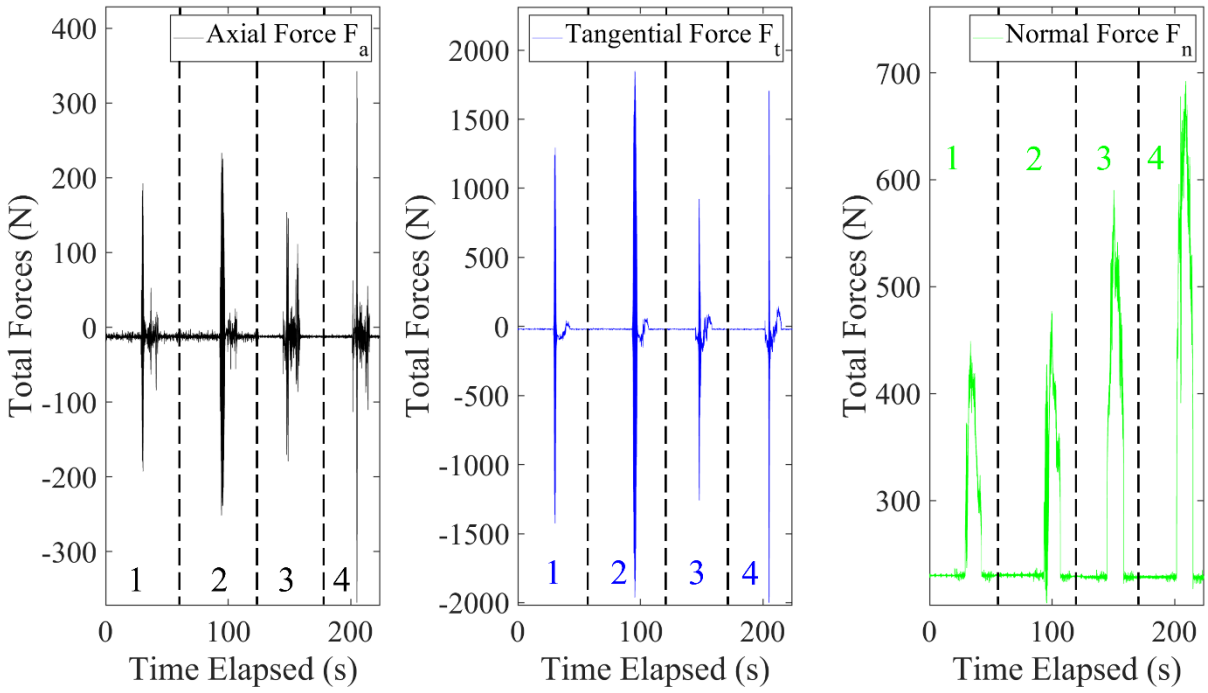

Figure 97: Progression of the grinding forces measured during the face grinding passes conducted at 3000 rpm

A global overview of the relationship between the measured maximum tangential and normal component forces and the increasing grinding depth for the grinding passes conducted at 2000 rpm

and 3000 rpm is presented in Figure 98. The magnitude of the maximum tangential grinding forces recorded during the four grinding passes conducted at 2000 rpm included 192.4 N, 233.3 N, 153.8 N and 342.5 N respectively, while the maximum normal grinding forces recorded include 449.1 N, 477.2 N, 590.3 and 692.3 N respectively. Likewise, the maximum tangential forces recorded during the four grinding passes carried out at 3000 rpm included 350.0 N, 266.7 N, 291.8 N and 425.2 N respectively, while the normal grinding forces recorded were 597.4 N, 656.7 N, 777.3 N, and 1230.7 N respectively. The progressions of these force values are presented in the Figure 98 below.

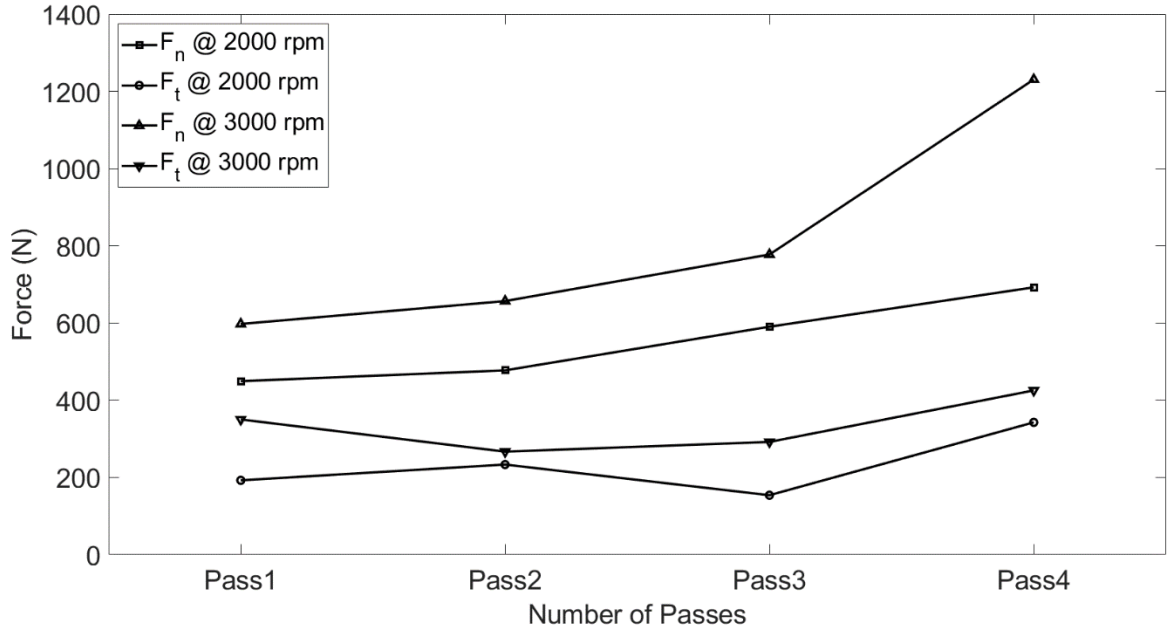

Figure 98: The maximum force per pass recorded during the passes conducted at 2000 rpm and 3000 rpm

The resultant component forces recorded during the 4 grinding passes which were performed at 2000 rpm are presented from Figure 99 to Figure 102. Likewise, the corresponding component forces recorded for passes performed at 3000 rpm are presented from Figure 103 to Figure 106. In order to identify the passes, it should be noted that each pass is named in the format "xxxx-xx-xxxx-Pass x", which signifies the convention of "'wheel speed' - 'feed rate' - 'depth of cut' – 'Pass number'".

The progression of the component grinding forces over time, as recorded during the first grinding pass at 2000 rpm, '2000-2-0.025 Pass 1' is shown in Figure 99. The maximum exerted force is recorded tangential (F_t) to the wheel. The general behaviour observed in the plots of the recorded tangential forces is expounded upon.

As the grinding pass commences, the front of the grinding wheel comes in contact with the edge of the rail section, all components of the grinding forces increase rapidly. Likewise, the plots show an increased amount of noise in the force signal in the first few seconds of the grind. The recorded

tangential force F_t remains steady for about 3 seconds and begins to increase as the full diameter of the grinding wheel interacts with the rail. As the wheel exits the cut, F_t decreases to a minimum. For each pass, it is also observed that the tangential force F_t changes from negative to positive as the grinding stone disengages from the rail at the end of the grinding pass. This signifies the reduction in the workpiece resistance to the rotation action of the wheel as it exits the rail surface.

The normal force F_n increases from the start of grind to a maximum. This maximum is attained when the full diameter of the wheel is in contact with the rail. The force F_n then decreases rapidly as the wheel exits the grinding pass. Additionally, a significant amount of noise is observed in the force signals at the start of the grind.

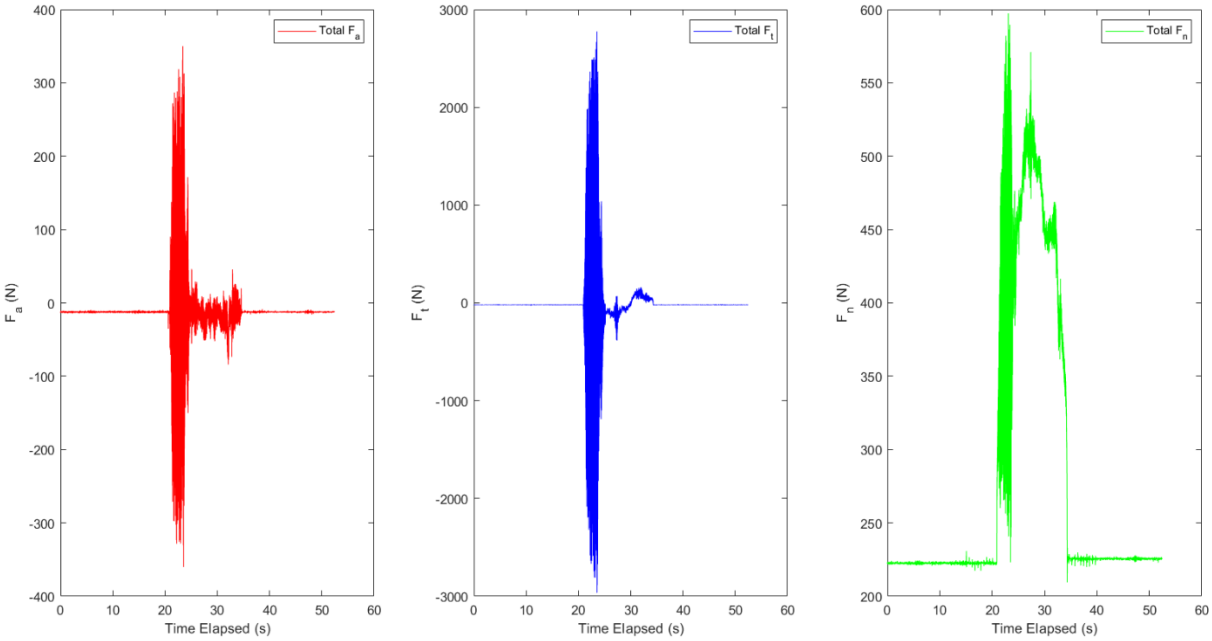

Figure 99: The component grinding forces measured during the first grinding pass '2000-2-0.025-Pass 1'.

The component forces recorded during the second pass at 2000 rpm are shown in Figure 100.

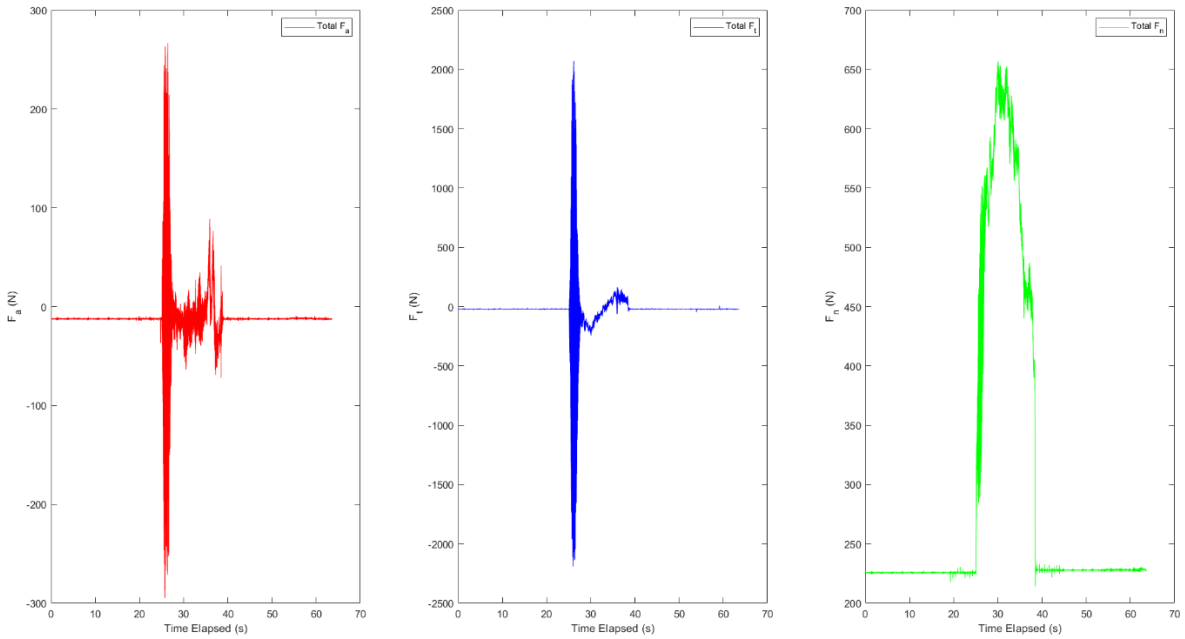

Figure 100: The component grinding forces recorded during the second grinding pass '2000-2-0.025-Pass 2'

The component forces recorded during the third pass at 2000 rpm are shown in Figure 101.

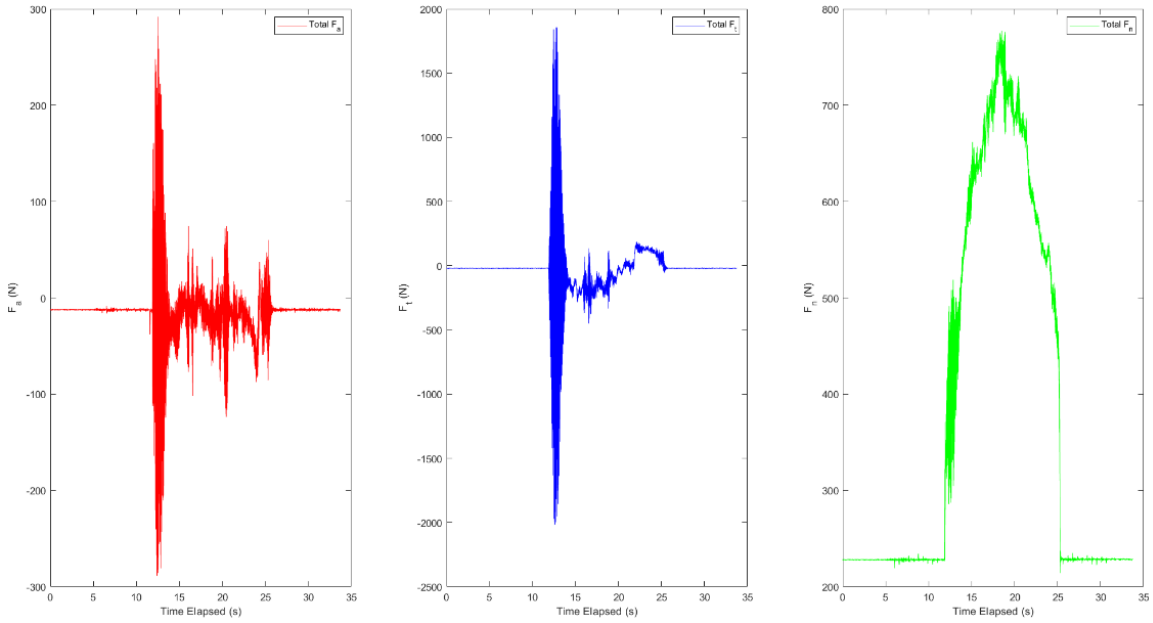

Figure 101: The component grinding forces recorded during the third grinding pass '2000-2-0.025-Pass 3'

The progression of the component forces recorded during the fourth grinding pass conducted at 2000 rpm are shown in Figure 102.

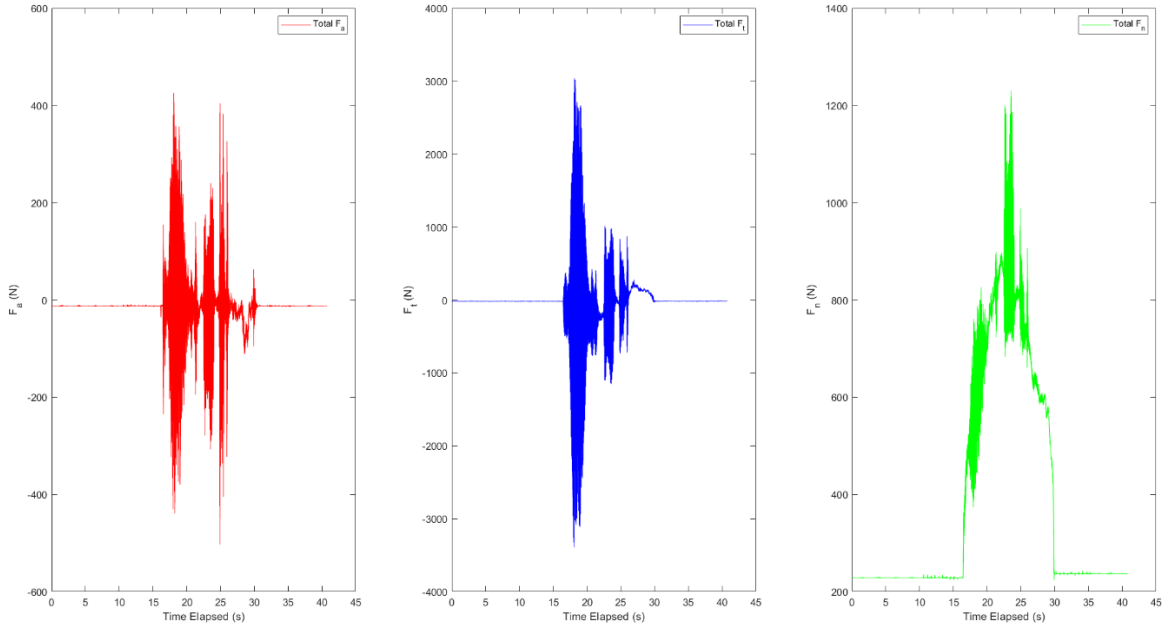

Figure 102: The component grinding forces recorded during the fourth grinding pass '2000-2-0.025-Pass 4'

The progression of the component forces recorded during the first grinding pass conducted at 3000 rpm are shown in Figure 103.

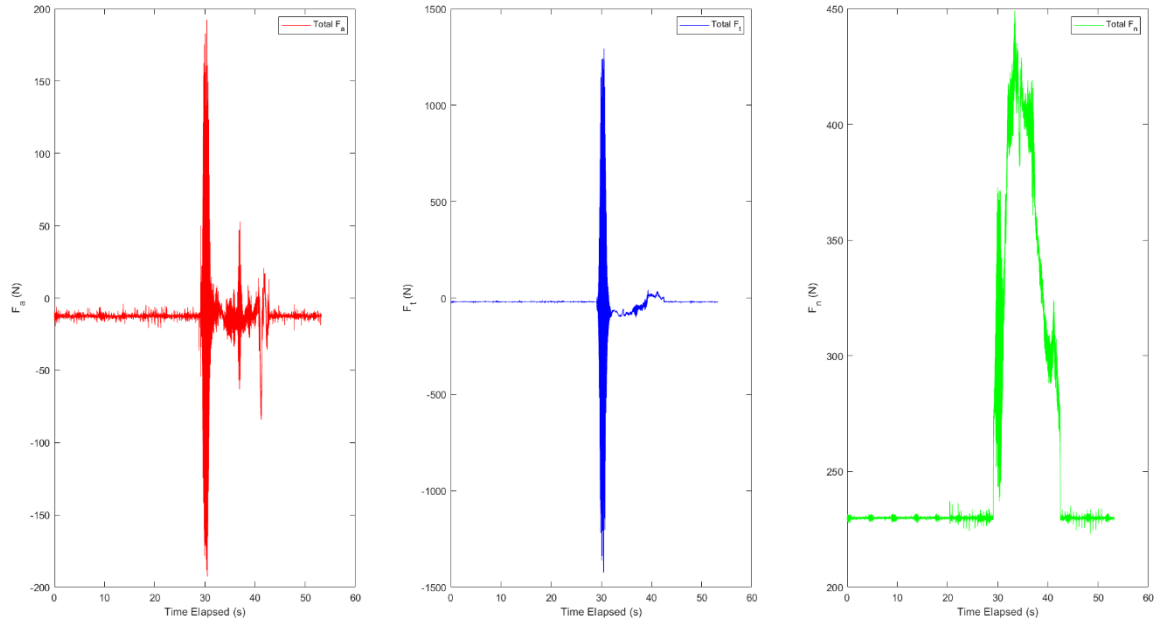

Figure 103: The component grinding forces recorded during the first grinding pass '3000-2-0.025-Pass 1'

The progression of the component forces recorded during the second grinding pass conducted at 3000 rpm are shown in Figure 104.

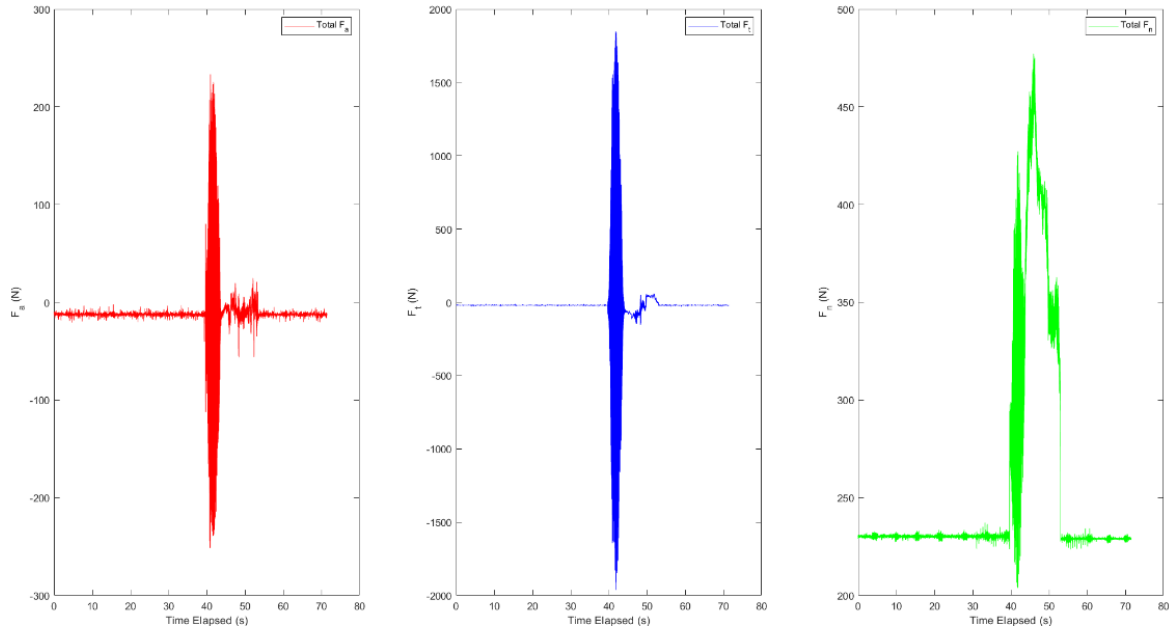

Figure 104: The component grinding forces recorded during the second grinding pass '3000-2-0.025-Pass 2'

The progression of the component forces recorded during the third grinding pass conducted at 3000 rpm are shown in Figure 105.

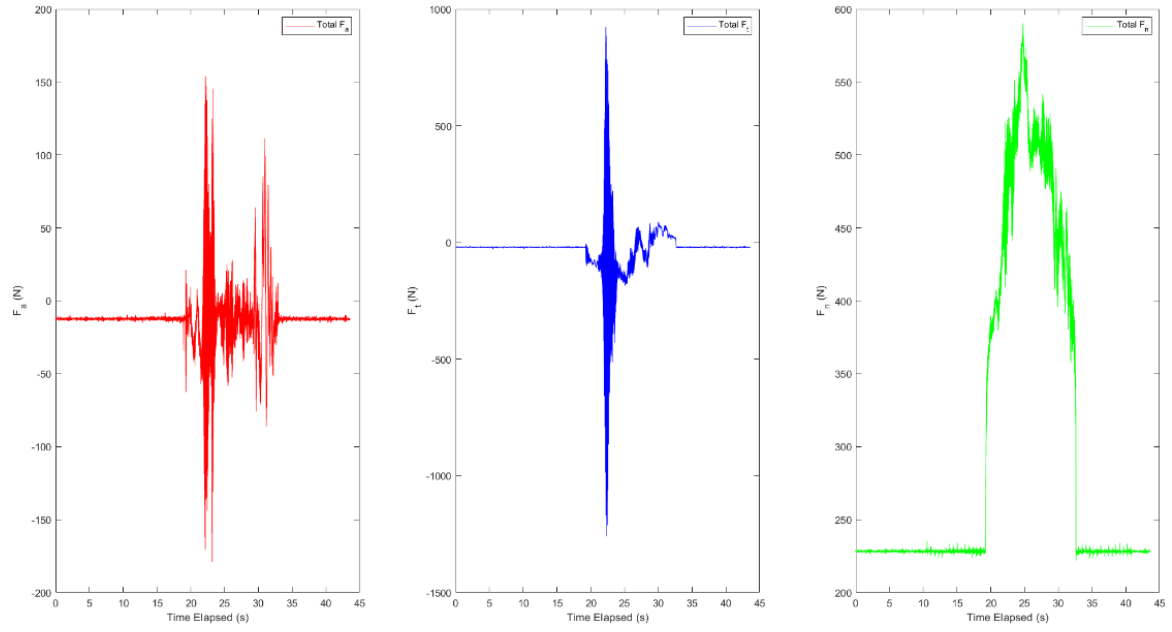

Figure 105: The component grinding forces recorded during the third grinding pass '3000-2-0.025-Pass 3'

The progression of the component forces recorded during the fourth grinding pass conducted at 3000 rpm are shown in Figure 106.

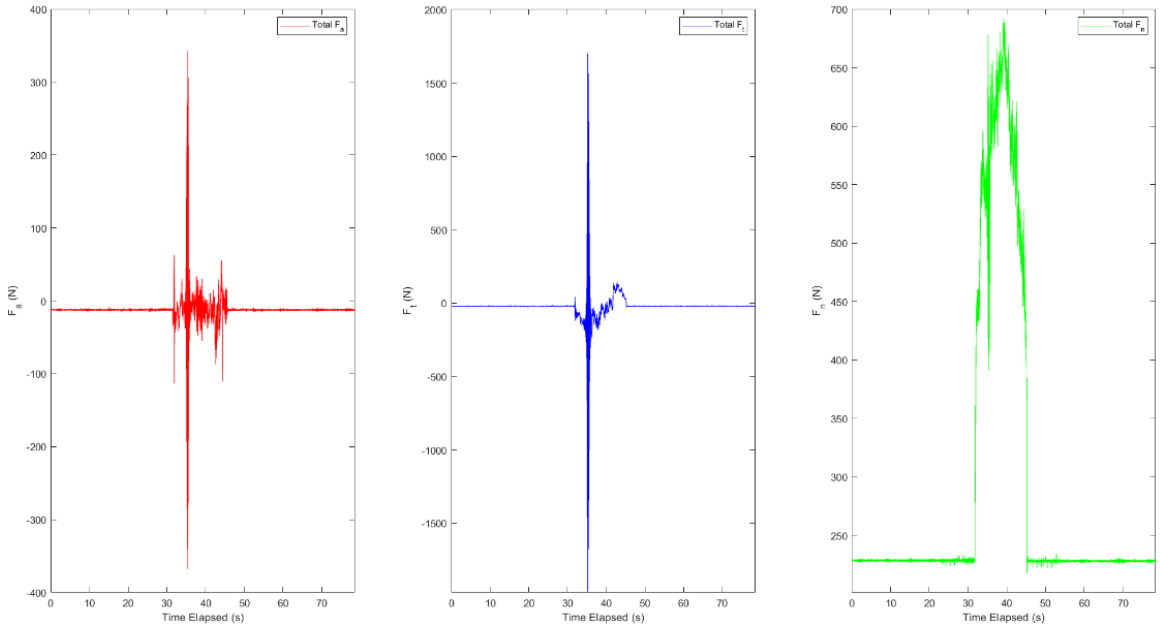

Figure 106: The component grinding forces recorded during the fourth grinding pass '3000-2-0.025-Pass 4'

4.3.2.3 Surface Roughness Analysis

The post-grind surface roughness measurements for the ground sample following the passes conducted at 2000 rpm are presented for three regions C, B and A along the railhead. These regions correspond to the entry of the wheel into the grind, the stable grinding period, and the exit of the wheel into the grind respectively. These regions are depicted in Figure 107.

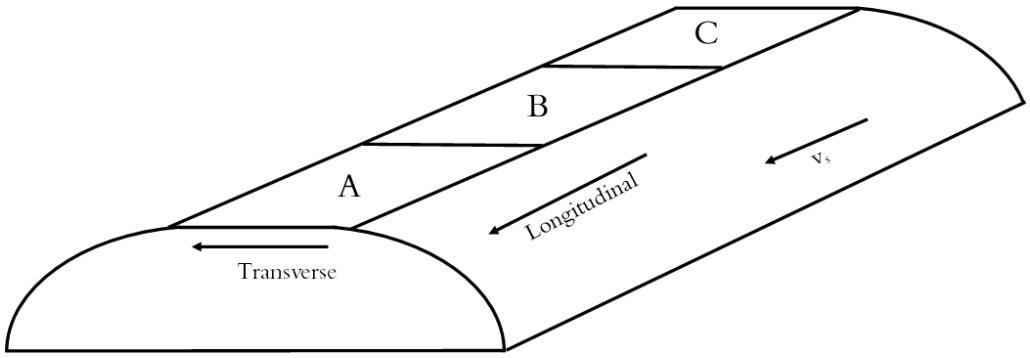

Figure 107: Designated regions of surface roughness measurements across the rail section subsequent to Face Grinding

Figure 108 presents the surface measurements R_a of the rail subsequent to grinding at 2000 rpm. The trend observed for the transverse measurements indicates an increase in the transverse roughness from start of the pass (Region C) to the end of the pass (Region A). The surface roughness values recorded were 0.21 µm, 0.55 µm and 0.57 µm from the Regions C, B and A respectively.

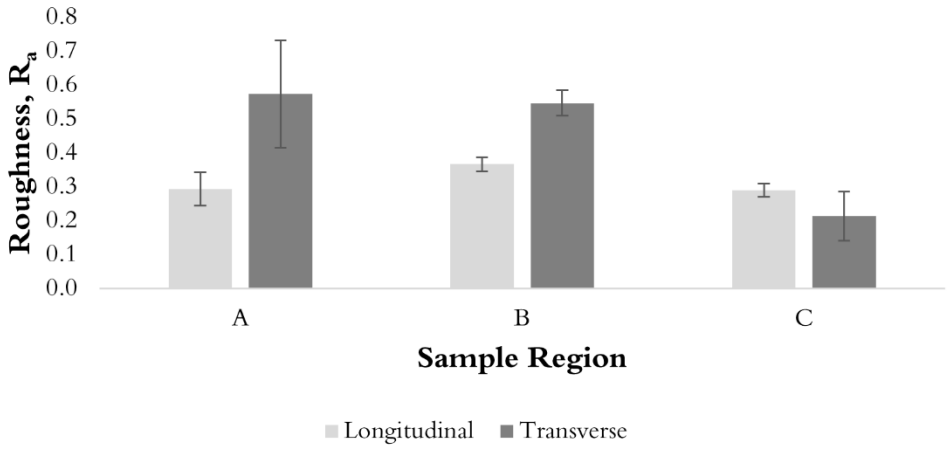

Figure 108: Surface roughness of rail sample subjected to face grinding at 2000 rpm

4.3.2.4 Post-Grind Workpiece Surface

Images of the surface rail head following the grinding passes are presented in this section. For the rail head images presented, the motion of the grinding wheel was from the right side to left. Figure 109 shows the condition of the surface of the rail after the grinding passes conducted at 2000 rpm.

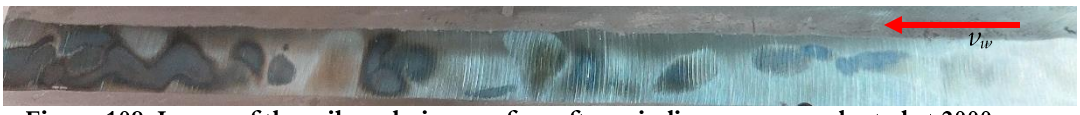

Figure 109: Image of the rail workpiece surface after grinding passes conducted at 2000 rpm.

The condition of the rail surface following grinding passes which were conducted at 3000 rpm is also presented in Figure 110.

Figure 110: Image of the rail workpiece surface after grinding passes conducted at 3000 rpm.

Both images obtained indicate the presence of oxidised grinding burn on the ground surfaces at different amounts. Areas of this grinding burn are observed on the sample ground at 2000 rpm. Visually, the occurrence of grinding burn appears to be more prominent across the rail surface which was ground at 3000 rpm. The colours observed of the grinding burn range from the normal colour of the rail to yellow grinding burn and then blue burn. Therefore, based on the burn classification presented by Lin et al. [35], it is deduced that the darker coloured surface areas (blue, dark blue) would have exceeded the austenitising temperatures during the grinding passes.

4.3.2.5 Post-Grind Microstructural Analysis

In order to assess the effect of the temperatures induced during the grinding operation on the surface integrity of the ground rail, metallurgical post-grind analysis was performed. Due to

limitations associated with the extraction of samples from the rail, metallurgical samples were obtained only from the rail which had been subject to conventional face grinding at 2000 rpm. The polished and etched cross-sectional samples were obtained from the Region A on the rail, which is described in Figure 107 as the region in which the grinding wheel exits the grinding pass. This area was selected in order to observe the appearance of the grinding burn reported in the previous section as well as any possible WEL that may have occurred.

Sectioning was performed in the longitudinal and transverse directions relative to the direction of the forward grinding motion of the wheel. In the context of the rail sectioning that was carried out, the longitudinal direction corresponds to the direction which is parallel to the forward motion of the grinding wheel during a pass, while the transverse direction corresponds to the direction which is perpendicular to the length of the rail.

Figure 111 presents the optical micrographs of the longitudinal cross-section of the rail which was ground at 2000 rpm. The measured average thickness of the WEL observed in the longitudinal cross-sections was 268 μm.

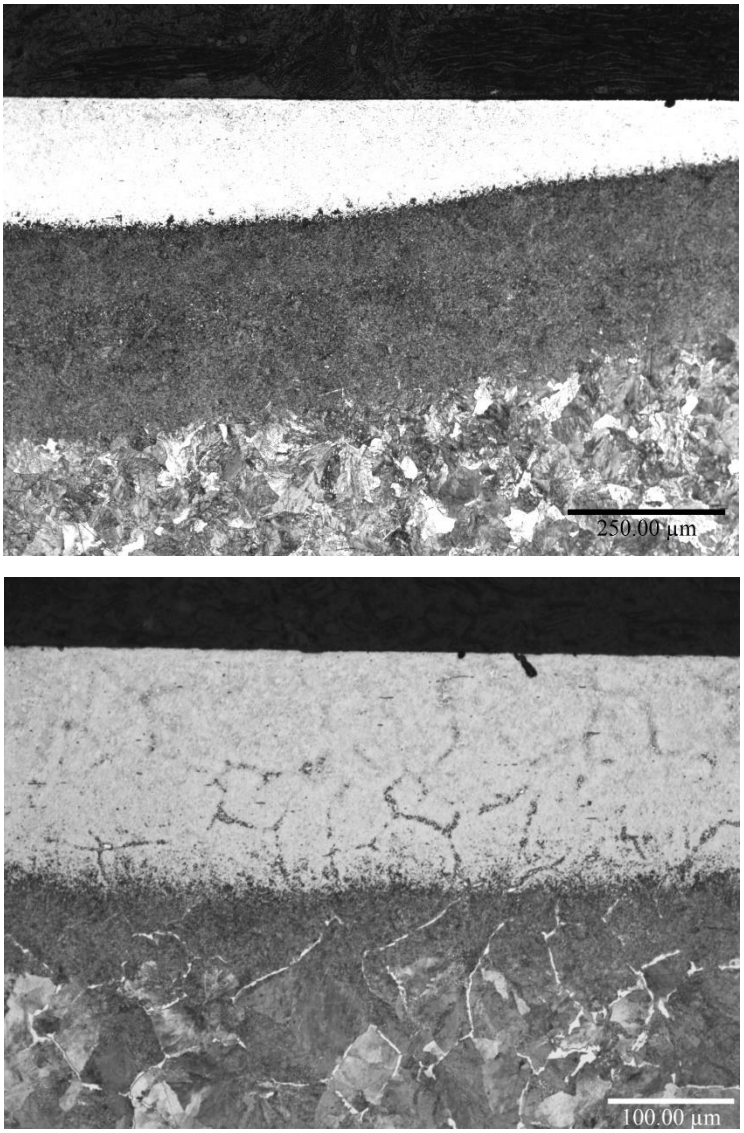

Figure 111: Longitudinal cross-sections of the rail surface conventional face grinding at 2000 rpm (10x and 20x magnifications respectively) showing the presence of WEL with average thickness of 268 µm.

The transverse cross-sections of the rail surface ground at 2000 rpm are also presented in Figure 112. The average thickness of WEL measured in the transverse cross-section was 211 µm.

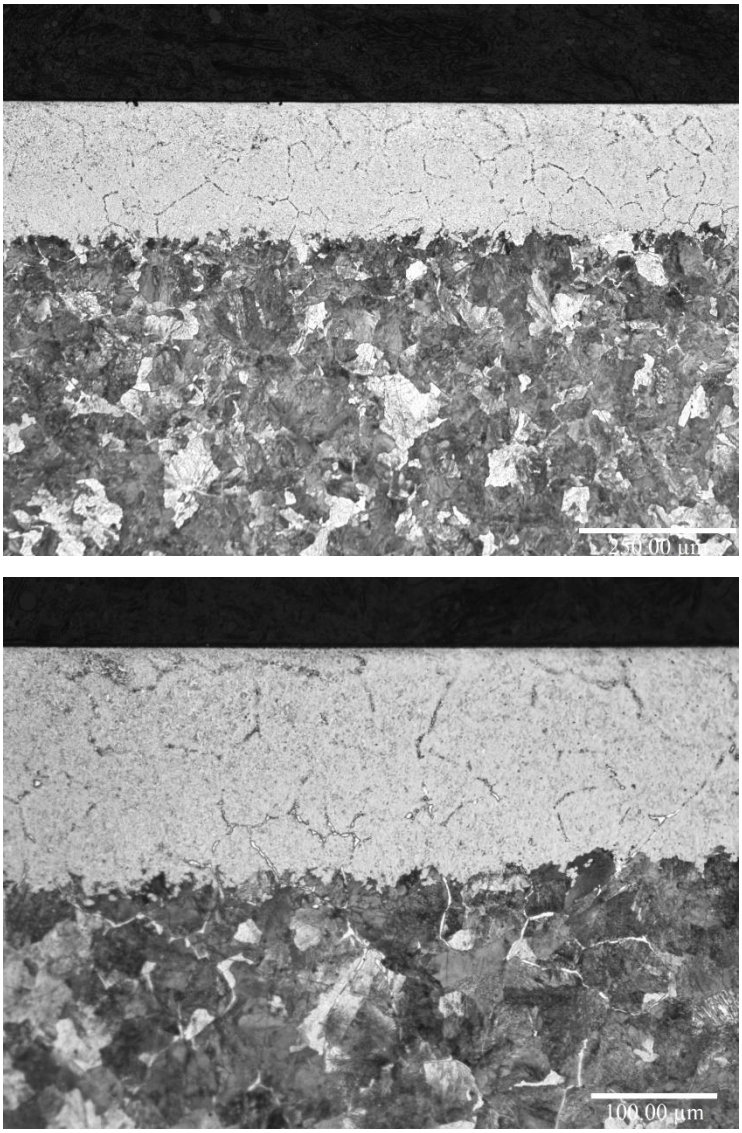

Figure 112: Transverse cross-sections of samples obtained from the rail (10x and 20x magnifications respectively) showing the presence of WEL with measured average thickness of 211 µm.

A white layer which appeared to be unaffected by the etchant was observed at the surface of the cross-sectioned samples assessed. This is identified as the martensitic WEL which had formed during the grinding process. In the longitudinal cross-sections, a sub-layer is also observed between the re-hardened WEL and the pearlitic microstructure of the bulk material. This layer is not visible in the transverse direction.

Microhardness testing was carried out to ascertain the characteristics observed in top surface layer of the cross-sectioned samples. A load of 0.3kg was applied to carry out the indentations. The microhardness and depth profile obtained is presented in Figure 113.

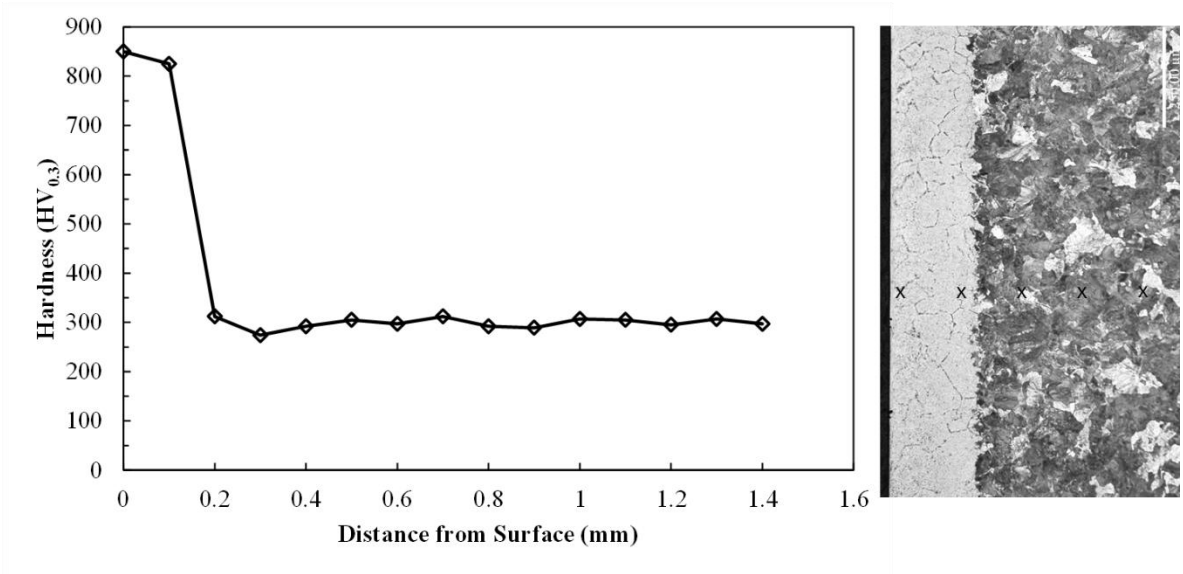

Figure 113: Hardness profile of longitudinal sample obtained from ground rail and a depiction of the location of the indents on the sample

The depth profile of the longitudinal sample indicates high hardness values of 850 $HV_{0.3}$ close to the surface of the sample followed by a drastic drop in hardness to about 200 μm from the surface. The general trend from 200 μm further into the bulk material remained at an average of 299 $HV_{0.3}$ as is consistent with the bulk hardness range of R260 rail.

4.3.2.6 Post-Grind Condition of Grinding Wheel

Figure 114 and Figure 115 present the edge and the centre of the active surface of the MV3 grinding wheel which performed the conventional face grinding trials. This imaging condition was carried out following the passes conducted at 2000 rpm. The brown-coloured areas in the figures (red oval indicators) represent the bond material of the wheel, while the black regions (green indicators) indicate the active AlO_x grains. The white regions (indicated in yellow) are deduced to be the loaded wheel on which the rail workpiece material was smeared.

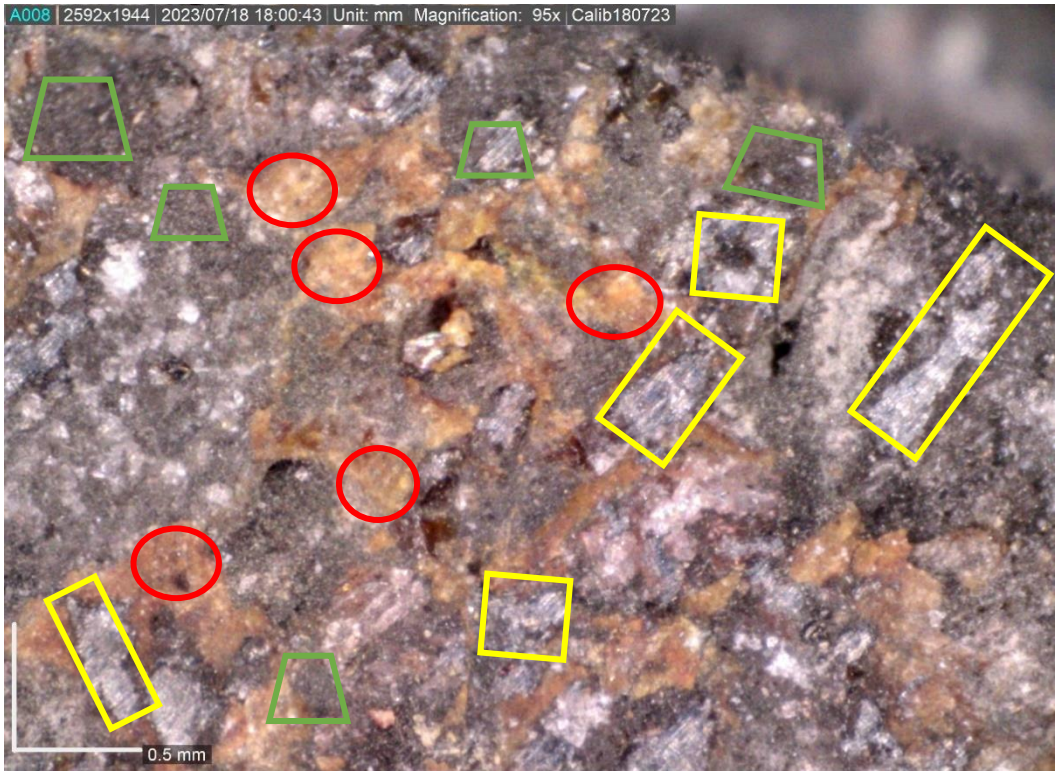

Figure 114: Condition of the edge of the MV3 grinding wheel following the grinding passes performed at 2000 rpm

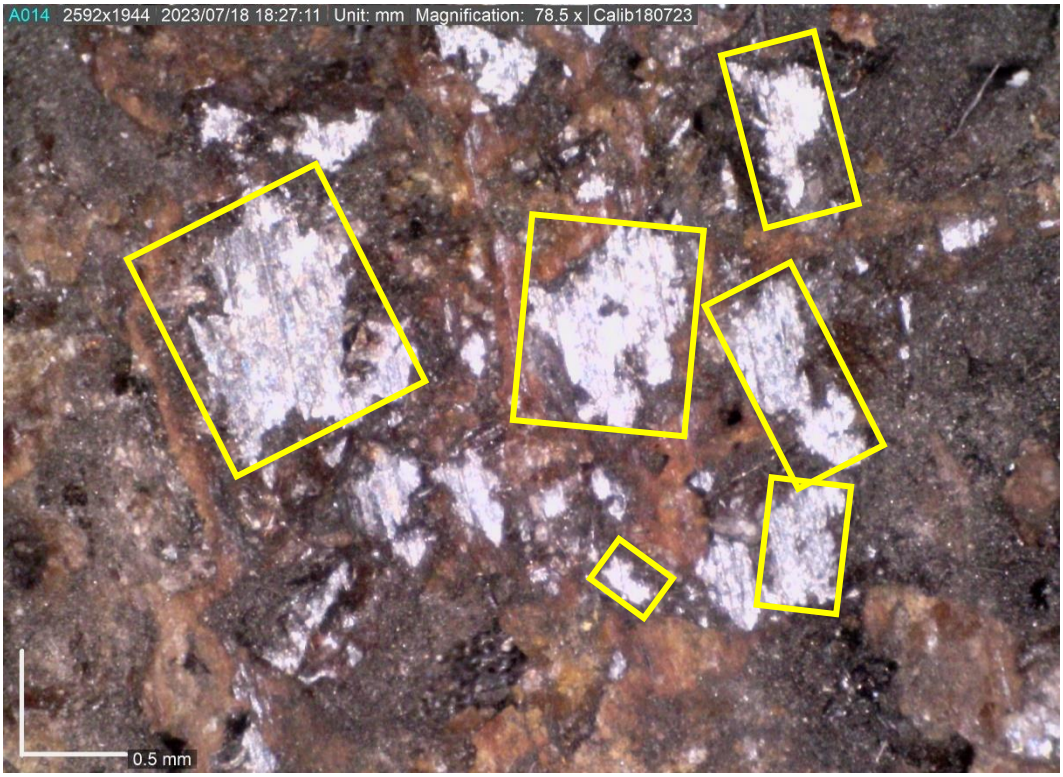

Figure 115: Condition of the centre of the MV3 grinding wheel following the grinding passes performed at 2000 rpm

The simulation study by Zhou et al. [85] postulated that the abrasive grains located towards the centre of the face grinding wheel do not actively participate in the cutting action during a grinding pass but are mainly engaged in ploughing and smearing actions; whereas the grains situated closer to the edge of the grinding wheel largely achieve the cutting action on the workpiece surface. This therefore gives basis to the increased amount of loaded material which is observed in the central area of the wheel, as the cutting edges of the grains are loaded with the rail workpiece material over the course of the grinding pass.

4.3.3 Peripheral Grinding with Conventional Peripheral (Frog) Wheel

4.3.3.1 Temperature Data in Conventional Peripheral Grinding

The temperature data collected for the passes conducted at this grinding orientation include those gathered by the thermocouple as well as those gathered by the thermal camera. A summary of the maximum temperatures recorded by the thermocouples and the thermal cameras during the passes conducted at 2000 rpm and 3000 rpm are presented in Figure 116.

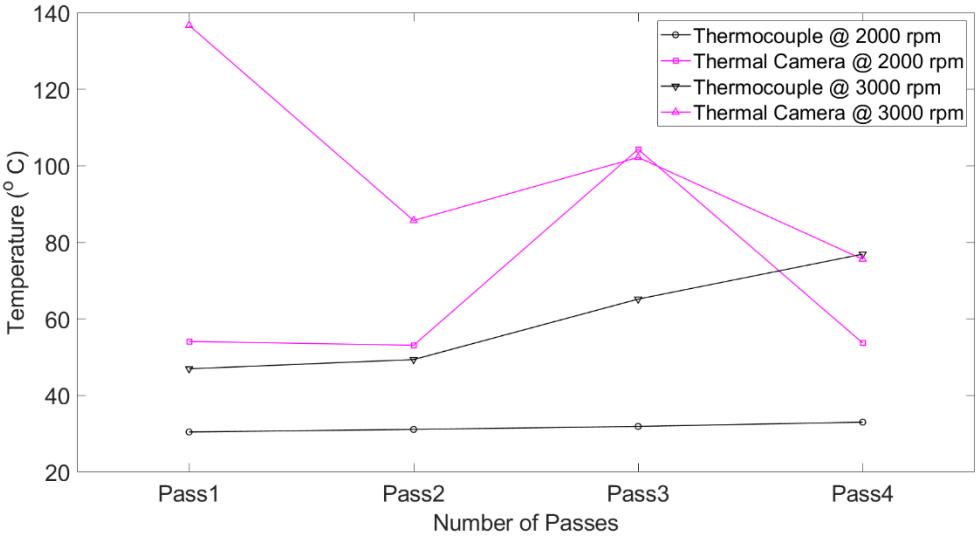

Figure 116: The maximum temperature per pass as recorded by thermocouple and by thermal camera for conventional peripheral grinding passes carried out at 2000 rpm and 3000 rpm

Overall, the values of the maximum temperature per pass as recorded by the thermocouples are lower than the values measured by the thermal camera. The induced thermal energy of the grinding pass is dissipated from the ground surface into the subsurface of the rail by conduction, therefore it appears that the thermal energy is released into the bulk of before it is captured by the embedded thermocouples. Therefore, the thermal camera is able to measure slightly higher temperature values before dissipation from the surface.

The progression of the temperatures recorded by the 8 thermocouples for each grinding pass conducted using the conventional peripheral grinding wheel are also individually presented alongside the temperatures recorded by the thermal camera. The placement locations of the

embedded thermocouples T1-T8 are described in Section 4.2.1.1, where T1 corresponds to the thermocouple which is closest to the rail surface and T8 corresponds to the thermocouple which is placed farthest into the bulk material. For the thermal camera readings, Area 1 corresponds to the grinding contact zone, while Areas 2 and 3 correspond to static points on along the railhead.

The plotted temperature progressions observed by the thermal camera and thermocouple for every pass depict three distinct stages over the course of the grinding pass. In the plots of the thermocouple readings, the first stage observed is a rapid increase in the temperature as the grinding commences, followed by a maximum temperature and then a stage of slow cooling. The pattern of behaviour observed by the thermal camera differs in the rapid rising and cooling of the observed grinding zone. By virtue of the slow cooling observed at the end of grind, it is surmised that the thermocouple measurements do not immediately return to room temperature. As the thermocouples are embedded beneath the rail surface, the thermal energy induced in grinding is primarily lost by conduction. On the other hand, the exposed ground rail surface loses the thermal energy through convection and radiation in the air. Therefore, the thermal camera which is directed at the exposed surface of the rail will observe the dissipation of heat more rapidly.

Figure 117 presents the temperature progression of the initial pass conducted at 2000 rpm.

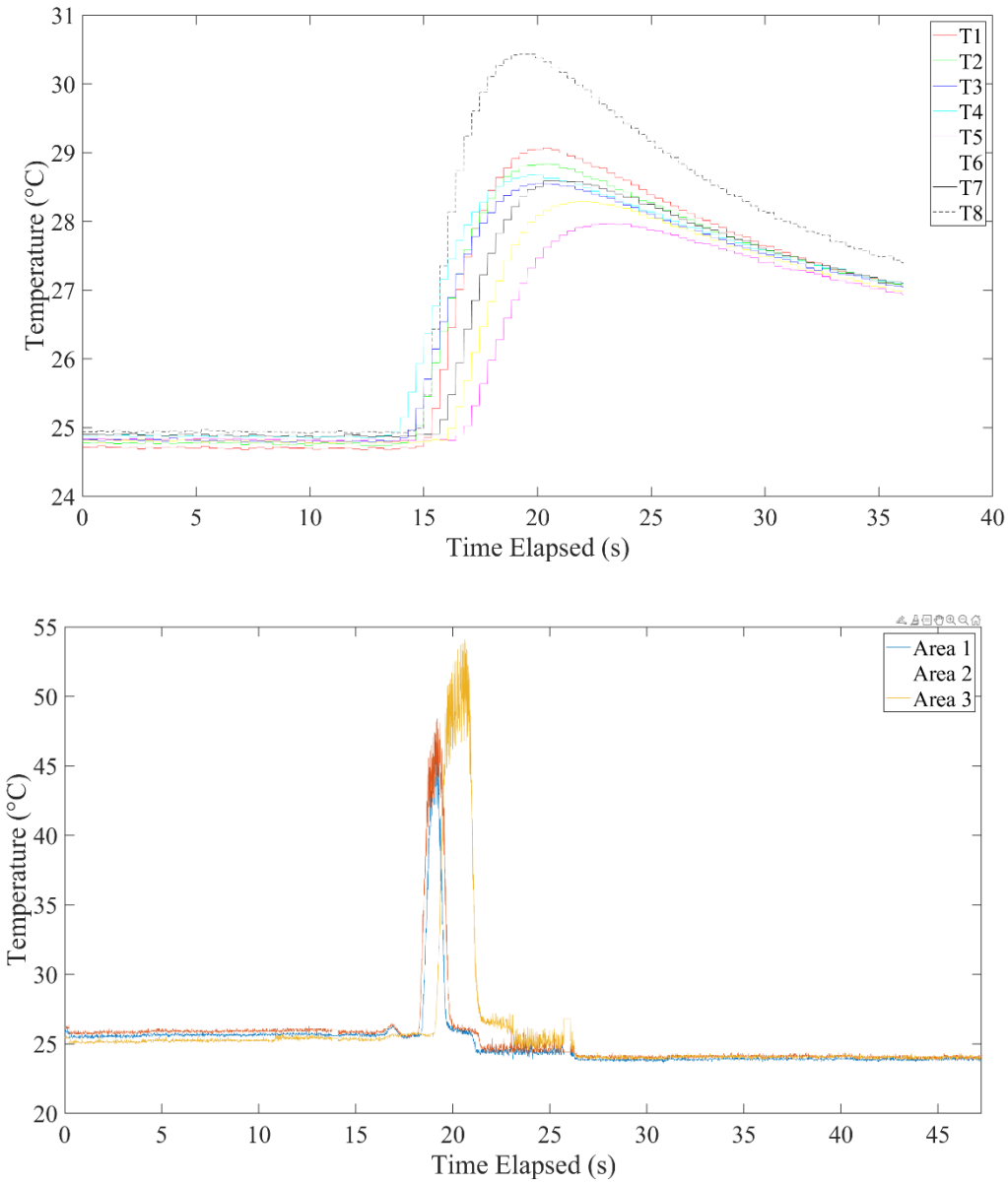

Figure 117: Recorded temperature of the rail subsurface as recorded by thermocouples and rail grinding contact area as recorded by a thermal camera during the first grinding pass conducted at 2000 rpm.

The progression of the temperature as recorded by the eight thermocouples as well as the thermal camera during the second grinding pass conducted at 2000 rpm is presented in Figure 118.

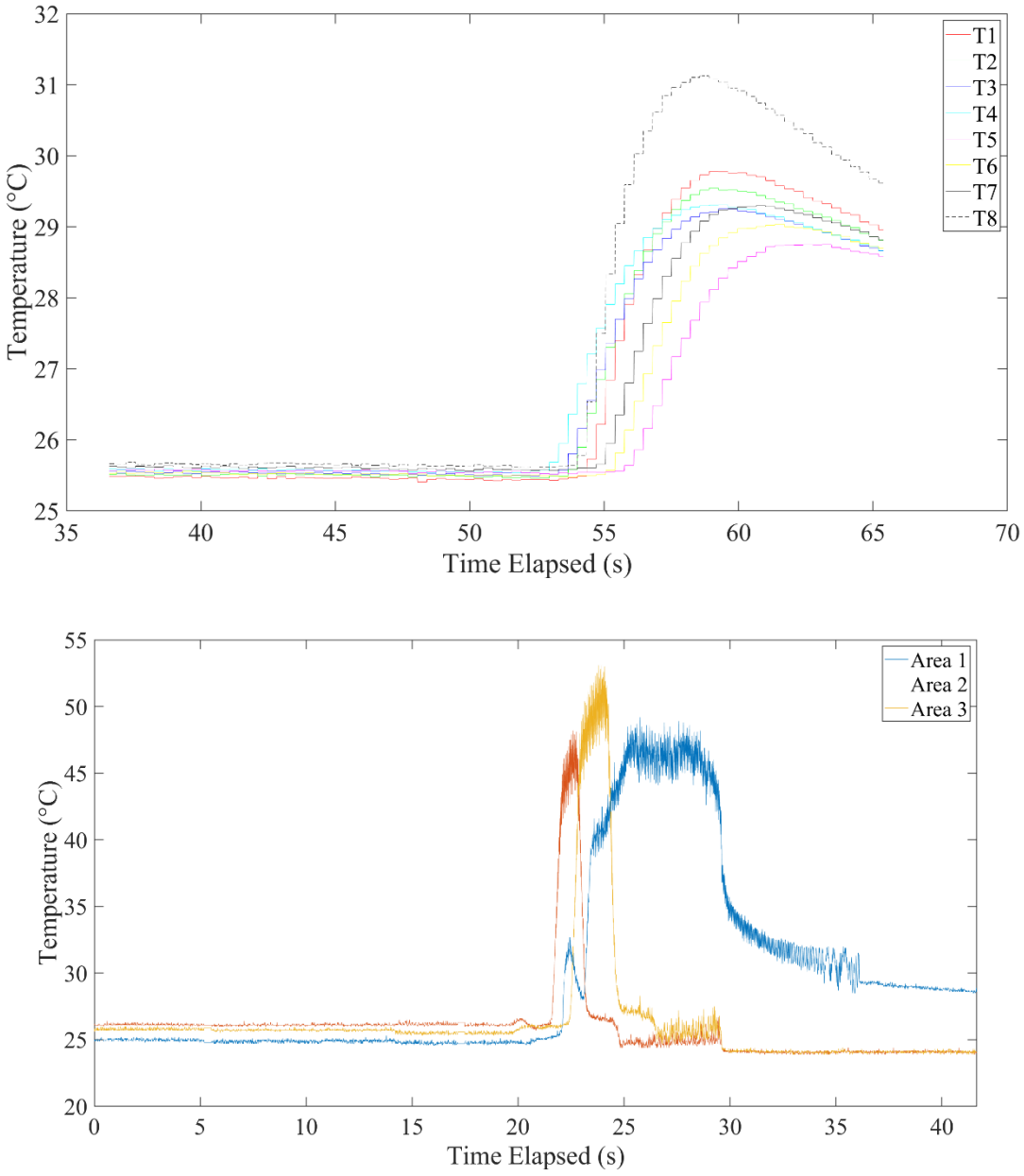

Figure 118: Recorded temperature of the rail subsurface as recorded by thermocouples and rail grinding contact area as recorded by a thermal camera during the second grinding pass conducted at 2000 rpm.

Figure 119 shows the progression of temperatures which were recorded by the thermocouples and the thermal camera during the third pass conducted at 2000 rpm.

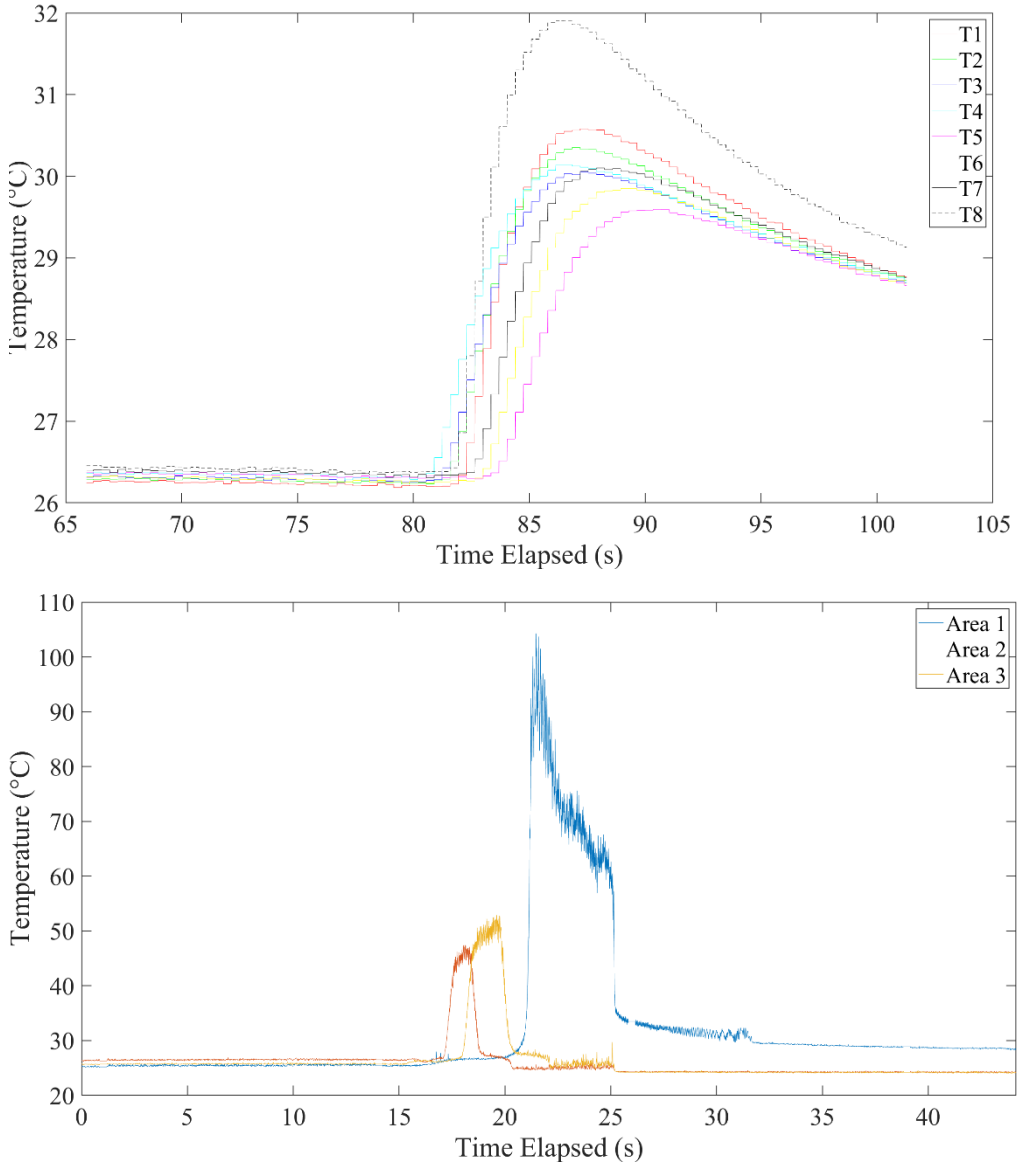

Figure 119: Recorded temperature of the rail subsurface as recorded by thermocouples and rail grinding contact area as recorded by a thermal camera during the third grinding pass conducted at 2000 rpm.

The progression of temperatures recorded by the thermocouples and the thermal camera during the fourth pass performed at 2000 rpm are presented in Figure 120.

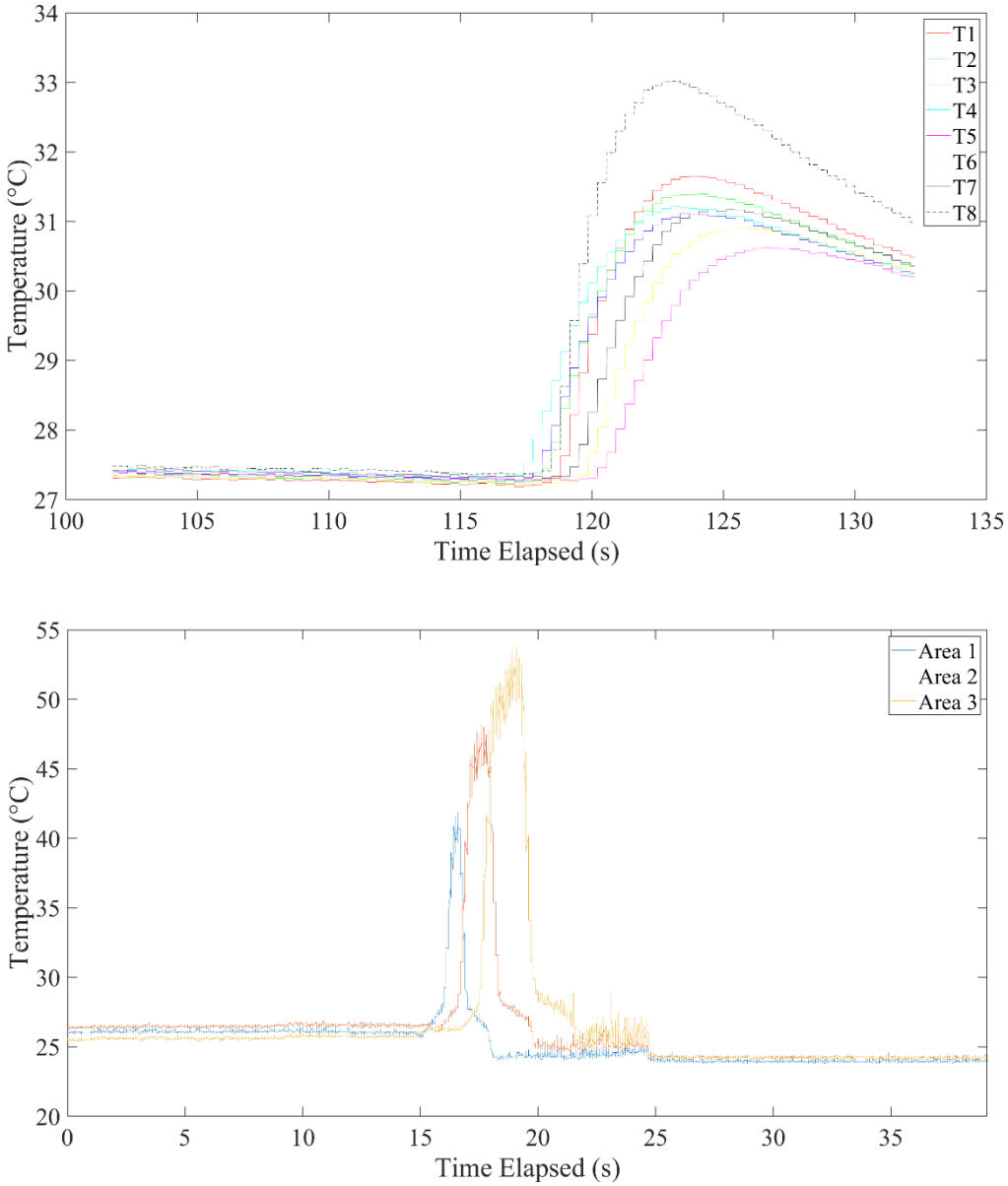

Figure 120: Recorded temperature of the rail subsurface as recorded by thermocouples and rail grinding contact area as recorded by a thermal camera during the fourth grinding pass conducted at 2000 rpm.

The temperature progressions which were recorded by the thermocouples and the thermal camera during the first pass conducted at 3000 rpm are presented in Figure 121.

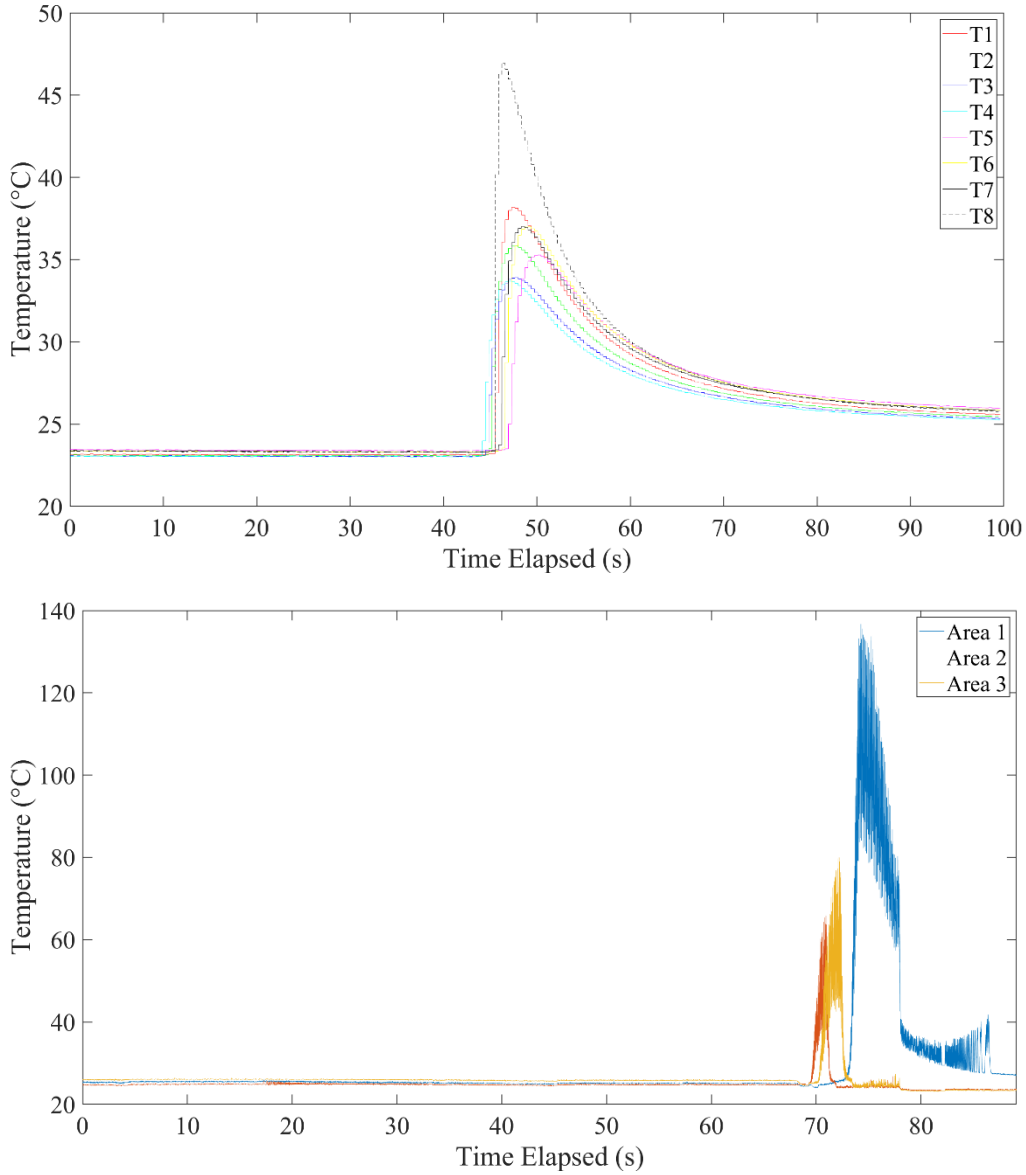

Figure 121: Recorded temperature of the rail subsurface as recorded by thermocouples and rail grinding contact area as recorded by a thermal camera during the first grinding pass conducted at 3000 rpm.

Figure 122 shows progressions of the temperature which were recorded by the thermocouples and the thermal camera during the second pass conducted at 3000 rpm.

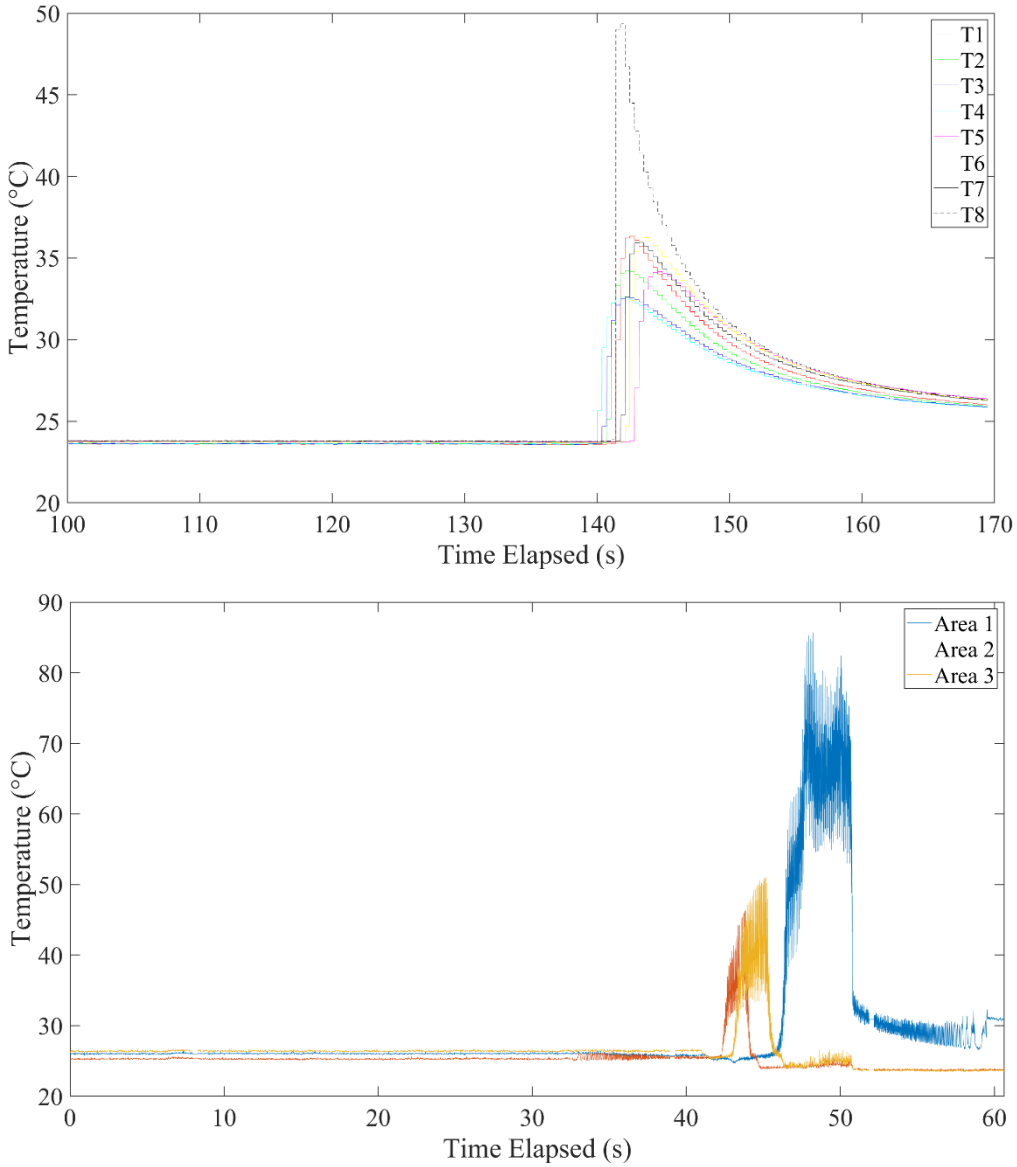

Figure 122: Recorded temperature of the rail subsurface as recorded by thermocouples and rail grinding contact area as recorded by a thermal camera during the second grinding pass conducted at 3000 rpm.

The progression of the temperatures recorded by the eight thermocouples and the thermal camera during the third pass conducted at 3000 rpm are shown in Figure 123.

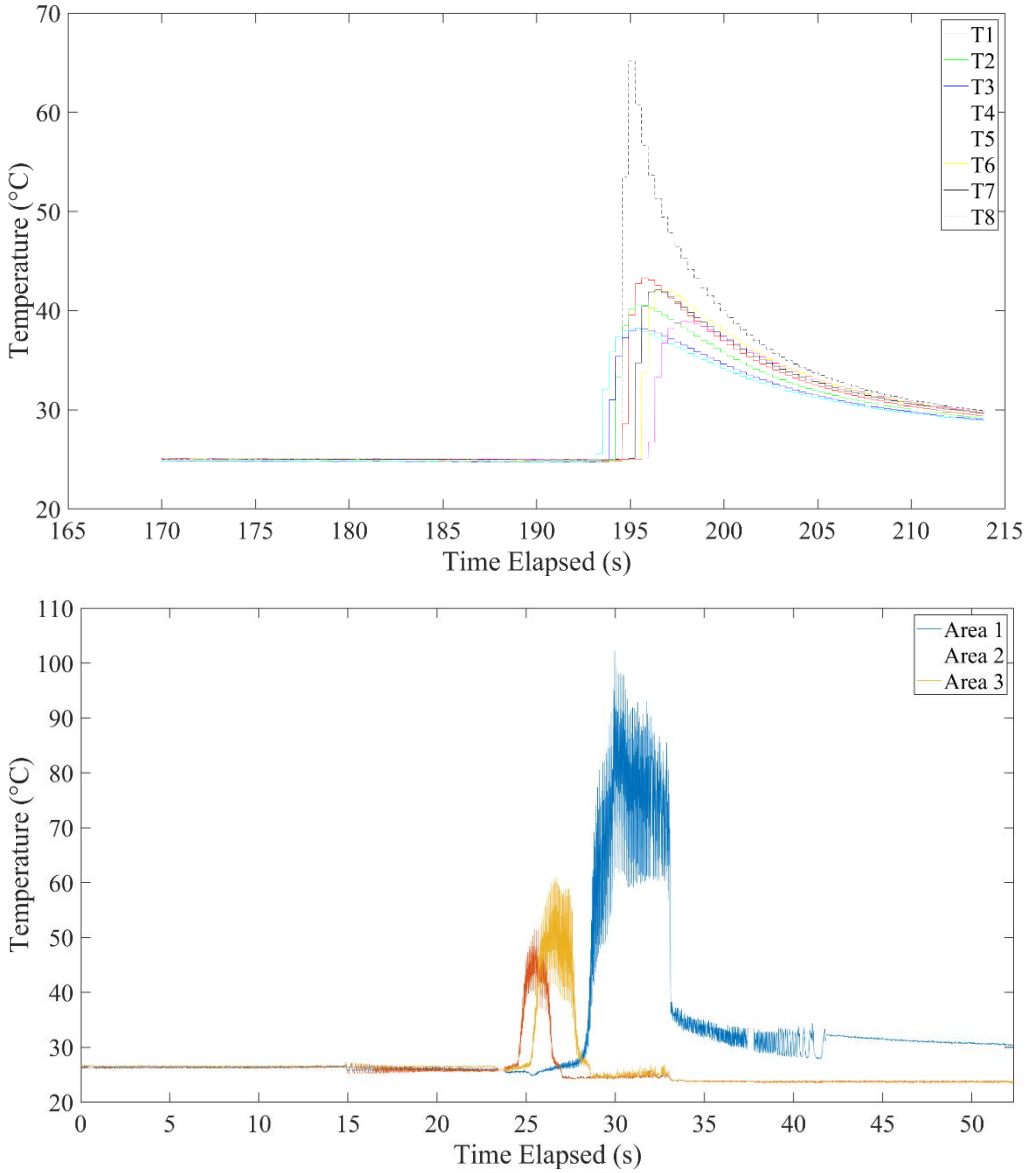

Figure 123: Recorded temperature of the rail subsurface as recorded by thermocouples and rail grinding contact area as recorded by a thermal camera during the third grinding pass performed at 3000 rpm.

Figure 124 presents the recorded grinding temperature as recorded by the array of thermocouples as well as the thermal camera during the fourth grinding pass conducted at 3000 rpm.

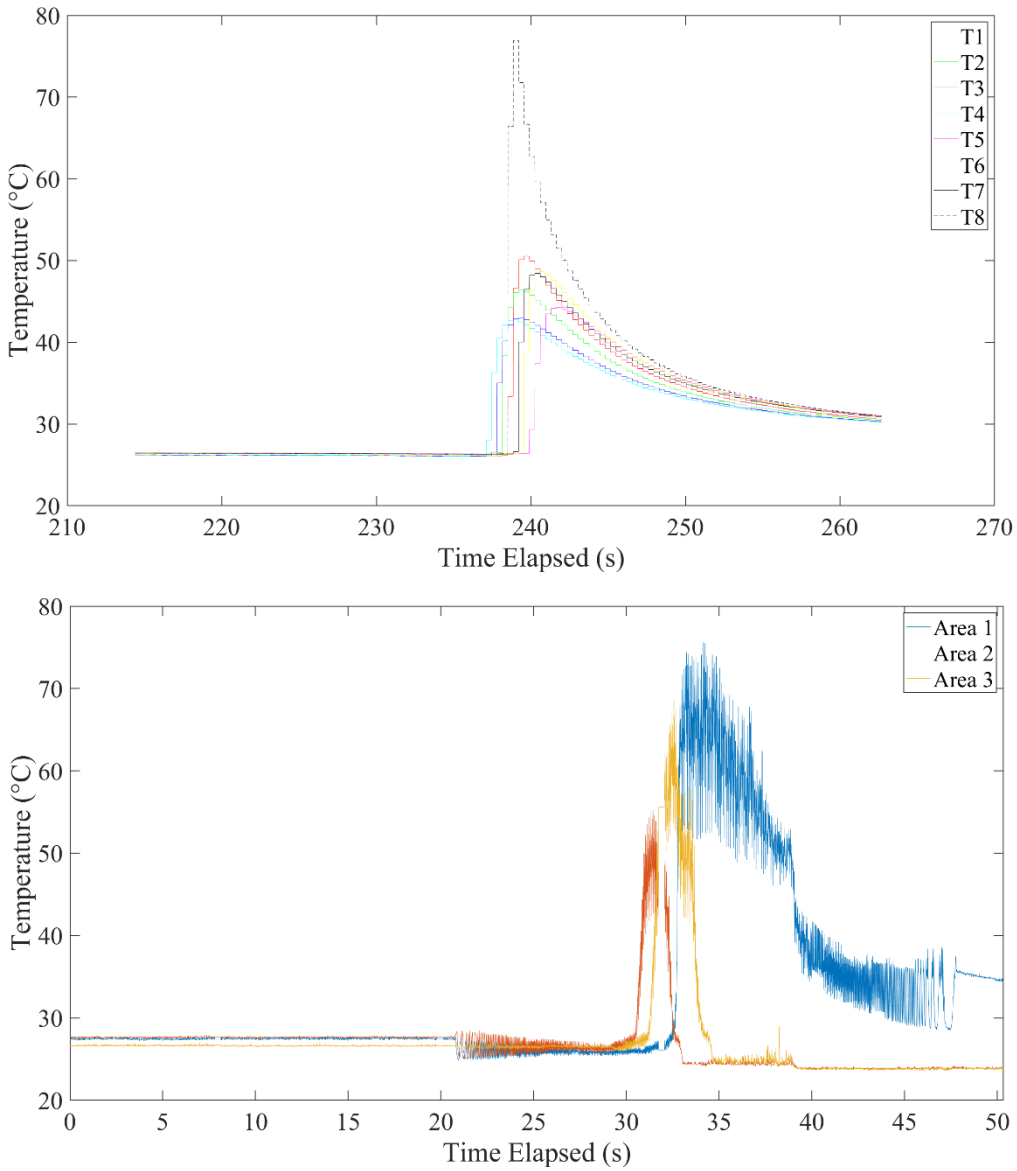

Figure 124: Recorded temperature of the rail subsurface as recorded by thermocouples and rail grinding contact area as recorded by a thermal camera during the fourth grinding pass conducted at 3000 rpm

Thermocouple measurements were not obtained for the passes conducted during the conventional face grinding trial. Therefore, in comparing the temperatures recorded by the thermal camera, it is observed that the range of grinding temperatures recorded in the peripheral grinding passes (2000 rpm: 54 – 104 °C; 3000 rpm: 76 – 136 °C) appear to be less than the range of maximum temperatures recorded in the conventional face grinding trials (2000 rpm: 72 – 194 °C; 3000 rpm: 53 – 275 °C). This is attributed to the grinding forces which are generated during the conventional face grinding passes. The grinding forces observed for the peripheral grinding passes conducted are presented in the next section.

4.3.3.2 Force Data in Conventional Peripheral Grinding

The grinding force output is a vital parameter which is related to the specific grinding energy. The components of the grinding force acting on the grind zone during the grinding passes are detailed in this section. Initially, the evolution of the maximum forces recorded per pass are presented for the two grinding wheel speeds explored in the study. Following this, the progression of the component forces for the individual passes are then detailed. The orientation of the normal and tangential grinding forces F_n and F_t which act on the rail during the grinding pass carried out using a peripheral grinding wheel is depicted in Figure 125.

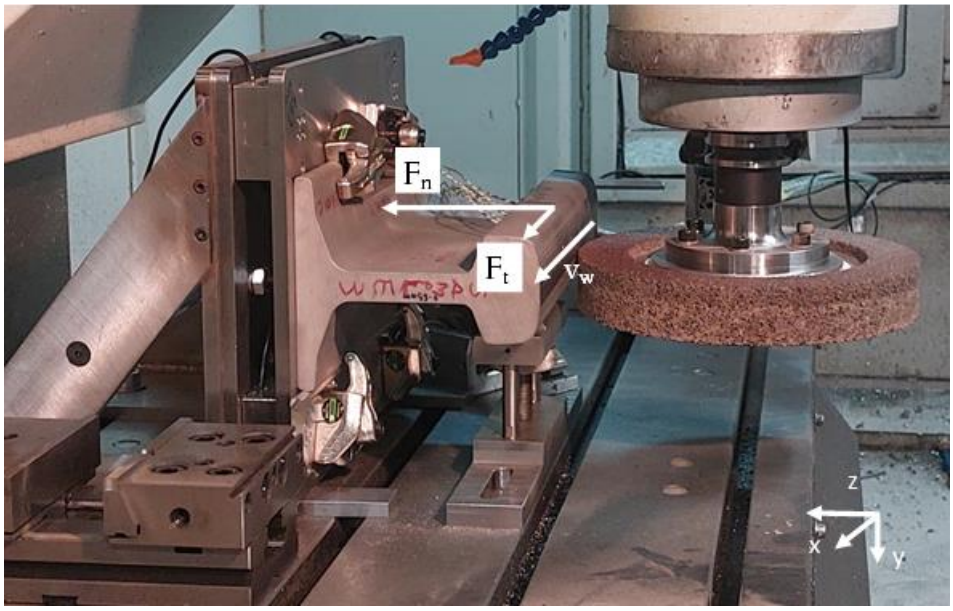

Figure 125: The orientation of the component grinding forces F_n and F_t which act on the rail and grinding wheel interface during a peripheral grinding pass.

As shown in Figure 125 and based on the orientation of the rail and the wheel, the component forces which are active during the grinding pass include the normal and the tangential forces. The component force which acts in the downward direction is potentially related to the vibrations of the spindle and the CNC machine. Therefore, prior to the grinding trials, it was predicted that the forces would be close to zero. The based on the observed force readings, the downward forces are considered negligible relative to the other two component forces F_n and F_t and will not be focused on in this study.

A summary of the progression of the component forces F_n and F_t which were recorded during each pass conducted at 2000 rpm and 3000 rpm are presented in the Figure 126 and Figure 127 below.

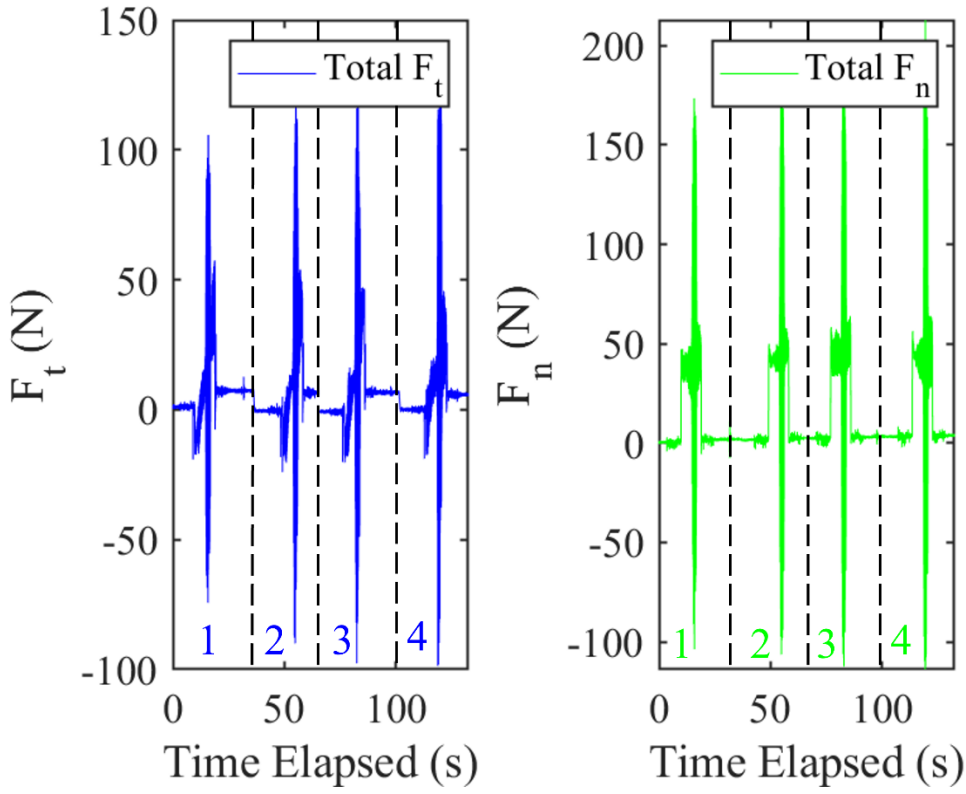

Figure 126: Progression of the grinding forces measured during the peripheral grinding passes conducted at 2000 rpm.

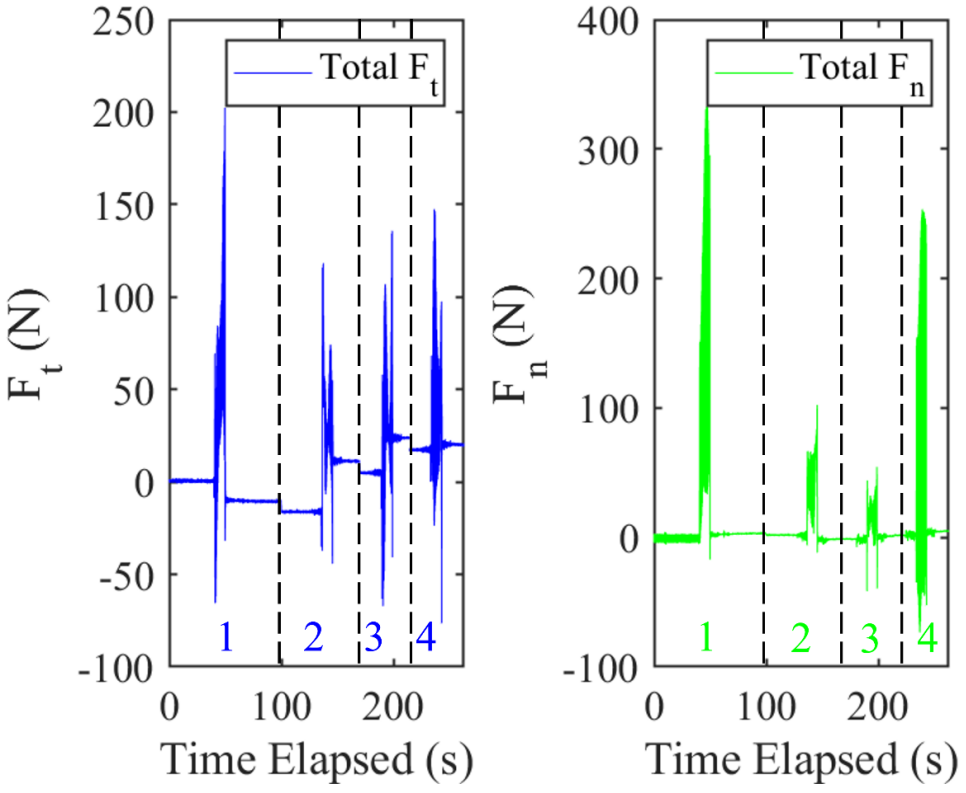

Figure 127: Progression of the grinding forces measured during the peripheral grinding passes conducted at 3000 rpm.

To establish a global overview of the relationship between the grinding force and the increasing depth of cut up to a total a_e, the progression of the grinding forces is presented with respect to the maximum recorded force per pass. The maximum values of the force components F_n and F_t measured during the passes which were conducted at the grinding wheel speeds of 2000 rpm and 3000 rpm are presented in Figure 128.

The magnitude of the maximum tangential grinding forces recorded during the four grinding passes conducted at 2000 rpm included 105.7 N, 118.4 N, 123.8 N and 124.5 N while the normal grinding forces included 173.5, N181.7 N, 192.7 N, and 212.9 N for the four respective grinding passes. Likewise, the maximum tangential forces recorded during the four grinding passes carried out at 3000 rpm included 202.4 N, 118.2 N, 135.8 N and 147.4 N, while the normal grinding forces recorded were: 344.8 N, 102.3 N, 54.4 N and 253.4 N for the four respective grinding.

With each pass, the results showed a gradual increase in the values of F_n and F_t measured during the four passes conducted at 2000 rpm. On the other hand, the results show differing force responses between F_n and F_t in the passes conducted at 3000 rpm. The plot further indicates a sharp decrease in the maximum F_n at 3000 rpm until the third pass, followed by an increase in the grinding force in the fourth pass. Likewise, the evolution observed for F_t at 3000 rpm depicts an initial decrease in the maximum force from the largest value in the initial pass followed by a steady increase in the passes thereafter.

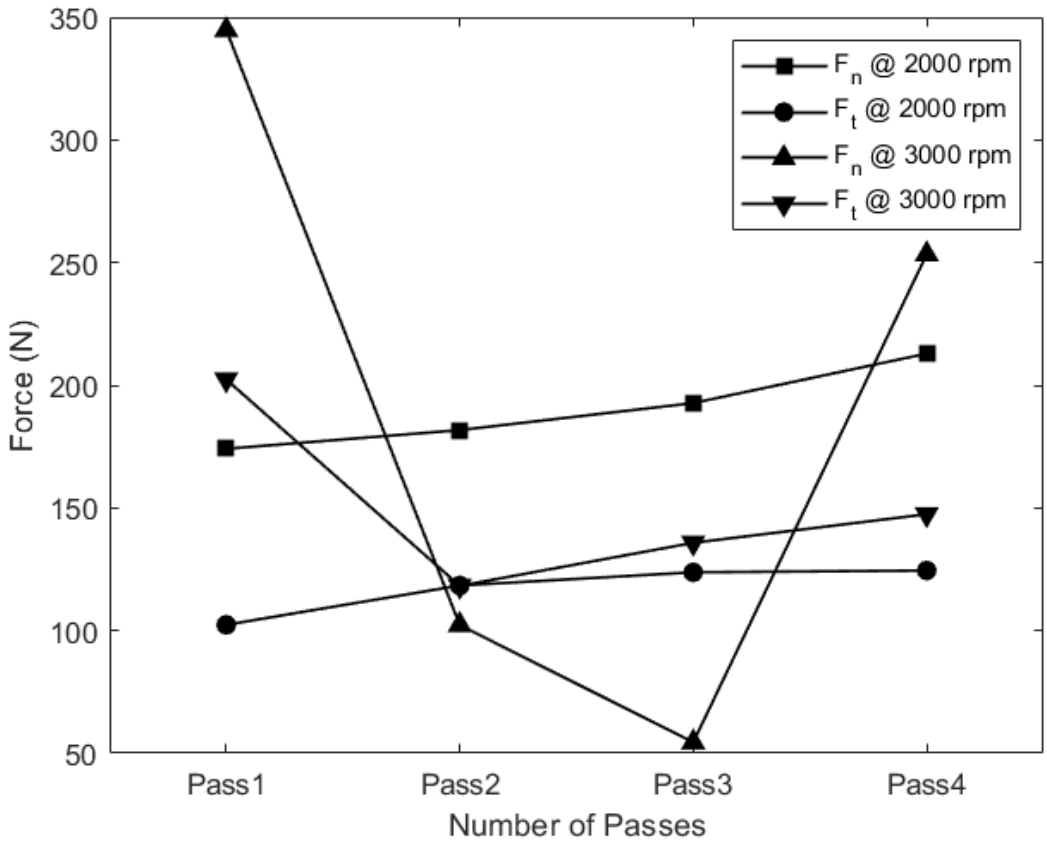

Figure 128: Evolution of the maximum grinding forces with the number of peripheral grinding passes conducted at wheel speeds of 2000 rpm and 3000 rpm.

In the results previously presented for the face grinding approach (Section 4.3.2.2), a steady increase in the maximum grinding force per pass is observed for all component forces generated at both 2000 rpm and 3000 rpm. This is not observed in the passes conducted in the peripheral grinding orientation. The grinding forces observed in the peripheral grinding orientation show a steady increase in the grinding forces per pass for the passes conducted at 2000 rpm and an initial decrease in the grinding forces recorded at 3000 rpm followed by an increase as the passes progress.

The plots of the grinding forces recorded during the passes performed at the rotation of 2000 rpm are presented from Figure 129 to Figure 132. The three distinct stages which are common for all force plots obtained from the grinding passes conducted at 2000 rpm are depicted in Figure 129. These include stages 1 and 3, where the grinding wheel is not in engagement with the rail surface and the grinding forces remain at a pregrind threshold. Stage 2 signifies the period of upgrinding. At the start of stage 2, the tangential grinding force F_t initially falls to a value below the pregrind threshold and steadily increases above the pregrind threshold throughout the remainder of the grinding pass. On the other hand, as the wheel engages the rail workpiece at the start of grinding pass, the normal grinding force F_n increases to an initial maximum and decreases until halfway through the pass, where the normal force appears to generally increase once more until the pass is completed. At the end of stage 2, a rapid reduction is observed in the tangential and normal grinding forces due to the disengagement of the grinding wheel from the rail workpiece.

Another notable observation which is common to the plots of the tangential and normal forces for the passes ground at 2000 rpm is the increased amplitude of the force signal which occurs after halfway into the grinding pass. It is in this period of increased amplitude that the maximum grinding force per pass is recorded. This period of increased grinding force amplitude is attributed to the local action of the abrasive grits as the cutting edge is dulled. The thermal energy generated by the friction action of the wheel and the rail surface causes the softening of the surface material, which may lead to smearing of the abrasive grits and diminishes the cutting action of the cutting edge. The diminished cutting action leads to further rubbing and ploughing which in turn increases the grinding forces. The period of increased grinding force amplitude ceases after a duration of about three seconds then the grinding forces return to their prospective trajectories until the grinding pass is completed.

The progression of the normal and tangential component forces (F_t and F_n) which were recorded during the first grinding pass conducted at 2000 rpm are shown in Figure 129.

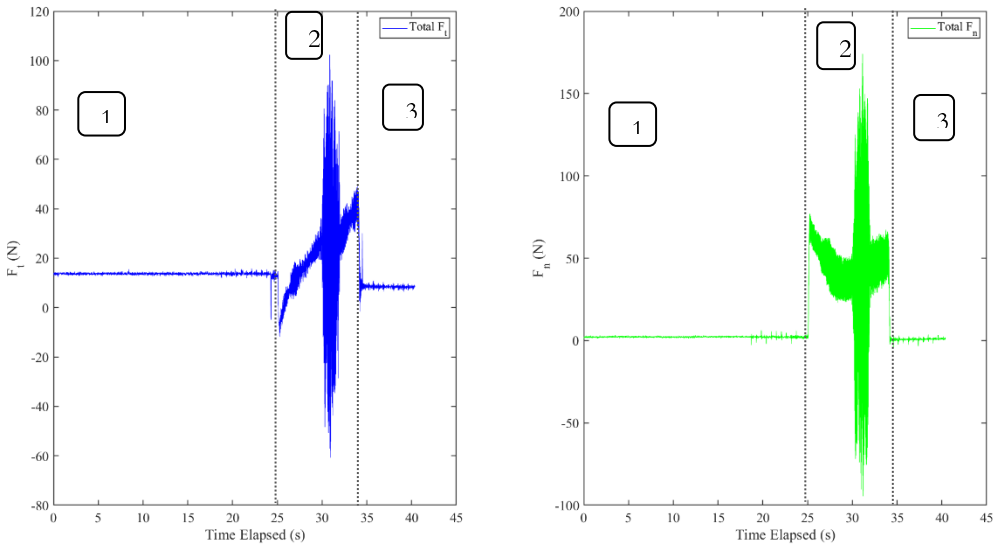

Figure 129: The component grinding forces recorded during the first grinding pass '2000-2-0.025-Pass 1'

Figure 130 shows the progression of the normal and tangential component forces (F_t and F_n) which were recorded during the second grinding pass conducted at 2000 rpm.

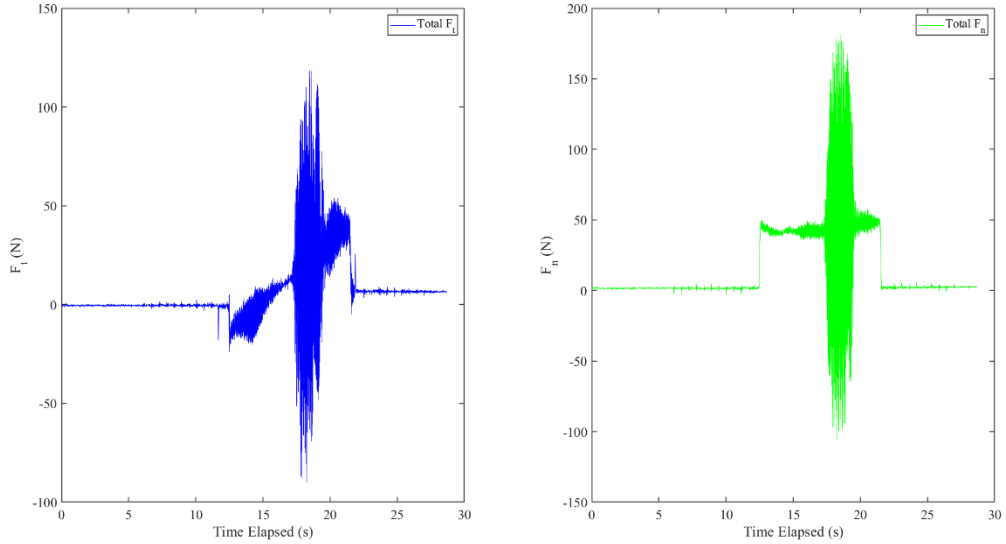

Figure 130: The component grinding forces recorded during the second grinding pass '2000-2-0.025-Pass 2'

Figure 131 shows the progression of the normal and tangential component forces (F_t and F_n) which were recorded during the third grinding pass conducted at 2000 rpm.

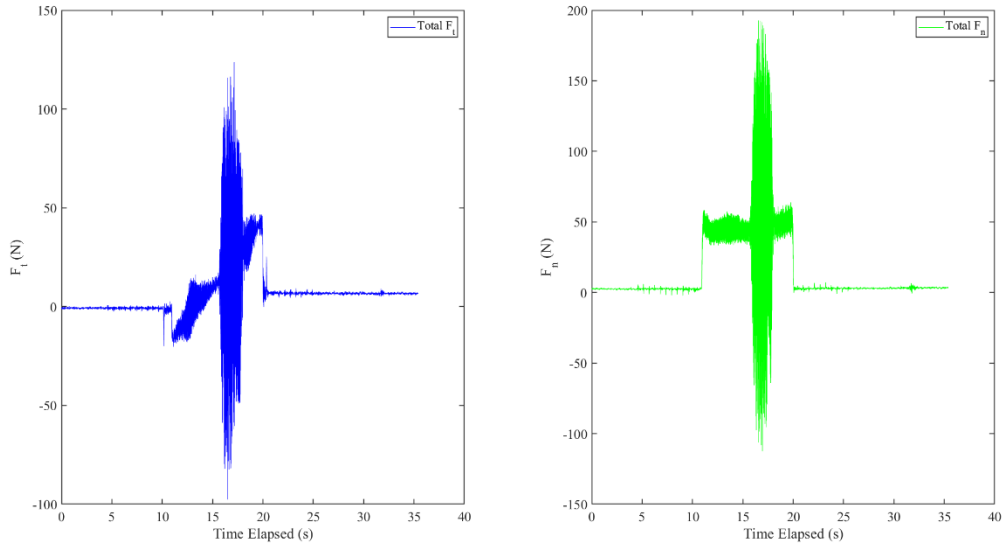

Figure 131: The component grinding forces recorded during the third grinding pass '2000-2-0.025-Pass 3'

The progression of the component grinding forces recorded during the fourth grinding pass conducted at 2000 rpm are presented in Figure 132.

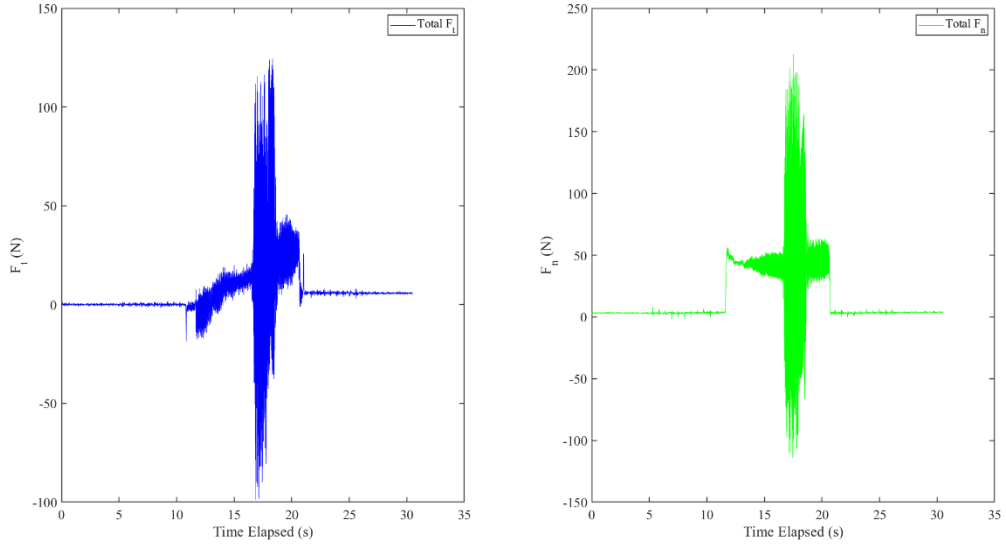

Figure 132: The component grinding forces recorded during the fourth grinding pass '2000-2-0.025-Pass 4'

The plots of the grinding forces recorded during the passes performed at the rotation of 3000 rpm are presented from Figure 133 to Figure 136. Similar to the passes conducted at 2000 rpm, the force plots are observed in the stages 1, 2, and 3, with stage 1 and 3 being the periods where the grinding wheel is not in contact with the rail surface. The highest values maximum grinding forces are recorded in the first and fourth passes. The corresponding tangential and normal force plots of these two Passes 1 and 4 are also observed to have significantly higher amounts of noise across their respective grinding passes than the plots of the Passes 2 and 3. Due to the noisy signal which is observed in Pass 1 and Pass 4, it is difficult to fully elucidate on the force behaviour that may have occurred during these passes. Meanwhile, the grinding forces observed for Pass 2 indicates an undulation of the tangential grinding force from a maximum at the start of the engagement of the grinding wheel then to a reduction to a minimum, followed by an increase until the end of the grinding pass. A similar undulation is observed in the tangential forces recorded for Pass 3; however, at the start of the pass, the grinding force appears to be below the threshold in the negative direction. This indicates an initial resistance of the workpiece surface to forward motion of the grinding wheel. When this workpiece resistance is overcome by the grinding wheel, the global grinding forces begin to increase.

The progression of the component normal and tangential component grinding forces (F_t and F_n) recorded during the first grinding pass conducted at 3000 rpm are presented in Figure 133.

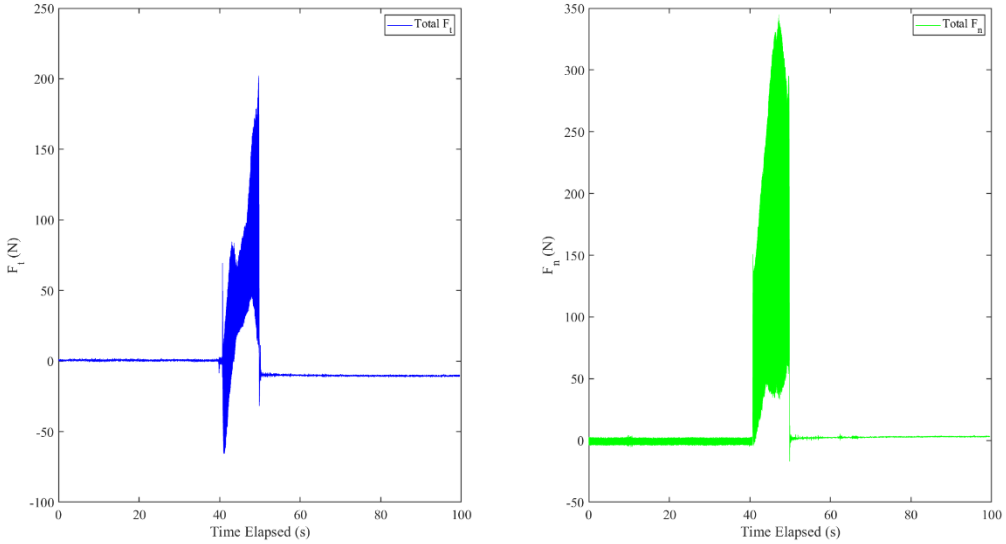

Figure 133: The component grinding forces recorded during the first grinding pass '3000-2-0.025-Pass 1'

The progression of the component normal and tangential component grinding forces (F_t and F_n) recorded during the second grinding pass conducted at 3000 rpm are presented in Figure 134.

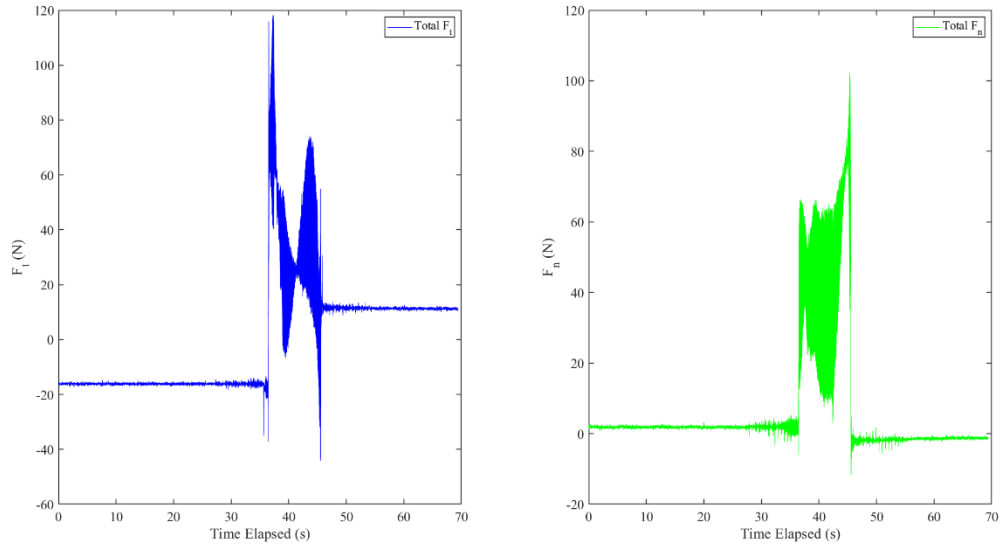

Figure 134: The component grinding forces recorded during the second grinding pass '3000-2-0.025-Pass 2'

The progression of the component normal and tangential component grinding forces (F_t and F_n) recorded during the third grinding pass conducted at 3000 rpm are presented in Figure 135.

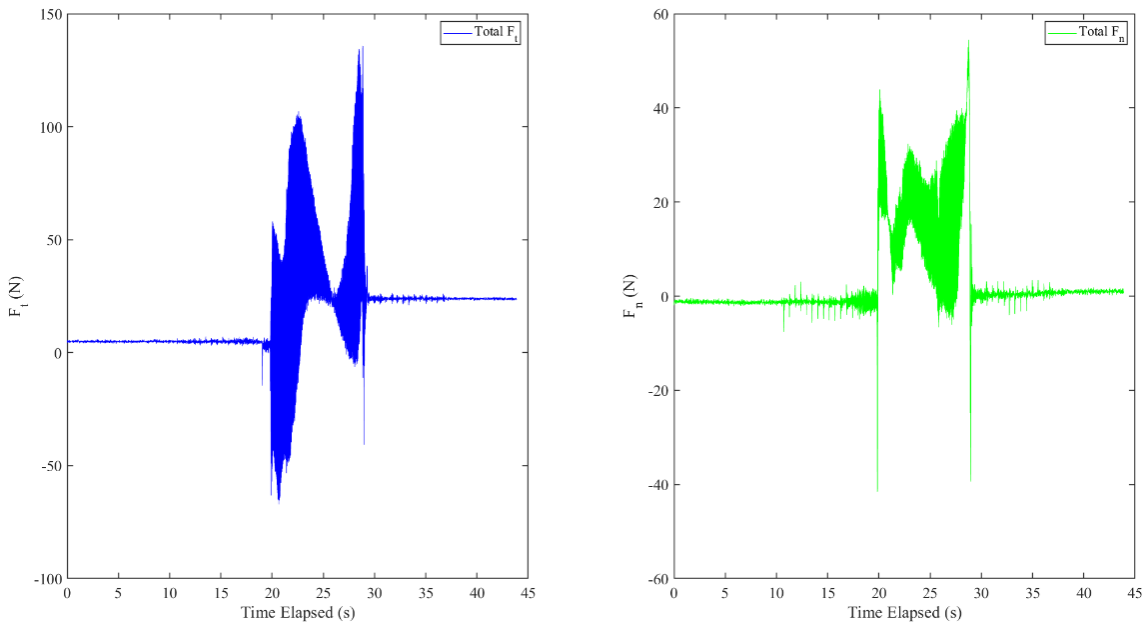

Figure 135: The component grinding forces recorded during third grinding pass '3000-2-0.025-Pass 3'

The progression of the component normal and tangential component grinding forces (F_t and F_n) recorded during the fourth grinding pass conducted at 3000 rpm are presented in Figure 136.

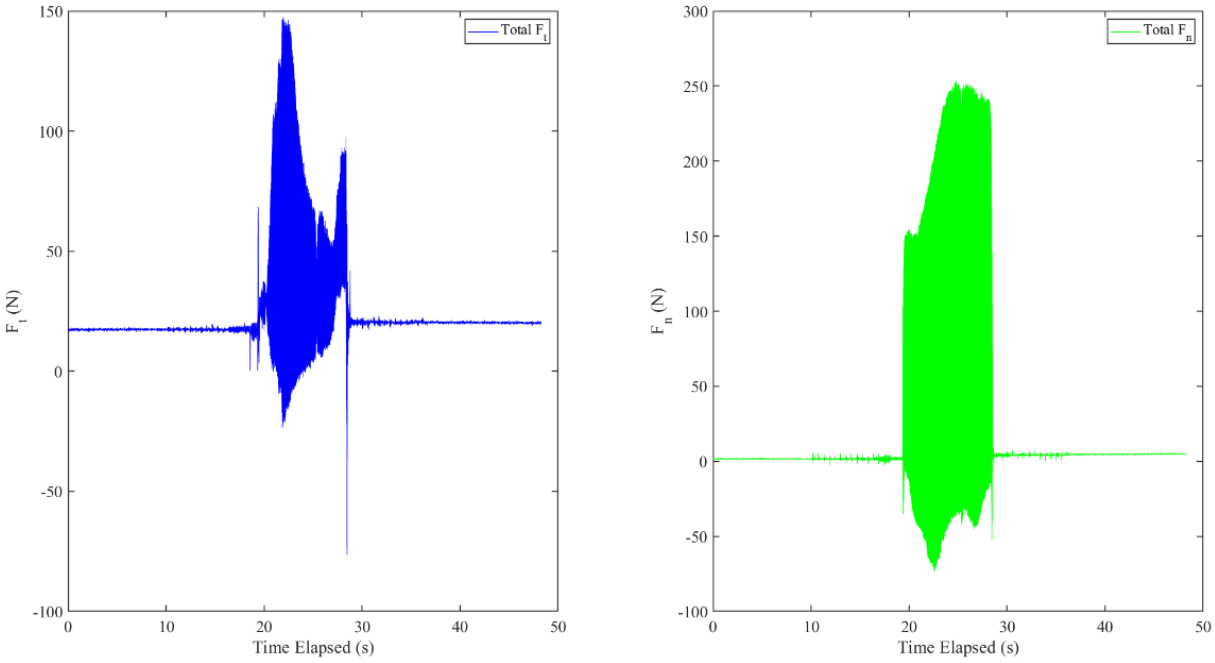

Figure 136: The component grinding forces F_t and F_n recorded during fourth grinding pass '3000-2-0.025-Pass 4'

4.3.3.3 Post-Grind Workpiece Surface Analysis

The condition of the rail facets which were ground at 2000 rpm and 3000 rpm can be observed in Figure 137. With Region A indicating the start of the grind and Region C depicting the end of the grinding pass, visual observation of the rail facets show that the condition of the rail is uniform

across the grinding facet of the section ground at 2000 rpm. Grinding burn, which is signified by the darkening of the ground surface is observed on the facet ground at 3000 rpm. Based on the classification by Lin et al. [35], the grinding burn observed in the fact ground at 3000 rpm is classified as yellow-blue. It is also observed that the grinding burn appears to gradually increase from the start (Region A) to end (Region C) of the grind.

Figure 137: Condition of rail facets subsequent to rail grinding passes at 2000 rpm and 3000 rpm.

4.3.3.4 Surface Roughness Analysis

The post-grind surface roughness of the rail samples after the grinding at 2000 rpm and 3000 rpm are presented. The regions from which the surface roughness measurements were obtained are presented in Figure 138. These measurements were obtained from three different regions A, B, C across the rail, which correspond to the start of grind (as the peripheral wheel begins its cutting action on the rail head), the stable grinding period and the end of grind (where the wheel exits the rail head) respectively.

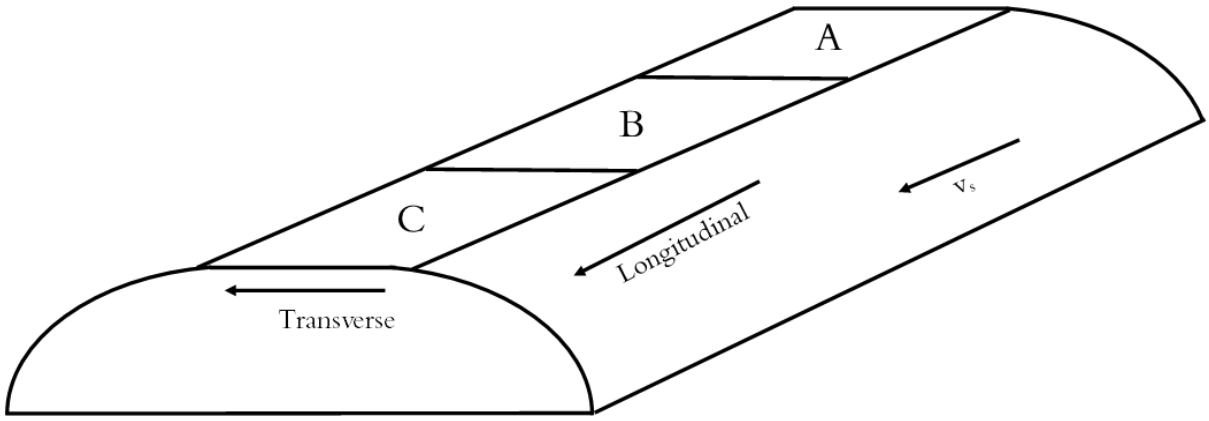

Figure 138: Designated regions of surface roughness measurements across the rail section subsequent to Peripheral Grinding

For the passes conducted at 2000 rpm, the transverse roughness values which were measured across the length of the rail from the start (A) to end of the grinding pass (C) were 1.1 µm, 1.05 µm and 1.15 µm respectively, while the transverse roughness values for the passes conducted at 3000 rpm were 0.98 µm, 1.02 µm and 0.99 µm from the start (A) to the end of pass (C) respectively. The surface roughness values measured appear to be up to double the average surface roughness values measured in the face grinding orientation; however, the roughness values measured following the peripheral grinding passes show lesser variance in the results. The surface roughness measurements obtained from the regions A, B and C on the rail head after the grinding pass at 2000 rpm are presented in Figure 139.

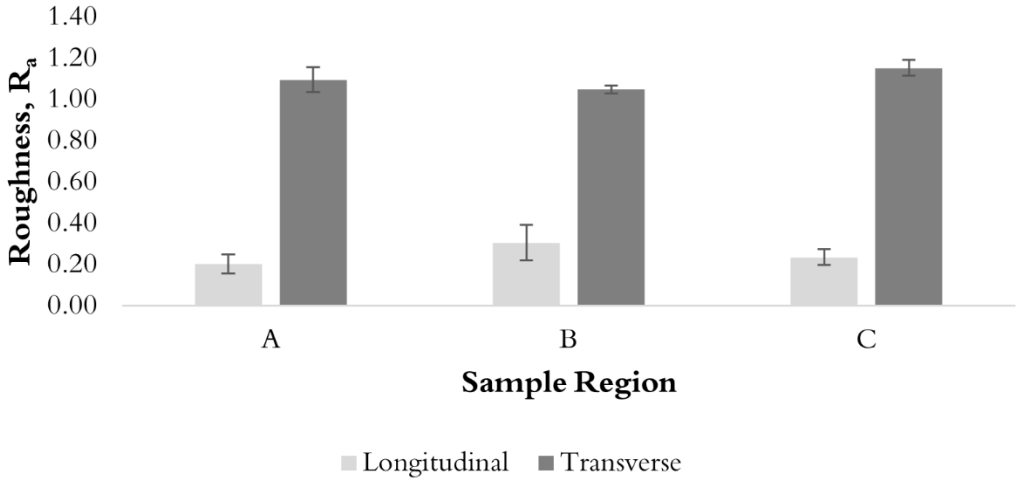

Figure 139: Surface roughness of rail surface subject to peripheral grinding at 2000 rpm

The surface roughness readings obtained from the regions A, B and C on the rail head following grinding at 3000 rpm are shown in Figure 140.

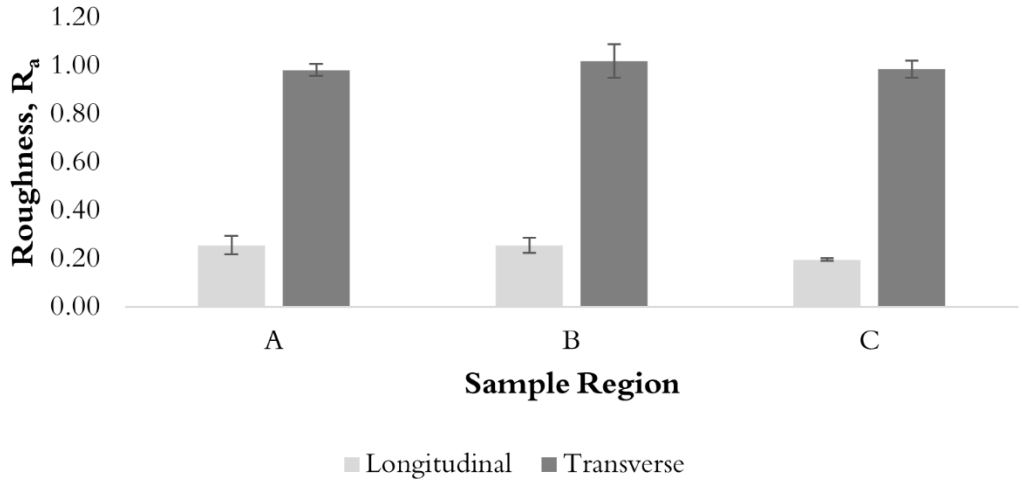

Figure 140: Surface roughness of rail surface subject to peripheral grinding at 3000 rpm

4.4 Discussion of Results

The results for the performed grinding trials have indicated that there is a decrease in the measured temperature when grinding is changed from superabrasive grinding to conventional grinding. The lack of data has led to comparisons not being possible between the same form of grinding temperature measurement across all tests. Temperature measurement was performed using thermocouples and the thermal camera in the superabrasive grinding trial, but due to the insufficient placement of thermocouples, the only comparison that can be made is with the temperature measurements of the HSS-HFR tests.

However, in the conventional face grinding trials, temperature measurement was done solely by the thermal camera while both thermocouple embedment and thermal camera equipment were utilised in the conventional peripheral grinding. As such, while it is not possible to make a direct

comparison between them, it is clear that all the three temperature measurement methods are able to provide valuable information about the grinding behaviour, most especially with respect to the progression of grinding passes.

The identified colours of the burn are also related to excessiveness of the temperatures induced, as more oxidations occur with increasing temperature. A significantly higher amount of grinding burn is observed on the surfaces ground at higher wheel speeds. This is common in both types of conventional grinding operations and is attributed to the higher grinding temperatures which have occurred at the higher wheel speeds.

Analysis of the surface quality has shown that though the temperature values measured by the measurement apparatus may be low, surface grinding burn and WEL can still occur in the ground surface. This is because the measured temperatures may not have been entirely representative of the extent of grinding burn which occurred on the conventionally ground rail materials. Based on the grinding burn classifications presented by Lin et al. [35], the apparent grinding burn which was observed on the surfaces of the conventionally ground samples indicate that the grinding temperatures may have exceeded 735 °C in the face ground material and may have been between 600 – 735 °C in the peripheral ground material. Likewise, the presence and thicknesses of WEL which were observed in the conventional face grinding samples is further indication of temperatures in excess of 600 °C.

The transverse surface roughness has been shown to be consistently higher than the longitudinal readings. The conventionally ground samples have also indicated lower surface roughness values than the superabrasive grinding samples, but all values have remained within what is acceptable in the rail industry.

The experiments conducted have shown that the in-situ observation of the temperature progressions through any these measurement media may provide insight for the operator about the related grinding parameters to avoid detriment to the surface quality.

4.5 Summary

Laboratory experiments have been conducted to implement thermocouple embedment, thermography and force measurements for the grinding of rail samples within a CNC machine. Through superabrasive and conventional face and peripheral grinding, these methods of temperature measurement have been established as viable; however further testing may be required in order to make more direct comparisons at different parameter combinations for the same type grinding trial.

5 Trolley Based Grinding

As established in the literature review, the optimal use of superabrasive wheels lies within the High Speed Grinding (HSG) practice, wherein high wheel speeds are employed. For the superabrasive grinding wheel, assessment of the chip thickness as shown in Equation 1 depicts the effectiveness of chip removal at high wheel speeds. The maximum undeformed chip thickness decreases with increasing wheel speed. On a local level, this is due to the reduced grinding width of the grain which minimises the ploughing action and increases the sharpness of the grain. This in turn reduces the grinding force as well as the radial wheel wear in typical peripheral grinding operations, which also leads to the reduction of roughness of the ground rail [86, 35].

Findings in the study by Singleton et al. [4] showed a potential for improved productivity and tool life in rail grinding. Subsequently, trials were conducted to develop a superabrasive tool which is sufficient for use the face grinding orientation. Other findings from this study showed the susceptibility of superabrasive grains to wheel loading under dry grinding conditions, where adhesion of the workpiece material occurred in the pores which encompassed the grains. Therefore, a declogging mechanism was developed to mitigate the wheel loading which can occur in the use of superabrasive grinding on the rail.

From the grinding observation exercises which were introduced in Chapter 2, it was determined that the grinding trolley to be developed be a palletised module which could possibly be installed for use on the C21 grinding train in the future. Likewise, it was paramount that the auxiliary requirements including power and the declogging mechanism be localised in the single unit of the trolley.

The grinding trolley was designed to not just simulate the interactions between the grinding wheel and the rail but to perform rail grinding on an actual full size test track. For this purpose, a 10 m full size track panel was obtained to enable grinding trials to be conducted within the location of the trolley development. The constructed track panel can be observed in Figure 141. An enclosure was constructed around the track panel in accordance with health and safety guidance. The access to a test track allowed a controlled test environment and ensured easier access to the ground rail for post-test analysis. This is further discussed in the Health and Safety Considerations in Section 5.5.

Figure 141: The track panel set-up developed for the use of the grinding trolley.

5.1 Design Requirements

Following the initial assessment of the face (MV3) and peripheral (MC3) grinding trolleys which were discussed in Chapter 3, it was determined that in order to utilise superabrasive grinding tool with either trolley, a more robust system was required. To achieve the wheel speeds required to for superabrasive grinding, a spindle drive with higher rotational speed capacity would be required. The superabrasive grinding tool would require rotational speeds of over 9000 rpm.

In addition, it was determined that the energy required to operate the superabrasive should be less than or similar to the energy required to operate the conventional grinding stones which are rotated at 3000 rpm on the grinding train. For this reason, the weight of the superabrasive grinding tool was considered.

Likewise, in order to achieve this requirement, it was essential that the machine body be robust enough to support the weight of the required spindle as well as any auxiliary equipment (e.g., declogging) that may be required.

5.2 Spindle Motor

A spindle drive was selected based on a requirement for interchangeable use with both superabrasive and conventional grinding tools. In addition, it was essential that the achievable rotational speed of the spindle drive be sufficient to achieve superabrasive grinding. As such, a

commercially available GMN Paul Müller Industrie GmbH & Co. spindle was purchased. The manufacturer specifications for this spindle drive are detailed in Table 19.

Table 19: Manufacturer specification of spindle motor utilised in Grinding Trolley

Specification	Value
Maximum achievable spindle speed (RPM)	16,000
Available Torque (Nm)	29.4
Current (A)	93
Spindle Designation	HCS 230g - 16000/18|HSK-A63

Further calibration of the spindle has been performed and configured to the National instruments remotely controlled CompactRIO software to restrict the spindle to an initial spindle speed of 6000 rpm for the initial grinding tests with conventional wheels.

5.3 Trolley Design

Images of the trolley indicating the primary components are presented in Figure 142 and Figure 143.The grinding trolley consists of the grinding stone spindle, a spindle drive motor and a hydraulic control system. The spindle drive and positioning actuators are connected by valves within a hydraulic circuit to the hydraulic motor with which its angle of rotation across the rail head is controlled.

For the safe operation of the spindle and deployment of the wheel, a pressure vessel is connected to the "port" for tool clamping. The pump is interlocked to alternatively lock the hydraulics when the spindle is in operation and to disconnect the spindle electronics and engage the hydraulics during a tool change sequence.

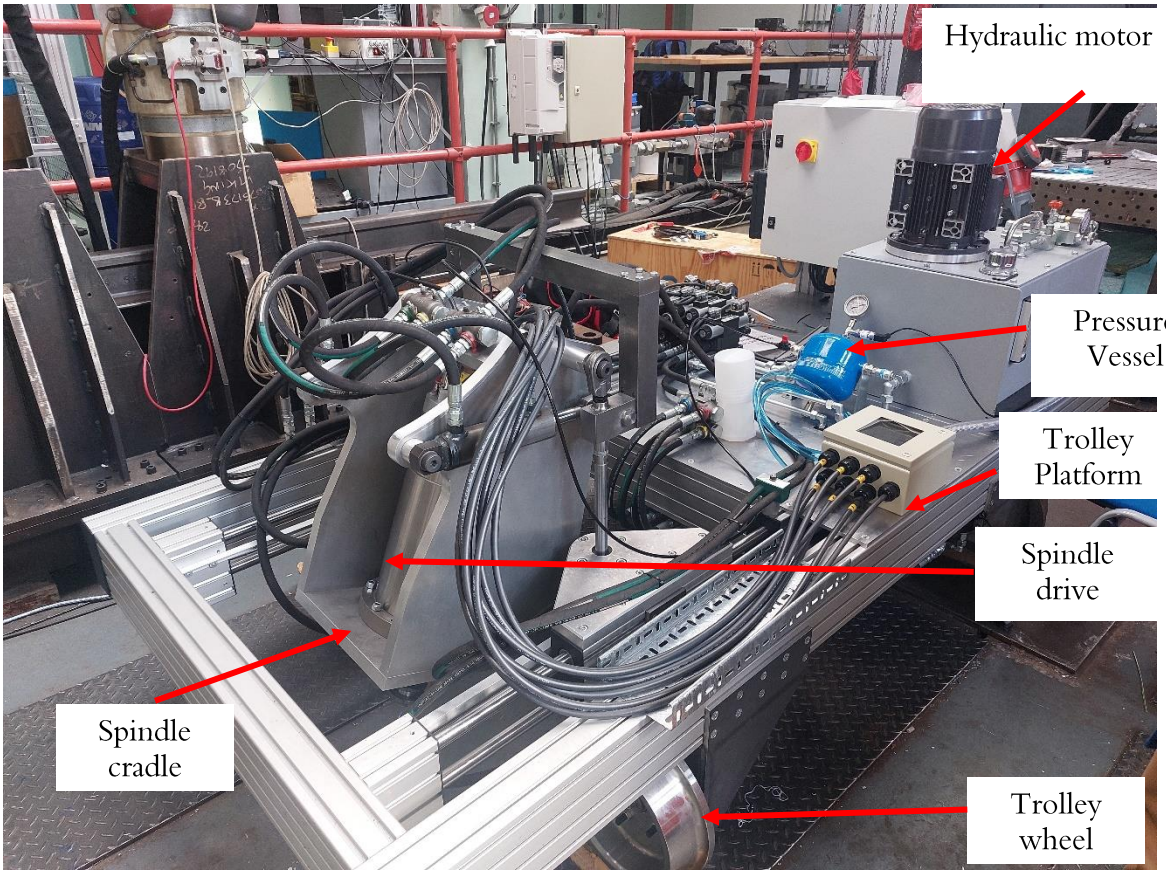

Figure 142: Image of the grinding trolley and some of its primary components for the performance of grinding operations

Figure 143: A close-up image of the spindle arbour and connected spindle drive

5.4 Grinding Wheel Design

In the initial commissioning of the trolley, the conventional AlO_x grinding wheels (MV3 and MC3) which have been introduced in Chapter 4 will be utilised. This will provide a benchmark

against the superabrasive grinding to be subsequently performed with the trolley. The bespoke grinding wheel produced for use with the grinding trolley is shown Figure 144. The grinding wheel designed by Tyrolit is a tapered wheel which is capable of both face and peripheral grinding orientations. This improves the efficiency of the wheel and ensures that the same wheel can be used when the grinder head is adjusted. The designated fixture used to attach the wheel to the spindle drive were two clockwise and anti-clockwise HSK63A arbours whose usage is dependent on the direction of rotation required.

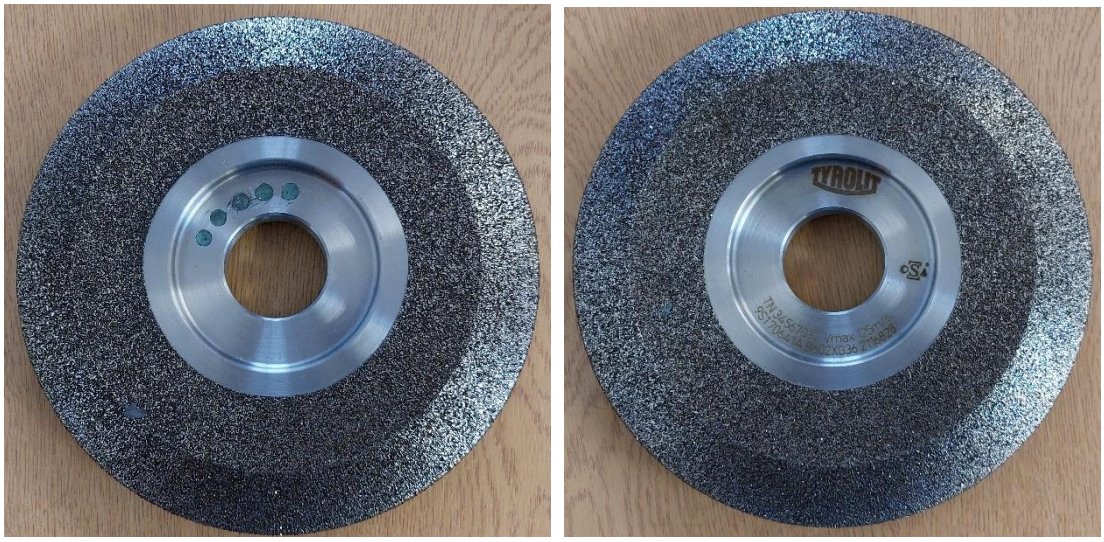

Figure 144: Bespoke grinding wheel designed by Tyrolit for the Grinding Trolley

5.5 Health and Safety Considerations

To enable the commissioning of the grinding trolley for testing, the following categories of considerations were observed.

1) Track Panel Enclosure:

   The track panel enclosure was comprised of gabion cages filled with ballast material as well as sleepers on both sides. The wooden sleepers were included as the initial barrier for possible high velocity material which may be expelled during the grinding process. Additionally, the sleepers could aid in absorbing potential noise during the grinding operation.

2) Spindle Operation:

   The National Instruments CompactRIO software has been programmed for the remote operation of the spindle. The remote operation of the trolley was configured to enact a safe start-up and spindown sequence of the spindle remotely from a distance from the track panel enclosure.

3) Lifting Plan:

   A bespoke lifting beam was designed and manufactured to safely lift the grinding trolley from its storage location to and from the track panel and onto rail in the field

environment in the future. The designed beam is also comprised of four lifting plates which will be attached to two parallel platform edges of the trolley. An image of the lifting beam is presented in Figure 145.

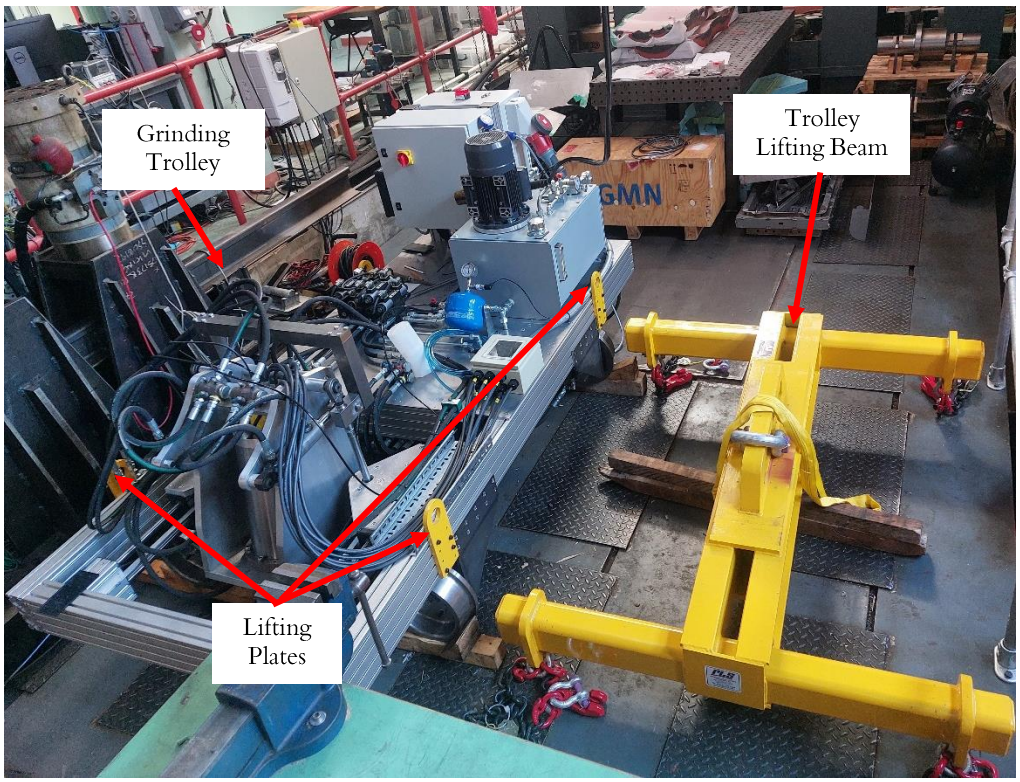

Figure 145: Image of the grinding trolley and the lifting beam fixture

5.6 Proposed Test Method

The trolley would be employed to perform both conventional and superabrasive grinding. Across the rail profile, two sets of grinding trials will be carried out with one side of the rail being used to perform superabrasive grinding and the other for the conventional grinding trials. Within each segment, the two grinding orientations of face and peripheral grinding will be employed. Face grinding will be performed on the rail crown while peripheral grinding can be performed on the facets close to the rail gauge. The propose testing orientations are depicted in Figure 146.

Following the grinding trials, sections will be extracted from the ground rail for surface integrity analyses. These include surface roughness measurements and metallographic evaluation. To perform metallographic analysis, samples will be sectioned, mounted and polished for optical and scanning electron microscopy. In addition, if the length of rail is fully utilised, the rail may be replaced for further tests.

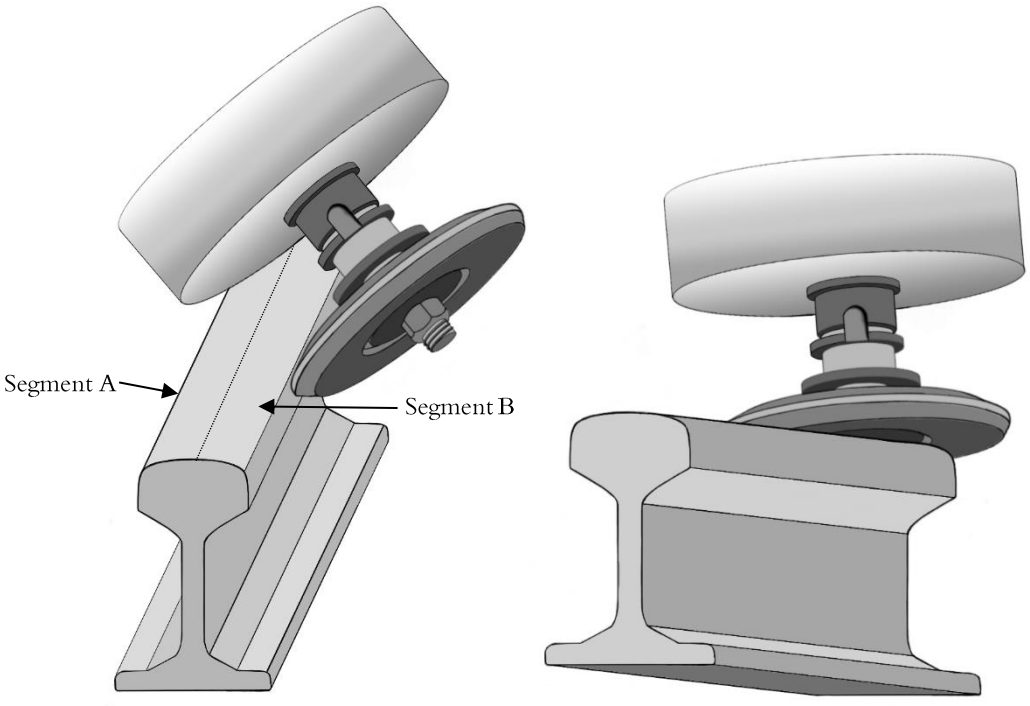

Figure 146: The peripheral and face grinding orientations of the wheel and spindle during the rail grinding trials

The use of the trolley presents economic benefits based on the increased material removal rate which can be realised through the use of superabrasive grinding. Likewise, the grinding trolley provides an avenue for the adoption of superabrasive grinding for material removal on harder rail and different rail grades in or out of service. Further areas of opportunity of the grinding trolley are as an attachment for a road rail vehicle for local grinding, where affected track regions are not easily accessible by the larger grinders (trains).

6 Discussion of Findings

6.1 Post-Grind Workpiece Surface Integrity of Superabrasive Grinding

The pearlite microstructure of the rail material can be observed in the optical micrographs of the longitudinal cross-section of the rail. On the top surface of the rail, a transformed microstructure can be observed and determined as the White Etching Layer (WEL). The WEL is identified as a white-appearing martensitic layer which was resistant to the chemical immersion etching which was carried out to reveal the microstructure of the rail samples. During the grinding process, the rail material undergoes an austenitic phase transformation from the pearlitic matrix microstructure into martensite as a result of the rapid cooling (quenching) from the high temperatures generated in the process.

The passes which were made at low feed rates exhibit lower thicknesses of WEL (2.36 μm, 2.21 μm) when compared to the thickness of the passes conducted at high feed rate (9.67 μm, 4.4 μm). This indicates an increase in the cutting forces and grinding temperature which induces larger WEL. This contradicts what is expected based on the literature which purports that higher feed rates would result in reduced thermal effects due to quicker chip thickness formation and reduced abrasive grain interaction at one time. However, when considering the spindle speeds at passes conducted at the same feed rate, it can then be surmised that largest amount of WEL is generated at lower spindle speeds as the larger grinding forces which are induced with higher engagement of the active abrasive grains with the rail workpiece material at lower wheel speeds.

The WEL thicknesses values generated by the superabrasive grinding tests signify lower thicknesses of one two orders of magnitude when compared to the typical WEL thicknesses of up to 50 μm which have been reported following the grinding of similar rail grades using conventional wheels [87, 22, 88, 80]. The WEL which were observed on the top surfaces of the samples ground using the superabrasive grinding were non-continuous across the running surface. As reported by Mesaritis et al. [89], the discontinuous pockets of WEL on the top surface are also likely to be delaminated during further run-in passes without solely contributing to detrimental effects such defects or poorer surface quality.

In the micrographs presented for all superabrasive grinding conditions (Figure 82, Figure 83, Figure 84, Figure 85), the absence of plastic deformation is also observed. By their intact appearance, it is surmised that the pearlitic microstructure beneath the WEL was largely unaffected during the grinding operation and was not significantly mechanically deformed. This is a consequence of the comparably reduced forces generated during the superabrasive grinding passes. However, to further confirm the absence of plastic deformation, the interface between the WEL and the bulk material may be assessed through SEM.

The range of surface roughness values (2.43 – 3.10 μm) which were observed following the various conditions using superabrasive grinding (Figure 81) are lower than has been reported in the

literature for conventional grinding of similar rail grades, such as Zhang et al. [16] who simulated transverse roughness values of up to 6 μm in the first pass and over 4 μm in a third grinding pass and recorded longitudinal roughness values of up to 14 μm in experiments.

With samples with the constant feed rate and varied spindle speed, it is observed that the transverse roughness values are nearly comparable (LFR: 2.43 μm and 2.68 μm; HFR: 3.21 μm and 3.10 μm). However, with varied feed rate and constant spindle speed, it is observed that the passes conducted at high spindle speed generate noticeably higher surface roughness values. The feed rate appears to have greater influence on the roughness values than the spindle speed for the superabrasive ground rail. Based on the chip thickness equation in Equation 1, this may be attributed to the increased speed ratio v_s/v_w, which causes an increase in the chip thickness thus causing higher roughness values.

6.2 Post-Grind Workpiece Surface Integrity in Conventional Face Grinding

In this section, the conditions of the surface integrity factors pertaining to the face grinding operations are discussed. These factors include the surface finish (through surface roughness) and the surface metallurgy.

The observed surface conditions of the rail heads shown in Figure 109 and Figure 110 are indicative of the presence of grinding burn at the two grinding conditions performed on the rail at 2000 rpm and 3000 rpm. This grinding burn is characterised by an oxidised layer which causes the discolouration of the rail surface due to the induced high grinding temperatures. The images show a gradual increase in the appearance of grinding burn from the start to the end of the grind. This is attributed to the build-up of thermal energy on the grinding wheel as it is traversed across the railhead. Likewise, the grinding temperatures will increase with the increasing grinding force across the grind [73]. Additionally, the range of burn colours observed on the railhead from normal to yellow and blue burn are consistent with increasing temperatures across the railhead.

Visual observations show that grinding burn is higher on the surface which was ground at 3000 rpm than in the sample ground at 2000 rpm. A likely cause of this is the reduced aggression factor which occurs at higher wheel speeds. The presence of grinding burn on the surface ground are attributed to the aggression of the grinding operations and correlates with the loaded grinding wheel conditions observed. A reduced aggression factor can increase the propensity for dulled grains on the grinding wheel.

When compared to the feed rates of typical rail grinding on trains which were conducted in a range of 3-15 km/h (50,000 – 250,000 mm/min), the laboratory face grinding trials were conducted at comparably slower feed rates (2000 mm/min). The slower feed rates are likely to cause more frictional interaction between the rail surface and the grinding wheel. This interaction will therefore induce high temperature which will generate the consistent band of WEL across the railhead.

Previous studies such as that of Zhou et al [80] have also established a link between the appearance of surface burn, WEL and the induced grinding temperature. Their study showed that along with increasing burn, the increase of the normal grinding force and the wheel speed can also lead to an increase in the thickness of the WEL. Though the WEL thicknesses were observed in the cross-section after the surface was ground at 2000 rpm, it is difficult to make a direct comparison against the WEL thicknesses reported in the literature for similar wheel speeds as the influences of the 2000 rpm nor the 3000 rpm were impossible to distinguish in this study. However, the measured forces may provide an insight into the formation of the WEL in the Section 6.4.

The WEL observed in the longitudinal and transverse cross-sections of the rail are consistent with the features expected by the reduced feed rates at which the face grinding trial was carried out. The temperatures generated by the friction interaction of the grinding wheel and the rail surface thereby resulting in thermal softening of the rail surface. Rapid cooling of this softened layer caused the formation of a rehardened WEL on the top surface. A heat-affected zone (HAZ) is also observed in the optical micrographs of the longitudinal sample. The sublayer which is observed in the longitudinal samples appear to be Brown Etching Layer (BEL), a feature which has not been widely reported but has been identified by Newcomb and Stobbs [90] and investigated by Li et al. [91], who proposed that this sublayer may have been generated due to plastic deformation and shear-induced ferritic dislocations. This BEL is characterised by distinct interfaces to the WEL and the bulk matrix. This layer may constitute a layer which did not undergo the full martensitic transformation which began at the top layer; however, further analysis through depth profile nano-indentation and Transmission Electron Microscopy (TEM) may be required to adequately characterise this layer.

The range of transverse surface roughness values (0.21 – 0.57 μm) which have been reported in Figure 108 for the rail sample machined by conventional face grinding proved contrary to the higher surface roughnesses expected based on findings in the same literature as mentioned in the previous section. Based on the study by Zhi et al. [92], the low surface roughness values are a likely consequence of the smoother surface generated by the increased local interactions of the abrasive grits on the surface of the rail workpiece as a result of the reduced feed rates which were employed in this study. Furthermore, these increased interactions of the grits are likely to lead to higher induced temperatures, which cause thermal softening and in turn exacerbate the adherence of the softened material onto the wheel surface. In addition, the increasing surface roughness values from the beginning of the pass to the end of the pass are also a likely indication of the interaction of the surface of the grinding wheel at the start of the pass where it has not achieved the full depth of cut compared to the end of grind, where the full depth of cut has been reached.

6.3 Post-Grind Workpiece Surface Integrity in Conventional Peripheral Grinding

At a constant feed rate, two grinding facets were machined using the conventional peripheral grinding tool at 2000 rpm and 3000 rpm. As discussed in the previous section, grinding burn manifests on a ground surface when a certain temperature threshold has been exceeded during the grinding pass. Therefore, the observed surface conditions of the rail head facets shown in Figure 137 provide an indication of the amount of grinding burn which may have occurred during the passes conducted at 2000 rpm and 3000 rpm. By virtue of the visibly unburnt (and normal colouring) surface which was observed on the facet ground at 2000 rpm, it can be deduced that the sample did not undergo grinding burn after four passes.

Adversely, yellow to blue grinding burn can be observed on the rail head sample which was ground at 3000 rpm. With respect to the rail grinding burn patterns presented by Li et al. [35], it has been determined that the grinding temperatures of between 600 – 735 °C may have caused the grinding burn behaviour which were observed on the ground surface of the facet ground at 3000 rpm. In addition, on the surface ground at 3000 rpm, it is observed that the grinding burn becomes more apparent from the start of the grinding pass (Region A) to the end of the grinding pass (Region C).

This phenomenon of increasing grinding burn from the start of pass to end is similar to what was observed in the samples which were ground in the face grinding orientation. However, the magnitude of visible grinding burn which is observed in the peripherally ground samples are noticeably lower than those ground in the face grinding orientation. This is because the grinding contact area of peripheral grinding orientation is smaller (grinding wheel width of 40 mm) when compared to that of face grinding (maximum available contact width of 128 mm). In accordance with Equation 7, the grinding temperature induced on the workpiece is expected to increase with larger grinding lengths; therefore, it can be deduced that the presence of grinding burn would be of higher intensity in the rail samples on which face grinding was performed.

6.4 Force & Temperature Analysis – Face Grinding

The maximum forces recorded for the passes generated using the face grinding orientation are shown in Figure 98. For both sets of grinding passes which were performed at 2000 rpm and 3000 rpm, the recorded forces show an upward trend and tend to increase with the increasing number of passes. The continual increase of the grinding forces is likely due to the increase in worn abrasive grits. Based on the work by Zhou et al. [80], it is also expected that an increase in the normal grinding force would increase the induced face grinding temperatures. Likewise, as expected, the dominant force which acted on the grinding area was the normal force, as the maximum normal grinding forces were observed to be higher than the tangential grinding forces. This is largely attributed to the weight of the grinding wheel which acts downward onto the rail workpiece surface.

Figure 98 also shows that the normal grinding force monotonically increases with each consecutive pass in the face grinding trials, while fluctuation is more characteristic of the tangential forces per pass.

With respect to the individual force progression plots which are presented in section 4.3.2.2, it is observed that the maximum tangential grinding forces occur when the grinding action commences at the start of the pass and the tangential forces progress from a negative value and climbs to a positive by the end of the grinding pass.

Prior to the initiation of the grinding action for each pass, the rotating grinding wheel is stepped down from an initial position which corresponds to the surface of the rail to the assigned depth of cut. Therefore, the high tangential grinding forces which are observed at the start of the force plot for each grinding pass corresponds to the initial resistance of the edge of the rail workpiece to the run-in action of the leading edge of the face grinding wheel. This effect of reaction to grinding wheel run-in which was observed in the tangential force progression plots was not a prominent occurrence with the normal grinding forces. In the field applications such as the grinding train, the Road/Rail vehicle as well as the grinding trolley, the mechanism of introducing the grinding wheel to run-in and run-out involves dropping the grinding wheel onto the railhead; therefore, the observed effect of a sudden increase in the tangential force at a grinding pass is unlikely to occur.

In addressing the force progression beyond the run-in effect, it can also be observed that the force signals presented for the grinding passes conducted at 2000 rpm and 3000 rpm become noisier with the increasing number of grinding passes. Likewise, for both sets of grinding passes, it is observed that the normal grinding force F_n rapidly increases to a maximum and followed by a rapid decrease to the threshold minimum at the end of the grinding pass.

The increase in the grinding forces as the number of passes increase is indicative of increased thermal input onto the surface. As shown in Equations 4, 6 and 7, the increase in the normal grinding force increases the local normal force acting on the abrasive grain and increasing the area of interaction between the grain and the workpiece material. Additionally, the increasing grinding forces will exacerbate the occurrence of wheel wear by loading, which occurs when the softened workpiece material begins to adhere to the exposed abrasive grits of the grinding wheel. Continuous wheel loading increases with increasing normal grinding force [93]. This is evidenced by the post-grind condition of the loaded grinding wheel presented in Figure 114 and Figure 115.

During the face grinding trials which were conducted, only the thermal camera could be implemented to capture information about the grinding temperature. The maximum temperature progression which is shown in Figure 86 indicates that the grinding temperature generally increases with each additional pass conducted at 2000 rpm and 3000 rpm. As the maximum grinding force plot presented in Figure 98 indicated that the grinding forces recorded for the passes carried out at 3000 rpm were higher than those for passes conducted at 2000 rpm, it was expected that the

recorded temperature behaviour would be mirrored. However, Figure 86 shows that with the exception of the final pass (Pass 4), higher temperatures were recorded for the first three passes conducted at 2000 rpm. While there is a chance that the thermal camera may have contributed to this deviation from the force-temperature relationship, the cause of this may be deduced through further grinding tests with increased number of passes.

6.5 Force & Temperature Analysis – Peripheral Grinding

When the grinding wheel comes in contact with the rail surface, the grinding forces increase. As with the first pass, the largest forces peaks are recorded at the start of the pass. In the passes conducted at both 2000 rpm and 3000 rpm, the maximum tangential grinding force F_t is achieved within the first 5 seconds of the grind. The normal grinding force is an important process parameter which is controlled in grinding with typical rail grinders. However, this not the case with manually operated grinding trolleys. Therefore, it is essential to understand the force behaviour which is observed when grinding with the wheels used on these machines.

The normal grinding forces F_n (downward pressure) observed in both sets of passes at 2000 rpm and 3000 rpm increase up to maxima and then decrease till the end of the pass. Likewise, for most passes, the normal force presents a noisy signal at the start of the grind, with the noise reducing as the pass progresses. This is likely due to the activity of the abrasive grains as they are rapidly subjected to smearing of the workpiece material, thus supressing their cutting action.

Likewise, the increase in the normal force up the maxima is attributed to the reduced action of the abrasive grains as they are loaded. The loaded abrasive grains will cause a ploughing action, which in turn further increases the normal grinding force. From the achieved maxima, it is observed that the normal grinding forces decrease till the end of grind. This is due to the exposure of new cutting grains on the active grinding surface. With freshly exposed grits, the grinding action generates more chip formation which in turn causes a reduction in the grinding force. With each new pass, the same phenomenon is observed to continue with an increased maximum normal force per pass.

As is typical with field grinding applications, a grinding force (also known as 'grinding pressure') is applied to achieve a desired depth of cut. However, the results indicate a variation in the force behaviour as the grinding pass progresses. The short span of time in which the grinding force varies is sufficient to adversely influence the metallographic surface integrity of the rail surface.

A further comparison can be made of the maximum force values recorded for the passes performed in the face grinding and the peripheral grinding orientation which were presented in Figure 98 and Figure 128 . For example, in the face grinding trials, the maximum recorded tangential and normal grinding forces in the fourth pass at 2000 rpm were 342.5 N and 692.3 N respectively and the maximum recorded tangential and normal grinding forces in the fourth pass at 3000 rpm were 425.2 N and 1230.7 N respectively. On the other hand, in the peripheral grinding trials, the maximum recorded tangential and normal grinding forces in the fourth pass at 2000 rpm

were 124.5 N and 212.9 N respectively, while the maximum recorded tangential and normal grinding forces in the fourth pass at 3000 rpm were 147.4 N and 253.4 N respectively. This indicates that the grinding forces observed in the conventional peripheral grinding orientation are consistently lower per pass than those recorded in the conventional face grinding orientation. Therefore, the reduced forces observed in the peripheral grinding orientation presents a promising basis for the proposed application with the superabrasive tooling.

The temperature measurements for the peripheral grinding passes conducted at 2000 rpm and 3000 rpm were performed using a thermal camera and thermocouples which were embedded at various depths between 0.55 – 1.5 mm. To compare the induced grinding temperatures during the same grinding conditions, the measurements captured by the thermal camera and the array of thermocouples have been presented in Figure 116. The maximum temperature per pass recorded by the thermal camera were found to be higher than the than those recorded by the thermocouples.

While the thermocouple readings of the temperatures progression across passes indicate a slight rise in the grinding temperatures per pass with the passes conducted at 2000 rpm, a distinct rise is observed in the recorded temperature per pass of passes conducted at 3000 rpm. On the other hand, it is difficult to establish a similar pattern with the thermal camera's measurements during both sets of passes which were conducted at 2000 rpm and 3000 rpm respectively.

However, the temperatures recorded by both measurement apparatuses in the passes ground at 2000 rpm are also shown to be lower than the temperatures measured during passes performed at 3000 rpm. This pattern is similar to the progression of the grinding forces, where higher grinding forces were observed in the passes conducted at higher wheel speeds.

Comparison to the thermal camera measurements indicate that the range of temperatures measured in conventional peripheral grinding (41.9 – 104.3 °C at 2000 rpm and 46.2 – 136.7 °C at 3000 rpm) are lower than the range of temperatures measured during the face grinding trials (40.2 – 193.5 °C at 2000 rpm and 37.0 – 275 °C at 3000 rpm). This is likely due to the larger contact area of the face grinding wheel compared to the peripheral grinding wheel. A larger contact area increases the number of active grits on the on the rail surface; however, this increases the susceptibility to increased temperatures as the grits are worn in the grinding operation.

It is noted that the thermal camera measured the temperature of the surface and followed the grinding wheel contact. On the other hand, the thermocouples provided an internal measurement of the subsurface (at least 0.55 mm from the surface). Therefore, while the temperatures recorded by both measurement apparatuses may differ in magnitude, it is understood that both sets of measurements provide a picture of the temperature behaviour during the grinding pass.

Upon individual exploration of the thermocouple readings in a single pass, it was observed that the deepest thermocouple (T8) appeared to attain the highest temperatures in most grinding passes, while the thermocouple closest to the surface recorded the lowest temperature values. It appears

that though magnitudes recorded were lower than were expected in the conventional grinding passes, this pattern was also common with the measurements conducted during the superabrasive grinding trial which was performed in the peripheral orientation.

A possible reason for the low measurements obtained by the thermocouple which was closest to the surface is the immediate loss of heat which occurs at the rail surface which is in contact with air. The thermal energy is lost quicker to convection and radiation than it is conducted into the thermocouple. In a study which considered grinding passes conducted at various wheel speeds which ranged from 2000 – 4000 rpm, the simulations carried out by Zhou et al. [80] showed that the grinding temperature is attenuated from high grinding temperatures to ambient by the depth of 2 mm from the rail surface. Therefore, the inducement of grinding temperatures can still be observed at the depths the thermocouples were embedded. Likewise, while the embedded thermocouples are able to make noticeable readings, a large amount of the induced thermal energy may have been lost on the rail surface.

Where the thermal camera has been used to obtain information about the induced temperature on the rail surface, and the embedded thermocouples have provided information on the temperatures induced in the rail's subsurface, both sets of readings are different but may be utilised to obtain a better picture of the grinding behaviour with respect to temperature. Furthermore, the temperatures measured at various depths from the railhead surface may also be applied in combination with the recorded surface temperatures for use within analytical temperature models and extrapolated to elucidate on the temperature information which was lost between the surface and the topmost thermocouple embedded at 0.55 mm.

6.6 Temperature Measurement in the Field Observations

The temperature measurements which were carried out in the field observations have been primarily discussed within the chapter. The highest grinding temperature (> 180 °C) measured during a grinding pass was at the Drax facility, where the camera was held by hand. This value was captured behind the Road/Rail Vehicle.

The plots generated from both the Metro dé Medellin (Figure 35 – Figure 37) and the Drax Grinding Trials (Figure 49 – Figure 51) show that a maximum temperature reading can be achieved when a reading is taken at a specific location on the rail as the grinder moves along that point. The difference in temperatures measured in the laboratory and the field may be due to better control of the environment and the lower distance of the measurement equipment to the grinding interface in the laboratory. It is also likely that the higher temperatures would have been recorded in less exposed environments.

The range of temperatures measured in several passes conducted in the Metro dé Medellín grinding trial was limited by the capabilities of the thermal camera, as the thermal camera readings indicated that there were likely temperatures which had exceeded 130 °C. The range of maximum

temperatures measured in the field trials (39.5 - 130°C, Metro de Medellin; 48 – 181 °C, Drax) fall within the ranges of temperatures measured during the conventional face grinding trials in the laboratory (40.2 – 193.5 °C at 2000 rpm and 37.0 °C – 275 °C at 3000 rpm).

Factors such as the high humidity may have impeded the infrared radiation and attenuated the signal from the object of view to the thermal camera. Likewise, the measurements taken may have been hampered by the rain which occurred throughout the grinding campaign, which may have limited the effectiveness of the thermal camera as a result of light scattering on rain droplets.

In addition, the accuracy of the camera may be affected by the motion of the grinding train. As the camera position was not fixed, the software of the camera may be unable to provide an exact temperature reading. Therefore, it is recommended that the thermal camera position be fixed for possible field temperature measurements in the future.

Another challenge for the utilisation of the handheld thermal camera was the standardisation across the various passes. A solution would be for the operator to be located at a measured distance for all tests; however, this has to be within the safe standing distance as stipulated by the health and safety guidance.

With both the grinding train and the Road/Rail grinder, side curtains were utilised to prevent grinding sparks from being emitted away from the immediate grinding area. These side curtains are surmised to have contributed to the possible attenuation of the recorded temperatures and increased the difficulty of measurement approach.

During the observations at the Drax facility, it was noted that a viewing window was present beneath the cabin of the Road/Rail Grinder. Due to the proprietary nature of the grinding equipment, it was impossible to view and assess the window. However, it is recommended that for a few grinding passes, the thermal camera be mounted and fixed such that it is directed toward the grinding zone. For a small section of the viewing window, an optical material such Zinc Sulphide (ZnS) ceramic may be utilised for thermal imaging.

6.7 Model of the Grinding Temperature

This section pertains to the results obtained through the analytical modelling of the grinding temperature with respect to the depth from the surface. Based on the equations presented in Section 2.6, MATLAB software was used to predict the maximum temperature rise which may occur during the superabrasive, conventional face and conventional peripheral grinding operations. These results are discussed with respect to the experimental findings previously discussed in this chapter.

The depth profiles of the maximum temperature rise T_{max} which was determined using a triangular moving heat source expression (Equation 11) are presented for the four parameter combinations LSS-LFR, LSS-HFR, HSS-LFR and HSS-HFR which were employed in superabrasive grinding trials.

The temperature-depth profile for the LSS-LFR (6000 rpm; 10000 mm/min) and HSS-LFR (6000 rpm; 10000 mm/min) are shown in Figure 147.

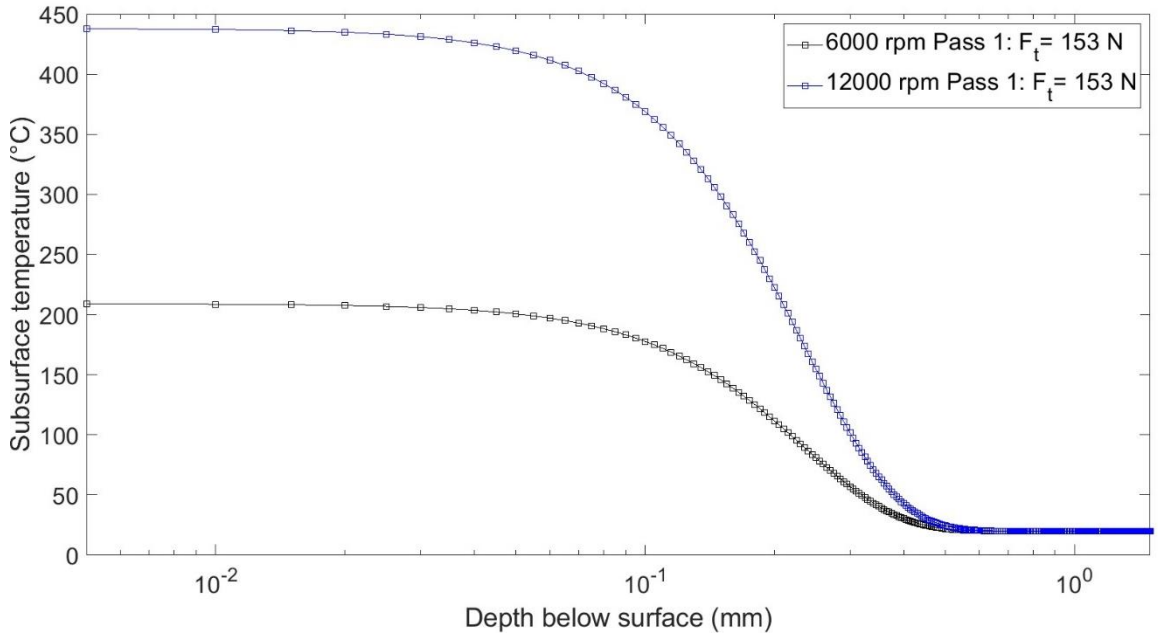

Figure 147: The depth profiles of the predicted maximum temperature rise during peripheral superabrasive grinding passes for LSS-LFR and HSS-LFR

The temperature-depth profile for the LSS-HFR (6000 rpm; 43000 mm/min) and HSS-HFR (12000 rpm; 43000 mm/min) are shown in Figure 148.

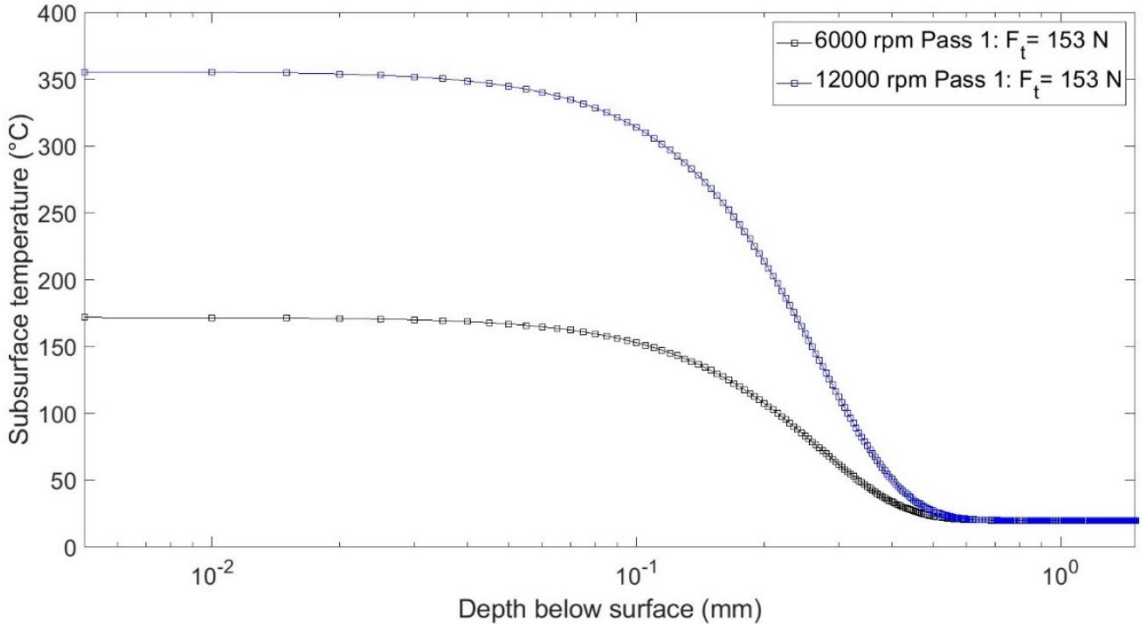

Figure 148: The depth profiles of the predicted maximum temperature rise during peripheral superabrasive grinding passes performed at LSS-HFR and HSS-HFR

Due to the lack of force measurements during the superabrasive grinding trial, an arbitrary tangential force value of 153 N was selected in order to predict the grinding temperature. While the predicted temperature-depth profiles shown in Figure 147 and Figure 148 provide information about the temperature decay behaviour from the surface into the bulk material, direct comparisons cannot be made with the conventional grinding temperature predictions or the actual measured temperatures.

The parameters related to the face grinding trial have been used to predict the temperature-depth profiles shown in Figure 149 for four passes conducted at 2000 rpm and 3000 rpm. Similarly, Figure 150 shows the predicted temperature-depth profiles of the grinding temperature during the four peripheral grinding passes conducted at 2000 rpm and 3000 rpm. To generate these profiles, the experimental maximum tangential forces which were presented in Chapter 4 have been utilised. Any additional assumed parameters which have not been mentioned in the thermal model in Section 2.6 can be found in Appendix D. The fourth pass in both the face and peripheral grinding passes presented the highest temperatures. The temperatures clearly correspond to the grinding force patterns observed in the individual grinding methods.

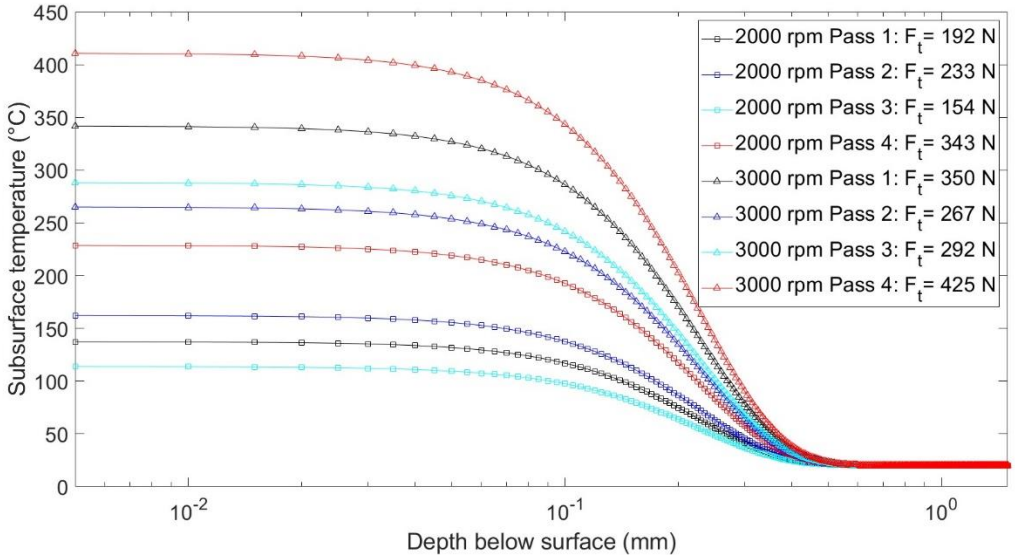

Figure 149: The depth profiles of the predicted maximum temperature rise during face grinding passes

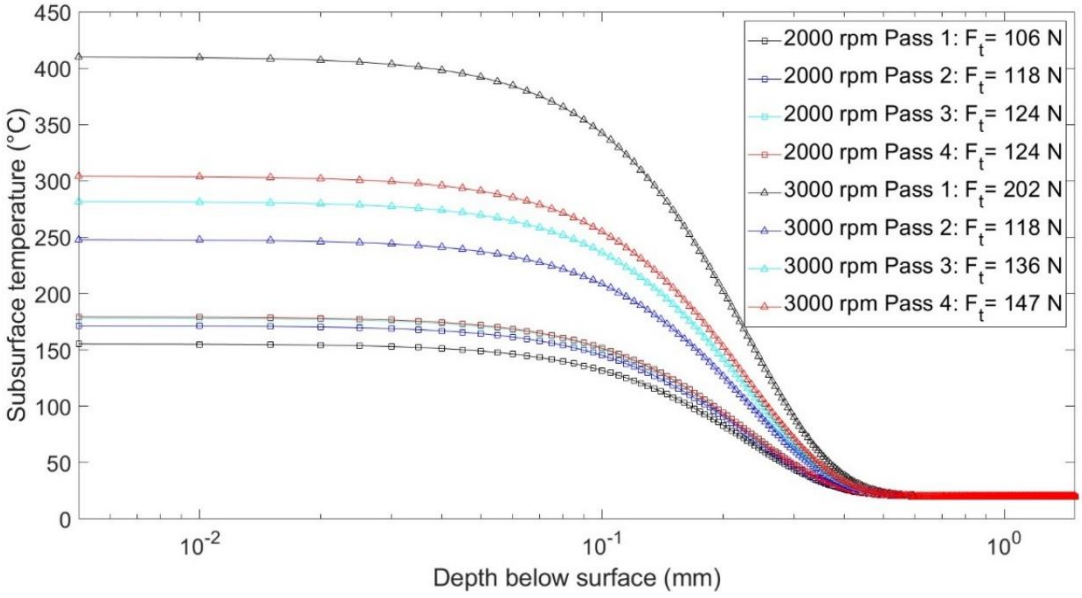

Figure 150: The depth profiles of the predicted maximum temperature rise during peripheral grinding passes

Through the model, the peripheral grinding temperature has been shown to be highest in the first pass. However, though the absolute values were lower, this observation is corroborated by the first pass temperature measured with the thermal camera.

7 Conclusions and Causes for Further Study

The investigation of the temperatures induced in superabrasive grinding has presented indications that the application of superabrasive tooling in rail grinding is attainable.

7.1 Conclusions of the Thesis

The peripheral grinding orientation has been determined to be optimal for the application of superabrasive tooling in rail grinding. This is buttressed by the lower forces observed in the peripheral grinding orientation when compared to the forces observed in the face grinding orientation.

The combination of higher wheel speeds and increased feed rates which have been utilised in the superabrasive grinding experiments conducted show reduced grinding temperatures in the peripheral grinding orientation. This gives basis to the increased productivity and workpiece quality which can be achieved through the use of superabrasive tooling in rail grinding,

The conclusions of thesis are discussed based on the research objectives which were presented in Section 1.2.

I. To assess different temperature measurement technologies and identify new approaches to improve temperature measurement in rail grinding operations.

Through an extensive literature review, the conventional rail grinding practices have been discussed. Temperature measurement technologies and methods of application such as optical fibres, thermocouples and thermography have been presented. Likewise, a temperature model of three types of grinding (peripheral superabrasive, conventional face and conventional peripheral) have been utilised and discussed. Based on the findings in the literature, the scope of temperature measurement in this research study was limited to thermocouple insertion in full-size rail and thermography.

II. To measure process temperatures during laboratory based conventional and superabrasive grinding.

The combination of superabrasive grinding with high-speed grinding technology has been reported by laboratory experiments within a CNC machine. Likewise, through the incorporation of temperature measurement techniques, the temperature response at varying depths from the surface have been discussed. The findings show that the process is suitable for superabrasive high-speed grinding of rail and thus presents improved grinding performance and surface integrity relative to the use of conventional AlO_x wheels.

The findings indicate that the grinding forces increase with increasing wheel speeds. This is further buttressed by the thermal measurement findings which indicate the increase in the grinding temperature with increasing number of passes and increasing wheel speeds.

III. To measure rail temperature during conventional grinding in field operations.

Two grinding campaigns performed on actual in-use tracks at the Drax Power Station and Metro dé Medellín were observed. For multiple passes, the measurement of temperature was performed using a thermal camera in various positions and directions against the grinding area. Though impeded by the side curtains of the train, temperatures of up to 181 °C were recorded by the thermal camera in congruence with the visually optimal conditions of the rail post-grinding.

IV. To assess the temperature effect on the track quality through assessment criteria which include workpiece surface roughness and workpiece surface microstructure.

Post-grind analysis of the microstructure has shown the presence of minimal amounts of WEL in samples ground by superabrasive grinding. Adversely, larger WEL thicknesses were observed in samples which were ground using conventional tooling methods. This effect is attributed to the significantly lower feed rates which were applied for the conventional tools. In the utilisation of typical grinding wheels used for manual grinding, the surface roughness values observed for the conventionally ground samples were found to be lower than reported for typical conventional grinding practices found in the literature.

V. To develop apparatus suitable for the trial of superabrasive grinding on actual track.

A grinding trolley has been developed with the capability to perform rail grinding on actual track. The trolley is equipped with a spindle which is capable of operating at spindle speeds which are sufficient to drive both conventional at low wheel speeds and superabrasive grinding tools at higher wheel speeds. As such, both conventional grinding trials may be performed to provide a benchmark for the planned superabrasive grinding trials. A recommended plan for trialling the grinding trolley has been presented to perform both superabrasive and conventional grinding on a dedicated test track.

7.2 Causes for Further Study

- A laboratory grinding trial is required to further understand the grinding force behaviour of superabrasive grinding wheel as it performs grinding passes on the railhead. Although this was not feasible for the superabrasive grinding trial reported in this thesis, subsequent superabrasive grinding trials must include the developed force measurements system.
- The use of multiple superabrasive grinding tools sequenced in multiple facets across the railhead to carry out grinding of the railhead surface in one
- The grinding temperature rise may be modelled from first principle using the grinding forces recorded in the grinding trials presented in this study as well as analytical models

utilised in research studies found in the literature. This model may also be utilised to extrapolate the recorded temperatures to the rail surface.

8 References

[1] B. W. Rowe, Principles of Modern Grinding Technology (Edition 2), Oxford: William Andrew Applied Science Publishers , 2014.

[2] F. Klocke, Manufacturing Processes 2: Grinding Honing, Lapping, Berlin: Springer-Verlag Berlin Heidelberg, 2009.

[3] X. Chen and W. B. Rowe, "Analysis and Simulation of the Grinding Process. Part II: Mechanics of Grinding," *International Journal of Machine Tools and Manufacture,* vol. 36, no. 8, pp. 883-896, 1996.

[4] R. Singleton, A. Bell, M. Marshall and R. Lewis, "New Techniques for Faster Rail Grinding For Network Rail," Sheffield, 2011.

[5] S. L. Grassie, "Squats and Squat-type Defects in Rails: the Understanding to Date," *Proceedings of the Institution of Mechanical Engineers, Part F: Journal of Rail and Rapid Transit,* vol. 226, no. 3, pp. 235-242, 2011.

[6] R. Singleton, M. Marshall, R. Lewis and G. Evans, "Rail Grinding for the 21st Century – Taking a Lead from the Aerospace Industry," *Proceedings of the Institution of Mechanical Engineers, Part F: Journal of Rail and Rapid Transit,* vol. 229, no. 5, pp. 457-465, 2015.

[7] Y. Satoh and K. Iwafuchi, "Effect of Rail Grinding on Rolling Contact Fatigue in Railway Used in Conventional Line in Japan," *Wear,* vol. 265, pp. 1342-1348, 2008.

[8] K.-j. Rong, Y.-l. Xiao, M.-x. Shen, H.-P. Zhao, W.-J. Wang and G.-y. Xiong, "Influence of Ambient Humidity on the Adhesion and Damage Behavior of Wheel–Rail Interface Under Hot Weather Condition," *Wear,* Vols. 486-487, no. 204091, 2021.

[9] J. W. Ringsberg, "Life Prediction of Rolling Contact Fatigue Crack Initiation," *International Journal of Fatigue,* vol. 23, no. 7, pp. 575-586, 2001.

[10] Fletcher, D. I., P. Hyde and A. Kapoor, "Growth of Multiple Rolling Contact Fatigue Cracks Driven by Rail Bending Modelled Using a Boundary Element Technique," *Proceedings of the Institution of Mechanical Engineers, Part F: Journal of Rail and Rapid Transit,* vol. 218, no. 3, pp. 243-253, 2004.

[11] E. E. Magel, "Rolling Contact Fatigue: A Comprehensive Review," Washington, 2011.

[12] S. L. Grassie, "Rail Corrugation: Characteristics, Causes, and Treatments," *Journal of Rail and Rapid Transit,* vol. 223, no. 6, pp. 581-596, 2009.

[13] M. Taubert, "High Speed Grinding - Preventative Rail Care," in *Proceedings of the 2009 Annual Conference: AREMA 2009 Annual Conference*, Chicago, September 2009.

[14] Y. Satoh and K. Iwafuchi, "Effect of Rail grinding on Rolling Contact Fatigue in Railway Rail Used in Conventional Line in Japan," *Wear,* vol. 265, no. 9-10, pp. 1342-1348, 2008.

[15] E. Uhlmann, P. Lypovka, L. Hochschild and N. Schröer, "Influence of Rail Grinding Process Parameters on Rail Surface Roughness and Surface Layer Hardness," *Wear,* Vols. 287-293, pp. 366-367, 2016.

[16] S. Zhang, K. Zhuo, H. Ding, J. Guo and W. Wang, "Effects of Grinding Passes and Direction on Material Removal Behaviours in the Rail Grinding Process," *Materials,* vol. 11, no. 2293, 2018.

[17] R. X. Wang, K. Zhou, J. Y. Yang, H. H. Ding, W. J. Wang, J. Guo and Q. Y. Liu, "Effects of Abrasive Material and Hardness of Grinding Wheel on Rail Grinding Behaviors," *Wear,* Vols. 454-455, no. 203332, 2020.

[18] K. K. Gu, Q. Lin, W. J. Wang, H. Y. Wang, J. Guo, Q. Y. Liu and M. H. Zhu, "Analysis on the Effects of Rotational Speed of Grinding Stone on Removal Behavior of Rail Material," *Wear,* vol. 342–343, pp. 52-59, 2015.

[19] W. J. Wang, K. K. Gu, K. Zhou, Z. B. Cai, J. Guo and Q. Y. Liu, "Influence of Granularity of Grinding Stone on Grinding Force and Material Removal in the Rail Grinding Process," *Proceedings of the Institution of Mechanicla Engineers, Part J: Journal of Engineering Tribology,* vol. 233, no. 2, pp. 355-365, 2018.

[20] Y. Kanematsu and Y. Satoh, "Influence of Type of Grinding Stone on Rail Grinding Efficiency," *Quarterly Report of RTRI,* vol. 52, no. 2, pp. 97-102, 2011.

[21] M. Steenbergen, "Rolling Contact Fatigue in Relation to Rail Grinding," *Wear,* Vols. 356-357, pp. 110-121, 2016.

[22] C. J. Rasmussen, S. Fæster, S. Dhar, J. V. Quaade, M. Bini and H. K. Danielsen, "Surface Crack Formation on Rails at Grinding Induced Martensite White Etching Layers," *Wear,* Vols. 384-385, pp. 8-14, 2017.

[23] G. Baumann, H. J. Fecht and S. Liebelt, "Formation of White-Etching Layers on Rail Treads," *Wear,* vol. 191, pp. 133-140, 1996.

[24] W. Österle, H. Rooch, A. Pyzalla and L. Wang, "Investigation of White Etching Layers on Rails by Optical Microscopy, Electron Microscopy, X-ray and Synchrotron X-ray Diffraction," *Materials Science and Engineering: A,* vol. 303, no. 1-2, pp. 150-157, 2001.

[25] K. Zhou, H. Ding, R. Wang, J. Yang, J. Guo, Q. Liu and W. Wang, "Experimental Investigation on Material Removal Mechanism During Rail Grinding at Different Forward Speeds," *Tribology International,* vol. 143, pp. 1-18, 2020.

[26] S. Grassie, D. Fletcher, E. Hernandez Gallardo and P. Summers, "Studs: A Squat-Type Defect in Rails," *Part F: Journal of Rail and Rapid Transit,* vol. 226, pp. 243-256, 2011.

[27] S. Michaël, "Rolling Contact Fatigue in Relation to Rail Grinding," *Wear,* Vols. 356-357, pp. 110-121, 2016.

[28] K. Zhou, H. H. Ding, W. J. Wang, R. X. Wang, J. Guo and Q. Y. Liu, "Influence of Grinding Pressure on Removal Behaviours of Rail Material," *Tribology International,* vol. 134, pp. 417-426, 2019.

[29] M. Kuffa, D. Ziegler, T. Peter, F. Kuster and K. Wegener, "A New Grinding Strategy to improve the Acoustic Properties of Railway Tracks," *Proceedings of The Institution of Mechanical Engineers, Part F: Journal of Rail and Rapid Transit,* vol. 232, no. 1, p. 214–221, 2018.

[30] J. Lundmark, E. Höglund and B. Prakash, "Running-in behaviour of rail and wheel contacting surfaces," in *International Conference on Tribology*, Parma, Italy, 2006.

[31] L. C. Zhang, T. Suto, H. Noguchi and T. Waida, "A Study of Creep-Feed Grinding of Metallic and Ceramic Materials," *Journal of Materials Processing Technology,* vol. 48, no. 1-4, pp. 267-274, 1995.

[32] Cool-Grind, "Creep-Feed, Surface and Gear Grinding Nozzle Systems," Shopify, 2019. [Online]. Available: https://cool-grind.com/collections/creep-feed-surface-and-gear-grinding-nozzle-systems. [Accessed November 2019].

[33] S. Malkin and C. Guo, Grinding Technology: Theory and Applications of Machining with Abrasives, New York: Industrial Press, Inc, 2008.

[34] I. D. Marinescu, M. Hitchiner, E. Uhlmann, W. B. Rowe and I. Inasaki, Handbook of Machining With Grinding Wheels, Boca Raton, Florida: CRC Press/Taylor and Francis, 2007.

[35] B. Lin, K. Zhou, J. Guo and W. J. Wang, "Influence of Grinding Parameters on Surface Temperature and Burn Behaviors of Grinding Rail," *Tribology International,* vol. 122, pp. 151-162, 2018.

[36] J. C. Aurich, B. Linke, M. Hauschild, M. Carrella and B. Kirsch, "Sustainability of Abrasive Processes," *CIRP Annals - Manufacturing Technology,* vol. 62, no. 2, pp. 653-672, 2013.

[37] M. Duscha, F. Klocke, A. Entremont, B. Linke and H. Wegner, "Investigation of Temperatures and Residual Stresses in Speed Stroke Grinding via FEA Simulation and Practical Test," *Proceedings in Manufacturing Systems,* vol. 5, no. 1, pp. 1-6, 2010.

[38] C. Zeppenfeld and F. Klocke, "Speed Stroke Grinding of γ-Titanium Aluminides," *CIRP Annals,* vol. 55, no. 1, pp. 333-338, 2006.

[39] M. Duscha, B. Linke, F. Klocke and D. Dornfeld, "Higher Competitiveness of Speed-Stroke Grinding by Using Increased Wheel Speeds," in *Proceedings of the ASME 2012 International Manufacturing Science and Engineering Conference*, Notre Dame, Indiana, 2012.

[40] M. Weiß, F. Klocke and H. Wegner, "Process Machine Interaction in Pendulum and Speed-Stroke Grinding," in *Process Machine Interactions*, Berlin, 2013.

[41] R. Lizarralde, J. Á. Marañón, A. Mendikute and H. Urreta, "High Performance Grinding Machines," in *Machine Tools for High Performance Machining*, London, Springer, 2009, pp. 279-305.

[42] I. Inasaki, "Speed-Stroke Grinding of Advanced Ceramics," *CIRP Annals,* vol. 37, no. 1, pp. 299-302, 1988.

[43] J. Badger, "Practical Application of Aggressiveness and Chip Thickness in Grinding," in *Annals of the CIRP 3rd International Conference High Performance Cutting (HPC)*, Dublin, Ireland, 2008.

[44] B. Linke, F. Klocke and D. Dornfeld, "Combination of Speed Stroke Grinding and High Speed Grinding with Regard to Sustainability," in *Proceedings of the 2008 International Manufacturing Science and Engineering Conference (MSEC)*, Evanston, Illinois, USA, 2011.

[45] I. D. Marinescu, B. W. Rowe, B. Dimitrov and H. Ohmori, "Kinematic Models of Abrasive Contacts," in *Tribology of Abrasive Machining Processes (Second Edition)*, New York, William Andrew, 2013, pp. 36-72.

[46] M. Venables, "It's a Grind - New Grinding Technology is Allowing Manufacturers to Save Both Money and Time Without Affecting the Quality of the Finished Part," *IET Manufacturing Engineer,* vol. 85, no. 4, pp. 42-45, August/September 2006.

[47] C. P. R. Hill, J. R. Watkins, C. Ray and S. Ray, "Method and Apparatus for Grinding". Europe Patent EP0924028A2, 23 June 1999.

[48] R. Singleton, "Utilisation of Chip Thickness Models in Grinding," Sheffield, 2012.

[49] Tyrolit, "VIPER ULTRA High-Performance Vitrified Bonded Grinding Wheels for The Patented Viper Grinding Process," February 2015. [Online]. Available: https://www.tyrolit.at/fileadmin/products/doc/9b74c2638bd0_20055659-gb-0215_viper_ultra_rz_low.pdf. [Accessed August 2023].

[50] F. Klocke, S. L. Soo, B. Karpuschewski, J. A. Webster, D. Novovic, A. Elfizy, D. A. Axinte and S. Tönissen, "Abrasive Machining of Advanced Aerospace Alloys and Composites," *CIRP Annals - Manufacturing Technology,* vol. 64, pp. 581-604, 2015.

[51] T. Tawakoli, High-Efficiency Deep Grinding: Technology, Process Planning and Economic Application, Wiley, 1993.

[52] F. Klocke, S. Barth and P. Mattfeld, "High Performance Grinding," *Procedia CIRP,* vol. 46, pp. 266-271, 2016.

[53] M. Hitchiner, "Practical Challenges to the Application of High Wheel Speeds to Grinding," in *Proceedings of the International Technical Conference on Diamond, cubic boron nitride and their applications*, 2003.

[54] J. Kopac and P. Krajnik, "High-Performance Grinding - A Review," *Journal of Materials Processing Technology,* vol. 175, pp. 278-284, 2006.

[55] P.-Z. Liu, W. Zou, J. Peng and F. Xiao, "Investigating the Effect of Grinding Time on High-SpeedGrinding of Rails by a Passive Grinding Test Machine," *Micromachines,* vol. 13, no. 2118, 2022.

[56] P.-Z. Lui, W.-J. Zou, J. Peng, X.-D. Song and F.-R. Xiao, "Designed a Passive Grinding Test Machine to Simulate Passive Grinding Process," *Processes,* vol. 9(8), no. 1317, 2021.

[57] R. Komanduri and Z. B. Hou, "A Review of the Experimental Techniques for the Measurement of Heat and Temperatures Generated in Some Manufacturing Processes and Tribology," *Tribology International,* vol. 34, no. 10, pp. 653-682, 2001.

[58] M. A. Davies, T. Ueda, R. M'Saoubi, B. Mullany and A. L. Cooke, "On The Measurement of Temperature in Material Removal Processes," *CIRP Annals,* vol. 56, no. 2, pp. 581-604, 2007.

[59] T. Ueda, H. Tanaka, A. Torii and T. Matsuo, "Measurement of Grinding Temperature of Active Grains Using Infrared Radiation Pyrometer with Optical Fiber," *CIRP Annals,* vol. 42, no. 1, pp. 405-408, 1993.

[60] T. Ueda, M. Sato, T. Sugita and K. Nakayama, "Thermal Behaviour of Cutting Grain in Grinding," *CIRP Annals,* vol. 44, no. 1, pp. 325-328, 1995.

[61] T. Ueda, R. Nozaki and A. Hosokawa, "Temperature Measurement of Cutting Edge in Drilling -Effect of Oil Mist," *CIRP Annals,* vol. 56, no. 1, pp. 93-96, 2007.

[62] C. Baumgart, V. Heizer and K. Wegener, "In-process Workpiece Based Temperature Measurement," in *8th CIRP Conference on High Performance Cutting (HPC 2018)*, 2018.

[63] D. Liu, G. Wang, Z. Nie and Y. Rong, "An In-Situ Infrared Temperature-Measurement Method with Back Focusing on Surface for Creep-Feed Grinding," *Measurement,* vol. 94, pp. 645-652, 2016.

[64] C. Boehm, T. Seedorf, L. Meyer, E. Brinksmeier and J. Binder, "Temperature and Force Sensor Integrated Grinding Wheel for Process Monitoring," *Abrasives Magazine,* October/December 2001.

[65] E. Brinksmeier, C. Heinzel and L. Meyer, "Development and Application of a Wheel Based Process Monitoring System in Grinding," *CIRP Annals,* vol. 54, no. 1, pp. 301-304, 2005.

[66] L. Meyer, "Einsatz von Temperatur- und Kraftsensoren in Schleifwerkzeugen," Bremen, 2006.

[67] E. Brinksmeier, J. Eckebrecht and A. Wilkens, "Wheel Based Temperature Measurement in Grinding," *Advanced Materials Research,* vol. 325, pp. 3-11, 2011.

[68] S. Paul and A. B. Chattopadhyay, "Determination and Control of Grinding Zone Temperature Under Cryogenic Cooling," *International Journal of Machine Tools and Manufacture,* vol. 36, no. 4, pp. 491-501, 1996.

[69] Q. Lin, J. Guo, H.-y. Wang, W.-j. Wang and Q.-y. Liu, "Optimal Design of Rail Grinding Patterns Based on a Rail Grinding Target Profile," *Proceedings of the Institution of Mechanical Engineers, Part F: Journal of Rail and Rapid Transport,* vol. 232, no. 2, pp. 560-571, 2018.

[70] M. Burstow, "Understanding Wheel/Rail Interaction With Thermographic Imaging," in *Proceedings of the 22nd International Symposium on Dynamics of Vehicles on Roads and Tracks*, Manchester, 2011.

[71] D. Yamamoto, "Improvement of Method for Locating Position of Wheel/Rail Contact by Means of Thermal Imaging.," *Quarterly Report of RTRI,* vol. 60, no. 1, pp. 65-71, 2019.

[72] B. Firlik, T. Staskiewicz and M. Słowinski, "Thermal Imaging of the Wheel-Rail Interface," *Proceedings of the Institution of Mechanical Engineers, Part F: Journal of Rail and Rapid Transit,* vol. 237, no. 9, pp. 1195-1204, 2023.

[73] Z. Y. Zhang, W. Shang, H. H. Ding, J. Guo, H. Y. Wang, Q. Y. Liu and W. J. Wang, "Thermal Model and Temperature Field in Rail Grinding Process Based on a Moving Heat Source," *Applied Thermal Engineering,* vol. 106, p. 855–864, 2016.

[74] W. Rowe, M. Morgan, A. Batako and T. Jin, "Energy and Temperature Analysis in Grinding," *Transactions on Engineering Sciences,* vol. 44, pp. 3-23, 2003.

[75] H. S. Carslaw and J. C. Jaeger, Conduction of Heat in Solids, Oxford: Oxford University Press, 1959.

[76] J. C. Jaeger, "Moving Sources of Heat and the Temperature at Sliding Contacts," *Proceedings of the Royal Society of New South Wales,* pp. 203-224, 1942.

[77] W. B. Rowe, M. N. Morgan, S. E. Black and B. Mills, "A Simplified Approach to Control Thermal Damage in Grinding," *CIRP Annals,* vol. 45, no. 1, pp. 299-302, 1996.

[78] W. Rowe and T. Jin, "Temperatures in High Efficiency Deep Grinding (HEDG)," *CIRP Annals - Manufacturing Technology,* vol. 50, no. 1, pp. 205-208, 2001.

[79] D. Anderson, A. Warkentin and R. Bauer, "Experimental Validation of Numerical Thermal Models for Dry Grinding," *Journal of Materials Processing Technology,* vol. 204, no. 1-3, pp. 269-278, 2008.

[80] K. Zhou, H. Ding, M. Steenbergen, W. Wang, J. Guo and Q. Liu, "Temperature Field and Material Response as a Function of Rail Grinding Parameters," *International Journal of Heat and Mass Transfer,* vol. 175, no. 121366, 2021.

[81] P. Cuervo, J. Santa and A. Toro, "Correlations between wear mechanisms and rail grinding operations in a commercial railroad," *Tribology International,* Vols. 265-273, no. 82, pp. 265-273, 2015.

[82] C. M. Hartsough, J. W. Palese, G. Schmitzer, J. C. Espindola and T. G. Viana, "Optimized Rail Grinding Through Dynamic Positioning and Powering of Grinding Motors," in *ASME Joint Rail Conference*, Columbia, 2016.

[83] The British Standards Institution, *BS EN 13674-4: Railway Applications - Track - Rail - Part 1,* The British Standards Institution , 2019.

[84] British Steel Limited, "Steel Products for Rail Applications," British Steel Limited, Scunthorpe, 2020.

[85] K. Zhou, H. H. Ding, S. Y. Zhang, J. Guo, Q. Y. Liu and W. J. Wang, "Modelling and Simulation of the Grinding Force in Rail Grinding That Considers the Swing Angle of the Grinding Stone," *Tribology International,* vol. 137, pp. 274–288, 2019.

[86] M. Duscha, B. Linke and D. Dornfeld, "Higher Competitiveness of Speed-Stroke Grinding by Using Increased Wheel Speeds," in *Proceedings of the ASME 2012 International Manufacturing Science and Engineering Conference - MSE2012*, Indiana, 2012.

[87] R. X. Wang, K. Zhou, J. Y. Yang, H. H. Ding, W. J. Wang, J. Guo and Q. Y. Liu, "Effects of Abrasive Material and Hardness of Grinding Wheel on Rail Grinding Behaviors," *Wear,* Vols. 454–455, no. 203332, 2020.

[88] M. Mesaritis, M. Shamsa, P. Cuervo, J. F. Santa, A. Toro, M. B. Marshall and R. Lewis, "A Laboratory Demonstration of Rail Grinding and Analysis of Running Roughness and Wear," *Wear,* Vols. 456–457, 2020.

[89] M. Mesaritis, J. F. Santa, L. F. Molina, M. Palacio, A. Toro and R. Lewis, "Post-Field Grinding Evaluation of Different Rail Grades in Full-Scale Wheel/Rail Laboratory Tests," *Tribology International,* vol. 177, no. 107980, 2023.

[90] S. B. Newcomb and W. M. Stobbs, "A Transmission Electron Microscopy Study of the White-etching Layer on a Rail Head," *Materials Science and Engineering,* vol. 66, no. 2, pp. 195–204, 1984.

[91] S. Li, J. Wu, R. . H. Petrov, Z. Li, R. Dollevoet and J. Sietsma, ""Brown Etching Layer": A Possible New Insight Into the Crack Initiation of Rolling Contact Fatigue in Rail Steels?," *Engineering Failure Analysis,* vol. 66, pp. 8–18, 2016.

[92] S. Zhi, J. Li and A. Zarembski, "Predictive Modeling of the Rail Grinding Process Using a Distributed Cutting Grain Approach," *Proceedings of the Institution of Mechanical Engineers, Part F: Journal of Rail and Rapid Transit,* vol. 230, no. 6, pp. 1540–1560, 2016.

[93] S. Malkin and N. H. Cook, "The Wear of Grinding Wheels - Part 1 - Attritious Wear," *Journal of Engineering for Industry,* vol. 93, no. 4, pp. 1120-1128, 1971.

9 Appendix A – Thermocouple Time-Temperature Plots

This section concerns the time-temperature plots of the second, third and fourth grinding passes of the various grinding conditions conducted using the superabrasive grinding wheel as reported in Section 4.3.1.

9.1 Low Spindle Speed – Low Feed Rate (LSS-LFR)

Pass 2

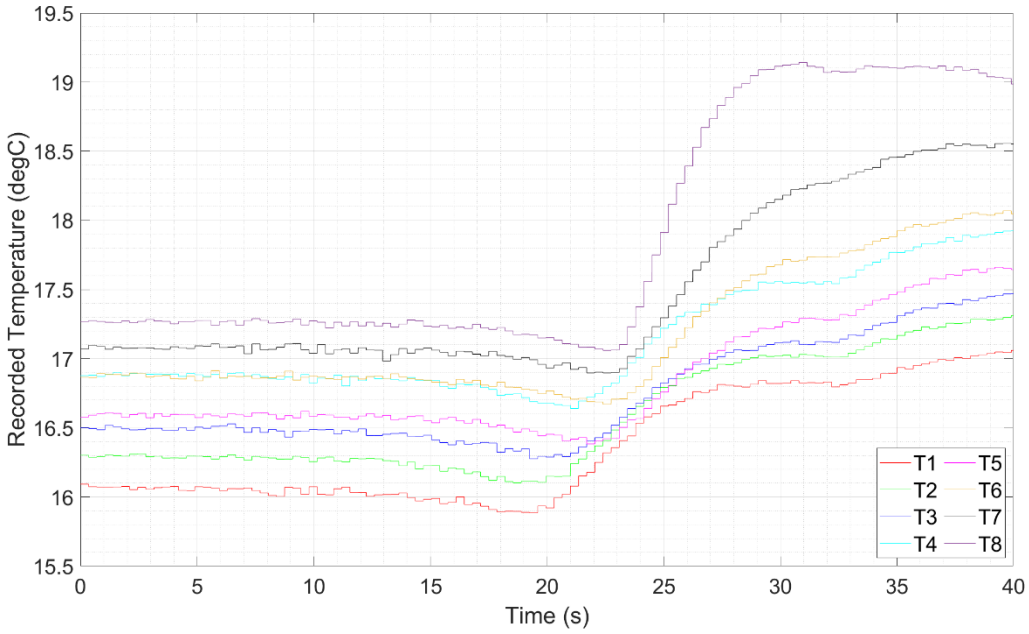

Pass 3

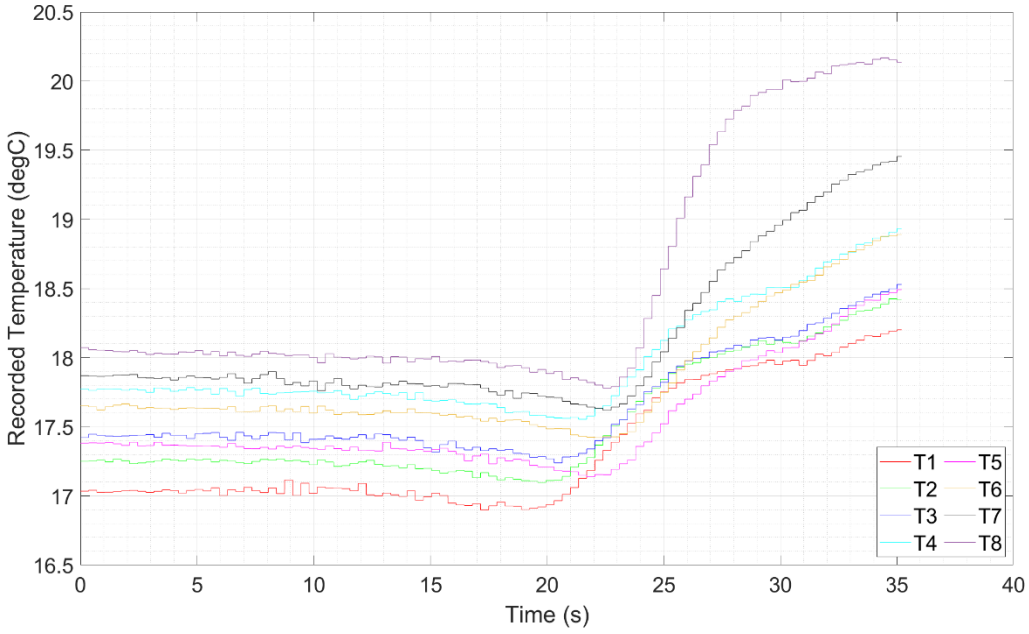

Pass 4

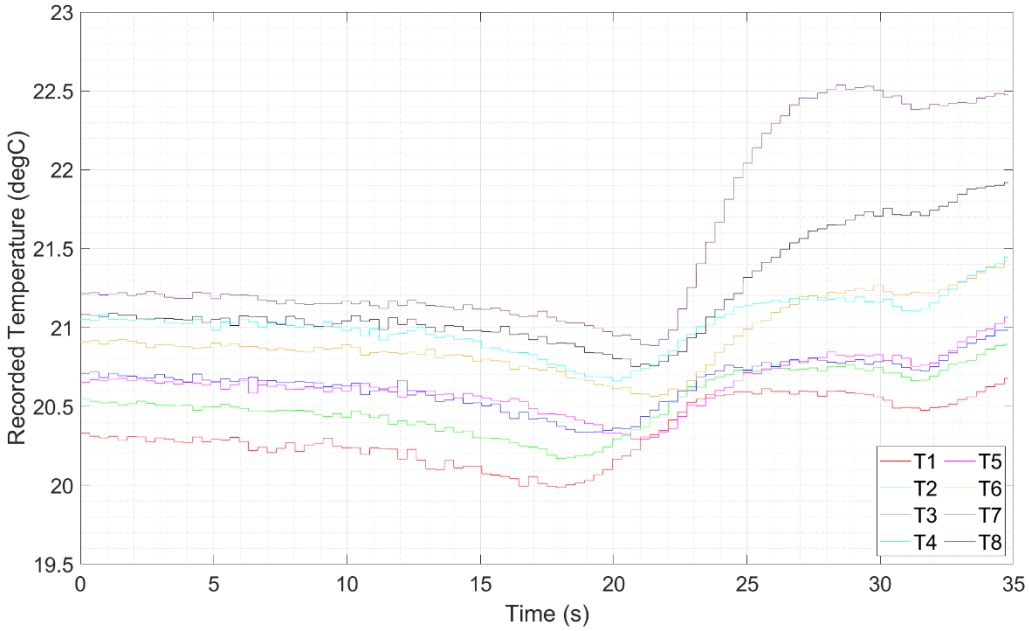

9.2 Low Spindle Speed – High Feed Rate (LSS-HFR)

Pass 2

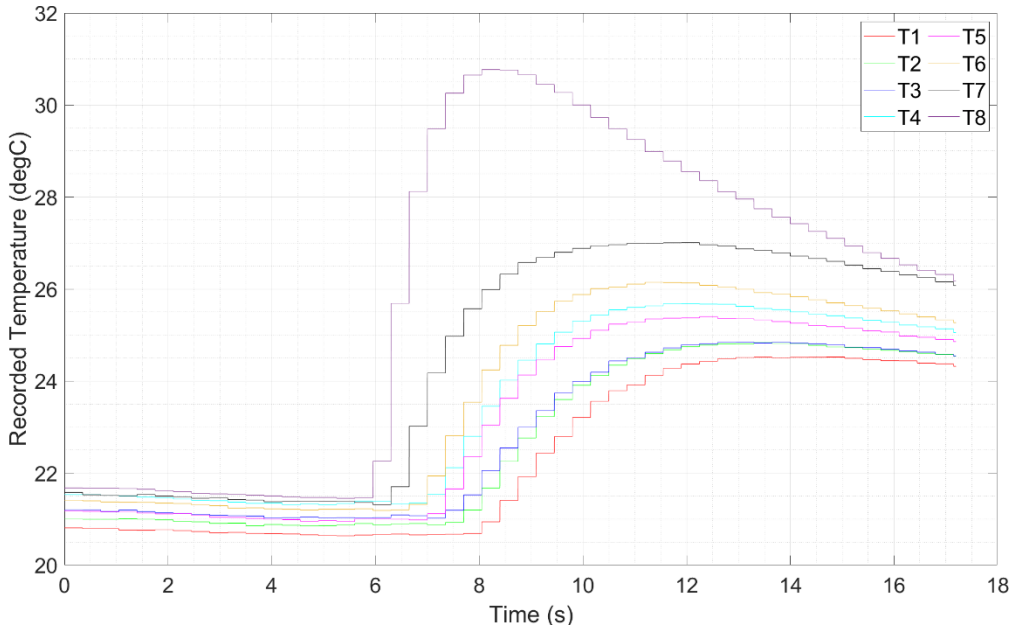

Pass 3

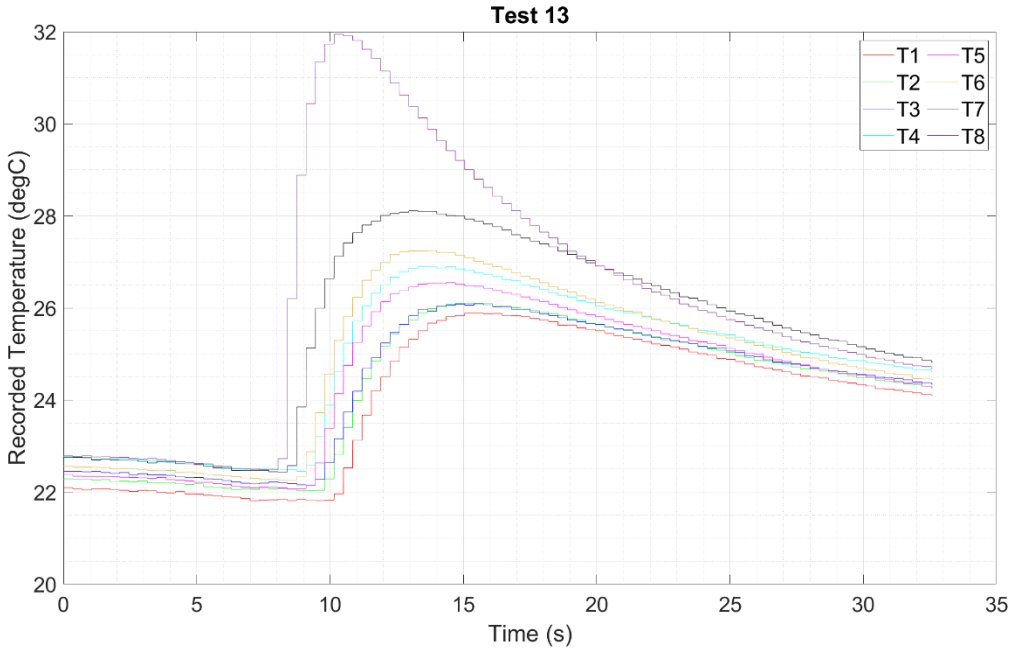
Test 13
Recorded Temperature (degC)
Time (s)
T1
T2
T3
T4
T5
T6
T7
T8

Pass 4

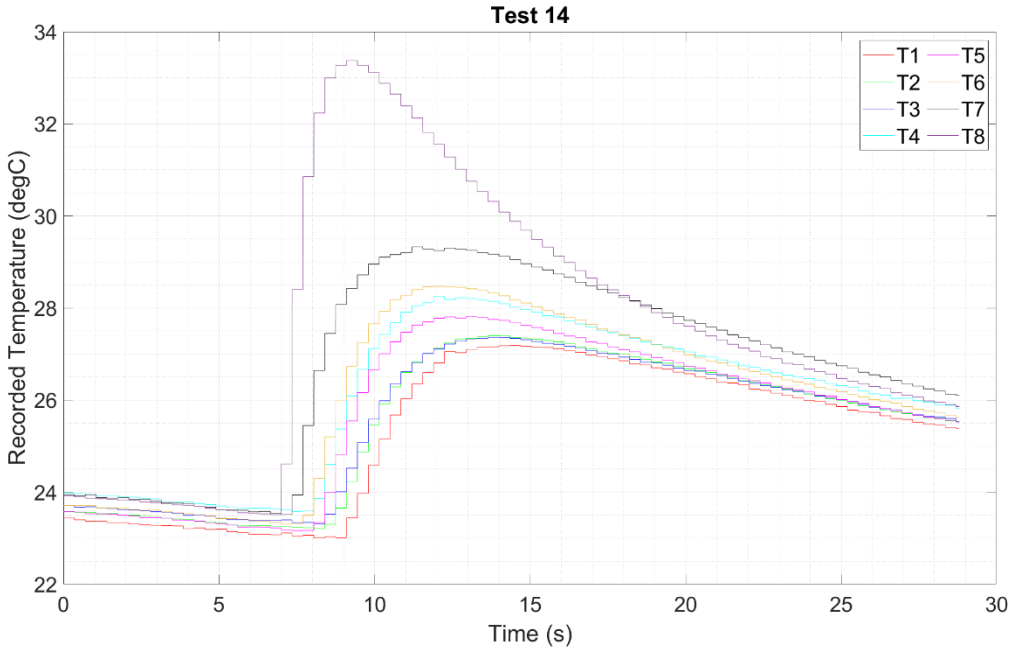
Test 14
Recorded Temperature (degC)
Time (s)
T1
T2
T3
T4
T5
T6
T7
T8

9.3 High Spindle Speed – Low Feed Rate (HSS-LFR)

Pass 2

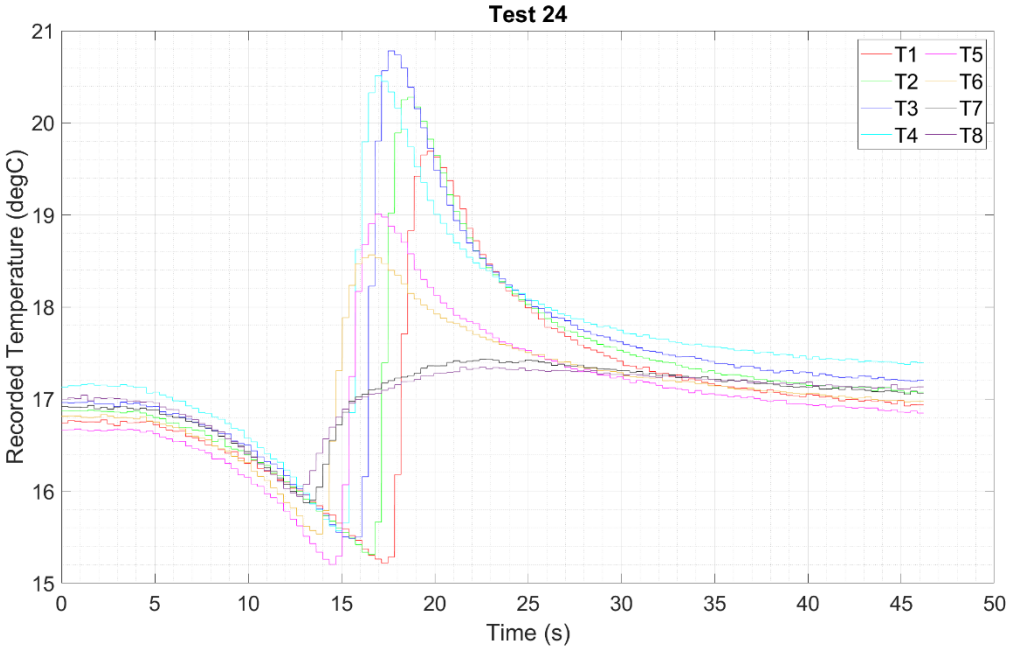

Pass 3

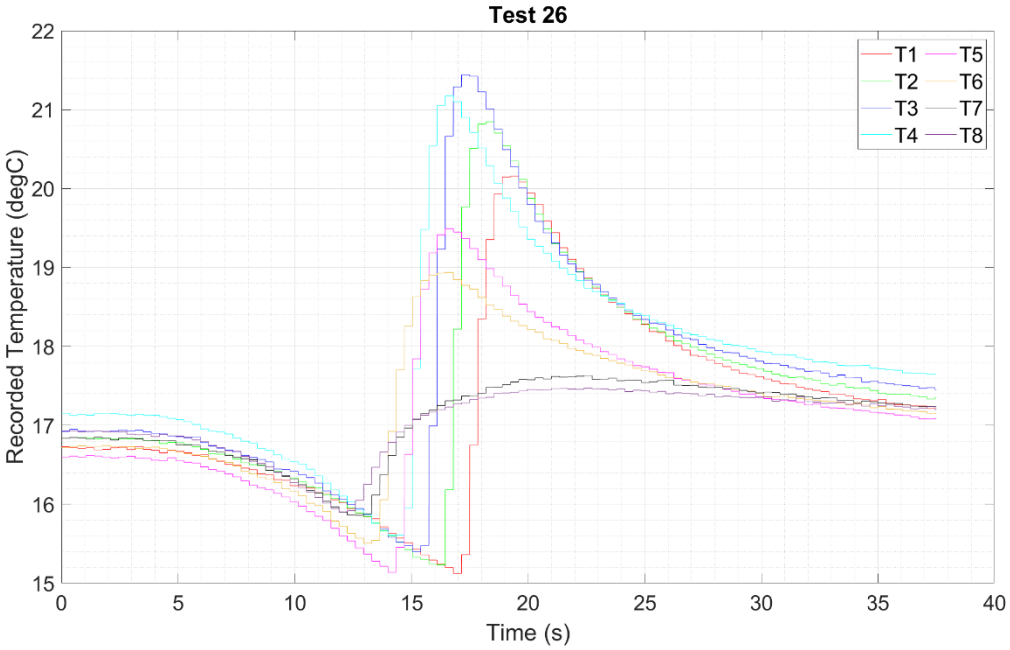

Pass 4

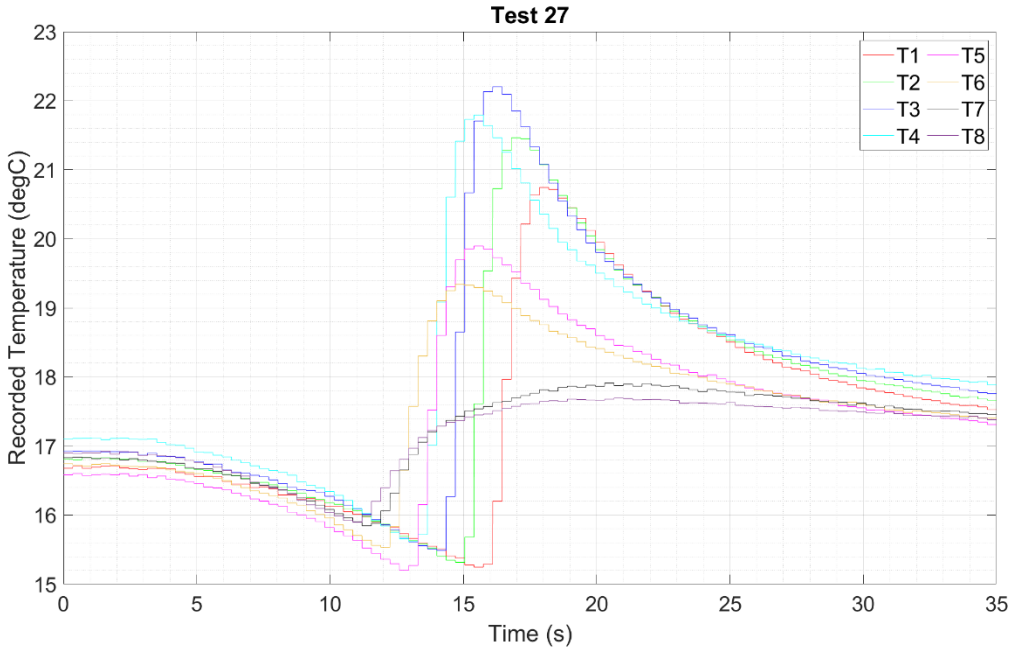

9.4 High Spindle Speed – High Feed Rate (HSS-HFR)

Pass 2

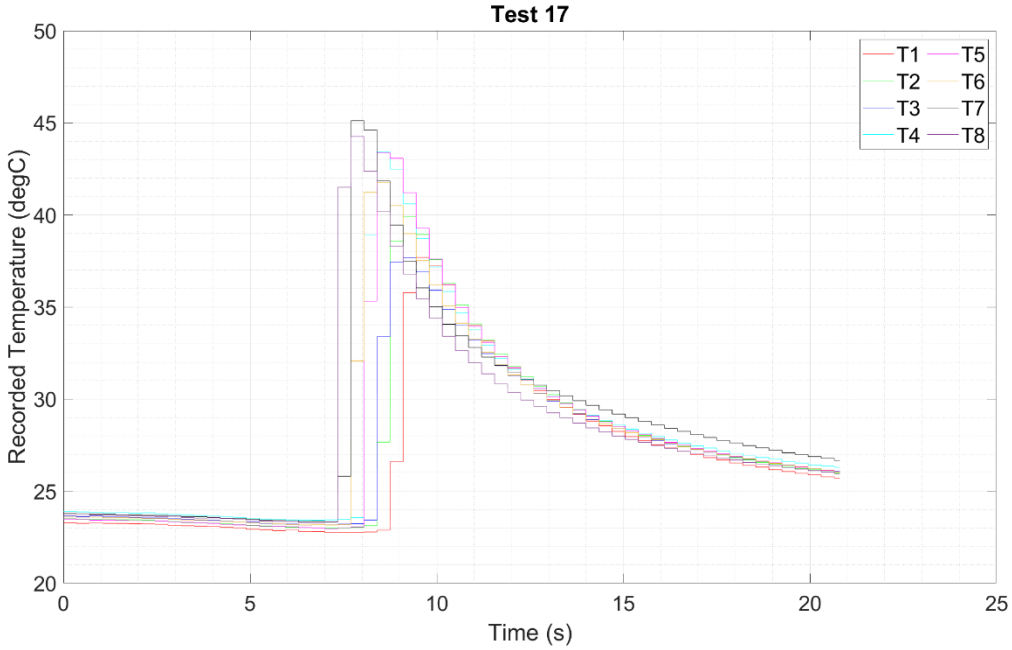

Pass 3

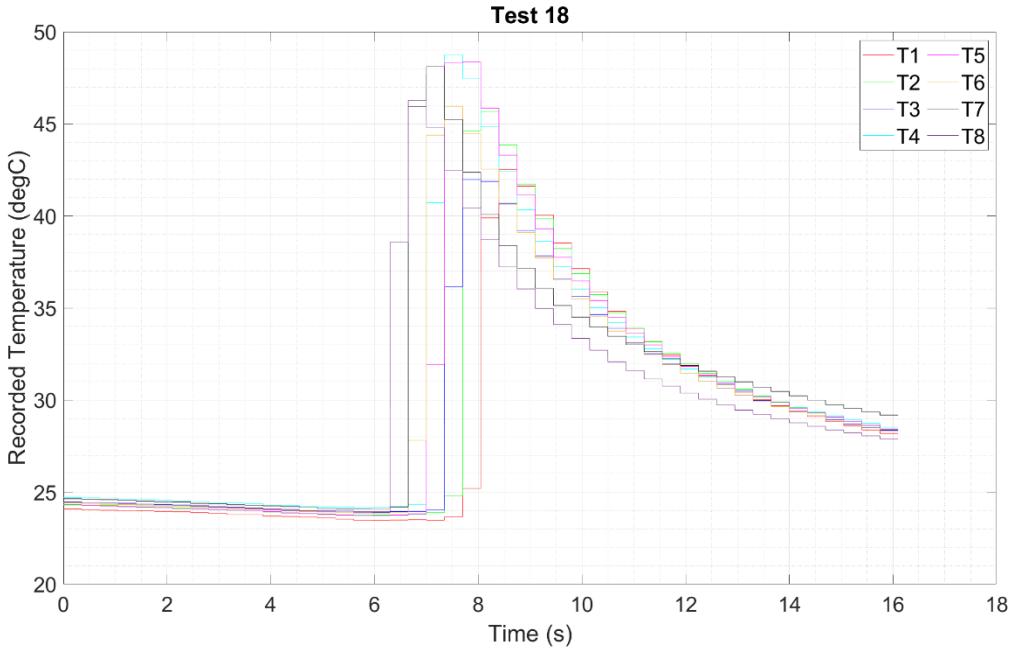
Test 18
Recorded Temperature (degC)
Time (s)
T1
T2
T3
T4
T5
T6
T7
T8

Pass 4

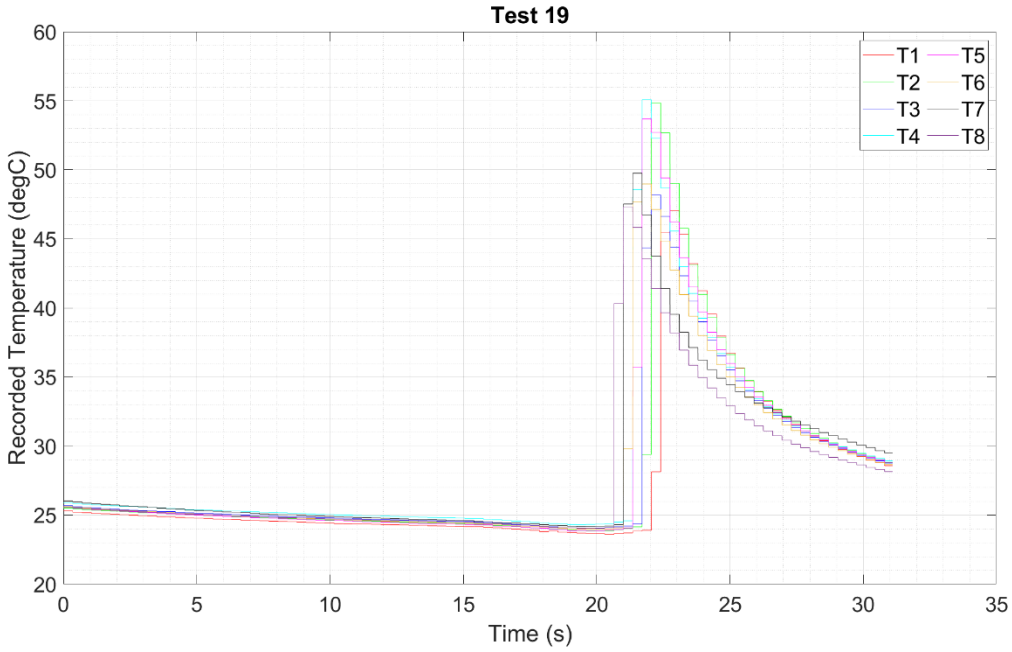
Test 19
Recorded Temperature (degC)
Time (s)
T1
T2
T3
T4
T5
T6
T7
T8

10 Appendix B – Thermal Images of Grinding Passes

The additional thermal images recorded in the passes conducted during superabrasive grinding trial are presented in this section.

10.1 Low Spindle Speed – Low Feed Rate (LSS-LFR)

Pass 2

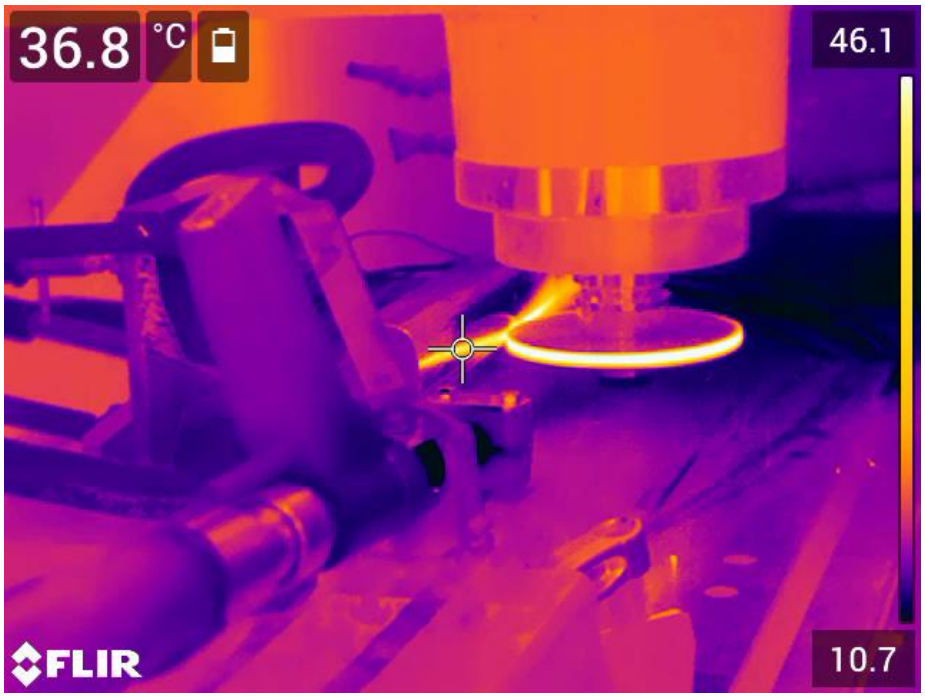

Pass 3

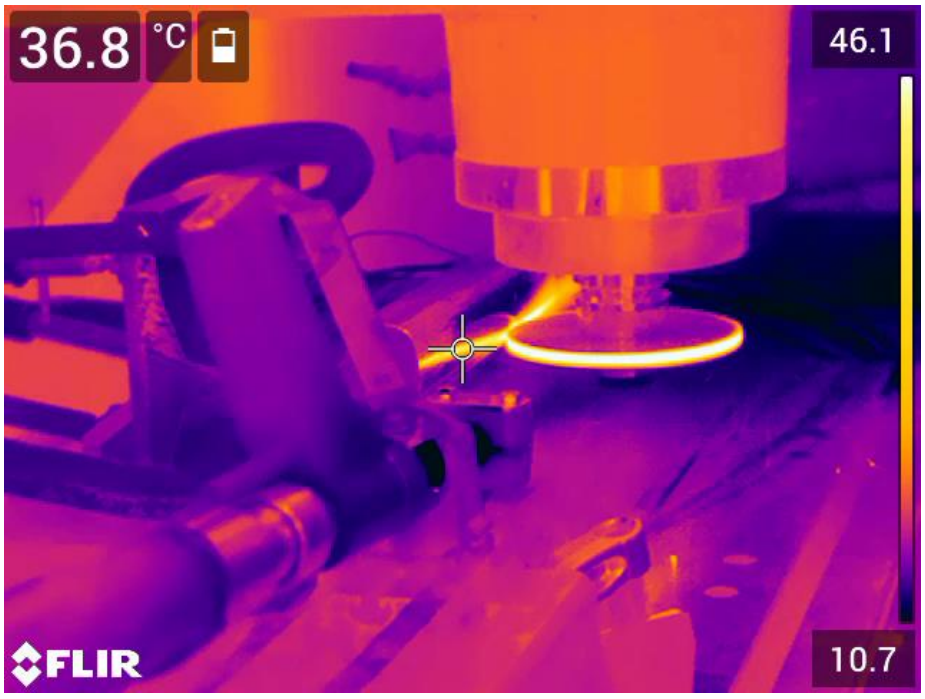

Pass 4

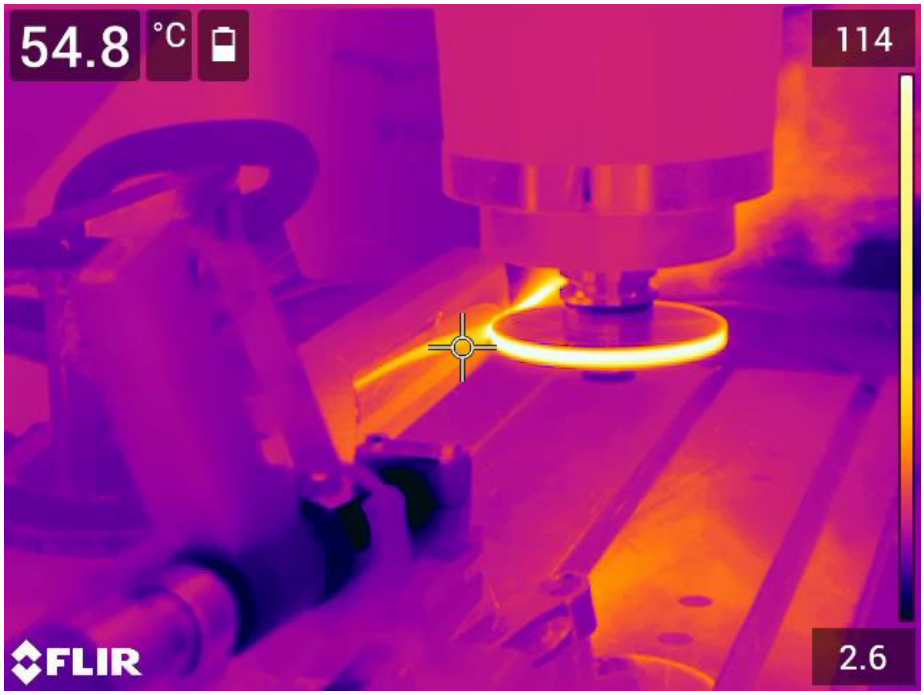

10.2 Low Spindle Speed – High Feed Rate (LSS-HFR)

Pass 2

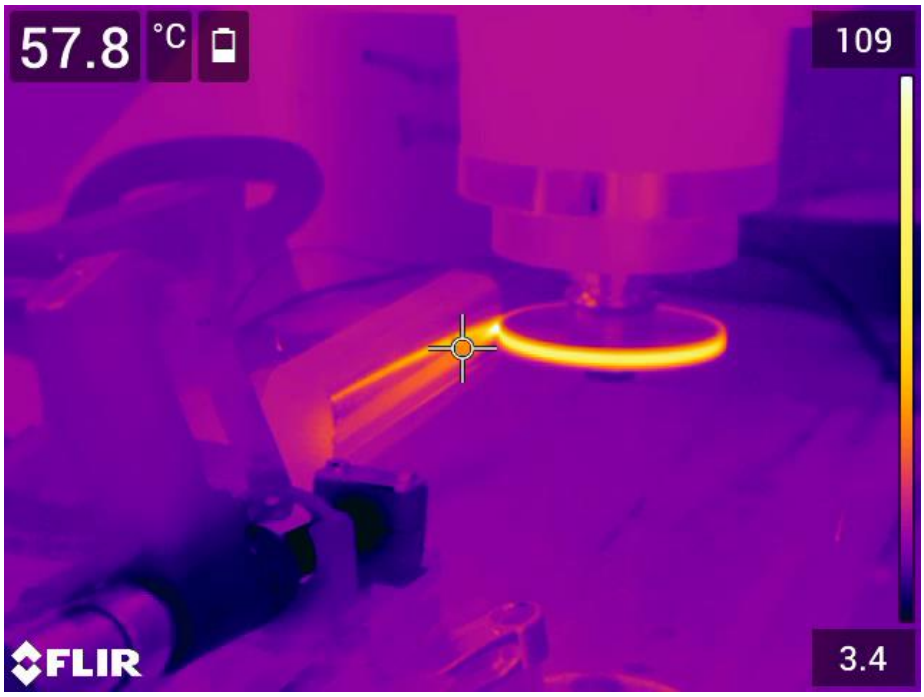

Pass 3

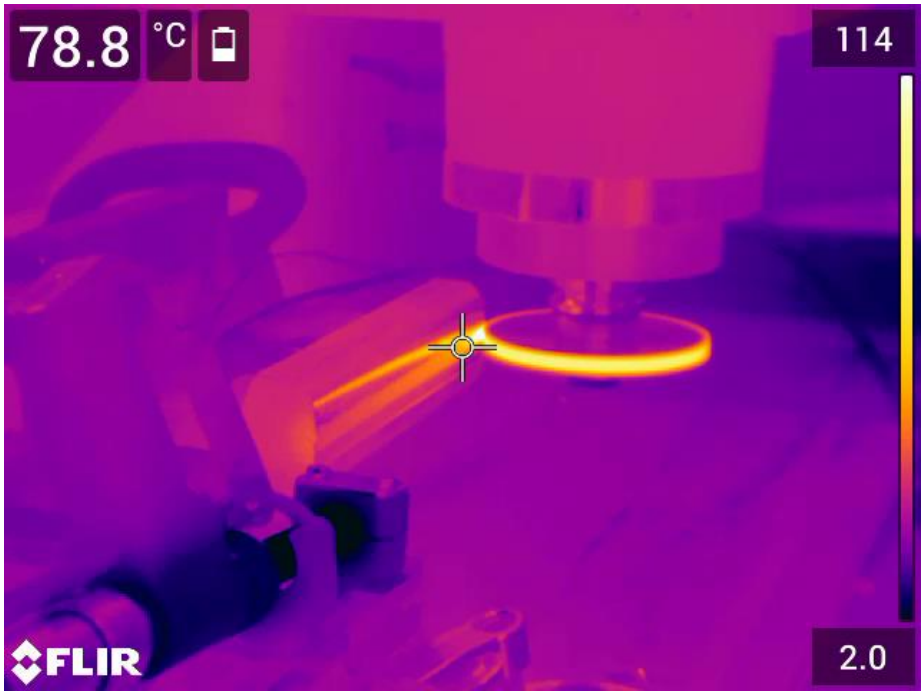

Pass 4

10.3 High Spindle Speed – Low Feed Rate (HSS-LFR)

Pass 2

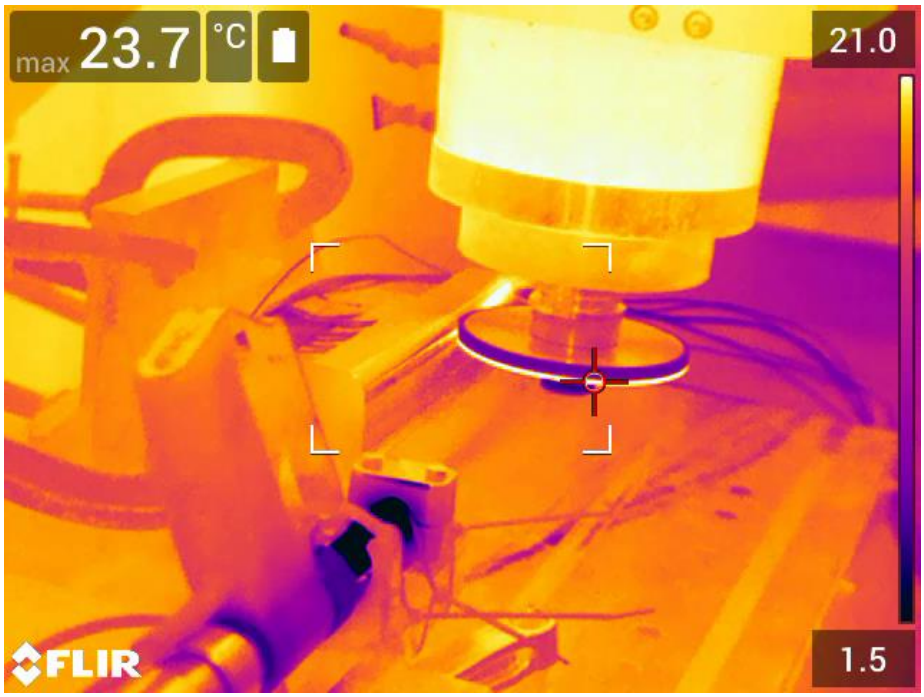

Pass 3

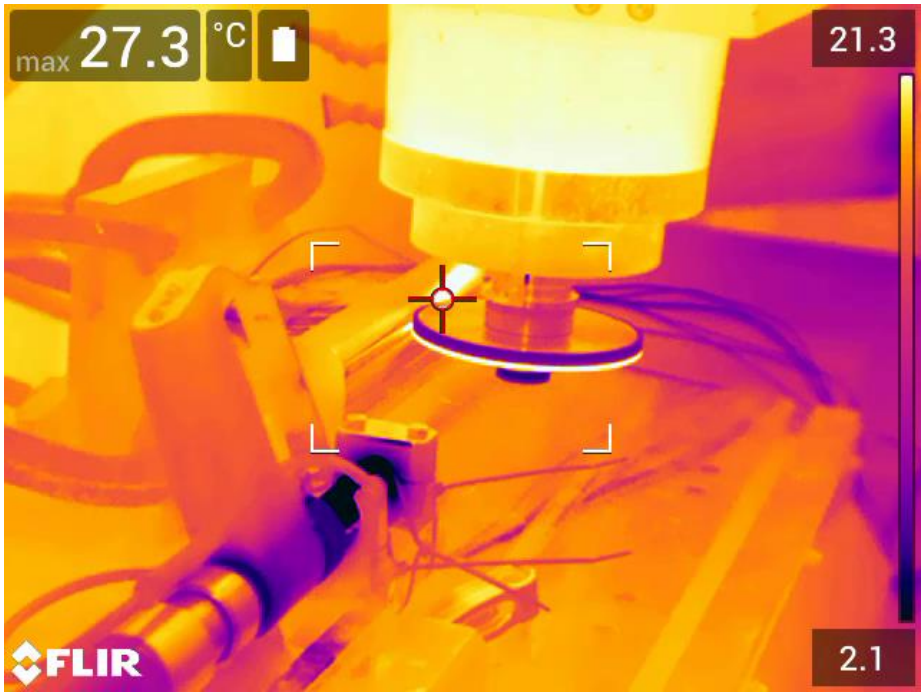

Pass 4

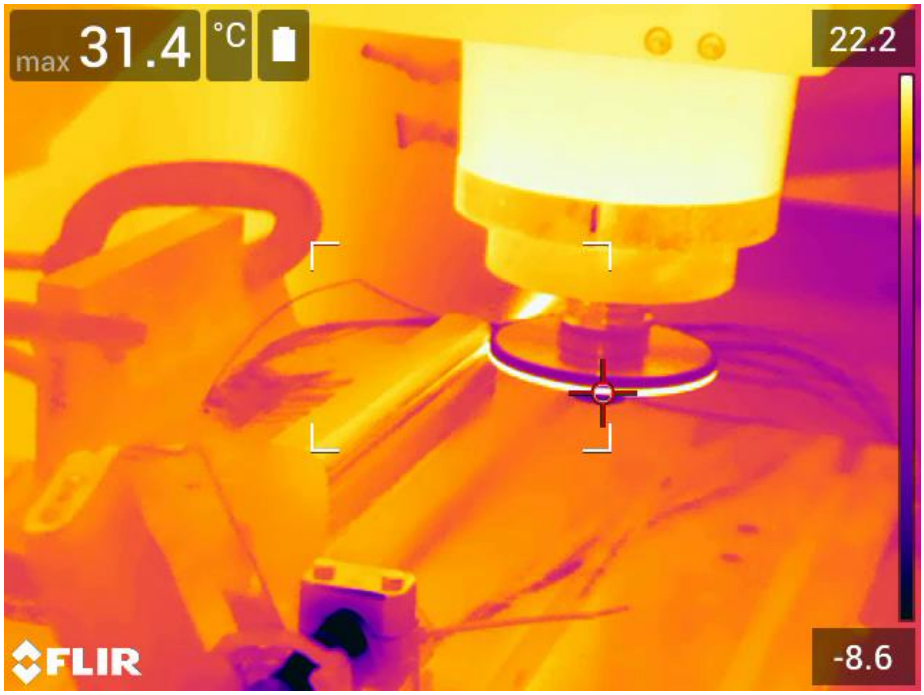

10.4 High Spindle Speed – High Feed Rate (HSS-HFR)

Pass 2

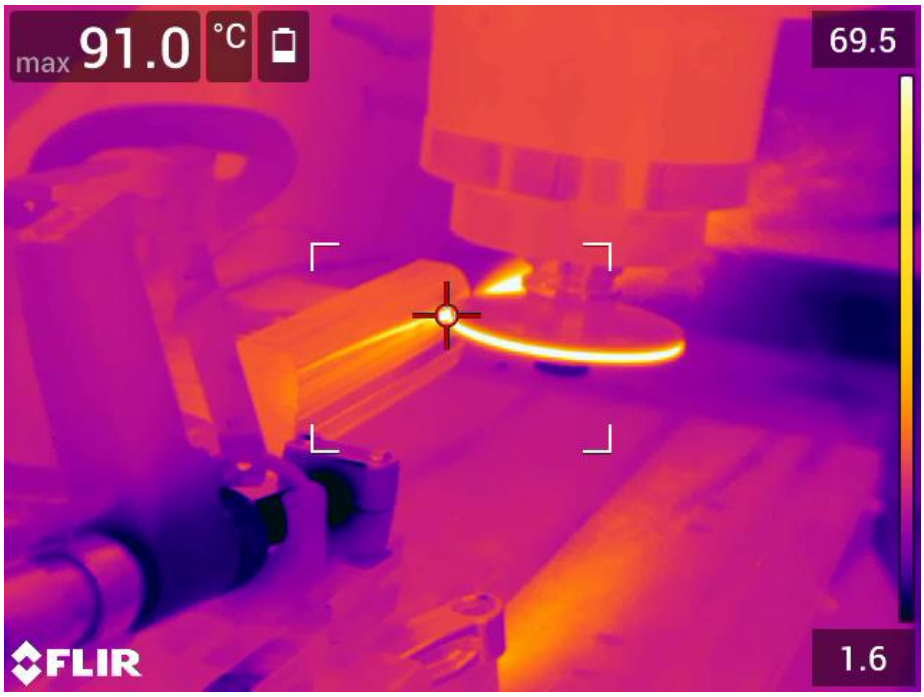

Pass 3

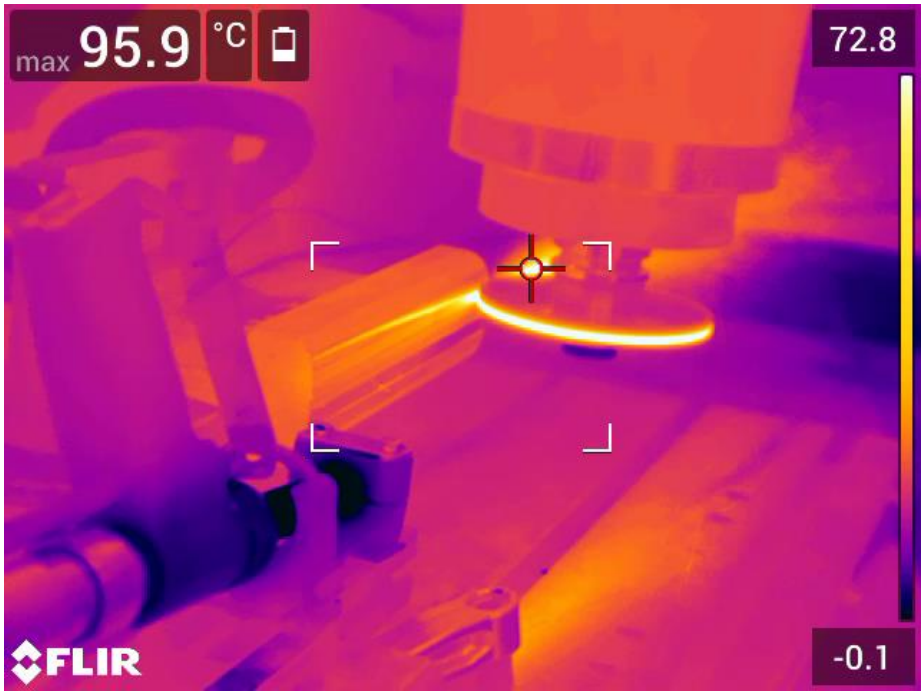

Pass 4

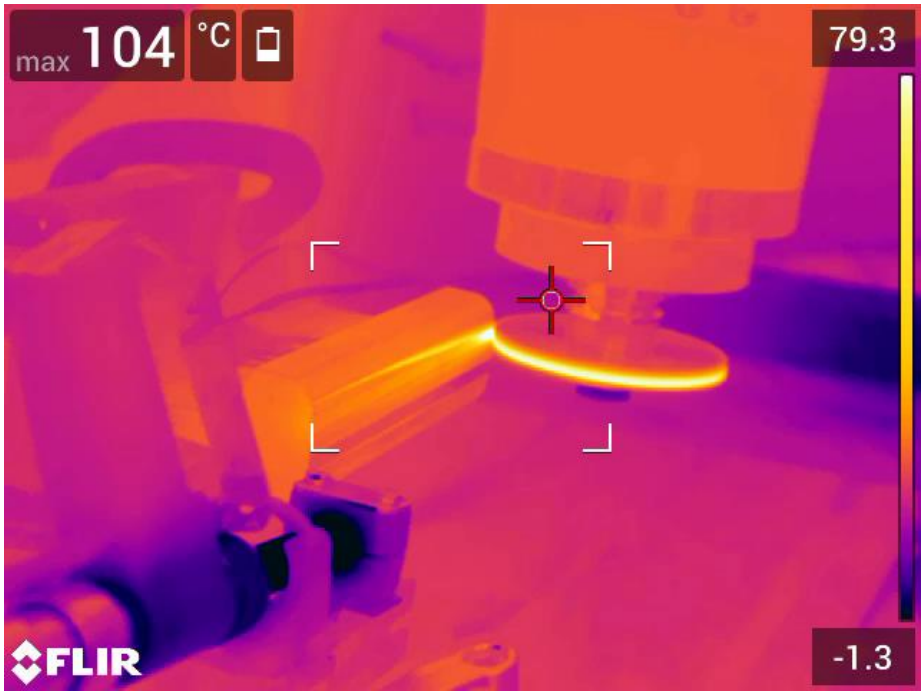

11 Appendix C – Thermal Images of Grinding Passes Conducted on Metro dé Medellín Line A

Pass 5

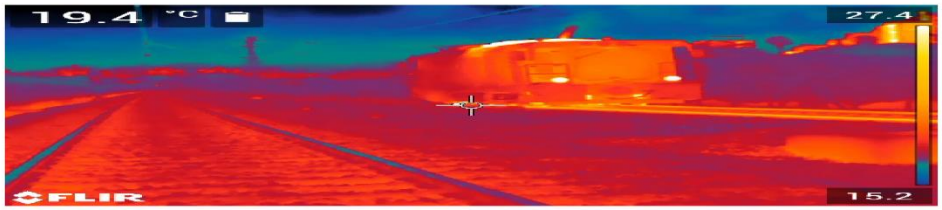

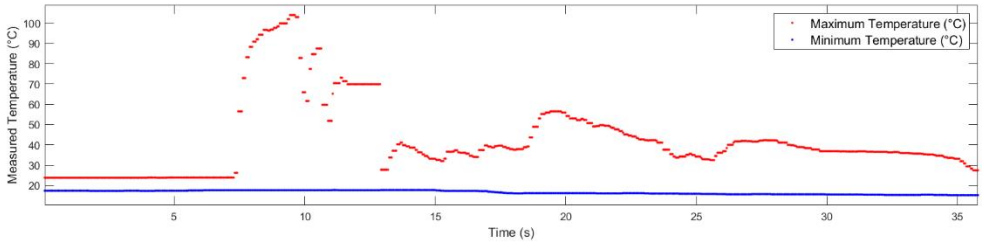

Pass 6

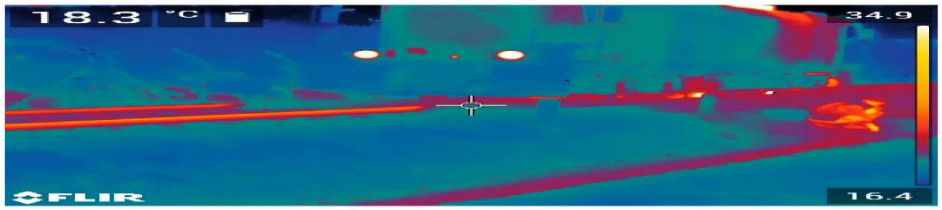

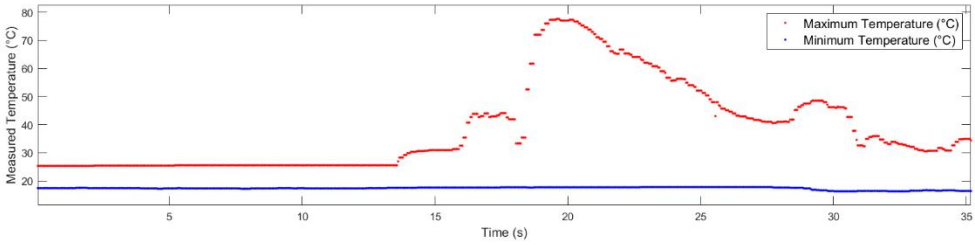

Pass 7

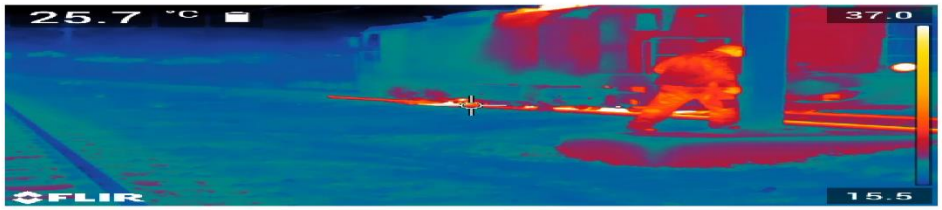
25.7 °C
37.0
15.5
FLIR

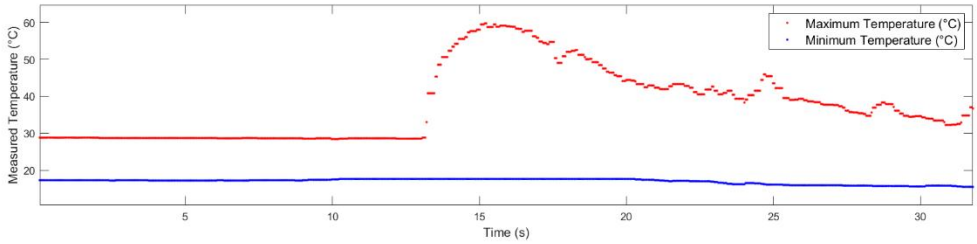
Maximum Temperature (°C)
Minimum Temperature (°C)
Measured Temperature (°C)
Time (s)

Pass 8

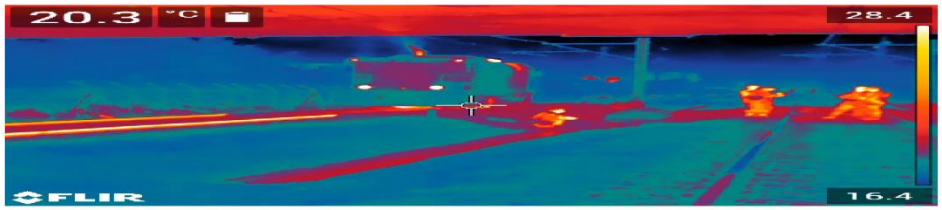
20.3 °C
28.4
16.4
FLIR

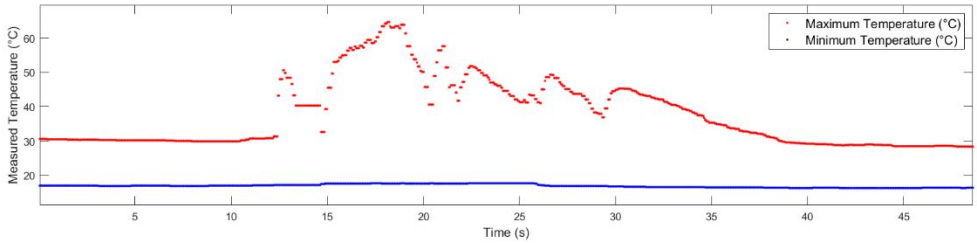
Maximum Temperature (°C)
Minimum Temperature (°C)
Measured Temperature (°C)
Time (s)

Pass 9

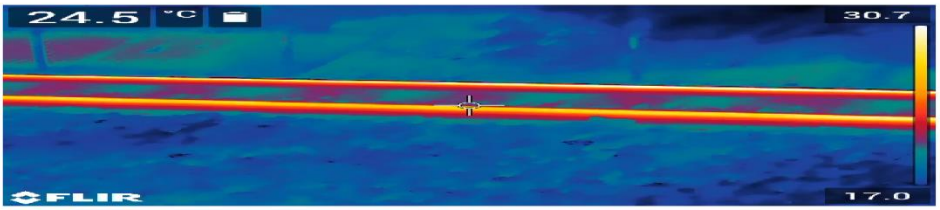

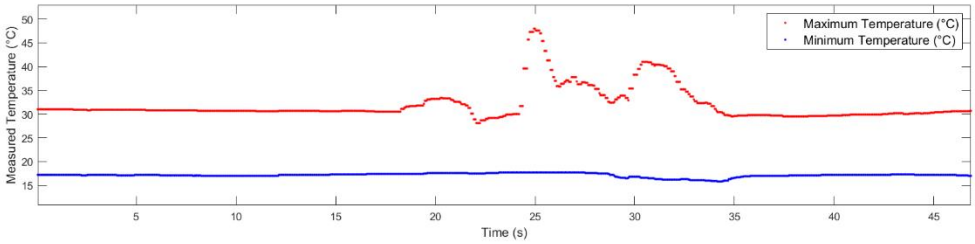

Pass 10

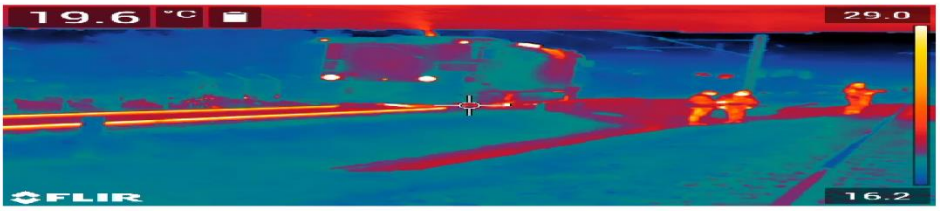

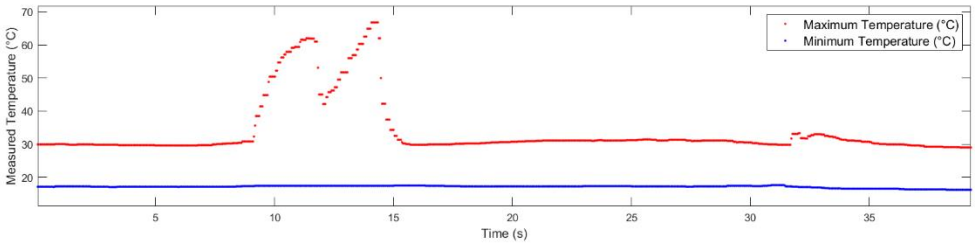

Pass 11

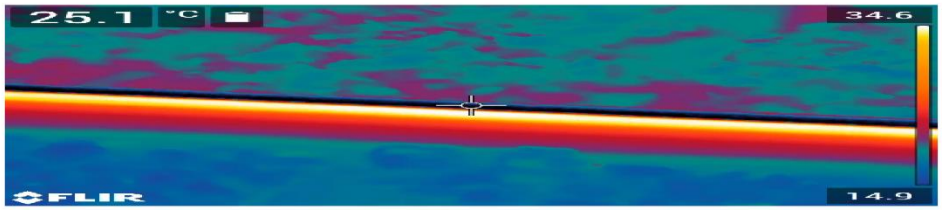

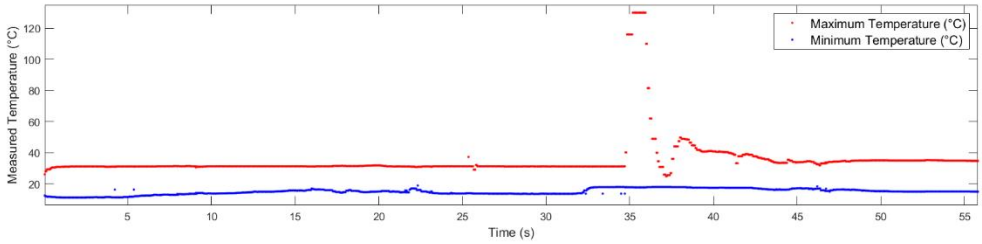

Pass 17

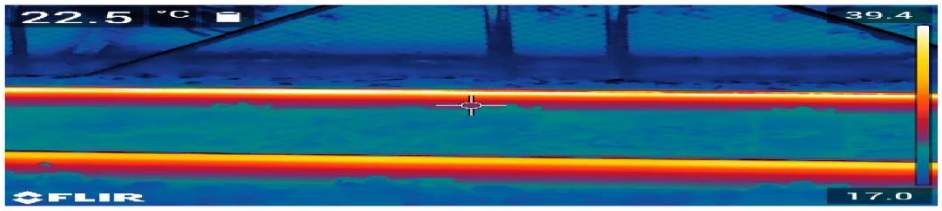

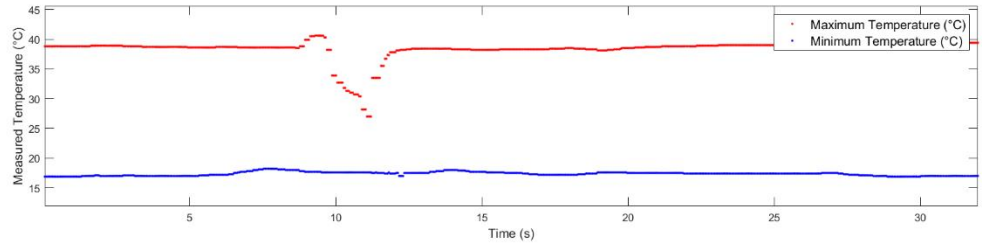

Pass 18

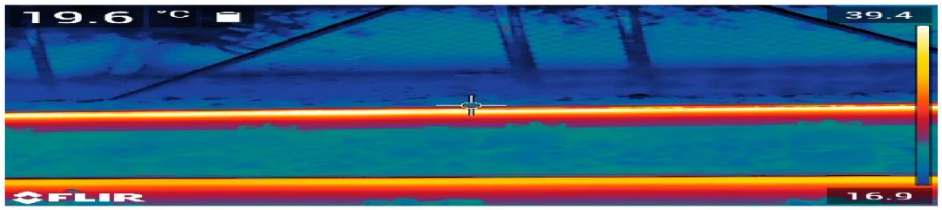

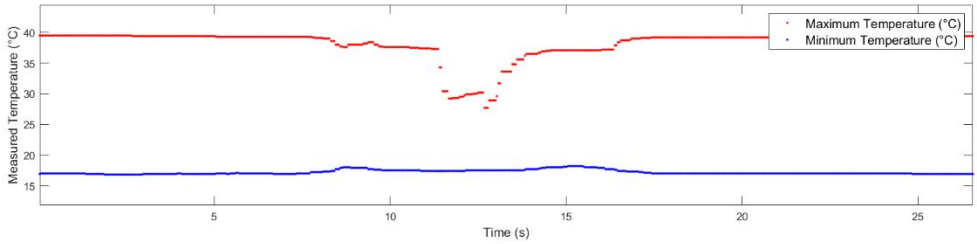

Pass 19

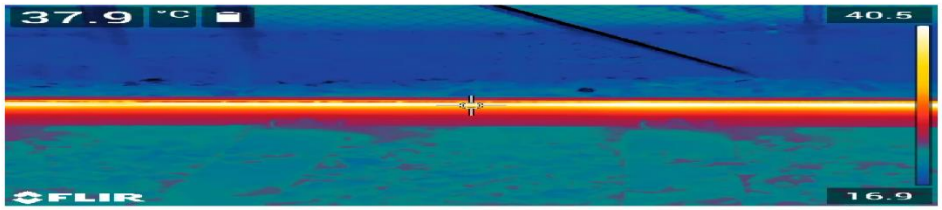

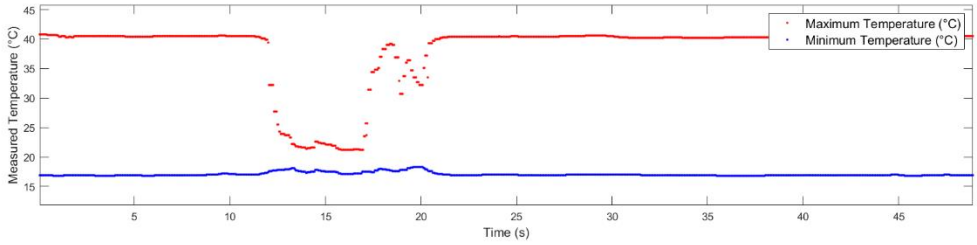

12 Appendix D – Analysis Codes

The following MATLAB code was written to analyse the thermal video recordings are presented in this section.

```
clear variables

%CHANGE the PATH NAME in line 7 to LEAD TO THE SAME DIRECTORY as where your
%videos and csv files are - THE CODE WILL NOT WORK IF THE VIDEOS AND CSV
%FILES ARE NOT IN THE SAME DIRECTORY - GOOD LUCK

cd("INSERT WORKING DIRECTORY WHICH CONTAINS YOUR CORRESPONDING CSV AND VIDEO" +
...
    " OR THIS IS CODE IS ON TRACK TO NOWHERE")
a = dir('*.csv');
b = cell(1,length(a));
for i=1:length(a)
    val = a(i).name;
    b{i} = val;
end

%Choose which video you want to view
vid = input('Video ID: '); % user inputs the video ID
s = strcat('*',vid,'*','.csv'); % this format tells matlab to search for any csv
file with the ID
vid_name = dir(s).name; %this line carries out the search (it's called a wildcard)
tempData = readmatrix(vid_name); %reads the temperature data

frameNumber = tempData(:,1);
maxFrame = length(tempData);

%Subplot set up
ax1 = subplot(2, 1, 1);
ax2 = subplot(2, 1, 2);

filename = vid; % name of video file in the format 'File name'
v = VideoReader(filename);
lastFrame = read(v, inf);
numFrames = v.NumFrames;
FrameRate = numFrames/v.Duration;
% This is a more accurate way to find the number of frames & it equals that of the
csv files
%It's more accurate because the other method is an estimate, but it's only
%accurate if MATLAB has read all the frames, hence line 29 exists

%All of video was read so has no frames left, so object needs to be reassigned
v = VideoReader(filename);

%Display the first frame in the top subplot
vidFrame = readFrame(v);
image(vidFrame, 'Parent', ax1)
ax1.Visible = 'off';

%Load the Temperature Data
time = 1/FrameRate:1/FrameRate:v.Duration; %converts from frame to seconds
tempMax = tempData(:,2);
```

```
tempMin = tempData(:,3); % Allocating these variables to the columns isn't really
necessary, but it helps with legibility

index = 1:numFrames;
i = 2;

%Display the plot corresponding to the first frame in the bottom subplot
h1 = plot(ax2, time(1:index(i)), tempMax(1:index(i)),'r.');
hold on
h2 = plot(ax2, time(1:index(i)), tempMin(1:index(i)),'b.');
%Fix the axes
ax2.XLim = [time(1) time(end)];
ax2.YLim = [tempMin(index(i))-5 tempMax(index(i))+5];
xlabel('Time (s)','FontSize',12)
ylabel('Measured Temperature (°C)','FontSize',12)
legend(["Maximum Temperature (°C)" "Minimum Temperature (°C)"],'FontSize',12,
'Location','northeast')


%%Animate
while hasFrame(v)
    if i == maxFrame
        break
    end
    pause(1/FrameRate);

    vidFrame = readFrame(v);
    image(vidFrame, 'Parent', ax1);
    ax1.Visible = 'off';

    ax2.YLim = [min(tempMin(1:index(i)))-5 max(tempMax(1:index(i)))+ 5];

    i = i + 1;
    set(h1, 'YData', tempMax(1:index(i)), 'XData', time(1:index(i)))
    set(h2, 'YData', tempMin(1:index(i)), 'XData', time(1:index(i)))
end

M= max(tempMax);
fprintf('The maximum temperature observed is %2f degC. \n', M)
```

The MATLAB code utilised to predict the temperature-depth profile for superabrasive grinding passes is shown below.

```
clc
% %The rail used in this study will be of grade R260
% %Aim of this code is to determine the temperature depth profile of a ground
% %rail. It is expected that this will tend to an asymptote
%
%
%
%
% % Q'=; %Material removal to be utilised
a_e= 0.025/1000; %depth of cut (m)
b_w= (64.45)/1000; %wheel width (m) %%%%%CHECK%%%%%%
v_w= (0.6*1000)/(60*60); %workpiece feedrate at 0.6kph and 2.58 kph converted to
m/s
F_t=[153, 153]; % Average tangential force in first pass (N)
```

```
F_t_label = ["6000 rpm Pass 1:"+" F_{t}= "+num2str(F_t(1),3)+" N", "12000 rpm Pass
1:"+ " F_{t}= " + num2str(F_t(2),3) + " N"];
F_t_colour = ["k-s","b-s", "c-s","r-s","k-^", "b-^", "c-^","r-^"];
%%Wheel properties
d_s = 156/1000; %convert grinding wheel diameter from mm to m
r0 = 25*10^-6; %estimated radius of a reasonably sharp grain (m) (Duscha et al.,
2010)

%%%%%%%%%%%%%%%

%Thermal properties
k_w = 51; %W/mK %thermal conductivity of workpiece (@20 deg)
k_g = 240; %W/mK thermal conductivity of CBN grain (Rowe et al., 2013)
rho = 7840; %kg/m3 density of steel
c_w = 500; %J/kgK specific heat capacity of the workpiece material (Zhou et. al,
2021)
alpha_w=k_w/(rho*c_w); %thermal diffusivity of workpiece (m^2/s)
T_mp= 1400 + 273.15; %melting temp used in the calculation of chip energy of
steels (Rowe et al, 2013)
%derived parameters
l_c= sqrt(d_s*a_e); %geometric contact length
beta_w = sqrt(k_w*rho*c_w); %thermal effusivity of the workpiece
%beta_g = 0.14*10^9; %Units J^2*m^4*K^2, from Malkin and Guo et al
Pe=(v_w*l_c)/(4*alpha_w); %According to Rowe et al (2013), the Peclet number
determines the C-factor
if (Pe > 10)
    C=1.06;
elseif (0.2<Pe && Pe<10)
    C=(0.95/pi)*((2*pi)+(Pe/2))^0.5;
else
    C=0.76;
end
%%%

h_ch=(rho*c_w*v_w*a_e)/l_c; %heat conduction coefficient of chips
h_w=(beta_w/C)*(sqrt(v_w/l_c)); %conduction coefficient for workpiece (W/m^2*K)

h_f=0; %convection coefficient of fluid
t_c=l_c/v_w; %contact time or duration of heating across contact area, unit (s)

%basic thermal rise
%Temperature rise based on net heat into the workpiece

% deltaT = q_w*(C/beta_w)*(l_c/v_w)^0.5; %


t_len=0.001:0.001:0.003; %units in (s)
z_len=0:0.000005:0.0015; %According to Rowe(2013)this should be a range up to the
3mm

T=zeros(length(z_len),length(t_len), length(F_t)); %returns zeros of the length of
matrix
counter_t=0;
for i=1:length(F_t)
    if i<=1
        Spindle_Speed=6000; %12000rpm for superabrasive grinding
    else
        Spindle_Speed=12000; %rpm
    end
```

```
    v_s = Spindle_Speed*(d_s/2)*2*pi/60; %convert cutting speed (grinding wheel
velocity) from rpm to m/s


    Power= F_t(i)*v_s; %grinding power (W) or (N.ms^-1)
    %Assuming that the grinding power is converted into heat
    q_t=(Power)/(l_c*b_w); %total heat flux (W/m^2)

    R_ws=(1+(k_g/(beta_w * sqrt(r0*v_s))))^-1; %Estimate worpiece-wheel heat flux
ratio (dimensionless)
    q_w= R_ws*q_t; %heat flux into the workpiece (W/m^2)
    T_max= (q_t-(h_ch*T_mp))/((h_w/R_ws)+h_f);   %Max temperature for dry grinding
of rail
    fprintf('%d is the approximate maximum temperature. \n', T_max);
    for j=1:length(t_len) %units in (s)
        M=4*q_w*(t_len(j)^(0.5))/sqrt(pi*k_w*rho*c_w);
        counter_t=counter_t+1;
        counter_z=0;
        for k=1:length(z_len) %According to Rowe(2013) this can be a range up to
about 3mm where
            counter_z=counter_z+1;

            N=(1-(2/3*(t_len(j)/t_c)-((z_len(k)^2)/(6*alpha_w*t_c))))*exp(-
(z_len(k)^2)/(4*alpha_w*t_len(j)));
            O=(2*q_w*z_len(k)/k_w)*(1-(t_len(j)/t_c)-
((z_len(k)^2)/6*alpha_w*t_c))*(1-erf(z_len(k)/sqrt(4*alpha_w*t_len(j))));
            intValue = M*N -0;
            T(k,j, i)= intValue; %maximum temperature of the subsurface

        end
    end
end
%figure
%plot(t_len,T(1,:))


figure
for m=1:length(F_t)
    semilogx(z_len*1000,T(:,1, m)+ 20, F_t_colour(m)) %The ambient temperature is
taken as 20 degC; 293.15 KELVIN)
    hold on
end
legend(F_t_label)
fontsize(20,"points")
xlabel('Depth below surface (mm)')
ylabel('Subsurface temperature (°C)')
% Plot
```

The MATLAB code utilised to predict the temperature-depth profile for face and peripheral grinding passes is shown below.

```
clc
% %The rail used in this study will be of grade R260
% %Aim of this code is to determine the temperature depth profile of a ground
% %rail. It is expected that this will tend to an asymptote
%
%
```

```
%
%
% % Q'=; %Material removal to be utilised
a_e= 0.025/1000; %depth of cut (m) - 2nd feed rate will be 2.58
b_w= (64.45)/1000; %wheel width (m) %%%%%CHECK%%%%%
v_w= 0.033333333333333333; % (2.58*1000)/(60*60); %workpiece feedrate (m/s)
F_t=[192.402647, 233.236497, 153.838871, 342.514007, 350.05384, 266.670772,
291.841418, 425.224416]; % Average tangential force in first pass (N)
F_t_label = ["2000 rpm Pass 1:"+ " F_{t}= " + num2str(F_t(1),3) + " N", "2000 rpm
Pass 2:"+ " F_{t}= " + num2str(F_t(2),3) + " N", "2000 rpm Pass 3:"+ " F_{t}= " +
num2str(F_t(3),3) + " N", "2000 rpm Pass 4:"+ " F_{t}= " + num2str(F_t(4),3) + "
N", "3000 rpm Pass 1:"+ " F_{t}= " + num2str(F_t(5),3) + " N", "3000 rpm Pass 2:"+
" F_{t}= " + num2str(F_t(6),3) + " N", "3000 rpm Pass 3:"+ " F_{t}= " +
num2str(F_t(7),3) + " N", "3000 rpm Pass 4:"+ " F_{t}= " + num2str(F_t(8),3) + "
N"];
F_t_colour = ["k-s","b-s", "c-s","r-s","k-^", "b-^", "c-^","r-^"];
%%Wheel properties
d_s = 150/1000; %convert grinding wheel diameter from mm to m
r0 = 25*10^-6; %estimated radius of a reasonably sharp grain (m) (Duscha et al.,
2010)

%%%%%%%%%%%%%%%

%Thermal properties
k_w = 51; %W/mK %thermal conductivity of workpiece (@20 deg)
k_g = 8.4; %W/mK thermal conductivity of aluminium oxide (Zhou et. al, 2021)
rho = 7840; %kg/m3 density of steel
c_w = 500; %J/kgK specific heat capacity of the workpiece material (Zhou et. al,
2021)
alpha_w=k_w/(rho*c_w); %thermal diffusivity of workpiece (m^2/s)
T_mp= 1400 + 273.15; %melting temp used in the calculation of chip energy of
steels (Rowe et al, 2013)
%derived parameters
l_c= sqrt(d_s*a_e); %geometric contact length
beta_w = sqrt(k_w*rho*c_w); %thermal effusivity of the workpiece
%beta_g = 0.14*10^9; %Units J^2*m^4*K^2, from Malkin and Guo et al
Pe=(v_w*l_c)/(4*alpha_w); %According to Rowe et al (2013), the Peclet number
determines the C-factor
if (Pe > 10)
    C=1.06;
elseif (0.2<Pe && Pe<10)
    C=(0.95/pi)*((2*pi)+(Pe/2))^0.5;
else
    C=0.76;
end
%%%

h_ch=(rho*c_w*v_w*a_e)/l_c; %heat conduction coefficient of chips
h_w=(beta_w/C)*(sqrt(v_w/l_c)); %conduction coefficient for workpiece (W/m^2*K)

h_f=0; %convection coefficient of fluid
t_c=l_c/v_w; %contact time or duration of heating across contact area, unit (s)

%basic thermal rise
%Temperature rise based on net heat into the workpiece

% deltaT = q_w*(C/beta_w)*(l_c/v_w)^0.5; %
```

```
t_len=0.001:0.001:0.003; %units in (s)
z_len=0:0.000005:0.0015; %According to Rowe(2013)this should be a range up to the
3mm

T=zeros(length(z_len),length(t_len), length(F_t)); %returns zeros of the length of
matrix
counter_t=0;
for i=1:length(F_t)
    if i<=4
        Spindle_Speed=2000; %12000rpm for superabrasive grinding
    else
        Spindle_Speed=3000; %rpm
    end
    v_s = Spindle_Speed*(d_s/2)*2*pi/60; %convert cutting speed (grinding wheel
velocity) from rpm to m/s

    Power= F_t(i)*v_s; %grinding power (W) or (N.ms^-1)
    %Assuming that the grinding power is converted into heat
    q_t=(Power)/(l_c*b_w); %total heat flux (W/m^2)

    R_ws=(1+(k_g/(beta_w * sqrt(r0*v_s))))^-1; %Estimate worpiece-wheel heat flux
ratio (dimensionless)
    q_w= R_ws*q_t; %heat flux into the workpiece (W/m^2)
    T_max= (q_t-(h_ch*T_mp))/((h_w/R_ws)+h_f);   %Max temperature for dry grinding
of rail
    fprintf('%d is the approximate maximum temperature. \n', T_max);
    for j=1:length(t_len) %units in (s)
        M=4*q_w*(t_len(j)^(0.5))/sqrt(pi*k_w*rho*c_w);
        counter_t=counter_t+1;
        counter_z=0;
        for k=1:length(z_len) %According to Rowe(2013) this can be a range up to
about 3mm where
            counter_z=counter_z+1;

            N=(1-(2/3*(t_len(j)/t_c)-((z_len(k)^2)/(6*alpha_w*t_c))))*exp(-
(z_len(k)^2)/(4*alpha_w*t_len(j)));
            O=(2*q_w*z_len(k)/k_w)*(1-(t_len(j)/t_c)-
((z_len(k)^2)/6*alpha_w*t_c))*(1-erf(z_len(k)/sqrt(4*alpha_w*t_len(j))));
            intValue = M*N -0;
            T(k,j, i)= intValue; %maximum temperature of the subsurface

        end
    end
end
%figure
%plot(t_len,T(1,:))


figure
for m=1:length(F_t)
    semilogx(z_len*1000,T(:,1, m)+ 20, F_t_colour(m)) %The ambient temperature is
taken as 20 degC; 293.15 KELVIN)
    hold on
end
legend(F_t_label)
fontsize(20,"points")
xlabel('Depth below surface (mm)')
ylabel('Subsurface temperature (°C)')
% Plot
```